

**ASSOCIATED PARTICLE NEUTRON ELEMENTAL IMAGING FOR
NONINVASIVE MEDICAL DIAGNOSTICS**

by

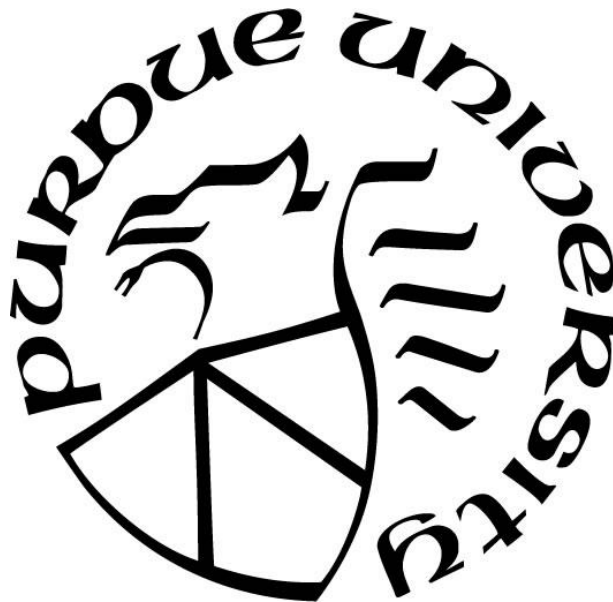
Michael Robert Abel

A Dissertation

Submitted to the Faculty of Purdue University

In Partial Fulfillment of the Requirements for the degree of

Doctor of Philosophy



School of Health Sciences

West Lafayette, Indiana

May 2019

**THE PURDUE UNIVERSITY GRADUATE SCHOOL
STATEMENT OF COMMITTEE APPROVAL**

Dr. Linda Nie, Major Professor

School of Health Sciences

Dr. David Koltick

Department of Physics and Astronomy

Dr. Jim Schweitzer

School of Health Sciences

Dr. Keith Stantz

School of Health Sciences

Approved by:

Dr. Shuang Liu

Head of the Graduate Program

To my family

ACKNOWLEDGMENTS

I would like to extend the warmest appreciation to my major professor, Dr. Linda Nie, who not only championed my admission to the Purdue University graduate program, but provided the patient and steadfast guidance of the greatest professional mentor I have ever known. Thank you also to my committee members – Dr. David Koltick, Dr. Jim Schweitzer, and Dr. Keith Stantz – for their valuable insight, as well as to Dr. Jason Harris for his constructive comments as an exam committee member and fellow health physicist. To my past and current lab members, to the Couch Bros, and to the HP team at Honeywell as I knew it, I raise a glass and say cheers! Thank you for all of the help over the years, and more importantly, for the laughs and friendship. And finally, thank you to Lindsay, Mom, Dad, Nick, and even Revan for the enduring love and support; we made this journey together.

TABLE OF CONTENTS

LIST OF TABLES	9
LIST OF FIGURES	10
ABSTRACT	12
CHAPTER 1. INTRODUCTION AND BACKGROUND.....	13
1.1 Overview.....	13
1.2 Elemental Disease Signatures	17
1.2.1 Principles and Background	17
1.2.2 Cancer	18
1.2.3 Alzheimer’s.....	21
1.2.4 Parkinson’s	22
1.2.5 Other Diseases	24
1.2.6 The Significance of Iron in Disease Diagnostics.....	26
1.2.7 Conclusions.....	29
1.3 Diagnostic Imaging in Medicine.....	29
1.3.1 Principles and Background	29
1.3.2 X-Ray Radiography	31
1.3.3 X-Ray Computed Tomography	34
1.3.4 Single Photon Emission Computed Tomography.....	36
1.3.5 Positron Emission Tomography	39
1.3.6 Magnetic Resonance Imaging.....	42
1.3.7 Ultrasound.....	43
1.3.8 Photoacoustic Imaging.....	44
1.3.9 Neutron Radiography.....	45
1.3.10 Conclusions	47
1.4 Neutron Activation Analysis.....	47
1.4.1 Principles and Background	47
1.4.2 Types of NAA.....	48
1.4.2.1 Delayed-Gamma.....	48
1.4.2.2 Prompt-Gamma	51

1.4.3	Non-Medical Applications.....	55
1.4.4	Medical Applications.....	58
1.4.5	Competing Analytical Modalities.....	64
1.4.6	Conclusions.....	65
1.5	The Associated Particle Neutron Imaging Technique	66
1.5.1	Principles and Background.....	66
1.5.2	Sealed Tube Neutron Generators.....	67
1.5.2.1	Construction and Operation.....	67
1.5.2.2	Applicability to APNEI	69
1.5.2.3	Deuterium – Deuterium vs Deuterium – Tritium	71
1.5.3	Imaging Plate.....	73
1.5.4	Projective Imaging Resolution	75
1.5.5	Depth Imaging Resolution.....	77
1.5.6	Conclusions.....	78
CHAPTER 2.	FEASIBILITY OF APNEI.....	79
2.1	Overview.....	79
2.2	Materials and Methods.....	81
2.2.1	Monte Carlo Simulations.....	81
2.2.2	Model of a Reference Man	82
2.2.3	Model of APNEI System Components and Properties.....	82
2.2.4	The APNEI Process in MCNP.....	84
2.3	Results.....	87
2.3.1	Simulated Iron Gamma-Ray Counts.....	87
2.3.2	Radiation Dose Assessment and Iron Gamma-Ray Counts Normalized to Dose	89
2.3.2.1	Radiation Dosimetry.....	89
2.3.2.2	MCNP Dose and Iron Gamma-Ray Count Approximation.....	91
2.3.2.3	Tritium Buildup and 14 MeV Neutrons	93
2.3.3	Image Simulation.....	95
2.3.3.1	Idealistic APNE Image	95
2.3.3.2	Realistic APNE Image.....	96
2.4	Discussion.....	99

2.5	Conclusion	101
CHAPTER 3. MONTE CARLO SIMULATIONS OF SPATIAL RESOLUTION		103
3.1	Overview.....	103
3.2	Materials and Methods.....	106
3.2.1	Monte Carlo Simulations.....	106
3.2.2	Simulation Model and Technical Basis	107
3.2.3	Projective Resolution.....	110
3.2.4	Depth Resolution	113
3.2.5	Three-Dimensional Resolution	114
3.3	Results.....	115
3.3.1	Projective Resolution.....	115
3.3.2	Depth Resolution	121
3.3.3	Three-Dimensional Resolution.....	127
3.4	Discussion.....	133
3.5	Conclusion	136
CHAPTER 4. FAST NEUTRON SCATTER ANALYSIS AS A SURROGATE		137
4.1	Overview.....	137
4.2	Materials and Methods.....	141
4.2.1	Fast Neutron Inelastic Scatter Analysis.....	141
4.2.1.1	Adelphi DD Neutron Generator	142
4.2.1.2	Sodium Iodide Detector and Photomultiplier Tube.....	142
4.2.1.3	Supporting Apparatus and Operating Protocol.....	144
4.2.2	Monte Carlo Simulations.....	146
4.2.2.1	FNISA Monte Carlo Model.....	147
4.2.2.2	Gaussian Energy Broadening of Gamma Spectra	149
4.2.2.3	Associated Particle Collimation	150
4.3	Results.....	153
4.3.1	FNISA Surrogate Experiment.....	153
4.3.2	Spectral Validation Using Monte Carlo Simulations	157
4.3.3	Collimated vs Un-collimated Gamma Spectra	158
4.3.4	Improved Iron LLD due to Associated Particle Collimation.....	161

4.4 Discussion	162
4.5 Conclusion	166
CHAPTER 5. SUMMARY AND FUTURE DIRECTIONS	167
LIST OF REFERENCES	172

LIST OF TABLES

Table 1.1 – Selected elemental concentrations in cancerous vs normal human tissue	16
Table 1.2 – Selected elemental concentrations in AD vs normal human tissue	22
Table 1.3 – Iron concentrations in diseased vs normal human tissue	28
Table 1.4 – Comparison of sensitivities for fast (n,n' γ) reactions and DGNAA reactions	54
Table 1.5 – The concentration of Cl and Na in blood using a DGNAA technique	60
Table 2.1 – Number of counts detected by HPGe detectors as determined by MCNPX	87
Table 2.2 – Number of gamma-ray counts normalized to 5 mSv equivalent dose to the liver.....	92
Table 3.1 – Ideal coincident count contributions from target voxels to corresponding pixels...	117
Table 3.2 – Coincident count contributions to time-defined pixels in the depth dimension	123
Table 3.3 – Coincident count contributions - target voxels to corresponding pixels in space ...	129
Table 4.1 – Experimental vs simulation full-width at half maxima	150

LIST OF FIGURES

Figure 1.1. Fluorescence spectrum of signature elements in liver tissue.....	19
Figure 1.2. ^1H and ^{23}Na images of a patient with carcinoma and edematous tissue.....	20
Figure 1.3 Total levels of iron in PD and age-matched control human autopsy brains.....	23
Figure 1.4 Regulation of cellular iron concentrations.	28
Figure 1.5 Bremsstrahlung x-ray spectrum.....	32
Figure 1.6 Basic components of projective radiography	34
Figure 1.7 Complementary functional & anatomical information in SPECT/CT	36
Figure 1.8 Gamma camera cross section	38
Figure 1.9 Principles of coincident counting in PET	40
Figure 1.10 Classic neutron radiograph of a rose in a lead flask.....	45
Figure 1.11 Radiographs of a rat head using epithermal neutrons and 42 kV x-rays.....	46
Figure 1.12 Schematic of the neutron capture process	49
Figure 1.13 Decay scheme of Mn-56.....	49
Figure 1.14 Apparatus for PGNAA of tibia phantom.....	52
Figure 1.15 Example of a $(n,n'\gamma)$ nuclear reaction	53
Figure 1.16 Calculated detection limits for NIST-operated PGNAA system.....	57
Figure 1.17 Simple schematic of NSECT system.....	61
Figure 1.18 NSEC Tomographic images of elemental concentrations in renal cancer	62
Figure 1.19 Simulated tomographic resolution in NSECT.....	63
Figure 1.20 Adelphi DD-110 neutron generator.....	68
Figure 1.21 Schematic of the APNEI technique.....	70
Figure 1.22 Effects of pixelated detector on projective resolution.....	73
Figure 1.23 Cross section of a ZnO:Ga α -particle detector	75
Figure 1.24 Neutron source spot and damage due to insufficient cooling.....	76
Figure 1.25 Effects of source spot diameter and pixelated detector on projective resolution	77
Figure 2.1 A longitudinal cross section of the human body model defined in MCNPX.....	83
Figure 2.2 A transverse cross section of the human body model in MCNPX.....	84
Figure 2.3 Inelastic scatter gamma ray counts with voxel iron concentration - to pure iron.....	88
Figure 2.4 Inelastic scatter gamma ray counts with voxel iron concentration - to 10,000 ppm...	89

Figure 2.5 DD generator x-ray spectra (using HPGe), with and without lead shielding	91
Figure 2.6 Cube-shaped voxel simulation with perfect reflection about point source spot.....	96
Figure 2.7 Cube-shaped voxel simulation with reflection about 2 mm source spot.....	98
Figure 2.8 Example of a pinhole image - projected onto a wall through a hole in the ceiling	99
Figure 3.1 A transverse cross section of the imaging model	109
Figure 3.2 A cross section of the target array in the projective dimension	111
Figure 3.3 A transverse cross section of the imaging model for depth resolution.....	113
Figure 3.4 Nine-voxel interrogated object, shaded according to iron concentration.....	116
Figure 3.5 Quasi-perfect 2D image of the target object on the pixelated imaging plate	117
Figure 3.6 Realistic 2D image of the target object on the pixelated imaging plate	119
Figure 3.7 Quasi-perfect 2D image of the target object in the depth dimension	123
Figure 3.8 Realistic image of the target object in the depth dimension in space.....	124
Figure 3.9 Time slice layout in the depth dimension for generating tomographic images.....	128
Figure 3.10 Realistic 6-slice aggregate image of the 9-voxel target array	130
Figure 3.11 [1-6] Series of tomographic images of the iron-containing target array	131
Figure 4.1 Schematic of FNISA System – not to scale.....	144
Figure 4.2 Incomplete shielding arrangement of FNISA system	145
Figure 4.3 Complete shielding arrangement of the FNISA system	145
Figure 4.4 Longitudinal cross section of the FNISA system as defined in MCNP	148
Figure 4.5 Transverse cross section of the FNISA system as defined in MCNP	148
Figure 4.6 Diagram of the spatial collimation employed in MCNP using neutron kill zones....	152
Figure 4.7 Photon spectrum from NaI-based FNISA system	154
Figure 4.8 Photon spectrum from the gamma-ray region of interest with fitted curve	156
Figure 4.9 Photon spectrum from the MCNP overlaying the experimental spectrum.....	157
Figure 4.10 Comparison of photon spectra from MCNP.....	159
Figure 4.11 Comparison of photon spectra from MCNP in the region of interest	160
Figure 4.12 Calibration line for iron in the simulated FNISA system.....	162

ABSTRACT

Author: Abel, Michael, R. Ph.D.

Institution: Purdue University

Degree Received: May 2019

Title: Associated Particle Neutron Elemental Imaging for Noninvasive Medical Diagnostics

Committee Chair: Linda H. Nie

A novel system has been simulated with accompanying experimental data that is designed to provide spatial information of elemental concentrations at biologically relevant levels. Using a deuterium-deuterium (DD) neutron generator, two large high-purity germanium (HPGe) detectors operating in tandem, and the associated particle imaging (API) technique, elemental iron concentrations as low as 100 ppm have been resolved *in vivo* in the liver of a simulated reference man with an equivalent dose to the region of interest of < 5 mSv and an estimated whole body dose of 0.82 mSv. Using the Monte Carlo Neutral Particle (MCNP) transport code, achievable spatial resolutions in the projective and depth dimensions of < 1 cm and < 3 cm are achievable, respectively, for iron-containing voxels on the order of 1,000 ppm Fe – with an overall 225 ps system timing resolution, 6.25 mm² imaging plate pixels, and a Gaussian-distributed DD neutron source spot with a diameter of 2 mm. Additionally, as a departure from Monte Carlo simulations, the underlying concepts of fast neutron inelastic scatter analysis as an initial surrogate to true associated particle neutron elemental imaging (APNEI) were demonstrated using a DD neutron generator, iron-made interrogation targets, a sodium iodide detector, and physical neutron/gamma shielding, which yielded an approximate detection limit for iron of 3.45 kg which was simulated to improve to 0.44 kg upon incorporation of the associated particle collimation methodology.

The API technique allows concentrations of elements such as iron to be quantified due to time-tagged electronic collimation and corresponding background signal reduction. Inherent to the API process is the collection of spatial and temporal information, which allows the perceived origin of a photon signal to be identified in 3D space. This process was modeled algorithmically in MCNP and employed using relevant equipment and shielding geometries. By leveraging the capabilities of modern-day neutron generator and coincident timing technologies with high throughput signal processing discrimination, the applicability of APNEI to disease diagnostics and etiological research is promising.

CHAPTER 1. INTRODUCTION AND BACKGROUND

1.1 Overview

Cancer is the second leading cause of death in the United States, and one of the reasons many types of cancer are so often deadly is that they may progress to a late stage without causing apparent or distinctive symptoms in an affected individual. Despite the initial lack of distinguishing physical illness in an individual afflicted by some early-stage cancers or other neurological diseases such as Alzheimer's and Parkinson's, biological changes including shifts in the concentrations of various trace elements (such as iron) in affected tissues very frequently occur [1, 2, 3]. And while it is established in the literature that certain elemental concentrations in humans and animals may be measured by neutron activation analysis (NAA) *in vivo* [4, 5, 6], application of the technology to the diagnosis and characterization of cancers with elemental signatures remains limited. The lack of research in the area of NAA as it pertains to human health and disease is due, in part, to the inability of the technology to provide spatial information for trace elements at biologically relevant concentrations [7]. Such was the purpose of the Associated Particle Neutron Elemental Imaging (APNEI) study at hand – to develop a neutron imaging methodology which reduces background noise while maximizing the trace elemental inelastic scatter gamma-ray signal through the spatial and temporal collimation of fast neutrons. As APNEI has thus far only been attempted *in vitro* for objects of sizes and elemental compositions irrelevant to a biological system [8], the prospective sensitivity and resolution of an associated particle neutron imaging system for *in vivo* elemental analyses have been largely undefined – obscuring pathways to early disease diagnosis, etiological study, and intervention.

There is evidence in the literature that NAA techniques are useful in the diagnosis and management of some disorders as well as in body elemental composition analysis. However, the application of NAA technologies to *in vivo* medical diagnostics of trace elements remains largely undefined, predominantly owing to past technological limitations and the accompanying low signal-to-noise ratio (SNR) and loss of spatial information. But now that many radiation detection, imaging, and electronics technologies have evolved to theoretically yield a clinically useful SNR and spatial resolution for trace elemental concentrations *in vivo* using the associated particle technique [9, 10, 11], it is no longer necessary to accept the informational gap inherent of

conventional NAA. The contribution of the research presented in this document is thus expected to be an innovative imaging system optimized for *in vivo* application, one that is capable of delineating the location of target nuclei (in this case, Fe-56) and producing an image with a clinically valuable resolution by applying the associated particle methodology to spatially and temporally collimate fast neutrons. This contribution will be significant because it is the next step toward the development of a new tool in the field of medical imaging – one that is expected to be capable of detecting some asymptomatic cancers and neurological diseases earlier than ever before, as well as to offer insight into the etiology of certain diseases according to the observable elemental profiles. Such elemental signatures are the subject of considerable ongoing study with regard to early detection and tumor type differentiation [2, 9, 12], and the high rates of mortality of cancer and Alzheimer's in the U.S. are well known. A contribution in the field of APNEI is thus expected to enable subsequent thinking and research which will alleviate these issues and improve public health by providing a mechanism to fundamentally enhance the understanding of the development and progression of a variety of diagnostically challenging diseases.

APNEI can be viewed as a subset of neutron activation analysis (NAA), which is a rather broad field encompassing the use of fast, epithermal, or thermal neutrons as well as the detection of prompt or delayed gamma-rays resulting from capture or inelastic scatter nuclear reactions. By analyzing the resulting gamma-rays which are characteristic markers of the de-excitation of activated nuclei, an elemental profile of the interrogated volume may be established. However, research into NAA methodologies using fast neutrons and prompt inelastic scatter gamma-rays is lacking due to inadequate elemental sensitivity, particularly for trace elements *in vivo* which are applicable in medical diagnostics [2, 9, 11, 12]. The long-term objective of the research contained herein is therefore to solve the issue of inadequate sensitivity to trace elements by designing and constructing a prototype neutron elemental analysis system which will utilize the associated particle technique to maximize the relevant SNR, a methodology which simultaneously provides a mechanism by which the spatial information of target nuclei may be collected for imaging. The basis of the objective was to test the working hypotheses that 1) a trace element (i.e. iron) will be detectable at natural biological concentrations using fast neutron inelastic scatter analysis collimated for background signal reduction and that 2) iron-containing voxels at the scale of 1 cm^3 may be visualized *in vivo* using APNEI. The working hypotheses were tested using a systematic, two-pronged approach, where fast neutron inelastic scatter analysis (FNISA) experiments as a

surrogate to true APNEI allowed for the empirical determination of the sensitivity of the system to iron on one hand, while concurrent execution of Monte Carlo simulations on the other hand afforded opportunities for optimizing the interplay between the associated ion and gamma-ray detectors and thus the ability to identify the spatial resolution of the system for voxels composed of iron. Going forward, Monte Carlo (MC) simulation results and FNISA findings will form the basis for overall prototype design as well as provide iron sensitivity and spatial resolution expectations, and MC simulations will continue to supplement research progress through data validation, methodological improvement, and troubleshooting. The rationale for the undertaken work was to fill the gap in the base of knowledge of NAA regarding trace elemental analysis using associated particle collimation, the expectation for which is a focused application of NAA relevant to the fields of medical imaging and cancer diagnostics.

The justification of the need for this study is apparent upon reviewing the body of literature which currently exists for fast neutron scattering analysis and neutron elemental imaging. Not only is the majority of fast neutron activation analysis research concerned with the interrogation of bulk samples in homeland security and in geochemical survey applications requiring relatively low elemental sensitivities [13, 14, 15], but those that do explore *in vivo* applications tend to focus on biologically abundant elements such as carbon, nitrogen, and oxygen [4, 16]. Furthermore, in studies that specifically investigate *in vivo* neutron activation analysis of trace elements using a fast neutron source, many yet rely upon neutron capture reactions and their corresponding delayed gamma-rays, in which case the spatial information regarding trace elemental nuclei is lost [17, 18, 19]. And while the few fast neutron activation analysis studies which employed the associated particle technique have demonstrated its efficacy with high SNRs and reduced interference from clutter in both bulk ordnance detection and *in vivo* body composition analysis, they did so without consideration of human application for the detection of trace elemental disease signatures [20, 21]. So, while the concentrations of trace elements such as iron in a variety of primary and secondary tumors are known to vary from 40% to over 1,000% of the concentrations in the surrounding normal tissue [22], there are currently no means to noninvasively obtain spatial information of the trace elemental distribution *in vivo*.

The importance of trace elemental distributions in soft tissue is apparent upon reviewing the body of work regarding supposed elemental disease signatures. For example, Table 1.1 illustrates a small sample of the trace elemental concentrations affected in cancerous as opposed to normal

tissues [2, 9]. The data in Table 1.1 indicate that there are significant differences between cancerous and normal tissues regarding signature elemental concentrations. In the case of iron, the differences are more than adequate to discern cancerous from normal tissues, given a previously derived iron sensitivity of 40 ppm for a proposed APNEI system with a flux of 10^8 neutrons/cm² at the target tissue and corresponding dose of 50 mSv [9]. And while employing the associated particle technique would allow for the temporal collimation of gamma-ray signals from environmentally and biologically abundant elements (thereby greatly increasing trace elemental sensitivity), nearly all past studies have been conducted without *in vivo* applications in mind. Therefore, they have neglected many variables associated with optimizing the image resolution and sensitivity to trace elemental distributions, such as neutron beam spot diameter, ion detector pixel size, and ion and gamma-ray detector timing resolutions – with corresponding gaps in the use of phantoms that would be analogous to human organs with areas affected by cancer or other diseases having a trace elemental signature.

Table 1.1 – Selected elemental concentrations in cancerous vs normal human tissue [2]

Element	Tissue	Cancer ppm	Normal ppm
K	Breast	952	224 / 168
P	Breast	578 ± 79	223 ± 33
Fe	Kidney	440 ± 64	122 ± 35
Fe	Liver	1309	768
Fe	Lung	75.1 ± 9.7	199 ± 101
Fe	Prostate	1370	490
Ca	Lung	355 ± 42	886 ± 248
Ca	Prostate	2240	1870
Cd	Kidney	15.6 ± 0.9	181 ± 44

In summary, though the full scope of the project is not completed at the time of this writing, the expectation is to construct a functional DD-based FNISA system as well as a prototype DD-based APNEI system. MC simulations and preliminary FNISA indicate promising *in vivo* application of APNEI in noninvasive diagnostics for diseases with trace elemental signatures. The

focus of this dissertation will therefore be the MCNP simulations and foray into experimental FNISA prototyping, which have laid the groundwork for development of a neutron imaging system by providing data pertaining to system layout, elemental sensitivity, dosimetry, and resolution.

1.2 Elemental Disease Signatures

1.2.1 Principles and Background

One of the bases of all types of trace elemental imaging in medical diagnostics is that elemental homeostasis is affected in a variety of diseases, thereby offering opportunities for diagnosis, etiological research, and intervention given satisfactory sensitivity and specificity to the element(s) of interest. However, given that trace elements such as iron, cobalt, copper, manganese, fluorine, and zinc are present at such minute concentrations in the human body and that the corresponding absolute changes in concentration as the result of some state of disease are miniscule, there are very few imaging modalities which can be used clinically to noninvasively quantify *in vivo* elemental distributions. Indeed, in the majority of cases, a biopsy is required for diagnosis, and in the worst case, diagnosis is performed only through the evaluation of patient symptoms and cannot be substantiated until a postmortem tissue sample is excised and analyzed using such methods as inductively coupled plasma-mass spectrometry (ICP-MS) or x-ray fluorescence spectrometry [9, 23, 24].

As the previous statement implies, the vast majority of trace elemental analyses are only performed *in vitro* in the laboratory where bench top chemo-analytical instruments and clean room conditions may be maintained to allow a sensitivity on the order of one part per billion, or even better. And while such diagnostics are currently the gold standard in healthcare in the USA, tissue biopsies are not always advisable or definitive [25, 26]. Additionally, even after an invasive biopsy and a course of treatment is initiated, the margins of error surrounding the affected tissue given the very limited spatial scope of the sample can be large, leading to the unnecessary resection of healthy tissue or the inadvertent exclusion of diseased tissue [27]. This is compounded by the fact that benign and malignant tissues can be indistinguishable using physiological imaging modalities such as computed tomography (CT) and magnetic resonance imaging (MRI) [28, 29]. And more simply, there are some locations – for example, in the brain, spinal cord, and deep tissue – that are not safely accessible, even to needle aspirates.

While changes in trace elemental tissue composition can indicate states of disease development and progression, reliably evaluating these changes *in vivo* continues to prove challenging. It is not a question of whether such biological and chemical changes accompany diseases such as cancer, Alzheimer's, and Parkinson's; it is merely a question of whether the changes are measurable and can make a difference for the patient. It is outside the scope of this dissertation to discuss the mechanisms by which elemental homeostasis may be affected. In fact, it is apparent upon review of the literature that there is much uncertainty regarding whether such shifts in trace elemental concentrations arise from a particular diseased cellular mechanism or if the idiopathic accumulation or dilution of trace elements actually causes the mechanism to become diseased [30]. The pragmatic viewpoint is that trace elemental concentrations characteristically shift in a variety of conditions – often before the presentation of symptoms – thereby offering opportunities for timely diagnosis and tissue type differentiation by identifying and spatially distinguishing the so-named elemental disease signature.

1.2.2 Cancer

Cancer is perhaps the most intuitively obvious candidate for identification by a trace elemental disease signature. In uterine cervix cancer, for instance, the concentrations of chromium, iron, nickel and copper in the blood serum significantly increased as compared to the levels in healthy controls, while the concentrations of zinc and selenium significantly decreased [31]. Although the effects of different disease states on the elemental composition of various tissues are interesting to consider and certainly an avenue worthy of research with regard to the potential elemental contribution to disease progression and possible insight into new therapeutic pathways, systemic elemental changes such as those in the blood serum in uterine cervix cancer patients are not well suited to analysis by noninvasive quantitative imaging. Rather, local changes such as those observed in neoplastic tissue in the brain [12] present opportunities to visualize affected regions and to direct diagnoses and/or interventions accordingly.

Many solid cancers present as well-localized masses of cells which constitute their own unique environment, often consisting of unregulated chemical exchange pathways, dysfunctional angiogenesis, and uncontrolled mitosis [2, 32]. Interestingly, the tumor exists in immediate proximity to normally functioning tissue, often with discernible borders. Not only are these tumor borders generally distinct in classical diagnostic imaging, but tumor tissue is readily

distinguishable from healthy tissue via histopathology, which can be used in conjunction with trace elemental analysis.

As evidenced in Table 1.1, a wide variety of solid cancers exhibit distinctive and consistent variations in trace elemental concentrations from the normal ranges in health tissues, which may be used as diagnostic signatures. Though an exhaustive list of cancer types and their documented impacts on local elemental homeostasis would not be practical, there are several intriguing studies which warrant mentioning. For example, in ovarian neoplasms, copper, zinc, calcium, selenium, cadmium, lead, and mercury concentrations were found to be helpful in the differentiation between healthy tissue, benign tumors, borderline tumors, and carcinomas beyond the capabilities of histology alone [33]. Similarly, the development of one of the deadliest and least understood cancers, exocrine pancreatic cancer, has been associated with high concentrations of lead, nickel, selenium, arsenic, and especially, cadmium [34, 35]. Indeed, cancers of the breast, liver, colon, lung, kidney, and prostate have also been associated with anomalous concentrations of Cu, Fe, Zn, P, K, Mn, Ca, S, Rb, Pb, Se, Ni, Hg, Sr, As, and Br [9, 22, 36, 37]. Figure 1.1 illustrates some of the differences in trace elemental composition between a human liver tumor and normal tissue.

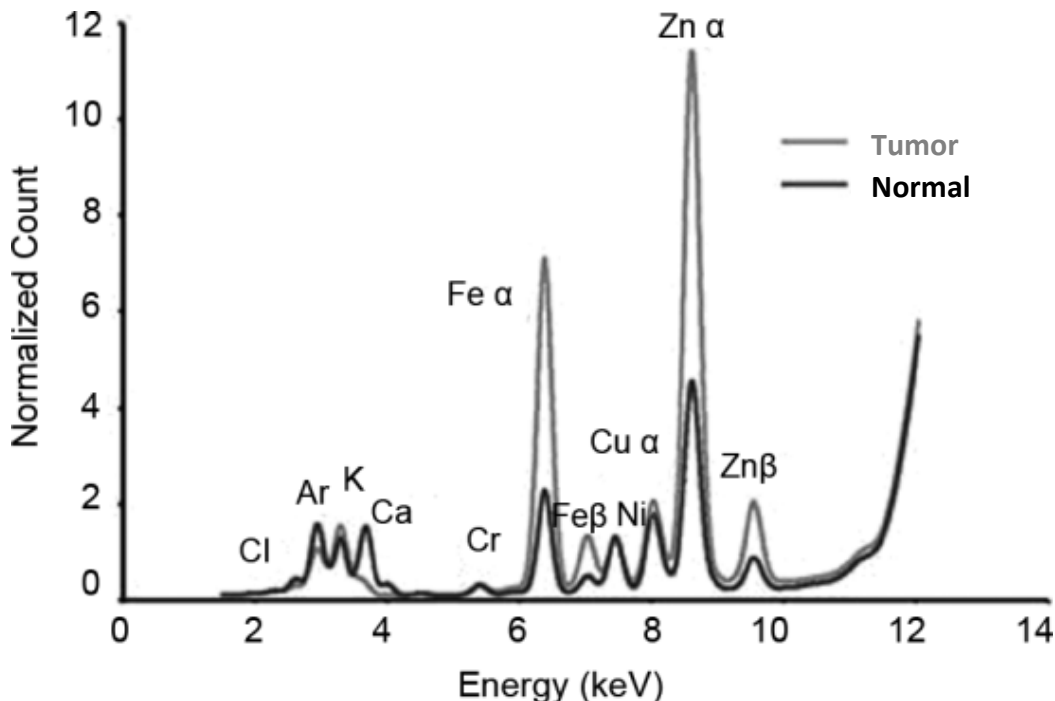


Figure 1.1. Fluorescence spectrum of signature elements in liver tissue – normal vs tumor [9]. Reproduced with permission of Professional Technical Group on Nuclear Science.

Whether the trace elements themselves act as carcinogens or are the result of underlying cancer development and progression is an active area of research and must be evaluated on a case-by-case basis, but the correlations are strong and consistent among cancer types. Additionally, it may be inferred from several trace elemental cancer studies that there is evidence showing malfunctioning cellular metabolic machinery prior to the development of structural anomalies, which lends credence to the potential for early detection with suitable screening technologies when biopsy, histology, or other *in vitro* analytics would not yet be indicated or effective. Additionally, trace elemental analysis is useful for distinguishing adjacent structures which, though well defined, may appear similar using tomographic imaging modalities which rely upon tissue density or water content. Of particular advantage are *in vivo* trace elemental quantification techniques which may be used to noninvasively complement physiological imaging modalities. Improved lesion specificity is demonstrated in the example in Figure 1.2, where sodium MRI serves as a metabolic accompaniment to traditional MRI such that the poorly differentiated carcinoma is more easily distinguished from the neighboring region of edematous glandular tissue, which displays higher sodium concentrations than the tumor [38]. Though sodium is present in higher concentrations in the body than a trace element, Figure 1.2 presents an example analogous to both the benefits of *in vivo* trace elemental imaging and the challenges – both that functional information regarding the state of health and composition of the tissue may be noninvasively collected and that the corresponding signal and resolution are decreased due to the more sparsely distributed imaging objective.

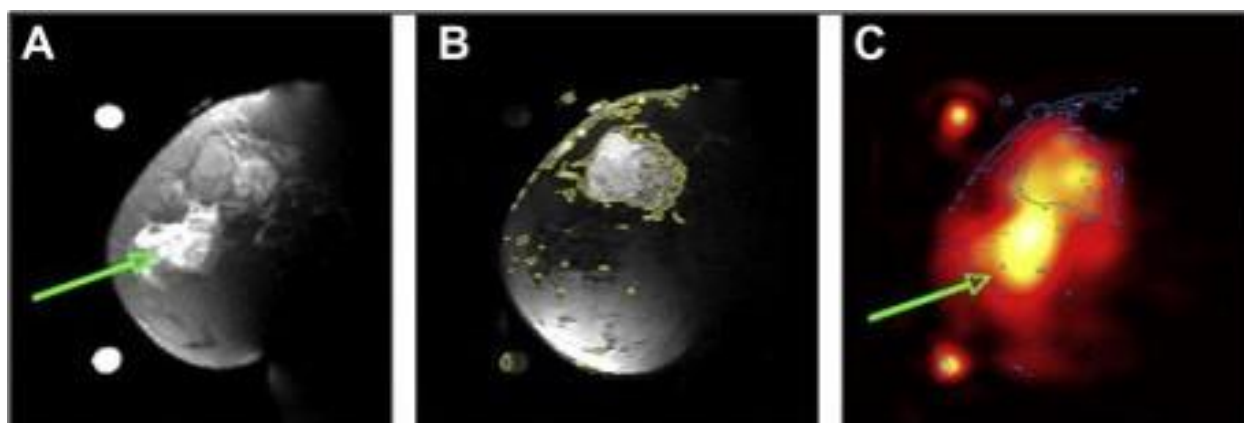


Figure 1.2. ^1H and ^{23}Na images of a patient with poorly differentiated carcinoma at the 12 o'clock position of the left breast and edematous glandular tissue at the 9 o'clock position [38]. (A) Fat suppressed T2W image (B) Co-registered, fat-suppressed T1W image with level contours in yellow (C) Co-registered ^{23}Na image with level contours from (B) superimposed in blue. Region of edema (indicated by green arrow) is discernible from cancer without Gd contrast administration. Reproduced with permission of Springer New York LLC.

It is evident from the literature that trace elements play a role in the development of a variety of solid cancers or arise in distinctive concentrations as a result of tumor pathogenesis. By quantifying the concentrations of these marker elements in tissue, it is possible to realize pathways to early cancer diagnosis, proper lesion identification, and enhanced marginal accuracy.

1.2.3 Alzheimer's

Cancer is not the only disease known to have a characteristic elemental signature. Non-neoplastic diseases of the brain also cause (or are caused by) local trace elemental changes which can be used in diagnostic analytics. Perhaps the most impactful of these is Alzheimer's disease (AD), which is ranked as the sixth leading cause of death in the United States and is the most prevalent cause of adult onset dementia. Alzheimer's is a neurodegenerative disease, the etiology and pathogenesis for which are not well understood [39]. It is characterized by structural and compositional changes in the brain, which ultimately result in the degradation of synapses and neurons in the cerebral cortex and subcortical regions. Advanced disease is marked by significant atrophy, generally in the temporal and parietal lobes [40]. Several hypotheses as to the development and progression of AD involve trace elemental neurotoxicity as a critical component. As the body of literature on the topic grows, this thought has been reinforced by the consistent presence of amyloid plaques, micro-tubular aggregates, and other local changes which seem to adversely impact the function of the adjacent neurons [41, 42]. However, while the manifest degeneration of the brain in advanced AD is easily observable using imaging modalities such as MRI and CT, such information does not provide a differential diagnosis for AD. Instead, the diagnosis of AD is based on patient symptoms and other potentially unreliable and indirect biomarkers and can only be confirmed upon postmortem microscopy of brain tissue samples, effectively rendering early detection and informed intervention impossible [43, 44].

However, as in cancer, opportunity exists for AD diagnosis and potential subtype distinction using *in vivo* noninvasive trace elemental analysis. Cross-sectioned samples from the autopsied brains of AD patients have shown manifold increases in the concentrations of copper, zinc, iron, calcium, silicon, lead, bromine, and mercury – with aluminum as an ongoing point of contention [1, 9, 39, 45, 46]. Table 1.2 provides examples of some of the signature elements affected in AD.

Table 1.2 – Selected elemental concentrations in AD vs normal human tissue [1, 9, 36]. Reproduced with permission of Professional Technical Group on Nuclear Science.

Alzheimer's	Copper ($\mu\text{g/g}$) Mean \pm S.E.M	Iron ($\mu\text{g/g}$) Mean \pm S.E.M	Zinc ($\mu\text{g/g}$) Mean \pm S.E.M
Senile plaque	25.0 \pm 7.8	52.5 \pm 13.7	69.0 \pm 18.4
Control neuropil	4.4 \pm 1.5	18.9 \pm 5.3	22.6 \pm 2.8

As one of the most financially costly diseases in developed countries, combined with a guarded prognosis, an often severe decline in quality of life for the patient and his/her immediate family, and significantly deviating patterns of onset and progression, AD will remain one of the most active fields of research for decades – particularly with regard to diagnosis, etiological origin, and pharmaceutical intervention. Correspondingly, as with many aspects of the disease, the role of trace metals as a potential causative factor or promoting factor for susceptibility is unknown; in actuality, the elemental homeostasis of diseased tissues may only be affected as a consequence of the formation of proteinaceous structures with irregular ion exchange mechanisms [39, 41, 42, 47]. Whether the trace elemental concentrations in the vicinity of such plaques may also be significantly altered remains to be seen. Additionally, the timeline of plaque formation in the progression of AD is unclear [48, 49]. Because these microscopic diagnostic signs of AD cannot be quantified or imaged *in vivo* using any existing method, it is difficult to discern when during the course of the disease the plaques manifest. And while it is not expected that any forthcoming elemental imaging technology will be capable of resolving microscopic structures in the brain of an AD patient, it is possible that voxels on the order of $< 1 \text{ cm}^3$ may be achieved. And while MRI and CT offer far better physiological resolutions, the diagnostic data provided by noninvasive trace elemental quantification – even at the scale of 1 cm^3 – could provide evidence of early AD as well as point to focused therapeutic options once a basis of actionable, analytical frameworks is established in the clinic.

1.2.4 Parkinson's

Another long-term neurodegenerative disorder is Parkinson's disease (PD), which – similar to AD – has an unknown origin with a variety of suspected risk factors and is diagnosed predominantly by patient symptoms [50]. Like AD, the symptoms of PD generally come on slowly and are difficult to initially distinguish from the normal aging process. In the case of PD, these

predominantly include motor system anomalies, such as tremors, rigidity, and difficulty moving, though dementia, depression, anxiety, and emotional problems can accompany the characteristic shaking, particularly in the later stages of the disease [51]. Deaths of nerve cells in the substantia nigra of the midbrain are generally accepted as the cause of the motor symptoms in patients with PD, and while the mechanism inciting this neuronal death is unknown, proteinaceous masses are again the leading culprit. Analogous to beta-amyloid plaques in AD are Lewy bodies in PD, which are irregular protein aggregates that develop within nerve cells and contribute to Parkinsonism, likely through some chemical means or through physical protein degradation [50, 52, 53]. Again, these local changes in affected tissue have thus far only been quantifiable *in vitro* and have provided a conclusive diagnosis of PD only upon microscopic analysis after patient autopsy. However, similar to AD, these structural changes in PD are often complemented by distinctive deviations in trace elemental composition.

Trace metals associated with PD pathology include iron, manganese, copper, lead, calcium, zinc, and aluminum – with iron playing a particularly important role as the most likely instigator of oxidative stress in the substantia nigra [3, 54]. Figure 1.3 shows the marked increases in iron in various regions of the brains of PD patients – greater than 130% that of the control group in some tissues of the basal ganglia (such as the substantia nigra, lateral putamen, and caudate nucleus). Significant increases in iron concentration are also evident in other diseases of the basal ganglia [55].

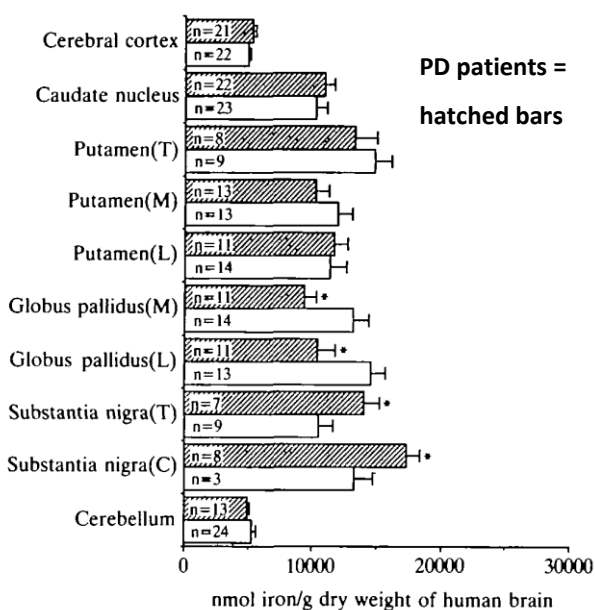


Figure 1.3 Total levels of iron in PD and age-matched control human autopsy brains [55]. Reproduced with permission of Oxford University Press.

Interestingly, many of the existing studies on heavy metal and trace elemental associations with PD focus on *in vitro* analysis of blood serum, cerebrospinal fluid, or urine in an attempt to elucidate potential biomarkers to assist in diagnosis as well as to offer insight into the etiology of the disease or into novel therapeutic options. However, as in AD, markers such as those in bodily fluids have proven tenuous; the most reliable and reproducible results have been obtained by analyzing thin section brain samples obtained postmortem, generally through ICP-MS, neutron activation analysis (NAA), or x-ray fluorescence spectrometry (XRF) [56, 57]. Again, actionable *in vivo* diagnostic information remains lacking. However, given the mounting evidence of a trace elemental signature for PD, noninvasive and sensitive assay technologies are an attractive clinical option.

1.2.5 Other Diseases

It goes without saying that diseases other than cancer, Alzheimer's, and Parkinson's may be indicated and/or staged by shifts in trace elemental homeostasis. As diagnostic detection capabilities improve and possibilities expand, the feasibility of *in vivo* application of a variety of techniques – including APNEI – increases. And fundamentally, the ongoing work into multifactorial disease etiology and progression continues to build the foundation of work which supports the local composition of affected tissue as an investigative tool in medicine. The area of research concerning elemental disease signatures is active and growing and continues to offer opportunities to make a difference in the lives of patients. A specific elemental signature is that of iron overload in the liver and its importance regarding the development of liver fibrosis, cirrhosis, and hepatocellular carcinoma. Frequently, a seemingly uncontrolled accumulation of iron in the liver is associated with the diagnosis of liver cirrhosis, even in the absence of systemically elevated iron concentrations [58]. Controlling the buildup of iron in such disorders has proven effective in mitigating the oxidative stress and anomalous cell signaling phenomena associated with the presence of excess iron, leading to significant improvement of liver functions. Furthermore, certain types of hepatitis may be disguised as iron overload syndrome, which can be differentiated using iron as a local tissue biomarker [59]. Finally, if the spatial distribution of iron in the livers of cirrhotic patients could be ascertained, surgical intervention could be more precisely planned and outcomes correspondingly improved. It has been demonstrated that various surgical scoring systems pertaining to patient prioritization and risk quantification are lacking [60].

Also, diseases of the bone such as osteoporosis – which can be a challenge with regard to finding diagnostic information *in vivo* due to the inaccessibility or invasiveness of many samples that may be taken from areas of the affected skeleton – are associated with a variety of quantifiable elemental changes. Osteoporosis – classically defined as a disease causing progressive bone weakness – often goes undiagnosed until an individual experiences a broken bone, which can occur without warning and generally leads to chronic pain and a loss of independence as everyday activities become more difficult to perform [61]. At that point, diagnosis is typically confirmed using conventional radiography, or preferably, by dual-energy x-ray absorptiometry – both of which measure bone mineral density [62]. In that sense, the diagnosis of osteoporosis is reactive rather than proactive. Preemptive screening is not widely practiced, and there is not much evidence with which to form a solid basis for early diagnosis or prevention efforts [62, 63]. However, trace elemental markers associated with osteoporosis may prove pivotal both diagnostically and pathogenically.

While osteoporosis is well documented as a multifactorial disease with hereditary, endocrine, and nutritional factors, the roles of trace elements in its development and progression have not yet been well defined. However, there are clear associations between accelerated bone loss and fluoride, magnesium, and aluminum concentrations [64]. Also, on a fundamental level, it is understood that elements such as zinc and copper are essential to skeletal health, while elements such as gallium and cadmium may increase bone brittleness by suppressing its natural turnover [64]. There is thus evidence that trace elemental concentrations in osteoporosis or pre-osteoporosis can provide important clinical information beyond mere bone density assessment using x-rays, which is the current gold standard.

Correspondingly, many trace elements – heavy metals in particular – may be taken up by the skeleton, in which case they may be used as long-lasting biomarkers of chronic exposures, which would be of interest in many industrial settings with regard to evaluating engineering controls designed to mitigate toxicological hazards, as well as for assessing heavy metal exposure to cohorts in developing nations such as China, where industrial hygiene is not a priority in most sectors. Lead exposure, for example, has traditionally been evaluated using the concentration of lead in the blood; however, the biological half-life of blood Pb is on the order of weeks and is not a good indicator of long-term exposure. This is particularly true in children, for whom the biological half-life of blood Pb is even shorter [65]. That is why several researchers have turned to the use of

methodologies such as XRF of bone *in vivo* in order to quantify bone lead concentrations, which are an effective biomarker of chronic, low-level exposures – both industrially and environmentally [65, 66, 67, 68]. Such integrated metrics are more meaningful than short-term measurements as many of the consequences of heavy metal toxicity are apparently stochastic, such as the development of cancer, heart problems, and neurodegenerative syndromes.

When NAA is added to the list of diagnostic tools, trace elements such as manganese, fluorine, and aluminum have also been quantified in bone *in vivo* and have been associated with heavy metal toxicity, industrial exposures, and the health of the bone itself [69, 70, 71]. And the bones are only one part of the body which may be selectively assessed for trace elemental signatures important to disease diagnostics and intervention. The heart, lungs, and gastrointestinal tract are other potential target sites which may be characterized according to elemental composition and distribution. So, while the data supporting the assessment of elemental disease signatures as an important medicinal tool is strong and varied, there are countless opportunities for expansion in the field. A far greater number of healthcare applications exist which are beyond the scope of this dissertation.

1.2.6 The Significance of Iron in Disease Diagnostics

Iron was selected as the target element in the simulations and experiments performed over the course of this APNEI study for a variety of reasons, foremost of which was the breadth of diseases in which iron homeostasis is impacted, thereby promoting extensive applicability of the experimental imaging technique in the field of diagnostic medicine. As heretofore mentioned, significant deviations in iron concentration from the normal range have been observed to occur in a variety of solid cancers, as well as Alzheimer's disease, Parkinson's disease, and diseases of the liver [1, 2, 3, 9, 36, 54, 58]. In some cases, iron concentrations can increase in diseased tissue by greater than an order of magnitude [72], which would allow for the evaluation of local differences in iron distribution *in vivo* using a relatively insensitive quantitative modality – a good starting point for as fledgling a concept as APNEI.

Well known are the important functions iron serves in the body, from oxygen transport as a constituent of hemoglobin in the blood to the metabolism of hundreds of essential enzymes and proteins involved in respiration, oxidation, reduction, and DNA synthesis at the cellular level [73]. And because iron excretion is very low (due predominantly to the fact that 75% of iron within an

adult human is attached to hemoglobin and must be continually recycled for oxygen transportation) while iron uptake is strictly controlled, many tissues come to have a well-documented equilibrium iron concentration, which serves as a consistent basis for comparison to tissues in various states of disease [74, 75]. An important complement to this equilibrium concentration is precise regulation of iron storage, which is accomplished through the action of protein complexes which deliver nutritional iron from the small intestine to tissues within the body. Once transferred from the gastrointestinal tract, the protein complexes are reduced – changing oxidations states – and stored for later use [76, 77].

Iron is not only pervasive in the body, but in the foods humans eat and in the earth itself, where it is the most common element by mass. Given that iron is involved in a great variety of basic functions in the body, it is no wonder iron is such a valuable biomarker of disease because there are many ways in which its storage, buildup, and/or transfer may be distinctly affected in a range of tissues. In cancer, for example, dietary iron overload is thought to have carcinogenic properties, while increases in iron concentration in a preexisting tumor due to angiogenesis or regulatory malfunction are believed to promote tumor growth [78]. Conversely, iron is crucial to such a multitude of non-pathological processes that if iron levels decrease in an individual either because of cancer directly or as a result of cancer treatment such as chemotherapy, efforts are undertaken to boost iron levels to prevent iron deficiency and anemia [78]. This speaks to an area of research touched upon in the previous sections – that while signature changes in iron concentration are associated with a variety of diseases, in many cases it is unknown whether the iron plays a role in the development and progression of the disease, or if iron imbalance is a consequence of the effects of the condition.

Regardless, what is known is that cellular iron levels are impacted by many variables – including the increased or decreased production or maturation of red blood cells, arterial blood oxygen tension, liver iron stores, inflammation, circulating iron concentrations, disruption of protein complexes involved in iron transport, changes in gene expression, and localized iron overload [79]. Figure 1.4 illustrates the complexity of only a small sample of the interrelated mechanisms responsible for iron regulation and the number of opportunities for idiopathic causative or pathogenic feedback malfunction. Furthermore, on a systemic level, when one considers that such sweeping symptoms as inflammation or effects on erythropoiesis or oxygen

tension can affect iron concentrations, one realizes the breadth of changes in the body which may ultimately manifest as a local disruption in iron homeostasis.

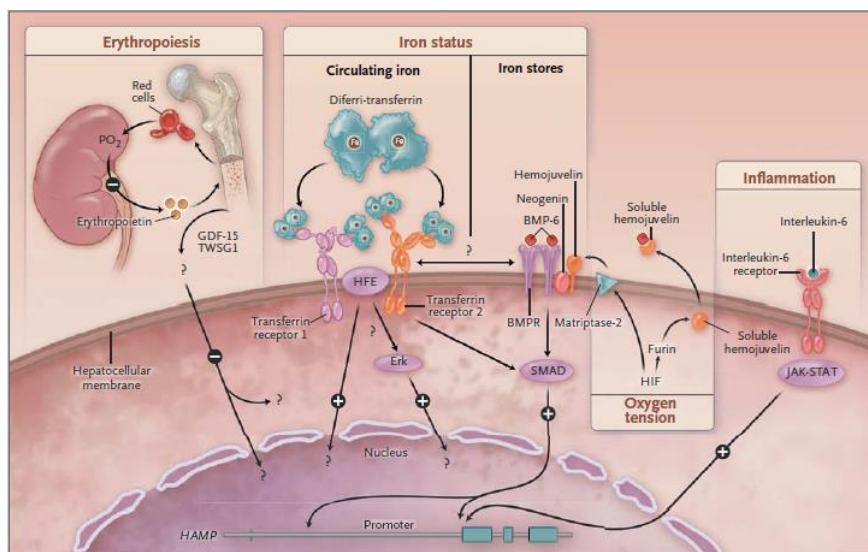


Figure 1.4 Regulation of cellular iron concentrations. It is apparent that the opportunities for disruption of cellular iron concentrations are varied and characteristically impacted in a variety of diseases. Reproduced with permission from [79], Copyright Massachusetts Medical Society.

Correspondingly, Table 1.3 summarizes a small sample of the conditions in which iron homeostasis is affected. It is established in the literature that iron is a suitable diagnostic target for *in vivo* identification, treatment planning, and research of a variety of illnesses.

Table 1.3 – Iron concentrations in diseased vs normal human tissue [1, 2, 9, 55, 80, 81, 82]

Condition	Disease ppm	Normal ppm
Alzheimer's disease	52.5 ± 13.7	18.9 ± 5.3
Parkinson's disease	1008	728
Kidney cancer	440 ± 64	122 ± 35
Liver cancer	1309	768
Lung cancer	75.1 ± 9.7	199 ± 101
Prostate cancer	1370	490
Multiple sclerosis	860 ± 64.7	748 ± 29.2
Liver iron overload	> 15,000	400 – 2,000
Huntington's disease	159	96

1.2.7 Conclusions

Changes in tissue composition which accompany a variety of diseases – from solid soft tissue cancers to diseases of the brain like Alzheimer’s and Parkinson’s – may be treated as signatures to evaluate not only the identity of the condition but the state of its progression. Generally defined by deviations in trace elemental concentrations, these signatures are critical to the development of early diagnosis and advanced screening strategies, and they may be fundamental to understanding the etiology of several multifactorial conditions for which the common causal variable is unknown. Additionally, as several of these types of diseases are characterized by a slow and insidious onset, the opportunities offered by the classification of unique trace elemental changes are multifold – both diagnostically and with regard to timely intervention, thereby potentially improving the quality of life and survivability of patients in a wide range of healthcare areas which are prognostically troublesome and economically draining.

Furthermore, while biopsies and contrast-enhanced CT and MRI will remain staples of diagnostic medicine, there are other developing modalities which may be better adapted to the quantification of trace elemental composition in diseased tissues. Fine needle aspirates are invasive and are not generally indicated for sensitive, deep, or naturally heterogeneous tissues such as the brain or liver. CT and MRI offer excellent physiological detail, but it remains difficult in many cases to distinguish benign from malignant structures. Also, such expensive imaging technologies are generally reactionary rather than proactive; in other words, they are employed only once symptoms of a particular disease manifest, at which point the condition has advanced to a late stage and often carries a poor prognosis. Systems for *in vivo* analysis of trace elements therefore fill a clinical gap, and those that offer spatial differentiation in addition to elemental quantification will prove particularly useful in the future.

1.3 Diagnostic Imaging in Medicine

1.3.1 Principles and Background

With a solid background in trace elemental disease signatures – both conceptually and operationally as an analytical target – it is worthwhile to provide an overview of the current state of diagnostic imaging in the US, which tends to focus less on the evaluation of elemental composition than on the assessment of overall tissue density, ligand-bound chemical metabolism,

or magnetic properties. Certainly, there are variants of the modalities currently in use which may be leveraged to provide elemental characterization of the target tissue to some extent. For example, Figure 1.2 shows how the functional information provided by MRI tuned to the dipole moment of Na-23 complements the anatomical resolution of traditional proton MRI to allow for improved tumor specificity in breast cancer [38]. However, such applications are often limited to very specific scenarios and to the quantification of a single element at a time, which – though useful in certain situations – is not ideal given the seemingly universal nature of localized diseases which may be distinguishable according to differences in the trace elemental compositions of the affected tissues.

Therefore, it is important to frame *in vivo* trace elemental imaging as an initial complement to established imaging modalities. In that context, a realistic view of the general diagnostic importance of APNEI may be defined – one that can act as a foundation upon which to build more ambitious and case-specific applications. To that end, *in vitro* analytical techniques will not be broached in this section as they require invasive sampling (or may be limited to postmortem sampling in some cases of trace signatures) and generally do not provide any spatial information. *In vitro* bench top analyses therefore do not offer as attractive an option for interventional diagnostics and have found wider applicability in etiological or toxicological studies requiring state-of-the-art sensitivity to pathogenic substances.

Conversely, the progress in the field of diagnostic imaging over the past several decades at the scale of discernible structures within the human body has been remarkable, manifesting as improvements in spatial resolution, data collection and processing times, artifact correction, software functionality, and patient comfort. With such technological improvements has come a greater availability of the many imaging options to patients, as well as a greater clinical emphasis on the responsible use of these important diagnostic tools. In fact, in the field of imaging utilizing ionizing radiation, the International Commission on Radiological Protection (ICRP) revised its estimate of the average annual dose to an individual from 360 mrem to 620 mrem based on the growing contribution of medical x-rays to the total dose. Currently, it is expected that half of the 620 mrem dose is the result of diagnostic imaging procedures [83]. And while this average increase in individual dose is not expected to result in adverse outcomes for patients, it is as important as ever to understand the different imaging modalities in order to justify their use, understand their strengths and limitations, and to recognize alternatives and complementary

benefits in cases of overlapping functionality – both for ionizing radiation-based technologies and otherwise.

1.3.2 X-Ray Radiography

Traditional x-ray radiography is perhaps the best known and most easily understood diagnostic imaging procedure in medicine. Ever since Röntgen produced and detected x-rays in 1895, which yielded the famous image of his wife’s hand, the applications of radiography have grown and changed dynamically as the hazards associated with ionizing radiation became better understood [84]. Today, the uses of x-rays in medicine have become very well defined and correspondingly have been refined to such an extent that the potential health benefits to a patient almost always outweigh the risks.

Traditional radiography is otherwise known as projective radiography – the simplest application of x-ray exposure whereby a two-dimensional image is generated based on differential absorption of the x-rays in tissues of dissimilar density and overall composition. The differences in absorption or x-ray attenuation between soft tissues and tissues such as bone predominantly owe to the presence of high levels of carbon as opposed to calcium, respectively. Calcium has a higher mass attenuation coefficient than carbon, which means that the probability of interaction of an x-ray of some typical diagnostic energy is higher in bone than in carbon. This explains why bones may be visualized as areas which appear white on photographic film – because fewer x-rays reached the film in those areas as opposed to dark areas which have been relatively overexposed due to the greater numbers of x-rays passing through the surrounding soft tissues. Algebraically, the initial x-ray intensity I_0 decays to $I(x)$ according to the Beer-Lambert law [85]:

$$I(x) = I_0 \exp \left(- \frac{\mu}{\rho} \rho x \right) \quad \text{Eq. 1.1}$$

where μ/ρ is the mass attenuation coefficient, ρ is the density of the attenuating material, and x is the distance the x-rays must traverse through the material. It is important to note that the value of the mass attenuation coefficient is dependent upon the energy of the incident x-rays, which is intuitive considering that higher energy x-rays are generally less likely to interact within a given medium.

The maximum x-ray energies employed in projective radiography generally fall in the range of 50 to 150 keV, though special applications such as mammography call for energies outside of

this range [86, 87]. In the clinic, x-rays are typically produced using an x-ray generator, the primary component of which is an x-ray tube, which is a vacuum tube capable of converting electrical current into x-rays [86]. In short, electrons are released from the tube cathode and accelerated to collection on the tube anode due to the presence of high voltage, which governs the electron energy and therefore, the maximum x-ray energy. The vast majority of electron energy upon reaching the anode contributes to heat generation; however, a small percentage of the electron energy is converted to x-ray photons and radiated via the bremsstrahlung effect. It is important to understand that due to the bremsstrahlung effect, x-ray energies are generally characterized according to the kilovoltage peak (kVp) setting of the x-ray tube because the energy spectrum of emitted x-rays is continuous up to a maximum energy in keV which is equal to the kVp setting, or the maximum energy to which electrons are accelerated across the voltage gap [88]. This continuous x-ray spectrum – though marked by characteristic x-ray peaks depending on the atomic composition of the target anode – is one drawback of the use of x-ray tubes in diagnostic medicine. The lower energy photons have a higher probability of interaction in the patient and therefore cause increased dose, while the complexity of the spectrum and differences in mass absorption at various energies require extensive operator expertise and consistency. Several studies have reported patient doses orders of magnitude apart for the same diagnostic x-ray procedure [89, 90, 91]. Figure 1.5 shows the typical form of a bremsstrahlung spectrum from a diagnostic x-ray tube. It is apparent in the figure that many of the lowest energy photons which are diagnostically unimportant can be filtered out of the beam using a material such as aluminum.

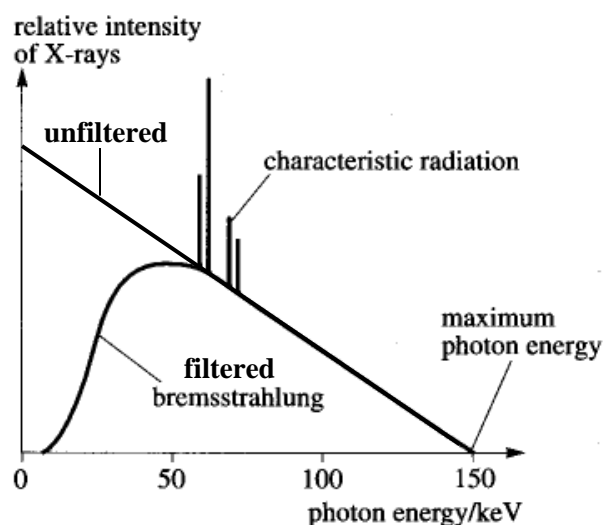


Figure 1.5 Bremsstrahlung x-ray spectrum

The bremsstrahlung curve may be approximated by Kramers' law, which relates the intensity I of the x-ray photons to the wavelength λ of the radiation emitted [92]:

$$I(\lambda)d\lambda = K \left(\frac{\lambda}{\lambda_{\min}} - 1 \right) \frac{1}{\lambda^2} d\lambda \quad \text{Eq. 1.2}$$

where K is a constant dependent upon the atomic number of the target element. Having briefly characterized the x-ray spectrum and its production, one must consider the radiographic components which are most often oriented opposite the x-ray tube (i.e. the imaging detectors).

In the past, photographic plates and then film provided a record of the intensity of the x-rays reaching the material – dark areas corresponding to higher exposure and vice versa. This was the result of exposed silver halide crystals in the media being converted to metallic silver upon development, which then blocked light and caused the photographic material to appear dark. Now however, these basic implements have been almost completely replaced by reusable devices capable of outputting a digital signal. Such detectors are often used in conjunction with a Bucky-Potter grid which decreases the proportion of scattered x-rays that reach the detector, thereby improving the contrast resolution of the image. However, because of the grid's general attenuation of the x-ray beam, a greater exposure to the patient is necessitated for the grid to be employed effectively [93].

In short, traditional radiography is straightforward and has a wide range of applicability; and while generally low cost in terms of price as well as potential radiation detriment, the modality has a high diagnostic yield. On the other hand, x-ray radiography allows the collection of only 2D projective images. There are also several variable settings and optional assistive devices for achieving optimal resolution in a multitude of applications, which can lead to significant inconsistencies in patient dose and clinical diagnostic interpretations between operators and facilities [89, 90, 91]. Additionally, traditional radiography is not capable of analyzing elemental composition relevant to disease signatures, at least not beyond overall tissue density and the accompanying photoelectric interaction probability which scales with effective atomic number.

Despite its fundamental nature, the background on radiography presented to this point may be used as a foundation not only to better understand the essentially universal 3D application of x-ray imaging in CT but as an analogy to APNEI, which is largely a projective imaging challenge. Many of the principles of projective radiography apply to more complex imaging modalities. Even

APNEI, which does not utilize x-rays at all, nevertheless relies upon an ionizing radiation generator, separately oriented photon detectors, and a variety of physical and electrical components designed to minimize the contributions of confounding signals to the image construction process. Figure 1.6 illustrates some of these universal components of projection imaging as applied in x-ray radiography.

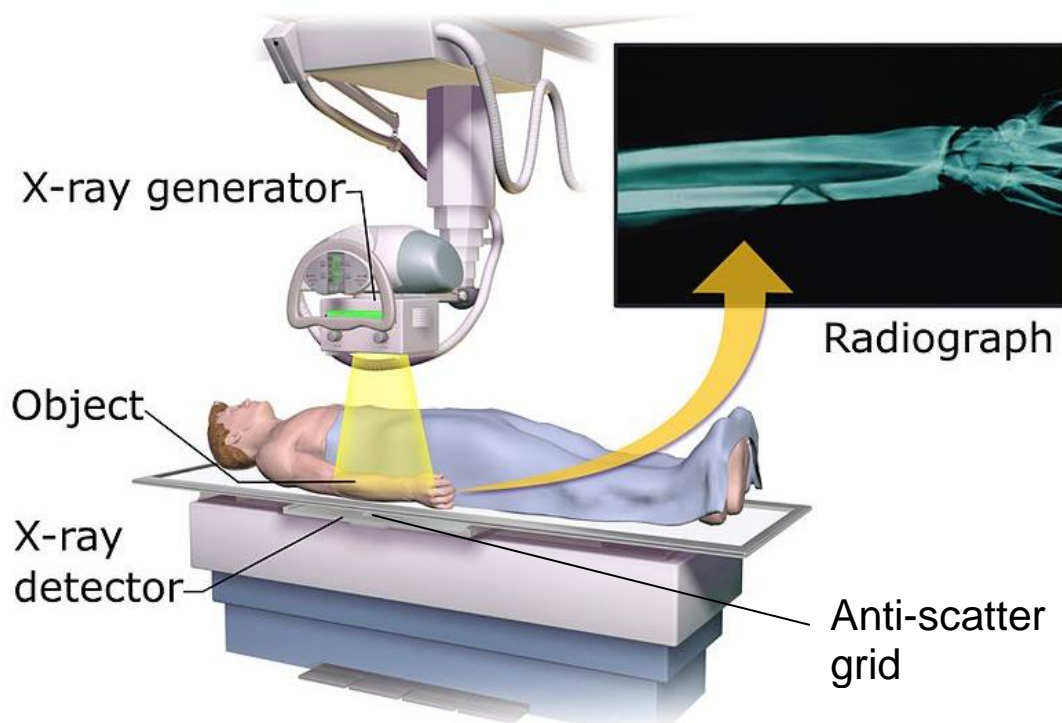


Figure 1.6 Basic components of projective radiography

1.3.3 X-Ray Computed Tomography

X-ray computed tomography is an advanced application of x-ray radiography which allows for 3D registration of anatomical structures by using multi-angle exposures and accompanying spatial processing algorithms. As in traditional radiography, the majority of x-ray CT machines have an x-ray tube mounted opposite a detector array. However, in order to produce tomographic images, the tube and detector assembly are constructed with the ability to spin around a patient so that data at many angles may be collected. The data collected are – as in projective radiography – simply representations of the average density and composition of the tissue through which the x-ray beam passed, which may be analogized to a shade in grayscale. Once the data are collected

for a particular tomographic slice, digital geometry processing is employed to reconstruct the three-dimensional object from its projections [94]. The key to most of these geometry processing algorithms is the Radon transform, where the sinusoidal x-ray projection data may be thought of as the product of the transform itself. Therefore, by taking the inverse of the Radon transform, one may calculate the density of the material through which the x-rays traveled [95].

Like traditional radiography, x-ray CT has a wide range of applicability and is used for imaging the head, lungs, heart, abdomen, and extremities. The added 3D information prevents non-target structures from becoming superimposed over the area(s) of interest and muddling the resulting image, thereby aiding in disease diagnostics and tissue specificity over projective radiography alone. For this reason, x-ray CT is very useful in the diagnosis and staging of tumors, chronic fibrotic processes, structural blood vessel degradation or blockages, cardiac anatomy, and complex fractures and dislocations [96, 97, 98]. Similar to radiography, x-ray CT has inherently high contrast and can differentiate between tissues that have densities which differ by as little as 1%. Furthermore, because such a significant component of x-ray CT is the digital image reconstruction process, the results of a single diagnostic procedure can be viewed from multiple planes – promoting additional analytical certainty in the clinic.

However, as in all imaging modalities which employ the use of ionizing radiation, such high contrast resolution and 3D information come at the cost of an increased radiation dose to the patient. Whereas a typical chest x-ray yields a whole body effective dose around 2 mrem [99], a typical whole body effective dose for a chest CT is in the range of 500-700 mrem [100]. Correspondingly, several estimates of the risk of cancer associated with CT scans are not negligible, though the preferential use of CT scans in the elderly helps to mediate the overall risk of long-term effects in the population [100]. In general, a single abdominal CT which imparts a dose of 800 mrem is expected to result in an added risk of cancer of 0.05% over the lifetime of the individual [101]. And while the radiation dose inherent to particular diagnostic procedures is unlikely to change drastically within a given modality provided consistent clinical operation, the sheer number of prescribed scans has caused the average dose to citizens of the US and other developed countries to climb significantly. The National Council on Radiation Protection and Measurements (NCRP) has indicated a six-fold increase in the use of x-ray CT procedures in the 20 years leading up to 2006 [102]. And the upward trend continues today – with some experts expressing concern that x-ray CT scans have become overused and that their current prevalence as

a diagnostic tool does not come with a correspondingly high rate of positive individual health outcomes [103, 104].

Nevertheless, x-ray CT will remain a mainstay of current diagnostic medicine with its breadth of useful applications and high anatomical resolution. Though again, CT is limited to the visualization of physiological differences in tissue density. It is not typically valuable in the characterization of trace elemental signatures or other changes which are usually metabolism-related. Because x-ray CT is lacking such functional diagnostic information, it is often coupled with positron emission tomography (PET) or single photon emission computed tomography (SPECT), offering enhanced tissue specificity at the cost of further compounding radiation dose. PET and SPECT are procedures in the field of nuclear medicine where specific radiolabeled tracer compounds are injected into a patient in order to preferentially highlight target tissues for imaging. Whereas x-ray CT is a projective technique concerned with the passage of x-rays through the body, in SPECT and PET radioactivity is first administered to the patient such that images may be obtained through the subsequent emission and detection of photons which originate inside regions of interest in the patient, thereby offering metabolic insight.

1.3.4 Single Photon Emission Computed Tomography

One of the reasons SPECT and PET are often accompanied by x-ray CT is that compared to x-ray CT, their spatial resolution is relatively poor. For instance, in the case of SPECT, pixel sizes tend to hover around 5 mm as opposed to 1 mm in conventional medical x-ray CT instruments [105]. It is apparent in Figure 1.7 that the capabilities of SPECT and CT together allow for the anatomical registration of a lymph node impacted by a local cancer – better than either alone.

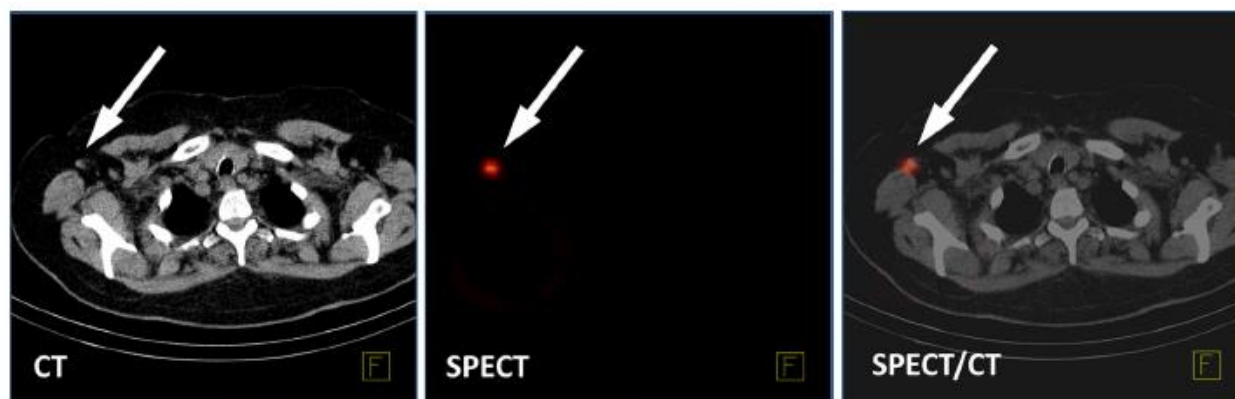


Figure 1.7 Complementary functional & anatomical information in SPECT/CT [105]. Reproduced with permission of Springer Italia Srl.

Figure 1.7 serves as another excellent example of the benefit of assessing local changes in tissue composition as a marker of disease. In SPECT, radionuclides with advantageous imaging properties are bound to particular ligands, which are chemical compounds with tendencies to covalently bond with certain tissues of interest. Once prepared and selected to the current purpose, these so-called radioligands are introduced into a patient, usually via injection. The radioactive compound is then incorporated into the body fluids and concentrates in those tissues for which it has the greatest chemical affinity. In this way, “hot spots” are formed in the body which may be readily imaged in true 3D by employing the use of a gamma camera. The best known radionuclide employed in SPECT is technetium-99m (Tc-99m), which has short physical and biological half-lives and emits 140 keV gamma-rays. This combination of properties allows for reliable photon detection without imparting excessive dose to the patient. Tc-99m may be attached to an assortment of compounds which seek different tissues in the body and is therefore important in a variety of diagnostic procedures.

In particular, SPECT is used effectively in functional cardiac and brain imaging, as well as tumor imaging, particularly for identifying metastases that have spread to the bone. Similar to x-ray CT, SPECT scanners have a rotating gantry which allows multiple 2D images to be collected and tomographically reconstructed in 3D along any chosen axis of the body. However, because the gamma-rays are originating from the radioligand within the patient, a source of radiation in the gantry – such as an x-ray tube – is unnecessary. Therefore, the gantry carries only the photon detector(s), which may be a single gamma camera, or more typically, are comprised of two or even three gamma cameras oriented at equal distances around the gantry. Gamma cameras are relatively simple devices which function on the principle of scintillation. A photon from the patient causes electron excitation in a flat crystal within the detector, which is made from a scintillating material such as thallium-doped sodium iodide (NaI(Tl)). Upon de-excitation of the electron, light is emitted and subsequently detected and the photoelectrical signal amplified by a photomultiplier tube. Then, because the gamma camera is composed of zones and is optimized to provide well-localized scintillation and spatial discrimination, a computer may tally the number of light collection events in each zone, thereby rendering an intensity-based image [106]. Also, as described for x-ray radiography, it makes sense that each gamma camera would be coupled with a grid-like collimator to further increase the accuracy with which excitation events in the scintillation crystal may be related to the inciting photon’s point of origin. It follows naturally that collimator

crosstalk and physical limitations within the gamma camera (e.g. imperfections in the mechanisms by which light is directed to the photomultiplier tubes, restrictions inherent of the collecting electronics, etc.) are responsible for the inferior resolution of SPECT compared to x-ray CT. After all, x-ray CT uses a controlled, directed x-ray beam, while the radiotracers employed in SPECT amount to volumetric sources upon incorporation in target tissues, the detection of which must be filtered to allow for clinically valuable imaging. Figure 1.8 details a basic cross section of a gamma camera, highlighting several of the features which must be optimized to increase spatial resolution to the extent practicable.

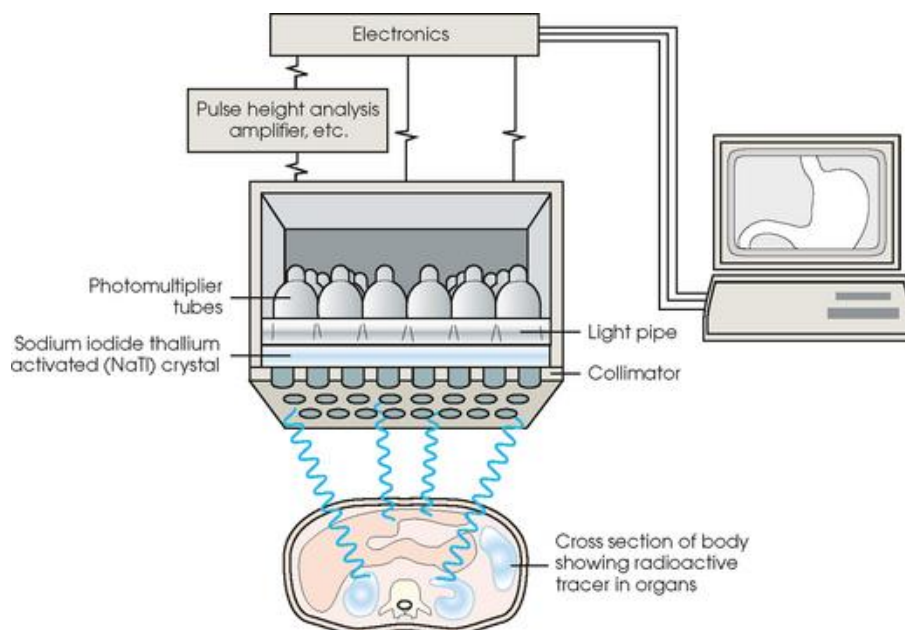


Figure 1.8 Gamma camera cross section

Unfortunately, such collimation again comes at the cost of increased patient dose. In general, as the spatial resolution of a SPECT system increases, its sensitivity decreases – meaning relatively large quantities of radioactive material must be present to obtain a useful diagnostic image in a reasonable amount of time [107]. In general, doses from SPECT are therefore greater than those from x-ray CT. For example, one study found an average dose of 1.15 ± 0.14 rem to patients undergoing a myocardial perfusion imaging procedure which utilized Tc-99m as the radiolabel. Even combined with CT localization, the dose resulting from administration of the radiotracer was greater than a factor of 20 higher than that from the x-ray CT [108]. Elevated radiation dose is thus one of the foremost concerns of SPECT and other nuclear medicine technologies. However,

SPECT provides a means to understand the importance of functional *in vivo* imaging, and while radioligand accumulation in SPECT is more a function of capillary blood flow in target tissues than local trace elemental composition, the analogy to APNEI is apparent. That is, diagnostic information beyond anatomical detail is useful in medical imaging. The goal of APNEI is to obtain such compositional information noninvasively (just as x-ray CT obtains density data noninvasively), while procedures such as SPECT and PET require the administration of radioactivity-labeled tracer compounds.

1.3.5 Positron Emission Tomography

A modality in the realm of nuclear medicine which competes with SPECT is PET. Similar to SPECT, PET requires the administration of a radiotracer. However, in the case of PET, rather than using a Tc-99m labeled gamma-emitting radioligand with known affinity to a certain tissue, a positron emitter is utilized in order to make use of the subsequent annihilation radiation. The most widely employed tracer compound in PET clinical oncology is fluorodeoxyglucose (FDG) labeled with fluorine-18, which is a positron emitter with a half-life of approximately 110 minutes. As an analogue of glucose, FDG concentrates in areas of high local glucose uptake and is therefore indicative of regions of elevated metabolic activity, such as cancer metastases [109]. This offers physiological information which is generally observed as a complement to an underlying x-ray CT scan. A downside of PET as compared to SPECT is that useful positron emitters tend to have very short half-lives, so they must be obtained in close proximity to the PET scanner, typically an on-site cyclotron (though the half-life of F-18 is long enough that 18-FDG may be manufactured and shipped commercially) [110]. This fact is the primary contributor to the high operating cost of PET machines [111]. Like SPECT, because radioactive material must be introduced into the body of the patient, the effective dose is generally higher than for projective imaging procedures such as x-ray CT. For example, a typical oncological scan utilizing 18-FDG imparts a dose of approximately 1.4 rem, which is on the order of the effective dose resulting from a Tc-99m myocardial perfusion imaging procedure in SPECT [112].

A fundamental difference in the method of operation of PET versus SPECT though is the importance of the coincident annihilation radiation. This aspect of PET proves to be a useful parallel to that used in APNEI, where satisfactory timing resolution is paramount to relating each detected gamma-ray to its point of origin with a high degree of certainty, thereby logging spatial

information which may be reconstructed to form a 3D image. The crux of a PET image is the physics of pair annihilation, in which case the positron emitted from a tracer such as 18-FDG travels a short distance before coming into contact with a free electron, its antiparticle. At that point, the mass of the two particles is converted to energy in the form of two 511 keV gamma-rays which are emitted in very nearly opposite directions, in accordance with the conservation of momentum given that the annihilation reaction takes place essentially at rest. It is for this reason that the primary feature of a PET scanner is the complete ring of scintillation detectors around the surface of the gantry – such that the annihilation photons may be coincidentally resolved. In coincidence counting in PET, the gamma-rays are assigned to the location of a perceived annihilation event only if the two gamma-rays have the appropriate energy and arrive at opposite detectors in the array within a predetermined time interval. The determination of the orientation of the annihilation event is correspondingly limited to a certain interval along each coincident line of response, which is governed predominantly by the resolving time of the detectors and the associated electronics [113]. Figure 1.9 illustrates the principles of pair annihilation and the resulting applicability of coincident counting. In some newer PET systems, time-of-flight (TOF) information from ultra-fast gamma-ray detectors (i.e. analysis of the difference in arrival time between the coincident gamma-rays) is utilized in order to more accurately define where along the line of response the annihilation event occurred [114].

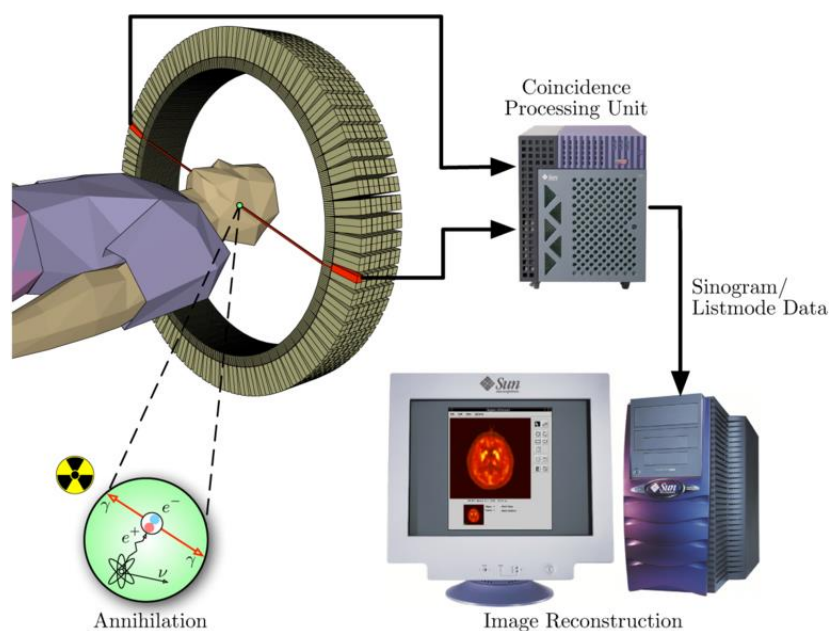


Figure 1.9 Principles of coincident counting in PET

Due to the electronic collimation provided by the coincident timing regime, photons which are detected without an associated 180° photon are ignored, reducing background and increasing SNR. Nevertheless, discrimination against confounding events is not perfect. As in other diagnostic imaging technologies, noise in PET systems arises from both photon scatter and technological limitations (e.g. random, unconnected events being registered by the PET system as coincident). Currently, it is difficult to trace the origin of an annihilation event to an interval of less than approximately 10 cm along a particular line of response [114]. An advantage of APNEI is that the 180° coincident emission of associated particles occurs at a location known to a high degree of certainty such that this aspect of the spatial ambiguity inherent of PET imaging is not a concern.

However, a challenge common to APNEI and PET is the optimization of timing resolution such that spatial resolution may be enhanced. In PET, the detectors employed are similar to the gamma cameras in SPECT, though the crystals are much smaller to allow for a large array of coincidence-sensitive detectors to be placed around the patient as well as to limit parallax error, which is when a gamma-ray enters the detector at an oblique angle and is falsely registered as coincident with an unassociated gamma-ray which is resolved within the temporal gate on the opposite side of the array [115]. In current PET detectors, a combination of Anger logic, pulse shape discrimination, and/or silicon photodetectors are utilized to perform depth-of-interaction as well as projective encoding, whereby the location of interaction of the annihilation gamma-ray within the scintillation detector itself may be approximated [115, 116, 117, 118]. In this way, a more accurate determination may be made as to the position of the line of response – limited not solely by the dimensions of each detector but by intra-crystal mechanisms so that the number of potential lines of response which may be perceived is greatly increased, thus increasing spatial resolution. Despite these advances in detector technology and following improvements to 3D image reconstruction algorithms, PET scans yield a typical spatial resolution of 4-6 mm – similar to that of SPECT [119, 120, 121]. Again, in continuous detector systems, spatial resolution is limited by changes in light distribution with depth-of-interaction of the gamma-ray inside the detector crystal [116], whereas discrete, pixelated detectors employing Anger logic only slightly increase spatial resolution at the expense of decreased sensitivity [119]. Such technological hurdles with regard to detector design, event discrimination, and timing resolution are well suited to discussions concerning the future of APNEI. Indeed, PET provides unique opportunities for

comparison to APNEI in the realms of functional imaging, detector timing regimes, and coincident counting circuitry. It is likely that many of the breakthroughs in PET detector technologies will play a shared role in the development of an APNEI prototype capable of discerning trace elemental disease signatures with a clinically valuable spatial resolution.

1.3.6 Magnetic Resonance Imaging

Though not as analogous to the fundamentals behind APNEI as the preceding entries, it is worthwhile to mention modalities which do not employ the use of ionizing radiation in order to round out the background on the current state of diagnostic imaging in medicine. One such medical imaging technique is MRI, which is classically used to produce anatomical 3D images through the use electromagnetic fields and radio waves. In short, the principles behind MRI are 1) the excitation of hydrogen nuclei (i.e. protons) with a pulsed magnetic field and 2) the measurement of the radiofrequency signal produced by the protons as they return to their equilibrium state. The radio signals from the protons in the process of “relaxing” can be decoded into spatial information by employing a gradient magnetic field such that the rate of precession of the proton’s magnetic moment is a function of (x,y,z) . Proton spin relaxation may be observed from different magnetic field planes depending on the integral state of magnetization, thereby allowing for preferential reduction or enhancement of certain tissues of interest to improve contrast resolution – so-called T1- and T2-weighted MR images. For example, T1-weighted images have a high signal for fatty tissues and paramagnetic substances such as gadolinium, manganese, and copper, while T2-weighted images have a correspondingly low signal for such materials [122, 123]. With its variety of analytical sequences (spin, echo, inversion recovery, diffusion weighted, etc.) which preferentially select certain tissues or even motion within tissues, MRI has wide applicability in disease diagnostics – including musculoskeletal, cardiovascular, gastrointestinal, and perhaps most importantly, neurological. The contrast between white and grey matter afforded by MRI have made it the diagnostic tool of choice in diseases of the brain and central nervous system [124]. Additionally, its wide applicability to the whole body and high physiological detail have instituted MRI as a valuable staging and intervention planning tool for a variety of solid cancers [125].

While proton-based MRI provides *in vivo* spatial resolution exceeding even x-ray CT (recent studies reporting resolutions on the order of micrometers [126]), it is important to note that such

high spatial resolving power relies upon the great abundance of hydrogen nuclei in the human body and can only be applied to nuclei with a net nuclear spin – limiting the functional imaging capability of MRI. Specific applications such as magnetic resonance spectroscopy (MRS) and functional magnetic resonance imaging (fMRI) measure concentrations of neurological metabolites and changes in blood flow to different areas of the brain, respectively [127, 128]. These techniques – because the imaging target(s) are far more specific and less profuse than overall tissue hydrogen content – yield significantly decreased SNRs as compared to traditional MRI.

As was illustrated in Figure 1.2, a similar decrease in SNR occurs when performing multinuclear imaging, such as on Na-23 or other nuclei with a net nuclear spin apart from that of hydrogen [38]. However, the signal obtained from Na-23 provided functional information which allowed the differentiation of malignant tissue from benign tissue, which is certainly valuable to the patient diagnostically and as a spatial detail informing potential intervention strategies. The importance of the functional aspect of imaging other elements in MRI is why research is ongoing with regard to potential ferromagnetic-based tracer compounds and multinuclear imaging for tissues such as the lungs and bones, which are currently not as well defined as neighboring tissues in traditional MRI due to the lower relative hydrogen content. In essence, multinuclear MR imaging shifts the focus from simple water content to target elements which are important on a case-by-case basis, like characteristic trace elemental imbalances in the development of cancer and other neurological disorders. For this reason, the fields of MRI research which focus on tissue function and metabolism are analogous to those which drive the development of an APNEI prototype system – microscopic changes in elemental homeostasis which may be detected and macroscopically located in order to direct diagnosis and treatment, while offering etiological insight. Furthermore, APNEI would not have the disadvantage of MRI's powerful magnets, which may not be applied to individuals with medical implants such as pacemakers, infusion catheters, or aneurysm clips.

1.3.7 Ultrasound

Though not closely related to APNEI or the tomographic procedures heretofore introduced, it is important to note that ultrasound imaging and its related technique – photoacoustic imaging – have their place in medical diagnostics, but their applications tend to be quite limited and the functional diagnostic gap relevant to diseases with elemental signatures remains open. For

example, as in x-ray CT, ultrasonic imaging relies upon differences in tissue density to reflect sound to varying degrees to a probe, which then interprets the received echoes as indicative of depths in the tissue at which the media changed (e.g. at the skull of a developing fetus relative to the surrounding amniotic fluid). In this way, structures of variable density may be resolved from one another *in vivo*. And while Doppler ultrasonography may be used to image functional impairments such as leaky heart valves, the technique still works on the principle of differential density and sound wave reflection rather than on elemental composition, which may significantly change between healthy and diseased tissues without altering the overall density of the tissue, which would generally remain dominated by the presence of water [129]. Additionally, it is very difficult to image deep tissue structures with ultrasonography as acoustic absorption causes significant loss of energy of the waves with increasing depth. It follows that performing effective ultrasound imaging of the brain through the skull is not feasible.

1.3.8 Photoacoustic Imaging

In the realm of ultrasonography is photoacoustic imaging, which differs from ultrasound imaging because while wideband ultrasonic wave detection is how the imaging data are collected, the tissue is interrogated with a pulsed laser rather than sound waves. The sound waves are the result of the photoacoustic effect, which is simply the generation of sound waves following light absorption through the processes of thermoelastic expansion and contraction [130]. Photoacoustic imaging has found applications in breast cancer diagnostics, the characterization of tumor angiogenesis, skin cancer investigation, and blood oxygenation mapping [131]. However, it is apparent upon reviewing the current primary applications of photoacoustic imaging in healthcare that they are relatively superficial. To an even greater extent than ultrasonography, the useful depth of photoacoustic imaging in tissue is severely limited, owing both to electromagnetic attenuation and acoustic absorption [132]. One study reporting on a method of deeply penetrating *in vivo* photoacoustic imaging with a clinical-based system was nevertheless limited to an effective depth of only a few centimeters [133]. While photoacoustic imaging is useful in the study of known tumors and in the detection of superficial neoplasms, because cancerous and healthy tissues respond similarly to the instigation by the pulsed laser, the imaging technique offers limited ability to differentiate between healthy and diseased tissue types, despite sub-millimeter spatial resolution at shallow tissue depths [134]. When radiofrequency radiation is employed, it is known as

thermoacoustic imaging, which has similar applications and drawbacks. The penetrability and characteristic mechanisms of interaction of neutrons in tissue may therefore offer a clinical advantage.

1.3.9 Neutron Radiography

The use of neutrons in medical imaging is not widespread but is also not a novel concept. In general, neutron radiography is inferior to and more costly than x-ray radiography in typical diagnostic applications, so it is employed in niche areas requiring specific material sensitivity or insensitivity [135]. However, the projective image collection process is essentially identical – neutrons being generated and used to penetrate a target, arriving at a collimator apparatus coupled with a reactive film or other electronic imaging plate in order to record differences in interaction among the distinct tissues through which the neutrons passed with valuable spatial resolution. The neutrons do not indicate differences in density like x-rays; rather, there are more complicated probabilities of interaction related to nuclear cross sections, which are dependent upon the energy of the incident neutrons. Given their unique penetrability, it is no surprise that neutron imaging is utilized in contraband detection and homeland security. For example, the image in Figure 1.10 would not be possible with x-ray radiography given the high attenuation of x-rays in lead [135].

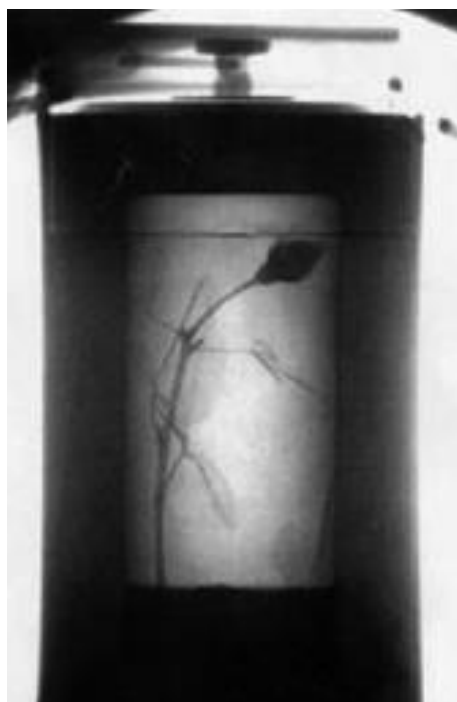


Figure 1.10 Classic neutron radiograph of a rose in a lead flask [135]. Reproduced with permission of Springer US.

However, the unique properties of neutron interactions with tissue most often hinder the use of neutron radiography in clinical settings. While neutrons elastically scatter with hydrogen nuclei with high probability – potentially offering forensic opportunities based on tissue water content as in MRI – x-ray radiography has proven far more diagnostically reliable given the direct nature of x-ray attenuation with increasing atomic number and electron density, as well as the tendency of neutrons to undergo multiple scattering events and consequently yield poor spatial resolution [135, 136]. The potentially greater dose imparted by neutrons while achieving lower diagnostic yield is also of concern. Differences in spatial resolution and contrast between neutron and x-ray radiography are shown in Figure 1.11 for imaging the head of a rat [135, 137]. Though aspects of the modalities may be thought of as complementary (e.g. clear view of the nasopharynx as indicated by the arrow in Figure 1.11(A)), x-ray radiography is the clear diagnostic preference.

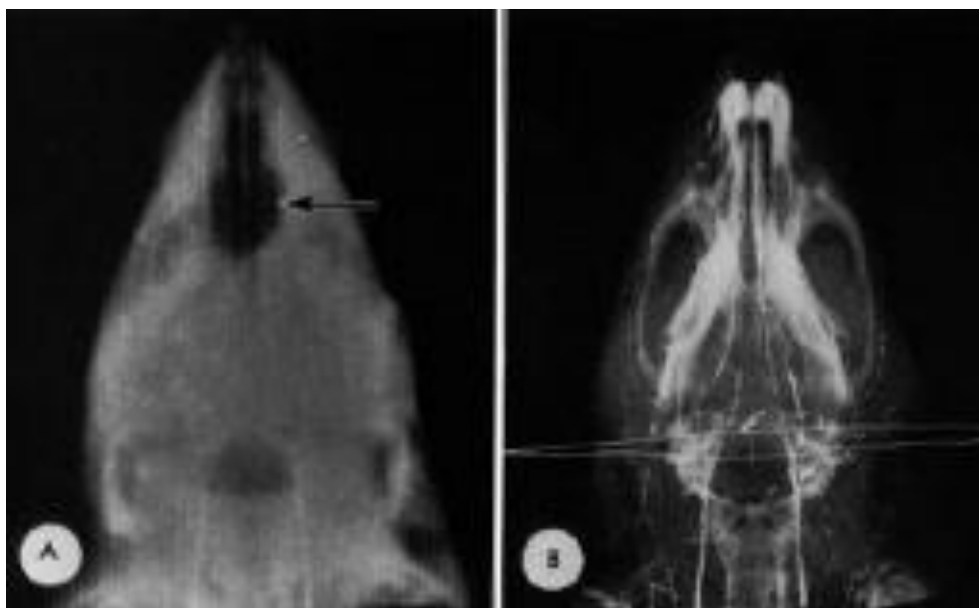


Figure 1.11 Radiographs of a rat head using (A) epithermal neutrons and (B) 42 kV x-rays [135, 137]. Reproduced with permission of Springer US.

Regardless, the applications of neutrons in medicine are not limited to projective radiography. As the following sections will elaborate, indirect measurement techniques can yield spatial and compositional information upon neutron interrogation which is important in disease diagnostics and tissue characterization. The unique properties of fast and thermal neutron interactions lend themselves to selective imaging applications capable of discerning slight changes in material composition – both *in vitro* and *in vivo*.

1.3.10 Conclusions

The background presented on the current state of medical diagnostic imaging in the US highlights the gap to be filled by neutron imaging – specifically the indirect imaging of target regions in the human body by resolving the temporal and energy information of fast neutron inelastic scatter gamma-rays by employing the associated particle technique. The target nuclei that will be imaged are those of trace elements known to function as signatures for a variety of disorders localized to certain tissues within the human body, which has the potential to solve one of the common limitations of established imaging modalities (i.e. the collection of compositional as opposed to only anatomical information). By looking at diagnostic imaging technologies ranging from traditional x-ray radiography to PET, MRI, and ultrasound through the lens of APNEI, the complementary advantages that APNEI can offer in the field of investigative medicine are clear, and the motivation for the research contributing to this dissertation is well defined.

1.4 Neutron Activation Analysis

1.4.1 Principles and Background

To understand APNEI, one must first appreciate the broad field of neutron activation analysis and the variety of ways in which it can be employed. The field of NAA includes the use of fast, epithermal, or thermal neutrons as well as the detection of prompt or delayed gamma-rays resulting from capture and/or inelastic scatter nuclear reactions. By analyzing the subsequent gamma-rays which are emitted in discrete energy quanta, an elemental profile of the interrogated sample may be assessed. While the concept of delayed-gamma neutron activation analysis (DGNAA) – generally defined by the activation of target elements by thermal neutrons and subsequent gamma-ray counting of the interrogated sample after some period of decay – has remained well established in the literature for more than 50 years [138, 139, 140, 141], research into NAA methodologies using fast neutrons and prompt inelastic scatter gamma-rays (PGNAA) is lacking predominantly due to technological limitations which yield inadequate elemental sensitivity as well as significant background and spectral interference problems owing to the simultaneous neutron irradiation and gamma-ray detection required in prompt-gamma NAA [4, 9, 142]. For example, in both thallium-doped sodium iodide (NaI(Tl)) scintillation and high-purity germanium (HPGe) semiconductor gamma-ray detectors exposed to neutron fields, activation occurs which complicates the

background gamma spectrum [4]. Additionally, certain types of HPGe detectors are prone to neutron damage, where neutron-induced defects in the lattice structure act as hole traps which cause a significant loss of energy resolution when holes are the majority carriers in the electron-hole pairs [143, 144]. These detector difficulties are in addition to the gamma-ray signals collected during simultaneous neutron irradiation which may be attributed to elements in the supporting apparatus and in environmental materials.

Nevertheless, as an analytical technique, DGNAA has proven sensitive to a variety of elements – including trace elements – both *in vitro* and *in vivo*. And while PGNAA lags behind DGNAA in terms of established laboratory applicability and clinical acceptance, the potential for growth in the domain of PGNAA has continued to improve with advances in detector technologies which allow improved spectroscopic capability and ultra-fast timing characteristics.

1.4.2 Types of NAA

1.4.2.1 Delayed-Gamma

In delayed-gamma NAA, neutrons are used to interact with target nuclei in order that those nuclei may be excited (i.e. activated or made unstable) such that the radiations emitted as a result of the decay of the activated nuclei may be detected and measured as a means to quantify the presence of certain element(s) within the sample. Because gamma-ray detector and energy spectroscopy technologies are commonplace and the mechanisms of interaction of photons with matter are well understood, the preferred mode of interaction by which DGNAA is employed is (n,γ) , where a neutron is absorbed by an atomic nucleus, the nucleus enters an excited isotopic state, and then de-excites with a distinctive half-life through the emission of a quantized gamma-ray or series of gamma-rays [145]. There is usually an accompanying beta particle emitted given that the nucleus becomes neutron rich as a result of the (n,γ) reaction, but the beta particle is unimportant from a detection/analytical standpoint given that it takes on a range of energies and is not likely to escape most sample volumes. In general, neutrons are captured most easily at thermal energies, which are defined as those below 0.025 eV (velocities around 2200 m/s). The probability of a certain neutron interaction taking place at a given neutron energy is measured in terms of the barn ($1 \text{ barn} = 100 \text{ fm}^2$), an interpretation of the effective cross-sectional area of a given nucleus. For reference, the fission cross section to thermal neutrons for U-235 – the fissile isotope of uranium most often employed in commercial nuclear reactors – is often stated to be around 600

barns [146]. By contrast, to relate to an element important to *in vivo* toxicological and etiological studies, Mn-55 has a thermal neutron capture cross section of 13.4 barns [147]. Figure 1.12 illustrates the general process of an (n,γ) reaction occurring at a target nucleus – including the basic difference between prompt and delayed gamma-rays, while Figure 1.13 details the corresponding decay scheme for Mn-56, in following up on the previous example. In Figure 1.13, it is apparent that stable Mn-55 has become radioactive Mn-56, which decays with a half-life of 2.58 hours. Detection and measurement of the delayed gamma radiations emitted by Mn-56 after thermal neutron interrogation demonstrate the principle behind DGNAA.

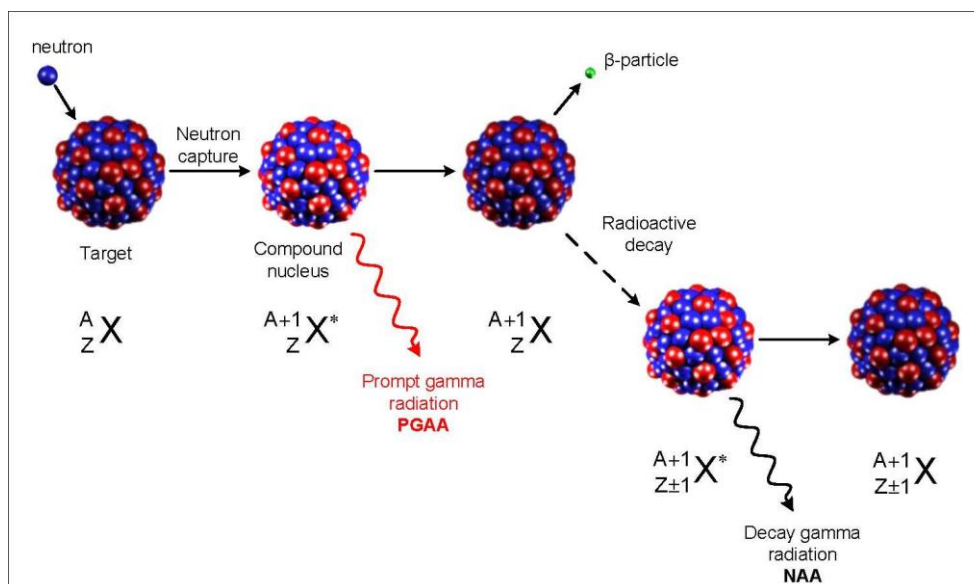


Figure 1.12 Schematic of the neutron capture process [148]

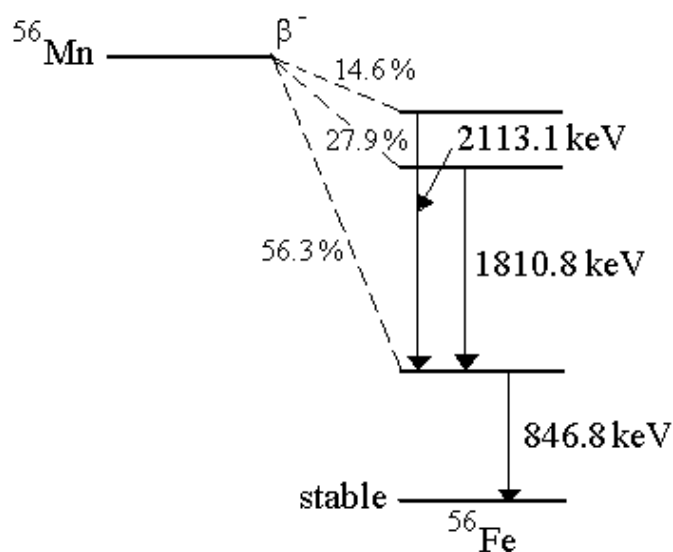


Figure 1.13 Decay scheme of Mn-56 [149]

In a practical sense, the detection limits for various trace elements to DGNA are dependent upon a number of factors, including 1) the volume of material being interrogated, 2) the neutron fluence rate across the sample volume, 3) the neutron energy spectrum upon which interaction cross sections are highly variable, 4) the irradiation time (which for *in vivo* studies is generally governed by local dose contribution), 5) the decay rates of the product target nuclei, and 6) the total gamma-ray spectroscopic data collection period. The neutron fluence rate, for example, is directly proportional to reaction rate within the sample; a greater number of interactions will yield a greater number of gamma-rays and correspondingly, a greater signal at the detector as recorded on the energy spectrum by the multichannel analyzer. Higher fluence rates generally allow for shorter irradiation times, which are certainly important in a clinical setting. However, as always, patient dose will ultimately decide the allowable exposure time for *in vivo* analyses.

Consideration of the neutron energy spectrum is also critical – not only from a dosimetry standpoint but with regard to the energy dependence of nuclear interaction probabilities. For example, in the case of the recurring Mn-55 example, thermal neutrons are the predominant instigators of the target reaction, so neutron moderators and reflectors – in material choice as well as geometry – should be optimized such that the thermal neutron flux at the target region is maximized. Performing such optimization tailored to the application at hand has the added benefit of allowing better characterization of the neutron energy spectrum, which can be used to more accurately predict the background and confounding gamma-ray signals from within the interrogated volume as well as the surrounding environment. Monte Carlo simulations are exceedingly useful in iteratively designing and improving neutron activation analysis systems for a specific purpose.

Once the neutron energy spectrum is known, it is possible to calculate (or simulate) each applicable nuclear reaction rate R over the range of neutron energies from E_{min} to E_{max} by [150]:

$$R = \int_{E_{min}}^{E_{max}} \phi(E)\sigma(E)dE \quad \text{Eq. 1.3}$$

where $\phi(E)$ is the neutron fluence rate and $\sigma(E)$ is the microscopic neutron cross section – each taken at energy E . The formula in Eq. 1.3 is the basis for a number of derivations in the literature which pertain to the production rate of radioactive nuclei, their subsequent disintegration, and their

equilibrium concentration. An advantage of DGNAA is that with knowledge of the production of radionuclides which may compete with the target nuclides in gamma spectrum contributions, counting of the activated samples may be postponed to preferentially select isotopes with longer half-lives for analysis. An advantage of neutron activation analysis in general is that the technique is nondestructive, so samples may be preserved and reused for recurring measurements or in future studies. However, some long-lived activation products may necessitate the handling of post-irradiation samples as radiological hazards or require such materials to be disposed of as radioactive waste, particularly following some *in vitro* analyses utilizing very high fluence rates and long irradiation times.

1.4.2.2 Prompt-Gamma

While delayed-gamma NAA systems have been shown to meaningfully quantitate *in vivo* concentrations of trace elements such as manganese, aluminum, fluorine, and selenium, such methods rely upon neutron capture reactions and their corresponding delayed gamma-rays, in which case the spatial information regarding trace elemental nuclei is lost [11, 17, 18, 19, 140, 151]. And while not all prompt-gamma NAA techniques utilize this potential imaging information, the opportunity to do so is now more feasible than ever as photon detector and signal processing technologies improve.

As evidenced in Figure 1.12, the difference between DGNAA and PGNAA is the timeframe of emission of the de-excitation gamma-rays of interest. Whereas DGNAA is concerned with photons which are emitted by an activation product in the interrogated volume after some period of decay, PGNAA targets the gamma-rays emitted nearly instantaneously upon neutron interaction and consequent compound nucleus formation (as denoted in red in Figure 1.12). This fact helps to explain why detector functionality plays such a major role in the effective application of PGNAA; all gamma-ray measurements must be made during neutron irradiation, which raises the background signals from activated or excited environmental materials, neutrons, and potentially other radiations such as x-rays which are produced as a result of running high voltage equipment inherent of many neutron sources or laboratory facilities. Some types of high-resolution detectors useful in gamma spectroscopy are also sensitive to neutron exposure, further complicating so-called “online” (i.e. during neutron irradiation) photon counting. It follows that in PGNAA, the construction of an experimental apparatus is not as straightforward as in DGNAA because the

irradiation and detection assemblies are not separate. In other words, there is no irradiation chamber optimized for maximum neutron fluence at the desired energies at one end of the laboratory and a separate lead-constructed counting cave outfitted with multiple HPGe detectors at the other end of the laboratory. The sample or tissue volume is to be interrogated with neutrons and simultaneously yet discriminately analyzed for gamma-ray emissions, so the system must have an integrated layout – one allowing for the photons of interest to reach the detector(s), while protecting the detector(s) from neutron damage, in addition to neutron moderation and reflection considerations. An example of a prompt-gamma NAA setup designed for *in vivo* application of fast neutrons to the extremities is shown in Figure 1.14 [142].

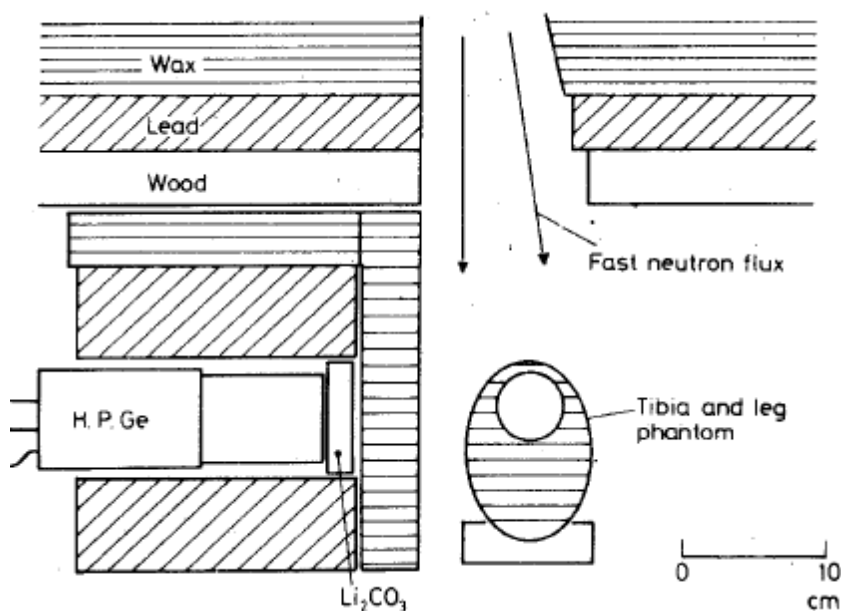


Figure 1.14 Apparatus for PGNAA of tibia phantom [142]. Reproduced with permission of Akademiai Kiado RT.

Note that the study by Kacperek et al. – which utilized the layout in Figure 1.14 – pursued the fast neutron reaction ($n, n'\gamma$) to quantify the concentrations of phosphorus, magnesium, sodium, calcium, copper, iron, zinc, and silicon in both tissue phantoms and beef samples, ultimately yielding measurement sensitivities as low as normal tissue concentrations [142]. For reference, the investigators' neutron source was a Van de Graaff accelerator operating in pulse mode, which bombarded a deuterium-loaded target with deuterium ions to produce 4.8 MeV monoenergetic neutrons. As shown in the study, the ($n, n'\gamma$) reaction with target nuclei is the predominant focus in PGNAA. While Figure 1.12 illustrates nuclear absorption of the neutron (still inciting the

emission of a prompt gamma-ray), most prompt gamma-rays of interest in PGNA are the result of inelastic collisions of fast neutrons with atomic nuclei, where the neutron imparts only some of its energy to the nucleus, thereby causing the nucleus to enter an isobaric excited state while the initiating neutron scatters away to potentially take part in further interactions. The study presented in this dissertation focuses on the inelastic scattering of fast neutrons with iron (Fe-56) nuclei. A generic example of a neutron inelastically scattering with a nucleus is shown in Figure 1.15. In such a reaction, it is important to note that while momentum is conserved (as always), kinetic energy is not. The kinetic energy of the incoming neutron is greater than that of the sum of the product nucleus and scattered neutron due to that kinetic energy which is converted to excitation energy of the target nucleus.

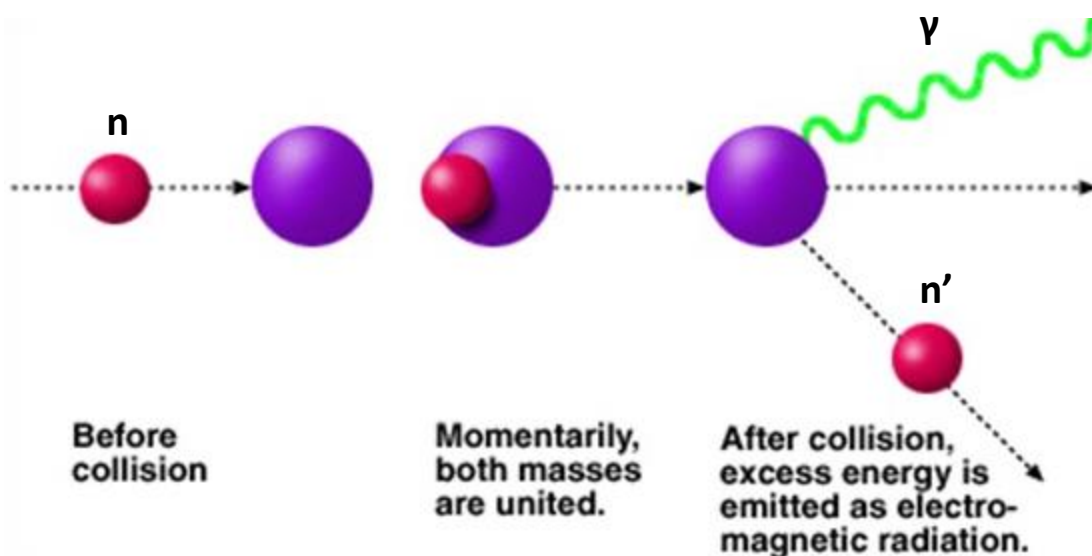


Figure 1.15 Example of a $(n,n'\gamma)$ nuclear reaction [152]

Because PGNA relies upon the quantized de-excitation of a nucleus from an excited state, the energy of the incident neutron is just as important as in DGNA. Not only should the energy spectrum be characterized and moderated as necessary in order to enable the estimation of activation product yields by considering the applicable nuclear interaction cross sections (as in DGNA), but in the case of inelastic collisions, higher energy neutrons have the potential to incite higher levels of excitation in a given nucleus. After all, since the neutron will impart some fraction of its kinetic energy in the nucleus of the target atom upon scattering, a higher incident energy means that higher nuclear energy quanta may be attained. And because subsequent de-excitation

through gamma-ray emission is the key to elemental species identification and quantification, more potential radiations from target nuclei as well as environmental nuclei will tend to complicate the electromagnetic spectrum and confound the task of spectroscopic analysis [142, 153]. For this reason, there is a fine balance in PGNAA between biasing toward fast neutrons of high energy for enhanced penetrability, while maintaining energies below some threshold such that only low-level nuclear excitation states are possible and the photon spectrum is correspondingly simplified. Increased neutron energy increases the probability for interactions which result in radiations that can compete with the area of spectroscopic interest.

Prompt-gamma NAA, like delayed-gamma NAA, is nondestructive and can be used to assess multiple elemental concentrations concurrently. Furthermore, while DGNAA tends to utilize thermalized neutrons and can thus suffer from attenuation or matrix effects at relatively shallow depths, PGNAA employing fast neutrons is not nearly as significantly affected by limitations pertaining to material penetration [153]. Despite these advantages of PGNAA and NAA in general, PGNAA has thus far proven far less sensitive than DGNAA in determining the elemental composition of interrogated samples, as compiled in Table 1.4. The relative sensitivities in the table were calculated using the corresponding neutron cross sections, gamma-ray branching ratios, and theoretical detection efficiencies under the assumption that the same detector was used for each measurement [138, 142].

Table 1.4 – Comparison of sensitivities for fast (n,n'γ) reactions and DGNAA reactions [142]

Element	Fast (n,n'γ)		Ratio of sensitivities
	Sensitivity	Sensitivity	
Fluorine	0.584	0.0038	155
Sodium	4.87	0.237	20.5
Magnesium	0.43	0.0033	104
Silicon	0.232	0.114	2.04
Phosphorus	14.7	1.57	9.4
Iron	0.07	0.00123	56.9
Copper	0.0075	0.000099	75.6
Zinc	0.018	0.00043	42.4

Due to the marked insensitivity of PGNAA – predominantly due to higher background environments, decreased SNR, and lower gamma yield as a result of there being no buildup of compound target nuclei regardless of irradiation time (i.e. the gamma yield is proportional only to

the fast neutron fluence rate) – the technique has found use in the analysis of bulk materials with large sample sizes such that the lacking sensitivity is offset by the large mass of material present. Geological mineral surveys such as well logging and bore hole analysis are current widespread applications of PGNAA [154].

1.4.3 Non-Medical Applications

To continue the previous thought, prompt-gamma NAA is predominantly employed in bulk material assays. Though sensitivities for PGNAA are generally not as impressive as for DGNAA, the technique nevertheless allows for 1) the measurement of compound nuclei which are not activation products and thus are essentially direct indications of the concentrations of stable isotopes, 2) the measurement of extremely short-lived nuclides without having to quickly transfer samples between irradiation and counting apparatuses, 3) potentially shorter irradiation times given that relatively long-lived activated nuclei do not need to build up to detectable levels, 4) data collection is maintained at a constant rate proportional to the neutron fluence rate rather than governed by exponential decay, and 5) the energies of gamma-rays emitted by compound nuclei are less likely to be similar than those of competing activation products in DGNAA [155]. The online analysis possible using PGNAA therefore lends itself well to the ongoing characterization of bulk geological materials as well as cargo containers storing waste or other products which may be quickly screened for homeland security purposes. PGNAA is also used as an exploratory tool because a device consisting of a neutron source with accompanying prompt gamma-ray detectors may be employed to scan the elemental composition of the surrounding environment.

For example, PGNAA has been used to identify the composition of coal to determine the characteristics it will exhibit upon burning in a commercial power plant as well as the feasibility with which a particular type of coal may be converted into some intermediate material that has advantageous properties to the coal conversion industry [156]. PGNAA has also been used in trace heavy metal detection in 55-gal drums of mixed, transuranic waste – in order to properly classify the contents of each drum according to the Resource Conservation and Recovery Act (RCRA) so that proper waste treatment (if necessary) and disposal are performed in accordance with the prospective disposal site's waste management permit [157]. And from the standpoint of exploration, PGNAA is widely employed not only in the mining industry but in security. While neutron bombardment certainly is associated with the detection of special nuclear materials, it is

also useful in the detection of traditional explosives – such as in vehicles crossing a country's border or military checkpoint, or even in the reclamation of unexploded naval ordnance on the sea floor [4, 13, 158].

Like DGNAA, PGNAA is also used in laboratory settings for elemental analysis. One of the greatest differences between applications is the selection of the neutron source. Industrial measurements tend to rely upon radioisotopic point sources such as californium-252, which has a half-life of 2.6 years and fissions spontaneously about 3% of the time, emitting nearly 4 neutrons per fission [159]. Alternatively, strong alpha-emitting nuclides such as americium-241 or plutonium-238 may be coupled with beryllium to exploit its low nuclear binding energy such that neutrons are emitted as a result of (α ,n) reactions. Such bulk applications may also use neutron generators – such as DD or DT – which have the advantage of being a minimal ionizing radiation hazard when not energized. However, in the laboratory, small sample analysis is generally performed using more direct neutron beams, such as those collimated from a nuclear reactor port or output by a particle accelerator. The dwindling number of operating nuclear reactors – both in the commercial and research sectors – is a clear limitation of the former neutron source, despite the very high neutron fluxes available for sample interrogation. The political climate, general public distrust in the nuclear industry – particularly in the wake of the Fukushima Daiichi disaster in 2011, and anti-proliferation concerns have shifted efforts away from more efficiently using reactors as neutron sources toward the development of charged particle accelerators with the capacity to produce high-flux neutron fields [160].

One process by which neutrons are produced using a charged-particle accelerator is called spallation. In general, high energy protons are accelerated toward a target with a high atomic number, such as lead, uranium, or tungsten. Interaction of such high energy protons (upwards of 120 MeV) with large nuclei in the target causes the initial release of high-energy neutrons, nuclear fragments, fission products, and pions which incite further neutron-producing reactions in the manner of a short-range chain reaction or cascade. With greater than 10 neutrons emitted per spallation sequence and significantly less heat production than in fission reactions, spallation-based neutron sources have wide applicability in research [161]. However, high capital, operational, and maintenance costs have limited their availability. Linear accelerators and cyclotrons may also be used to generate neutrons through the aforementioned DD (i.e. ${}^2\text{H}(\text{d},\text{n}){}^3\text{He}$) and DT (i.e. ${}^3\text{H}(\text{d},\text{n}){}^4\text{He}$) reactions, as well as other reactions such as ${}^3\text{H}(\text{p},\text{n}){}^3\text{He}$ and ${}^7\text{Li}(\text{p},\text{n}){}^7\text{Be}$

1.4.4 Medical Applications

Although DGNAA has some non-medical applications, it is important to note that most commercial uses of PGNAA are in bulk analytics (non-medical) while most uses of DGNAA are for much smaller scale samples due to the increased sensitivity, which is why DGNAA is increasingly being employed for the analysis of *in vitro* samples and *in vivo* elemental concentrations. From a functional standpoint, because it is noninvasive and nondestructive, NAA is well suited to *in vivo* analysis. Furthermore, because DGNAA utilizes activation products with a given half-life, a separate counting apparatus may be utilized specific to the task at hand – not only separate from the irradiation location and optimized for patient comfort but constructed in such a way as to maximize SNR from the target tissue(s). Given the framework of this dissertation, it is logical to consider DGNAA as the principle contributor to medical applications in the field of neutron activation analysis, a basis from which to understand the current role of NAA in medical diagnostics as well as how its functions may be expanded and improved with the addition of imaging and electronic background collimation capabilities as planned in APNEI.

Given the sensitivity of DGNAA to toxicologically important heavy metals (e.g. as compared to PGNAA in Table 1.4), the technique has found a place in the assessment of occupational and environmental exposures. For example, following up on the Mn-55 example introduced previously, several heavy metals such as manganese are known to build up in the bone as effective indicators of chronic exposure, whereas measurements of bodily fluids such as the blood may only be relied upon for acute exposure evaluation given the relatively short biological half-life and relatively high solubility of the compounds in those fluids [139]. So, there was motivation to develop a noninvasive means to quantify manganese in bone *in vivo*. After a Monte Carlo simulation study, Liu et al. developed a DD-based neutron generator and HPGe-based detector system with high sensitivity to bone manganese. The purpose of the simulations was to find the optimal system configuration, the goal being to quantify Mn in bone *in vivo* with a clinically useful detection limit and acceptable patient dose [139]. The simulations indicated viability of the device, and the lab group proceeded to construct and implement the system using a DD neutron generator, neutron moderation / reflection materials, manganese-doped human hand phantoms, and a high-purity germanium semiconductor detector. The study yielded an impressive and biologically relevant detection limit for Mn of 0.74 ppm, while imparting an equivalent dose of 85.4 mSv to the hand (i.e. the target bone volume) and a whole body effective dose of approximately 17 μ Sv

[140]. Through continuous efforts to prepare the system for use in a clinical study on a Mn-exposed cohort of welders, the detection limit and dose to the hand were improved to 0.64 ppm and 36 mSv, respectively [69, 165].

All in all, the background in the literature for the application of DGNAA to tissue equivalent phantoms and *in vivo* tissues for the quantification of trace elemental concentrations is well established. Elements ranging from manganese to fluorine, gadolinium, nitrogen, calcium, potassium, phosphorus, cadmium, chlorine, iodine, and sodium have been the target of *in vivo* neutron activation analysis, as the relevant concentrations pertain to the diagnosis and staging of osteoporosis, renal osteodystrophy, rheumatoid arthritis, metal toxicity, and other environmental or medical exposures [6, 16, 69, 71, 139, 140, 142, 151, 165]. In many cases where trace elemental evaluation is the goal, the irradiation target tissue in an extremity, such as the bones in the hand or the tibia. This is to assist in optimizing the geometry of both the irradiation and counting systems as well as to minimize dose to the patient by isolating the extremity as far from the trunk of the body as possible with shielding materials. However, some applications of *in vivo* NAA call for whole body irradiation, in which case PGNAA again plays a role because the volume of a reference man approaches the type of “bulk” analysis for which PGNAA is more classically known. In other words, enough interrogated material is present to allow for the prompt-gamma evaluation of certain elements in the body which are present in relative abundance.

For example, just as the proportions of hydrogen, oxygen, and nitrogen may be evaluated using PGNAA to identify unexploded ordnance in semi-trailers and intermodals, so may the same proportions be measured in the human body to determine overall tissue composition – namely fat, muscle, and water content [4, 166, 167]. In humans, such body composition analysis can be used after surgical intervention to evaluate proper nutritional uptake in various body compartments or to quantitate protein loss in cases of serious illness [4], which can aid in planning further intervention or to gauge the progress of patient recovery. Such noninvasive analysis of tissue composition is also important in livestock, where evaluation of the growth process in meat and dairy animal products helps to ensure that the application of specific diet protocols or hormonal therapies are having positive effects with regard to lean gains.

In addition to *in vivo* applications, DGNAA is certainly applicable *in vitro* as a state-of-the-art analytical technique offering better than μg -level elemental sensitivities without nearly the preparatory burden required of competing modalities such as atomic absorption spectrometry or

inductively-coupled mass spectrometry. In general, when samples are prepared, irradiated, and counted *in vitro* the detection limits are lower than those for elements *in vivo* due to improved geometries, efficiencies, and variable control. Hematology is one area where the application of DGNAA is becoming established. Many current blood tests have a turnaround time on the order of days and require chemical digestion processes which introduce other uncertainties that can complicate lab results, rendering diagnostics less definitive [168]. Two elements generally of interest in blood analytics are sodium and chlorine, the sensitivity for which was evaluated by Zamboni et al. for an absolute DGNAA technique for comparison to more conventional techniques which quantify elemental concentrations in blood for investigating the state of human organ functionality [169]. Table 1.5 summarizes a sample of their findings.

Table 1.5 – The concentration of Cl and Na in blood using a DGNAA technique [169]

Sample ID	Neutron flux ($\times 10^{11}$ n/s/cm ²)	Cl ($\mu\text{g}/\mu\text{L}$) serum ^a 3.44-3.76 ^b 3.41-3.69	Na ($\mu\text{g}/\mu\text{L}$) whole blood ^b 1.51-1.67
D1	1.16	3.36 \pm 0.11	1.69 \pm 0.05
D2	6.51	3.52 \pm 0.13	1.71 \pm 0.09
D4	6.08	3.77 \pm 0.11	1.57 \pm 0.09
D5	4.85	3.42 \pm 0.12	1.69 \pm 0.09
D6	4.99	3.96 \pm 0.15	1.70 \pm 0.09
D7	1.38	3.37 \pm 0.14	1.48 \pm 0.08
D9	1.35	3.26 \pm 0.19	1.41 \pm 0.08
D10	4.90	3.32 \pm 0.20	1.60 \pm 0.08
D11	3.34	3.76 \pm 0.13	1.74 \pm 0.06

^areference value from [170]

^binterval proposed by [169]

Looking at the results in Table 1.5, it is clear that the sensitivity offered by DGNAA is comparable to that offered by traditional chemistry-based procedures. The nuclear hematology method has been expanded to the detection of aluminum, bromine, calcium, potassium, magnesium, and manganese, traditional analysis for which can take days to weeks. However, employing DGNAA has allowed a nominal sample turnaround time of only 3 hours [169].

Additionally, induced activity in interrogated samples is minimal such that shielding is not required for storage, yet enough residual radioactivity is present to permit subsequent, confirmatory counting measurements. And because specialized reactants and laboratory equipment need not be maintained for each potential element of interest, DGNAA proves economical as well as timely in the analysis of blood *in vitro* [169].

In terms of imaging, neutron activation analysis technologies have only made an exploratory foray into the field of medical diagnostics. Beyond neutron radiography which has been outlined previously, a relative of NAA that has shown some promise with regard to spatial elemental assessments *in vivo* is neutron stimulated emission computed tomography (NSECT). The key to NSECT is the use of a collimated beam of neutrons. The neutrons cause nuclear excitations along their path of travel such that characteristic de-excitation gamma-rays are emitted and may be detected by photon spectroscopy equipment, as in PGNAA. However, in NSECT, the neutron beam is iteratively oriented at intervals around the interrogated volume so that the distributions of target nuclear concentrations may be reconstructed in three dimensions, as in x-ray computed tomography. Due to the capability of imaging elemental concentrations *in vivo* and the functional importance of deviations in elemental homeostasis to disease progression, NSECT has proven effective in cancer staging (particularly in breast cancer) and detecting iron overload disorders [171, 172]. Figure 1.17 shows a basic NSECT setup applied in GEANT4 simulations to determine the sensitivity to liver iron concentrations, which was found to be between 1 and 2 mg/g *in vivo* [173].

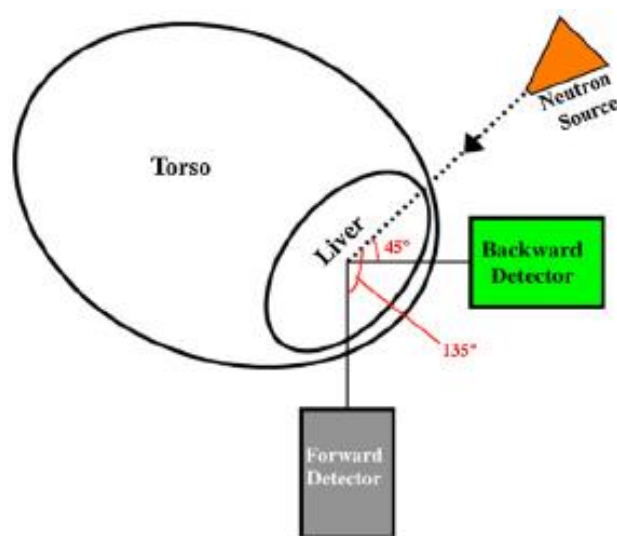


Figure 1.17 Simple schematic of NSECT system [173]. © Institute of Physics and Engineering in Medicine. Reproduced by permission of IOP Publishing. All rights reserved.

There are also ongoing investigations of applying NSECT to renal and brain cancers. With regard to renal cancer, elements of interest are potassium, sodium, and phosphorus. Using MCNP, the relative intensities were spatially mapped in a simulated human phantom, yielding the impressive images in Figure 1.18 while imparting an average effective dose of less than 4 mSv and 30 mSv equivalent dose to each kidney, the maximally exposed organs [174].

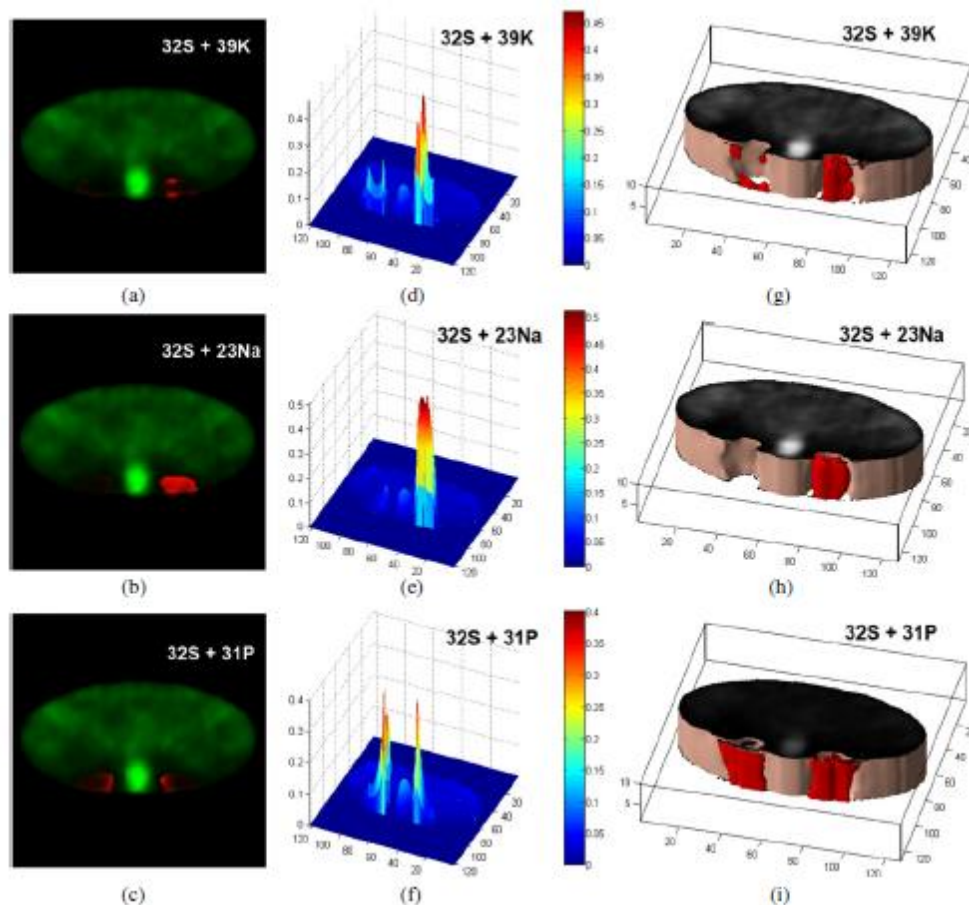
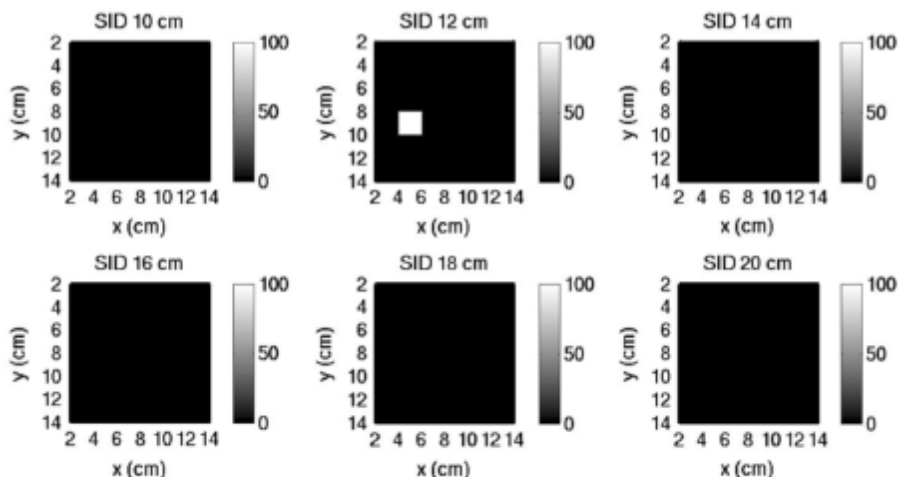


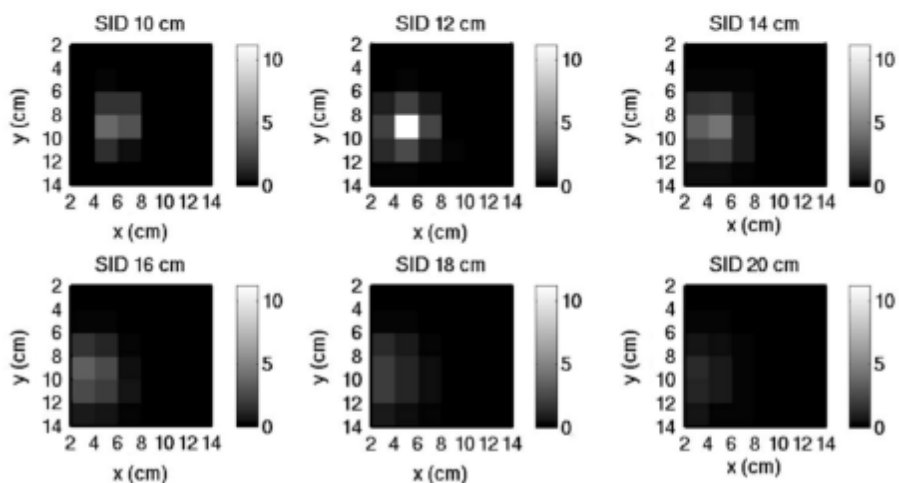
Figure 1.18 NSECT Tomographic images of elemental concentrations in renal cancer [174]. Left: 2-dimensional images. Middle: pixel intensities Right: volume-rendered 3D images. © Institute of Physics and Engineering in Medicine. Reproduced by permission of IOP.

In NSECT as in x-ray CT, the spatial resolution is governed in part by the number of projection angles and the corresponding dose imparted to the target tissue(s), as well as the effectiveness of the reconstruction algorithm. A separate study by the same research group produced tomographic images to more directly visualize the spatial resolution of a theoretical NSECT system in GEANT4 to a Na-22 point source. In the study, the system utilized HPGe detectors and a 10 cm x 10 cm x 10 cm field of view – as if for application in imaging breast cancer [175]. Figure 1.19 summarizes the spatial resolution capability of their hypothetical NSECT

system. Note that only one true tomographic slice should contain signal from the neutron-stimulated point source, but due to spatial uncertainty (i.e. blur), each of the slices in the reconstructed images indicate the apparent presence of activated elemental sodium.



2-D slices of the true image. Each slice is of the x,y plane.



2-D slices of the 3-D reconstructed volume.

Figure 1.19 Simulated tomographic resolution in NSECT [175]. Reproduced with permission of IEEE.

The background presented on NSECT is important because it is the most closely related modality to APNEI, in that it is also capable of imaging element-based organ functionality and is currently a proven complementary diagnostic tool in clinical settings. The great strides made in the realm of NSECT over the past decade indicate that the technique and its accompanying technologies are certainly avenues worthy of further research with regard to *in vivo* disease

diagnostics. However, the challenges of image reconstruction, the accompanying dose from multi-angle data collection, and corresponding necessary data collection times may become limiting. Interestingly, the leading research group in the field of NSECT has proposed the benefits of moving in the direction of associated particle imaging and time-of-flight gamma spectroscopy [176]. Given that the group had pursued NSECT with the use of a pencil neutron beam which required raster scanning and tomographic rotation, the duration of each scan – even for relatively small volumes such as the breast – could have been rendered clinically infeasible. By employing a fan-shaped neutron beam with associated particle tracking for projective resolution and time-of-flight detection for depth resolution, the need for tomographic rotation of the neutron source was eliminated. Using GEANT4, the group concluded that the associated particle methodology had the potential to reduce acquisition time by as much as an order of magnitude [176]. This is an excellent point in support of the underlying principles and feasibility of APNEI, though research in the area is still lacking.

1.4.5 Competing Analytical Modalities

Currently, *in vivo* trace elemental concentrations are examined using an array of technologies and methodologies, including x-ray fluorescence (XRF), and magnetic resonance imaging (MRI) through the quantitative susceptibility mapping (QSM) post-processing technique. Similarly, XRF may be employed to quantify certain trace metal concentrations *in vivo* for toxicity studies, but the distribution of the target element(s) cannot be discerned [68]. Even in the emerging field of XRF imaging, the limited penetrability of x-ray radiation through tissue as well as the necessity of raster scanning and its associated parameters have relegated the technology predominantly to rodent and *in vitro* models [177, 178]. Finally, while MRI can be performed *in vivo* and offers impressive spatial resolution, such images are indirect measures of paramagnetic species which do not quantify metal concentrations. In the case of iron – a trace metal whose variable deposition in the brain has been associated with numerous neurological and psychiatric disorders [179] – there has been some success in applying QSM to magnetic resonance images in order to measure and plot iron content *in vivo* [180, 181]. However, the QSM process involves broad assumptions which give rise to differences in the reliability with which iron levels may be assessed, even between adjacent tissue types in the brain (i.e. gray matter versus white matter). And because QSM relies upon the magnetic susceptibility of paramagnetic iron, other nonmagnetic biomarker elements

cannot be assessed; while at the same time, tissues containing additional diamagnetic species confound iron concentration determination [182].

As far as atomic absorption spectroscopy (AAS) and inductively-coupled mass spectrometry (ICP-MS), neither are applicable to *in vivo* studies – inherent to the natures of the analytical procedures required. Samples pertaining to biological study must be extracted from a particular specimen, digested, reduced, and otherwise prepared for elemental analysis, and are then destroyed during the measurement process. In AAS, each sample is atomized and may traditionally only be measured for a single element at a time. In ICP-MS – though far superior to AAS in terms of sensitivity, speed, and consistency – the sample is ultimately incorporated into a plasma and must often be diluted by several orders of magnitude in order to reduce interference and matrix effects, a process which introduces error and issues with repeatability. Again, in both AAS and ICP-MS, some of the sample is lost to each analysis, so samples with very little mass such as may be drawn from critical organs within a patient suffer not only from the potential for few checks for analytical consistency, but from chemical alteration of the sample upon preparation or from inadvertent contamination of the sample during the necessary laboratory procedures preceding ultimate analysis. The requirement for chemical solvents, reactants, heating elements, technical labor, and time also increase the cost of ICP-MS and AAS, while decreasing their convenience and *in situ* applicability. So, while such valuable tools in analytical chemistry offering better than part-per-billion sensitivity to most elements – ICP-MS and AAS have remained relegated to the bench top and are not as ideally suited as APNEI to quickly measure elemental concentrations without extensive wet chemical preparations. Furthermore, APNEI setups may be optimized for *in vivo* application, which is not a possibility for ICP-MS or AAS.

1.4.6 Conclusions

Neutron activation analysis has a proven niche in both industrial, defense-related, and medical applications as a noninvasive and nondestructive analytical technique. In industry, NAA is employed in geological surveying to determine bulk material mineral composition on a large scale. In homeland security, NAA is instituted as a border or transportation safeguard as it allows the rapid, localized detection of fissile materials as well as conventional explosives in large shipping containers. And as it directly pertains to this dissertation, NAA is used in medicine both *in vitro* and *in vivo* to perform elemental assays ranging from whole-body calcium content to liver

cadmium or iron concentrations – which are indicative of the state of disease of those tissues within a patient. In general, NAA is fast, requires very little sample preparation, and depending on the chosen neutron source, may be flexibly applied to a variety of diagnostic procedures. As the basic principle behind NSECT, a form of NAA is already in development which has shown promise in providing enhanced tissue specificity at clinically valuable resolutions for cancers of the breast, kidneys, and brain through targeted elemental imaging. And given the propensity for elemental homeostasis to be affected in malignancies and other disorders, such local tissue information has an important diagnostic role to play – the literature support for which is strong and growing every day. In other words, *in vivo* trace elemental measurements using a derivation of NAA may be employed to quantify changes in tissue function which accompany the development of a disease – even in its early stages. APNEI may therefore be thought of as an evolution of NAA and NSECT, a coinciding pathway which offers the potential to collect in real time compositional tissue information *in vivo* without the need for tomographic rotation and without prolonged counting times for activated nuclear species as they decay away after some period of delay. However, without tomography, the spatial component of APNEI which allows *in vivo* imaging relies upon the associated particle technique and associated timing resolution. This is the last piece of background required to appreciate the principles behind APNEI as well as to understand the motivation for ongoing research in the fields of detector technologies and electronic pulse processing equipment.

1.5 The Associated Particle Neutron Imaging Technique

1.5.1 Principles and Background

The associated particle technique is a nuance that may be used in conjunction with fast neutron inelastic scatter analysis in order to not only quantify elemental concentrations in the interrogated target, but to resolve the locations of nuclear collisions to a high degree of certainty, thereby allowing elemental distributions to be spatially mapped within the interrogated volume. Similar to the association of annihilation gamma-rays in PET imaging, associated particles in a neutron generator (such as may employ the DT or DD reaction) may be used to infer the direction of travel of the neutron. Furthermore, as in PET imaging, a timing component is incorporated with the purpose of excluding non-coincident events. In other words, if annihilation gamma-rays are

not detected 180° from one another within a predetermined interval in PET, the event is not registered and the data do not contribute to the reconstructed image. This principle is applied in APNEI as well, except the timing interval is instigated by the fast neutron's associated particle and concluded by the detection of a supposed inelastic scatter gamma-ray from a target nucleus in the interrogated volume. The process may be better understood by considering the sealed tube neutron generator itself and the underlying reaction from which the associated particle and neutron are produced.

1.5.2 Sealed Tube Neutron Generators

1.5.2.1 Construction and Operation

In short, neutron generators are transportable linear accelerators capable of fusing isotopes of hydrogen, thereby producing neutrons. The fusion reactions of interest are DD and DT, each of which produce a fast neutron and a spatially-associated recoil ion. Components of a sealed tube neutron generator include an ion source, a microwave source, accelerating and focusing electrodes, and a target where the fusion reaction is intended to take place. In general, the basic process takes place as follows: 1) Deuterium and/or tritium gas is ionized – typically by a Penning or RF-based ion source – through energetic electron collisions, 2) the gas ions are then extracted, accelerated, and focused onto the target material using electromagnetic field gradients as well as fixed magnets within the acceleration chamber, and finally, 3) the accelerated ions impact the target, yielding a DD or DT reaction which produces fast neutrons as one product. The plasma which forms along the anode axis and ultimately is responsible for ionizing the neutral gas molecules is initiated by the ion source and sustained by ensuing electron cascades [183].

The ion source employed in the neutron generator (i.e. Adelphi DD-110) utilized, in part, for the presented project was RF-based, which allowed for high power operation and correspondingly high neutron yield due to higher relative proportions of atomic rather than molecular hydrogen species [184]. The DD-110 – manufactured by Adelphi – operates as previously described, where the microwave source is used to guide the current from the RF-based ion source in the antenna, which provides a gradient through which the electrons in the plasma are energized and accelerated. The target is made of titanium, which over time becomes impregnated with deuterium up to a saturation state such that the DD reaction takes place at a consistent rate. Naturally, heat buildup at the target from the fusion reaction is undesirable, so continuous liquid cooling is employed, as

well as a novel V-shaped target which increases the effective surface area (similar to why rotating anodes are used in x-ray tubes) without unduly increasing the beam spot diameter.

Because excess deuterium gas must be continuously removed from the high voltage areas of the neutron generator to prevent electrical arcing, roughing and turbo pumps are applied to the volume of the generator head. This constant negative pressure is complemented by the digitally precise deuterium gas valve which may be incrementally adjusted with plasma pressure to maximize the percentage of deuterium atoms which are ionized. A heat exchanger (also known as a chiller) circulates and chills the fluid which is used to maintain temperature control of the target, RF supply, and plasma chamber. A simple schematic of the DD-110 neutron generator is shown in Figure 1.20 – without the support systems pertaining to gas supply, vacuum, and temperature control.

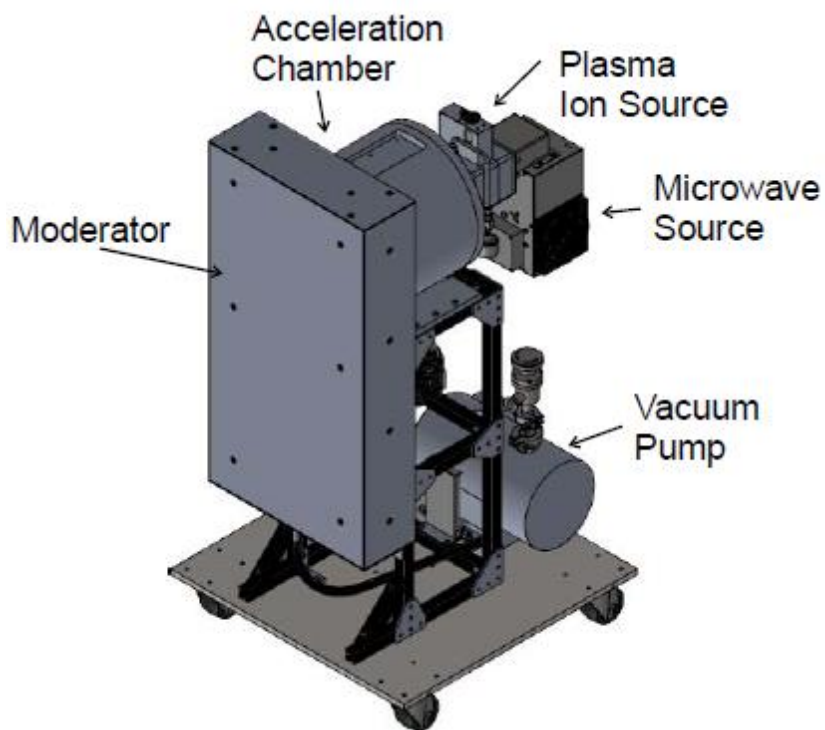


Figure 1.20 Adelphi DD-110 neutron generator [185]

The built-in moderator is partially modifiable for different experiments utilizing fast or thermalized neutrons. What the DD-110 does not include is the component which renders APNEI possible, a pixelated and temporally-calibrated associated particle (ion) detector. Instead, the neutron generator was utilized in fast neutron inelastic scattering analysis as an initial surrogate to

true APNEI. The requirements for the so-called imaging plate will be detailed in a forthcoming section. First, it is important to understand the APNEI process which is based upon the physics of the fusion reaction(s) taking place at the target within a sealed tube neutron generator.

1.5.2.2 Applicability to APNEI

The deuterium + deuterium (D+D) reaction yields a He-3 ion and a neutron with a kinetic energy of approximately 2.5 MeV (i.e. ${}^2\text{H} + {}^2\text{H} \longrightarrow {}^3\text{He} + \text{n}$). The deuterium + tritium (D+T) reaction yields a He-4 ion (α -particle) and a neutron with a kinetic energy of approximately 14.1 MeV (i.e. ${}^2\text{H} + {}^3\text{H} \longrightarrow {}^4\text{He} + \text{n}$). In each of the preceding reactions, the He-3 or He-4 ion is the associated particle of the corresponding neutron. In accordance with the conservation of momentum, the neutron and its associated particle are emitted at approximately 180° from one another at fixed speeds. Therefore, by relating the produced neutron with its associated particle using the nominal position of the neutron beam spot and the position of detection of the associated particle in a pixelated detector, one can determine the approximate path of travel of the neutron. By associating the neutron path-of-flight information obtained as described above with an electronically governed timing window, the prompt γ -rays incited to be emitted by interaction of the tagged neutrons with nuclei in the target object can be associated to the position of their origin – based upon the amount of time that elapses between ion detection and prompt γ -ray detection [4]. Figure 1.21 is a schematic of the APNEI technique which utilizes the D+D reaction.

With the calculated x-y-z locations of the neutron inelastic scattering events and the γ -ray energy associated with each event, it is possible to create a three-dimensional image of the interrogated volume – the data points for which correspond to a particular element or set of elements. As introduced previously, distinguishing between normal and abnormal trace elemental concentrations in certain tissues can provide diagnostic medical information. Indeed, it is established in the literature that both delayed gamma neutron activation techniques and prompt gamma neutron activation techniques are useful in the diagnosis and management of a variety of disorders [5, 6]. However, the application of associated particle techniques for *in vivo* imaging remains largely untested, predominantly due to the sources of uncertainty inherent of APNEI and the accompanying technological limitations [7]. The beam spot diameter, ion detector pixel size, neutron velocity, and timing constraints limit achievable spatial resolution [8]. Additionally, the γ -ray background – even when time correlated – can be high when attempting *in vivo* analysis due

to the volume of material being exposed to the neutron source and the competing nuclear reactions occurring both within and outside the predetermined target area. Also, the prospect of detecting prompt neutron activation γ -rays is complicated by the proximity of the neutron source to the γ -ray detector(s), which can be damaged by neutron exposure [143]. In the feasibility study presented in chapter 2 of this dissertation, the approach was to largely exclude such complicated considerations and test the concept of APNEI *in vivo* in a basic sense, one allowing for ease of distinction of the many variables through Monte Carlo simulation and acting as a foundation for extrapolating the results to more complex scenarios.

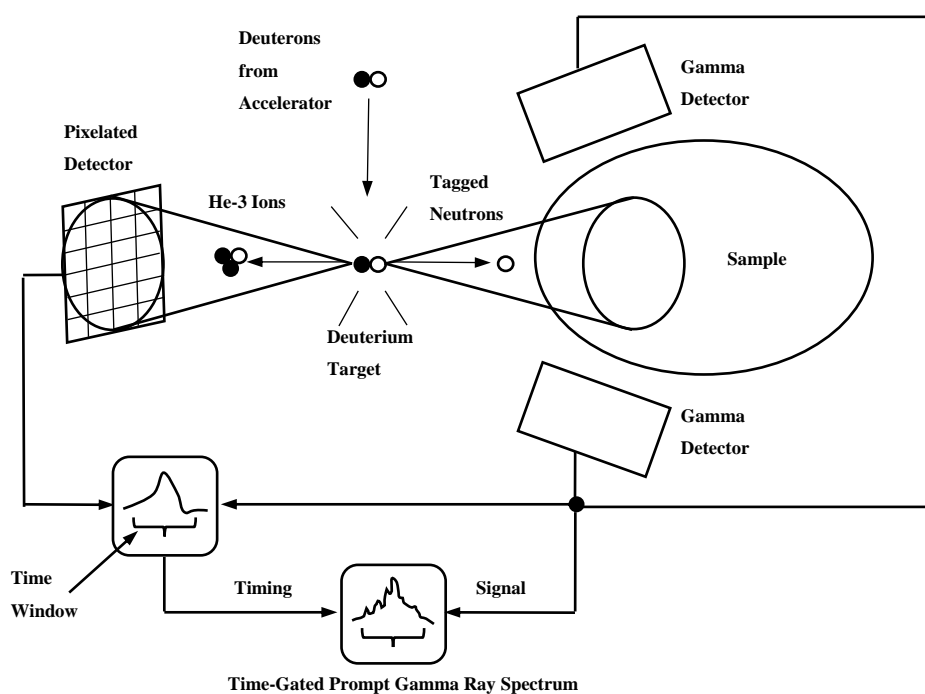


Figure 1.21 Schematic of the APNEI technique [10]

The associated particle (AP) collimation technique may also be employed to increase the sensitivity of a prompt-gamma NAA system to target elements as well as maximize the relevant signal-to-noise ratio (SNR), while simultaneously providing a mechanism by which the spatial information of target nuclei may be collected for imaging. The associated particle technique has been explored as a means of elemental imaging as well as background signal reduction in applications ranging from well logging and homeland security to *in vivo* medical diagnostics [8, 9, 166, 186]. A system which employs the AP technique spatially and temporally collimates (i.e.

“tags”) fast neutrons that arise from a deuterium + deuterium (DD) or deuterium + tritium (DT) fusion reaction by first logging the point of interaction of the associated DD or DT recoil ion at a position-sensitive imaging transducer, which is oriented on the side opposite the interrogated volume. As the recoil ion (He-3 in the case of DD fusion) is associated with its neutron by the conservation of momentum given that the reaction takes place essentially at rest, the path of travel of the tagged neutron may be inferred. Then, by measuring the time between associated particle (ion) detection and inelastic scatter gamma-ray detection (supposing a favorable inelastic collision), the time-of-flight (TOF) of the neutron may be calculated, which may be translated into the distance along the tagged vector that the neutron traveled prior to its first interaction in the target volume [4]. In this way, spatial information for both projective (x, y) and depth (z) dimensions may be collected – allowing for 3D imaging of elemental distributions. Another important feature of the AP methodology is that because the coincidence timing regime plays a large role in signal acquisition, background gamma-ray signals (i.e. all those signals which fall outside the predetermined coincidence window which corresponds to the time during which a neutron undergoes an inelastic collision within and only within the target volume) may be largely ignored [187].

1.5.2.3 Deuterium – Deuterium vs Deuterium – Tritium

Aside from the requirements of a sealed tube neutron generator designed for imaging – namely the incorporation of an imaging plate for associated particle detection and temporal tracking, the selection of the gas source itself yields different neutron and reaction characteristics which are beneficial to certain applications. The fusion reactions of interest are DD and DT. It is worthwhile to explore some of the benefits and challenges associated with each reaction type and to justify why a DD-based neutron generator was selected for the *in vivo* applications proposed in this dissertation.

DT-based generators have neutron yields orders of magnitude higher than DD-based generators. Additionally, the DT reaction produces higher energy neutrons which are more penetrating. For these reasons, DT-based neutron generators are more prevalent than DD-type generators in bulk material characterization such as in geological surveys and scans for dangerous or illicit materials, where the high yield and penetrability are advantageous. In biological systems, the 14.1 MeV DT neutrons are preferable to the 2.45 MeV DD neutrons because they have a

radiation weighting factor of 7.7 as opposed to 16.2, according to ICRP 103 [188]. This would help to mediate equivalent dose and overall effective dose in DT neutron irradiations. Moreover, the higher DT neutron yield corresponds to fewer competing fusion reactions at the neutron source spot, which have the potential to complicate associated particle detection in imaging applications. In other words, in the case of DD-based neutron generators, there may be triggers at the pixelated ion detector which do not correspond to the emission of 2.45 MeV neutrons (e.g. proton emission in the case of tritium production where the proton may be detected as if it were a He-3 ion) which will produce false coincident pathways in the temporal collimation system and introduce image noise. In general, the high energy recoil α -particle (3.5 MeV) which results from the DT reaction is somewhat easier to detect than the desired He-3 ion (0.82 MeV) from the DD reaction.

Conversely, because DD neutrons are produced at lower energy and therefore travel at a decreased velocity as compared to DT neutrons, their potential depth resolution in associated particle imaging technologies is enhanced. DT neutrons travel at approximately 5 cm/ns while DD neutrons travel at approximately 2 cm/ns. Furthermore, their lower energy has the potential to incite fewer quantum excitations in interrogated nuclei, thereby reducing subsequent gamma emissions and spectroscopic background. For these reasons, DD-based generators offer advantages over DT-based generators in imaging applications at the scale of the human body, where the increased penetrability of DT neutrons is not as meaningful as in bulk applications, and decreasing photon background while maximizing resolution in the depth dimension are paramount. In other words, the elemental complexity of organic systems is likely to be better spectroscopically deciphered using DD neutrons given their lower energy and correspondingly fewer energy-dependent nuclear interaction thresholds which may be instigated. Therefore, although the yield of the DT reaction is 50-100 times higher than that of the DD reaction and noise would be correspondingly higher in a DD based imaging system compared to a DT system due to competing fusion interaction pathways, a DD neutron source was chosen for the simulations and experimentation presented in this dissertation as the 2.5 MeV DD neutrons would aid in the elimination of background from organic media as well as allow for better longitudinal resolution than the faster 14.1 MeV DT neutrons [189]. Furthermore, it is much easier to shield a DD system. The nuclear interaction of primary interest in the work contributing to this dissertation is $\text{Fe-56} + n \longrightarrow \text{Fe-56}^* + n' \longrightarrow \gamma$. To a DD neutron of ~ 2.5 MeV, the inelastic scatter cross section of Fe-56 is approximately 1 barn. Fe-56 de-excites from its first or second excited state

predominantly through the emission of 846.8 keV or 1238.3 keV γ -rays, respectively [9]. However, for neutron energies up to about 3 MeV, nearly all of the Fe-56* decay occurs through the emission of an 846.8 keV γ -ray; so, the total inelastic scatter cross section of Fe-56 to D+D neutrons is essentially equal to the cross section for the production of 846.8 keV γ -rays [190]. This simplifies probabilistic considerations in Monte Carlo simulations and calculations, as well as the resulting gamma-ray spectrum. A final practical advantage of DD-based neutron generators is that they contain no radioactive tritium upon construction, so they do not present the regulatory burden that accompanies the acquisition of DT-based generators.

1.5.3 Imaging Plate

The imaging plate or pixelated ion detector for the associated particle generated as the result of the DD or DT reaction is one of the primary deciding factors of resolution in the projective dimension. Aside from the timing accuracy which is important in the depth or longitudinal dimension, the number of pixels on the imaging plate sets the bounds on the number of voxels which may be portrayed for a given interrogated volume. Figure 1.22 (A) illustrates an image with fine resolution as currently available in digital photography, while (B) is the same image which has a resolution that has been decreased by a factor of three and thus appears pixelated. Note that in both images, a single value in grayscale is attributed to each pixel; there is no intra-pixel resolution (i.e. just as in APNEI, a pixel on the imaging plate will correspond to a single intensity-weighted shade). The difference is that the pixels in (B) are visible to the naked eye.

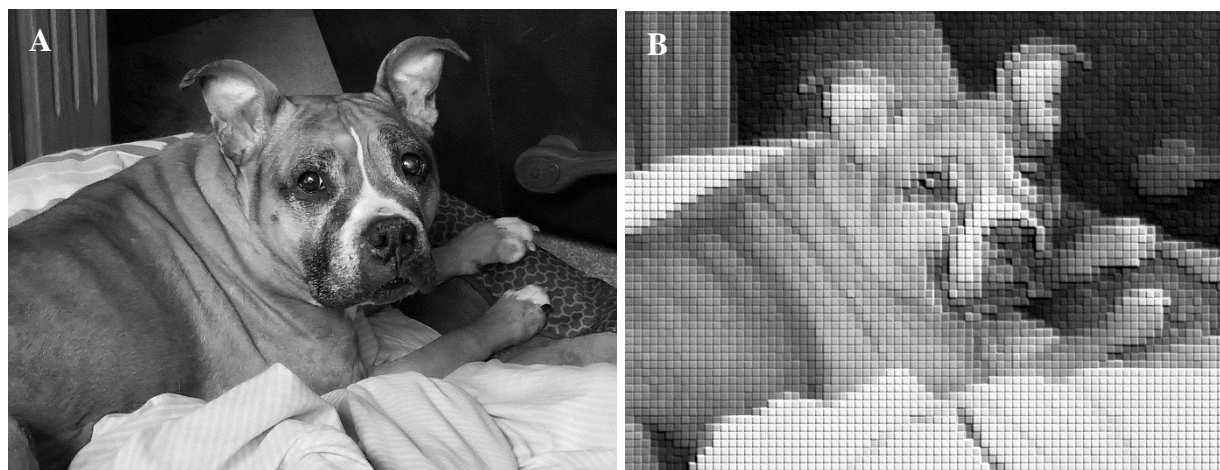


Figure 1.22 Effects of pixelated detector on projective resolution (subject: Revan, the best, a good and loving boy)

Because the DD generator employed in this study was not designed for associated particle imaging and therefore did not incorporate an imaging plate in the sealed vacuum tube, the inclusion of pixelated detector characteristics was largely included theoretically in the supporting Monte Carlo simulations or in data post-processing techniques, as will be detailed in the next two chapters. However, it is worthwhile to introduce the associated particle detector from an experimental perspective to understand its method of function and its accompanying limitations. In general, the ions are detected using inorganic phosphors such as zinc oxide doped with gallium (ZnO:Ga) and yttrium aluminum perovskite doped with cerium (YAP:Ce). While YAP:Ce tends to have greater scintillation output than ZnO:Ga, it has a decay time of approximately 30 ns, as compared to that of ZnO:Ga which approaches 1 ns [191, 192, 193]. These scintillation materials are fine, crystalline powders which are fabricated and refined in such a way as to bias toward crystals of relatively consistent size and shape in order to maximize light production and transmission. The fine powder may then be bound to a fiber optic faceplate, which provides the framework upon which to spatially resolve incident scintillation events. In other studies, it has proven necessary to apply a very thin coat of a metal such as aluminum over the scintillation powder in order to selectively shield against less penetrating ions which are not associated with the fast neutron's path of flight. This conductive layer also prevents the buildup of electrical charge on the surface of the detector [192]. This holds true in DD as well as DT-based sealed tube neutron generators. A limitation to keep in mind with regard to the selection of inorganic phosphors for use in associated particle imaging capable neutron generators is that the material must be able to withstand 350-400°C for several days, a procedure required in order to verify that the contents of the sealed tube are sterile and free of organic material.

A cross section of a ZnO:Ga-coated fiber optic faceplate used for associated particle (i.e. α -particle) detection in a DT neutron generator is shown in Figure 1.23 [194]. In this case, the metal coating was aluminum and is illustrated to block interfering ions such as deuterium, while neutrons pass through – an important consideration since the reaction products from the neutron source spot are emitted nearly isotropically. The study, which was performed by a partner lab at Purdue University, chose ZnO:Ga over YAP:Ce due to its superior timing characteristics [194]. It is interesting to note that many of the steps in the process of production of crystalline scintillators such as ZnO:Ga are affected by natural variability and spontaneous processes currently beyond experimental control, which yields significant inconsistencies in material properties. In fact, the

impressive ZnO:Ga scintillation composite employed in the study by Koltick et al. was manufactured in the 1960s and has not since been replicated [194, 195]. Efforts are ongoing to devise more consistent chemical methods of fluor synthesis, not only with regard to the selection of different reactants and temperature variability but in the evolution of methods to control microcrystal size distribution, orientation, and compaction [196].

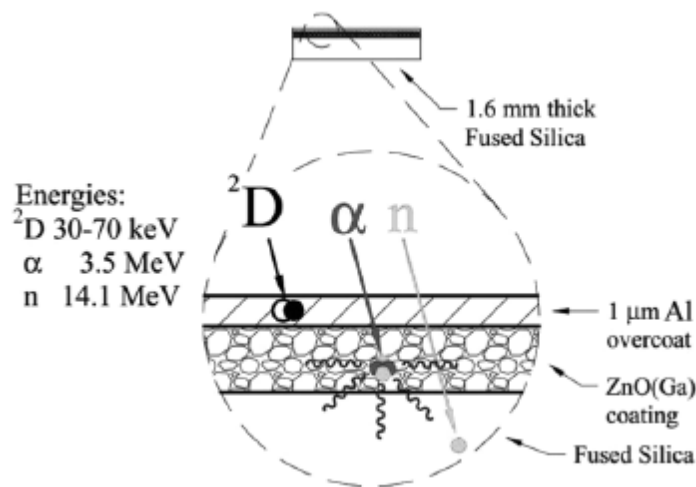


Figure 1.23 Cross section of a ZnO:Ga α -particle detector [194]. Reproduced with permission of IEEE.

1.5.4 Projective Imaging Resolution

Projective imaging resolution does not only rely upon the effective area of each pixel in a detector like that represented in Figure 1.23, however; it also relies – even more critically – upon the diameter of the neutron source spot. Just as in optics, the neutron source spot dimensions must be kept as small as possible so that the neutron emission point is known with as high a degree of certainty as possible. After all, it is a point through which the associated particle imaging system must trace all apparent neutron paths of travel once the He-3 ion (in the case of a DD neutron generator) is detected within a pixel at the imaging transducer. The neutron emission point is essentially a “known” within the system, and even though it cannot be made to be a perfect point source within the sealed tube of the neutron generator, attempts at reducing beam spot size on the target are critical to achieving high resolution in the x and y dimensions. The most advanced beam focusing techniques have yielded beam spots as small as approximately 1 mm in some neutron imaging systems [194, 197]. However, source spot cooling considerations become limiting, especially in high flux systems due to degradation of the beam target. Such target degradation is

shown in Figure 1.24, where a DT generator was intentionally run without cooling for the purpose of visualizing the source spot as well as the toll the heat of the fusion reaction takes on the titanium-coated target in the form of surface erosion [197].

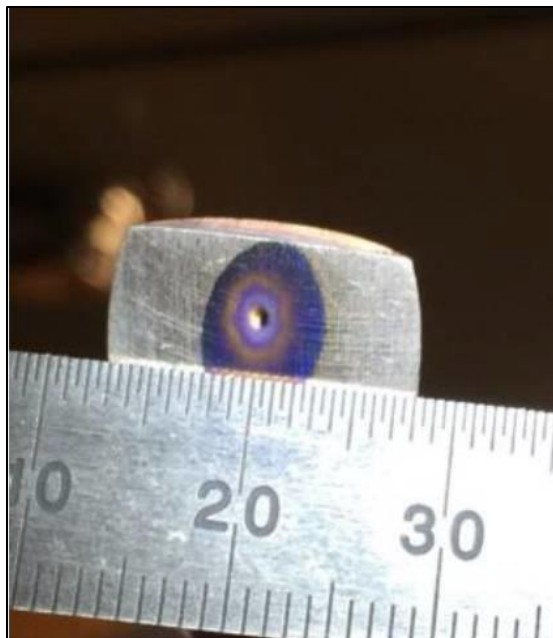


Figure 1.24 Neutron source spot and damage due to insufficient cooling [197]. Reproduced with permission of Elsevier.

In chapter 3 of this dissertation, a model was defined in MCNP to realistically simulate APNEI resolution attainable using technology available today. It is evident in Figures 1.25 (A) and (B) that increasing neutron beam spot diameter and ion detector pixel size correspondingly decrease projective resolution. Note the similarity of the APNEI geometry to a pinhole camera. Figure 1.25 (A) portrays a faithful 2D image of the interrogated object (point neutron source spot and point pixel resolution), whereas upon introducing realistic dimensions to the neutron source and associated particle detector pixels in (B), blur is introduced. The gamma-ray detector and coincidence timing concept are not shown in Figure 1.25. Though the neutron source spot is modeled as an isotropic source, it is important to keep in mind that while the neutrons are emitted isotropically from the site of DT fusion, DD neutrons are biased by a factor of more than two in the forward direction (i.e. at 90 degrees to the deuteron beam). In many DD-based neutron generator simulations, the source spot is nevertheless most often defined as an isotropic point because the results will be within the same order of magnitude, and the computational burden of defining an anisotropic source outweighs the statistical benefits of marginal increases in accuracy.

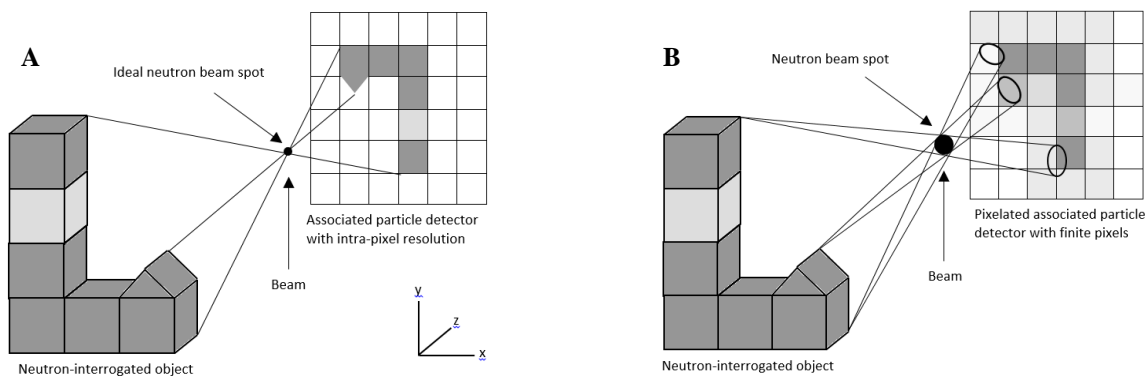


Figure 1.25 Effects of source spot diameter and pixelated detector on projective resolution [11]. (A) Ideal projective image, with a point source spot (perfect ray tracing) and sub-pixel ion detector resolution. (B) Realistic projective image, with a non-point source spot and finite detector resolution. Note the cones of spatial uncertainty.

1.5.5 Depth Imaging Resolution

Whereas projective resolution is predominantly dependent upon physical limitations in the x - y plane (i.e. source spot diameter and effective pixel area), depth resolution is governed by timing characteristics – of both the associated particle detector and the gamma-ray detector. Therefore, the depth resolution is improved by employing more slowly moving particles, one of the listed advantages of DD-based neutron generators over DT-based generators. Similarly, as touched upon previously, the fast scintillation decay characteristics of ZnO:Ga make it preferable to YAP:Ce when attempting associated particle or time-of-flight measurements. In principle, it is expected that a ZnO:Ga imaging plate coupled with a plastic scintillation detector and photomultiplier tube could produce timing resolution better than 100 ps [192]. Given the high sensitivity, efficiency, and localization of light-producing events in such a detector for relatively heavy and short-range ions, the gamma-ray detector becomes the truly limiting factor with regard to finding a balance between energy resolution and timing resolution. There are far more variables to consider, such as the effects of increasing detector volume, scintillation vs semiconductor operation, and detector placement and overall system geometry, not to mention the shielding material layout which is meant to permit gamma-rays of interest from the active volume while shielding from noise-inducing background photons and neutrons. For example, while sodium iodide scintillation detectors provide better timing resolution than HPGc – about 100 ps as compared to 1000 ps, respectively – HPGc detectors are employed almost exclusively in PGNAA studies due to their favorable background signal rejection properties and high energy resolution, facts which are particularly important in the mixed neutron/gamma-ray fields that accompany neutron generator

operation. And because spectroscopic measurements must be made during sample irradiation, the HPGe detector must be incorporated into the experimental apparatus, meaning the selection and orientation of shielding materials are critically important. Refer to Figure 1.14 for an example. Additionally, HPGe detectors (particularly the more common and inexpensive p-type) are vulnerable to neutron damage, so the neutron emission profile should be well characterized and the fluence rate at the detector measured and maintained so that an integrated neutron fluence may be weighed and tallied against an acceptable threshold in order to preserve peak energy resolution. Such are the challenges of optimizing an APNEI system for fast timing and therefore depth resolution.

1.5.6 Conclusions

The preceding sections did not introduce the three-dimensional spatial resolution achievable using APNEI as the topic of imaging resolution will be a highlight of the research summarized in the next three chapters. Indeed, the subject is one in which there is very little background and was one of the main drivers for undertaking the studies presented in this dissertation. However, it is important to note that the associated particle technique is successfully employed in a variety of large-scale operations to improve SNR through time-of-flight collimation and is a valuable complement to traditional PGNA. It is expected that upon further honing the technique in a sealed tube neutron generator system that imaging will be possible on a small scale while maintaining the elemental sensitivities for which NAA is renowned. Finally, such a system could be tailored to *in vivo* applications, yielding target tissue information noninvasively which could be used in disease diagnosis and treatment planning in a number of disorders affecting or caused by changes in elemental concentrations. However, because the concept of APNEI in disease diagnostics is novel, it is practical to begin with a basic model to examine its general feasibility. Monte Carlo simulations provide a convenient and well-defined avenue with a strong literature foundation to begin to approximate elemental sensitivity and *in vivo* trace elemental imaging resolution.

CHAPTER 2. FEASIBILITY OF APNEI

2.1 Overview

To begin to explore the potential range of applicability of APNEI to *in vivo* disease signatures through the quantification and spatial orientation of trace elemental distributions, a feasibility study needed to be performed. Once a sound feasibility study is developed and defined, there is a foundation from which to begin further studies with more complex scenarios in the realm of simulations and then making the leap to experiments in the laboratory. After all, if the technology is not likely to be successful, it is difficult to justify further pursuit of the research contributing to the application – particularly for an independent and relatively fundamental endeavor such as a student’s doctoral dissertation topic. Indeed, there was a single paper in the literature [9] which introduced the topic of APNEI as it pertains to trace elemental diagnostic imaging – both authors of which contributed to the research presented in this chapter, which builds upon their previous assertions and continues to build the literature background in the field of APNEI. It follows that the contents of chapter 2 form the backbone for all the research which comes afterwards and remains important for the much more involved MCNP simulations and surrogate experiments which are ongoing even at the time of this writing. It was particularly important for the authors to gain experience in considering prompt-gamma measurements as the bulk of the experience in their labs – both in their studies and in those performed by past graduate students – consisted of traditional delayed-gamma neutron activation analysis.

Historically, tagged neutron activation analysis techniques have been employed predominantly in the detection of contraband such as explosives and special nuclear material or in basic body composition studies; indeed, the prospect of using neutron associated particle methods for disease diagnostics and *in vivo* imaging has remained largely unexplored. For civil defense applications, the elements of interest are generally carbon, nitrogen, and oxygen – the proportions of which can be indicative of unexploded ordnance in cargo ranging from personal luggage bags to large shipping containers [166]. In body composition analysis, those same elements can be measured using a non-invasive associated particle technique and their relative proportions compared in order to determine total body protein, fat, and water simultaneously [167]. However, trace elements tend to have more diagnostically valuable changes in diseased tissues.

The purpose of the study presented in this chapter was therefore to develop a Monte Carlo (MC) simulation model for *in vivo* associated particle neutron elemental imaging and to study the feasibility of using APNEI to determine the iron distribution in a human liver with the defined model. The liver was chosen as it is known to be an important source of iron in the human body. Furthermore, as the liver is in the trunk of the body, it offered the potential to explore a worst-case scenario with regard to spatial resolution, background interference, and whole body effective dosimetry. The model was defined in MCNP by the basic geometry of the human body, the use of DD source neutrons, iron as the element of interest (as iron is known to vary heterogeneously in the liver as a result of manifest disease, particularly cancer [2, 9]), an iron-containing voxel in the liver as the target region, and 2 large, high-purity germanium detectors anterior and posterior to the trunk of the body. The f8 pulse height tally was employed in MCNP to determine the signal acquired from iron inelastic scatter gamma-rays at various iron concentrations in the target liver voxel. Correspondingly, the f4 average flux tally in MCNP was modified by a dose function such that the equivalent dose to the whole liver and the effective dose to the whole body could be estimated and used as the basis for a limiting number of neutron histories which could feasibly allow for the collection of a sufficient volume of data to construct a 2D image of iron distribution in the liver voxel.

Assuming an allowable equivalent dose to the liver of 5 mSv, it was found that 143 inelastic scatter iron gamma-ray counts (at ~847 keV) would ideally be registered at the germanium detectors for a 1 cm³ cube-shaped liver voxel with an iron concentration of 1,000 ppm. According to the simulation model, an image of iron distribution in the liver can be constructed with a 1 cm projective resolution at the level of 1,000 ppm iron. Collecting such an image would yield an estimated whole body dose of 0.82 mSv. The mathematical introduction of image uncertainty resulting from source spot diameter and detector timing resolution more closely approximated the result of real-world application.

In short, APNEI of certain elements *in vivo* appeared feasible given several timing, sensitivity, and resolution caveats. However, it was apparent that further study was required to determine what the detection limit of iron would be and what image resolution would be in an experimental setup as the presented model contained idealized assumptions which overestimated the signal attributable to iron inelastic scatter gamma-rays and preferentially reduced background photon signals, perhaps more than would be possible in an experimental environment.

It is important to note that this chapter consists predominantly of material included in a publication in the journal of *Medical Physics* entitled “Associated Particle Neutron Elemental Imaging *in vivo*: a feasibility study” [10], which was co-authored by Dr. David Koltick and Dr. Linda Nie. Some material from this publication has also been included in the preceding chapter as part of the topic’s introduction and background. The right to re-use of the publication (other than in journal articles) – in whole or in part – was retained by the author in the Wiley Copyright Transfer Agreement. Koltick and Nie introduced the concept of APNEI [9] and proposed several key ideas concerning achievable resolution and technological limitations, but they did not attempt to test their predictions through simulation. And while the concepts of using APNEI for imaging solid objects *in vitro* and of using prompt gamma ray neutron activation analysis *in vivo* to determine body composition or total elemental makeup are well established in the literature [8, 167], this research concerned the feasibility of employing both techniques simultaneously to allow for *in vivo* medical imaging applications.

To summarize, the objectives of this study were (1) to predict the response to iron *in vivo* of a basic APNEI setup, (2) to determine the effective dose to the target region and to the whole body as an initial indicator of potential exposure time in clinical application, (3) to generate a 2D image and simulate image resolution under ideal conditions, and ultimately (4) to develop a foundational case model upon which one can make predictions as to the system and timing requirements that would render the application of APNEI in medical diagnostics feasible. Having been introduced in this section as well as the previous chapter, the next sections will describe the research methods, results, and conclusions of the APNEI feasibility study performed at Purdue University in support of this dissertation.

2.2 Materials and Methods

2.2.1 Monte Carlo Simulations

As a three-dimensional Monte Carlo radiation transport code, MCNPX is a valuable tool in modeling the interactions of radiation with matter. Developed by Los Alamos National Laboratory, the code allows for the simulation of DD source neutrons as well as provides for the release of secondary photons from impacted nuclei using cross section data libraries included in the program. It is therefore well suited for use in simulating APNEI and is a cornerstone of this feasibility study.

2.2.2 Model of a Reference Man

To simulate the application of APNEI to a human, a torso was modeled similarly to a reference man – including the internal organs, bones, and their elemental compositions [198, 199]. For the purposes of this study, the model included the trunk, legs, and head of the body but not the arms. In order to simplify the distribution of iron in the body, it was excluded from any material other than the voxel of interest in the liver. According to ICRU 44, the fraction of iron by weight present in whole blood is 0.001 [198]; there was no consideration of the iron contained in blood in this MCNPX model. Additionally, the liver was defined in MCNPX to be made of ICRU 44 soft tissue, which does not include iron. So, in this model the liver (other than the target voxel) was defined to be iron-free. The only iron-bearing cell in the simulation model was the target voxel within the liver – that to be interrogated by the neutron source for sensitivity, dose, and image formation calculations. The assumption of ideal temporal resolution of the time gated associated particle system was what drove the exclusion of iron from materials outside the target voxel. Inelastic scatter gamma-ray signals attributed to iron nuclei outside of the target voxel would be filtered out given the tagged neutron time-of-flight collimation. The target voxel was a 1 cm³ cube located at the distal edge of the liver, at a depth of approximately 5 cm beneath the surface of the body. In determining the response of the system to the iron contained within the liver voxel, the iron concentration in the voxel was varied at intervals from 0 ppm to 10,000 ppm, and for ease of comparison, the non-iron component was defined as water.

2.2.3 Model of APNEI System Components and Properties

The other components of the model relevant to APNEI were the high-purity germanium detectors and the DD neutron source. The HPGe detectors were portrayed as identical cylinders with radii of 11.5 cm and thicknesses of 10 cm. The detectors were oriented such that they were essentially flush with and perpendicular to the surface of the body in order to maximize the gamma-ray signal from the iron-containing voxel in the liver. The dimensions of the germanium detectors were selected to allow for a simple and optimal layout of the APNEI system within MCNPX as well as to provide best case detection of the iron inelastic scatter gamma-rays. In keeping with the straightforward layout of this APNEI model, the DD neutron source was defined as an isotropic point. This was to allow for relatively simple calculation of the neutron flux at various locations throughout the system and to act as a surrogate for a DD neutron accelerator designed for imaging

purposes (the dimensions for which were not yet known as the investigators' lab contained only non-imaging sealed tube neutron generators typically used in delayed gamma neutron activation analysis). To improve counting statistics and computational efficiency in MCNPX, the neutron paths of travel from the source were geometrically biased in a cone configuration toward the target voxel and then normalized to isotropic emission. The isotropic source thereby provided sufficient flux at the target voxel for study of the iron content while limiting relative error. The neutron point source was located approximately 3 cm from the surface of the body and exactly 8 cm from the center of the cube-shaped target voxel in the liver. Figure 2.1 shows a longitudinal cross section of the human torso model (legs truncated in the Figure) used as the medium in which radiation transport and interactions were simulated in MCNPX. Figure 2.2 shows a transverse cross section of the human torso model at the height (along the axis of the spine) of the center of the target voxel in the liver, which is the same as the height of the isotropic neutron source. The images for Figure 2.1 and Figure 2.2 were obtained from the MCNPX Visual Editor, which is a companion to the MCNPX radiation transport suite and allows for the viewing and streamlined manipulation of the geometries used in the simulation model.

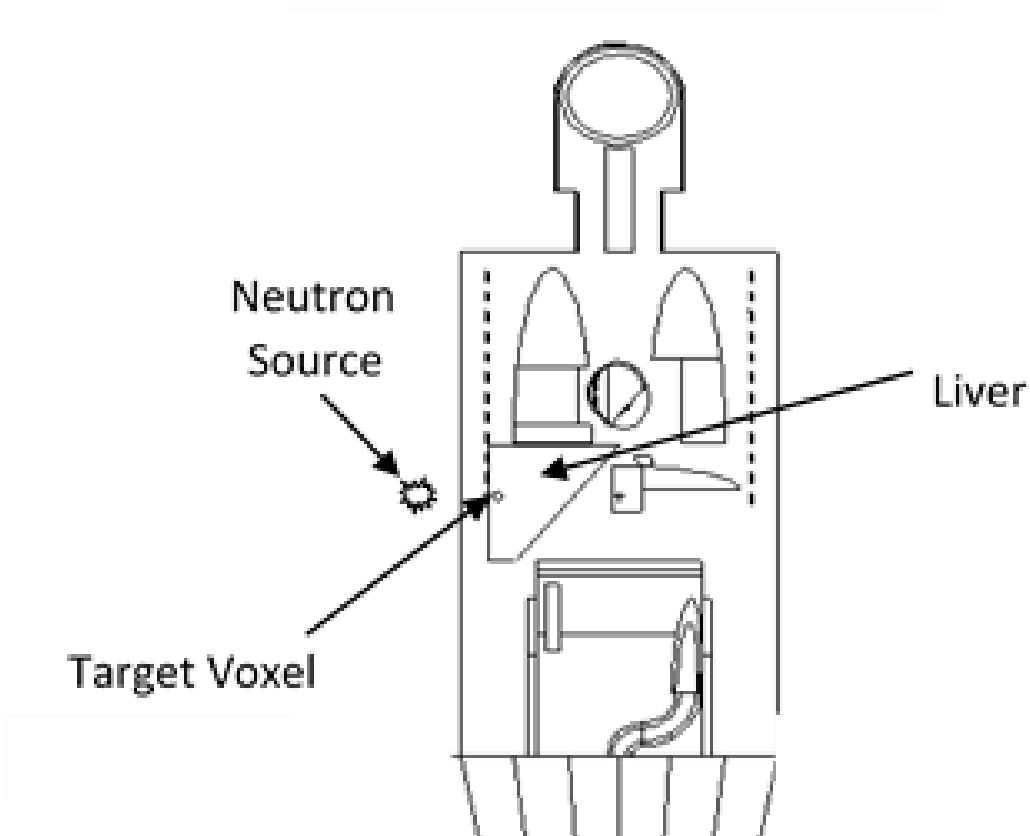


Figure 2.1 A longitudinal cross section of the human body model defined in MCNPX

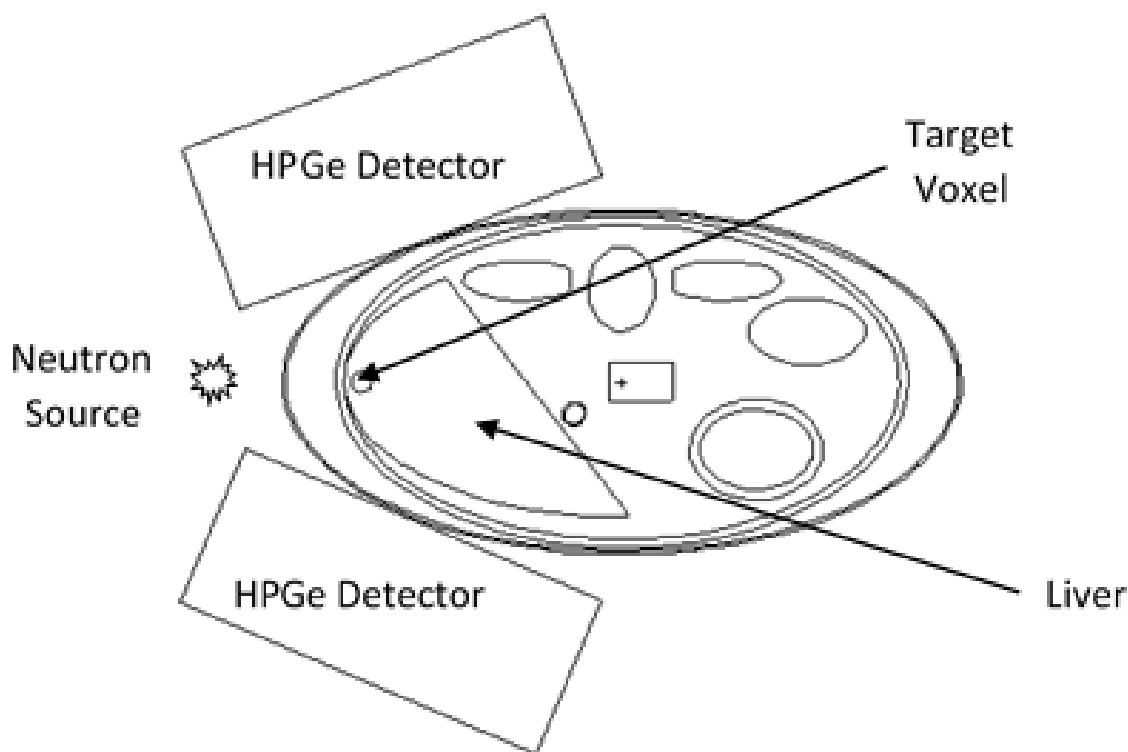


Figure 2.2 A transverse cross section of the human body model at the height of the target voxel and neutron source in MCNPX

2.2.4 The APNEI Process in MCNP

In modeling a specific case of the application of APNEI, it follows that one would choose (1) an element such as iron as the imaging objective due to its relatively high inelastic scatter cross section to DD neutrons (i.e. approximately 1 barn) and (2) a region at the periphery of the body (i.e. the distal edge of the liver) for placement of the iron-containing voxel to increase neutron flux at the target area as well as to increase the probability of the prompt inelastic scatter gamma-rays exiting the body and being detected at the HPGe detectors, thus facilitating the formation of a simulated image by APNEI.

Though the geometries contributing to the APNEI setup were relatively simple and optimized, the model of the human body consisted of complex geometries and elemental compositions of the various tissues. Because neutron interactions and neutron-induced photon reactions were the focus of the simulation, it was necessary to consider elements of the simulation separately and iteratively in order to reduce simulation runtimes and prevent the confounding of

important variables. In other words, the sequence of execution which defines APNEI was broken down into steps in MCNPX. In this way, the output from one step could be processed and optimized for use as the input for the next step.

In order to determine the response of the basic APNEI system model to iron in the voxel of interest, the simulation was executed with varying concentrations of iron in the liver voxel and with a variation of the model which excluded the human body, thereby eliminating background signals as would occur given perfect timing resolution. The non-iron component of the material in the voxel was considered to be composed solely of water, a simple approximation of soft tissue. By simulating the exposure of the voxel without the surrounding body to DD neutrons from the isotropic source, the signal for neutron-induced photons detected at the HPGe detectors for a perfect associated particle setup was obtained. For a given number of neutron histories, by comparing the accumulated gamma-ray signal in a narrow energy range (i.e. a “bin” which encompassed the applicable 846.8 keV γ -ray, as in a multi-channel analyzer) collected at varying target voxel iron concentrations, it was possible to determine the number of counts that would be registered at the HPGe detectors that were the result of a DD neutron inelastically scattering from the nucleus of an iron atom. In MCNPX, the photon pulse height tally (i.e. tally f8, in units of signal contribution / neutron history) was utilized to register the neutron-induced photon signal at the gamma-ray detectors; the corresponding photon energy bins were defined over a range of 0 to 2.5 MeV with each bin encompassing 0.001 MeV. The number of particle histories employed in each simulation was 2E9, which was sufficient to yield relative errors at least as low as 0.10 at biologically relevant iron concentrations without disproportionately extending computation time.

Similarly to the *in vivo* iron response determination, the equivalent doses to the whole target organ and whole body constituents were calculated using MCNP simulations as a first approximation of the local dose burden to a human patient and to provide a basis of the potential allowable exposure time of a human patient to a DD neutron imaging system. By converting the equivalent dose outputs from MCNP to effective doses using the applicable tissue weighting factors, one can relate the dose to established radiation protection regulations and to the stochastic health risk to the patient [83]. In MCNPX, the average flux tally (i.e. tally f4, in units of n/cm² for each selected volume within the model) was utilized to calculate the dose to the entire liver volume and to estimate the dose to the whole body. The tally logged the average neutron flux in the regions of interest over the course of the simulated exposure to the DD neutron point source. By modifying

the tally with a dose function – that is, pairing the tally with flux-to-dose conversion factors for a range of neutron energies – the equivalent doses were calculated. The flux-to-dose conversion factors were obtained from the MCNP General Monte Carlo N-Particle Transport Code, Version 5 User’s Guide: Vol. I, Table H.1, which have been tabulated from the literature [200, 201, 202, 203].

Using the simulation data collected during the trials for determination of the response of the APNEI system to iron as well as the MCNPX dose calculation outputs, one can simulate what a 2D image of the liver voxel might look like assuming ideal imaging plate and temporal resolution, a point isotropic neutron source, and perfect exclusion of background signals. In general, the sensitivity data collected were in terms of signal contributed to a particular energy bin per source neutron. After taking the gamma-ray detector pulse height in the 846.8 keV energy bin and multiplying by the number of neutron histories (i.e. 2E9 histories), the number of counts due to inelastic scatter gamma-rays from iron was established for various concentrations of iron within the liver voxel. With the number of inelastic scatter gamma-rays detected as a function of iron concentration, dose limitations were applied to establish an acceptable number of neutrons to which one could be exposed from the isotropic neutron source. The dose constraint allowed for the collection of an amount of data sufficient to yield an image of the iron concentration within the voxel. Additionally, the effects of neutron beam spot diameter and detector timing uncertainty on image resolution were examined by tracing the assumed points of interaction of the neutrons with iron nuclei in the target voxel through a beam spot with a 2 mm diameter (e.g. as opposed to a perfect “pinhole” as in optics) while concurrently introducing ambiguity along the neutron path of travel. The points of origin of the DD neutrons were assigned uniformly within the 2 mm beam spot using a random number generator. Similarly, the perceived point of interaction of each neutron in the target voxel was assigned according to a Gaussian distribution in order to simulate the depth resolution along the neutron path of travel as the result of time-of-flight measuring error in both the pixelated and gamma-ray detectors. The supposed point of inelastic scatter of each neutron within the target voxel was traced through the assigned point of origin of each neutron to an ideal imaging plate imagined to be 5 cm from the neutron source (on the opposite side of the human body model) using the equation of a line in canonical form [204]:

$$\frac{x - x(a)}{x(b) - x(a)} = \frac{y - y(a)}{y(b) - y(a)} = \frac{z - z(a)}{z(b) - z(a)} \quad \text{Eq. 2.1}$$

2.3 Results

2.3.1 Simulated Iron Gamma-Ray Counts

Using the MCNPX pulse height tally, the 846.8 keV inelastic scatter gamma-ray signal (i.e. pulse height) was determined over a wide range of iron concentrations in the 1 cm³ cube-shaped liver voxel. The accompanying background signal was negligible as the human body model was excluded from this series of simulations to approximate ideal temporal resolution of the associated particle tagging system. From these data, the number of counts from the inelastic scatter gamma-rays at the detectors was inferred for the various iron concentrations – the assumption being that each gamma-ray which contributed to the 846.8 keV energy bin was the result of an inelastic scatter interaction of a source neutron with an Fe-56 nucleus in the liver voxel. The liver voxel was assigned a volume of 1 cm³ as a preliminary estimate of discernible spatial resolution *in vivo* [205]. With 2E9 neutrons emitted isotropically from the point source located 8 cm from the liver voxel, the simulated number of neutrons per unit area inside the voxel was 2.5E6 n/cm². It is expected that because this model assumes a relatively superficial iron-containing target within the liver, the source neutron flux at the voxel will be close to the 2.5E6 n/cm² calculated previously even upon attenuation by approximately 5 cm of soft tissue. Indeed, the neutron dose transmission through 5 cm of water for 2.5 MeV neutrons is expected to be between 0.8 and 0.9 [206]. The number of inelastic scatter gamma-ray counts at the germanium detectors for different concentrations of iron in the target voxel are given in Table 2.1.

Table 2.1 – Number of counts detected by HPGe detectors as determined by MCNPX

Fe (ppm)	100	500	1,000	2,500	5,000	10,000
Counts	0.5 ± 0.11	2.0 ± 0.22	4.0 ± 0.32	10.0 ± 0.49	20.0 ± 0.70	39.0 ± 0.99

Though not shown in Table 2.1, it was observed that as iron concentration increased above around 50,000 ppm, the corresponding inelastic scatter gamma-ray signal increased nonlinearly. This was because the increases in Fe concentration yielded an apparently nonlinear increase in the number of iron atoms in the liver voxel, which was meant to be a simple approximation of a volume of tissue (with a classical density of about 1 g/cm³). For such a volume of tissue, as the iron content increased, the overall density increased. Therefore, at relatively high iron concentrations, the

atomic density of iron did not correspond linearly with increasing iron concentration, and thus neither would the gamma-ray counts increase linearly with increasing iron concentration. However, at lower iron concentrations – those that would be relevant *in vivo* – the density of the target voxel approaches 1 g/cm^3 and the inelastic scatter gamma-ray counts scale linearly with iron concentration and correspondingly, with the atomic density of iron. For reference, the nonlinear plot of 846.8 keV inelastic scatter gamma-ray counts versus iron concentration from 100 ppm to pure iron is illustrated in Figure 2.3. Figure 2.4 illustrates the response to iron only at lower iron concentrations – up to 10,000 ppm Fe, as recorded in Table 2.1 for potential *in vivo* iron concentrations. Again, note that Figure 2.3 expands upon the data in Table 2.1 to the extreme of pure iron, which was useful in developing and optimizing the MCNP input file as pure iron provides optimum gamma-ray counting statistics. However, such high iron concentrations are useful only in the academic sense, not in the clinical sense. Additionally, note the trend line and its accompanying equation and R^2 value (i.e. 0.999) in Figure 2.4, which reflect the expectedly ideal nature of the MCNP simulations.

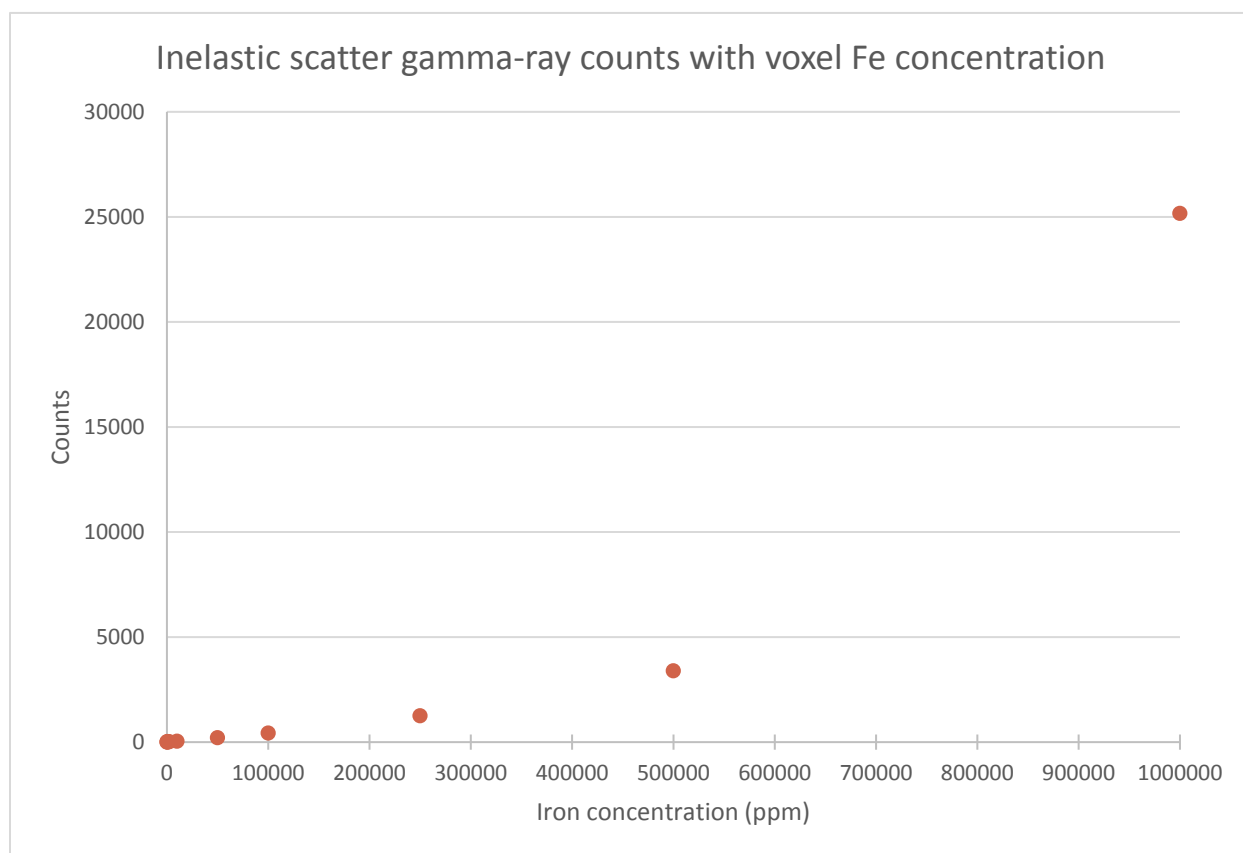


Figure 2.3 Inelastic scatter gamma ray counts with voxel iron concentration - 100 ppm to pure iron

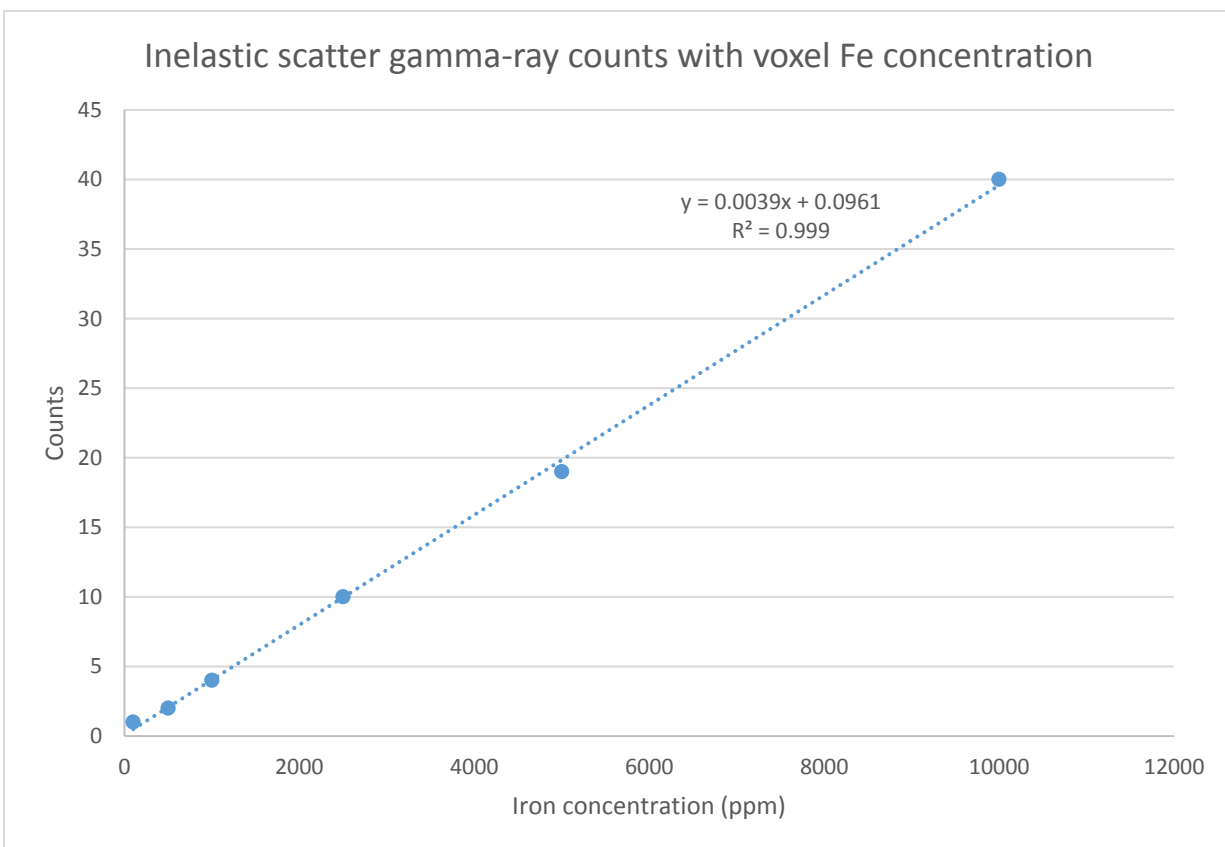


Figure 2.4 Inelastic scatter gamma ray counts with voxel iron concentration – 100 ppm to 10,000 ppm

2.3.2 Radiation Dose Assessment and Iron Gamma-Ray Counts Normalized to Dose

2.3.2.1 Radiation Dosimetry

In APNEI, there are multiple sources of radiation from which energy may be imparted to patient tissue – namely, neutrons from the source spot within the neutron generator, gamma-rays resulting from the de-excitation of neutron-excited nuclei, and bremsstrahlung x-rays from backstreaming electrons incident upon the aluminum plate within the generator apparatus. As the generator is DD-based, the prototypical, uncollided fast neutron energy is 2.45 MeV; however, a spectrum of neutron energies up to 2.45 MeV would need to be considered due to the presence of neutron moderation and shielding materials, including the hydrogen-rich volume of the patient. By tabulating the flux at each of several energy intervals of the neutral “particles” (i.e. neutrons and photons) entering a particular volume, MCNPX provides an avenue to translate to terms of energy absorbed in the medium using the appropriate conversion factors. Though the presented

model does not contain material such as high-density polyethylene (HDPE) – which is useful in neutron moderation – it is important to consider that such shielding would be necessary in a laboratory or clinical setting to minimize dose to the patient and to surrounding areas. In APNEI as opposed to traditional NAA though, the goal is to maximize the fast neutron fluence rate at the target volume such that the inelastic scatter gamma-ray yield is high and that as many neutrons remain true to their path as possible with regard to the associated ion detected at the pixelated imaging plate. The neutron energy spectrum at the patient and in areas surrounding the neutron generator will be significantly altered by the presence of hydrogenous and/or borated materials.

Additionally, it is well known that the 2.2 MeV gamma-rays resulting from the $^1\text{H} (n,\gamma) ^2\text{H}$ are the predominant contributor to dose in whole body thermal neutron exposure, which is an important consideration not only with regard to the potential of HDPE to thermalize fast neutrons which subsequently interact within the body, but that thermalized neutrons have an even higher probability of generating 2.2 MeV gamma-rays within the HDPE itself, thereby presenting an additional gamma-ray source external to the patient. Within the patient, the $^{14}\text{N} (n,p) ^{14}\text{C}$ reaction is also consequential as the resulting 0.58 MeV proton has a high rate of linear energy transfer and can therefore impart a high local dose. However, the $^1\text{H} (n,\gamma) ^2\text{H}$ reaction is still considered most important with regard to whole body dose due to the greater abundance of hydrogen than nitrogen in tissue. And though the 2.2 MeV gamma-rays from hydrogen dominate the prompt gamma spectrum, all gamma-rays from materials within and around the irradiation area contribute to the dose to the patient. MCNPX provides a convenient means to approximate the overall gamma-ray dose from all of the environmental media with its broad use of catalogued, energy dependent neutron interaction cross sections.

A characteristic of the neutron generator which is not as easily accounted for in Monte Carlo simulations is the generation of electrons at the target when deuterium ions are impacting the titanium. Some of these electrons, despite a secondary electron suppression electrode, travel in the direction opposite the deuterium ion beam (i.e. backstreaming) and subsequently come into contact with the aluminum aperture, producing bremsstrahlung x-rays (recall Figure 1.5). Fortunately, given that a DD generator is often operated in the realm of 120 kV – thereby producing x-rays in a typical bremsstrahlung spectrum up to 120 keV (similar to diagnostic x-ray beams) – the x-rays may be shielded very effectively by placing a thin layer of lead around the generator tube. This was demonstrated very effectively by Wharton et al. who measured the x-ray spectrum

produced by a DD generator (i.e. Thermo Scientific model P385) operated with a target current of 80 μA and an accelerating voltage of 130 kV – both with and without a 3.2 mm thick lead shield for 100 seconds each [207]. Because a lead shroud is incorporated into the neutron generator housing in the authors' lab, these relatively low energy x-rays are thought to have negligible contribution to patient dose, as illustrated in Figure 2.5.

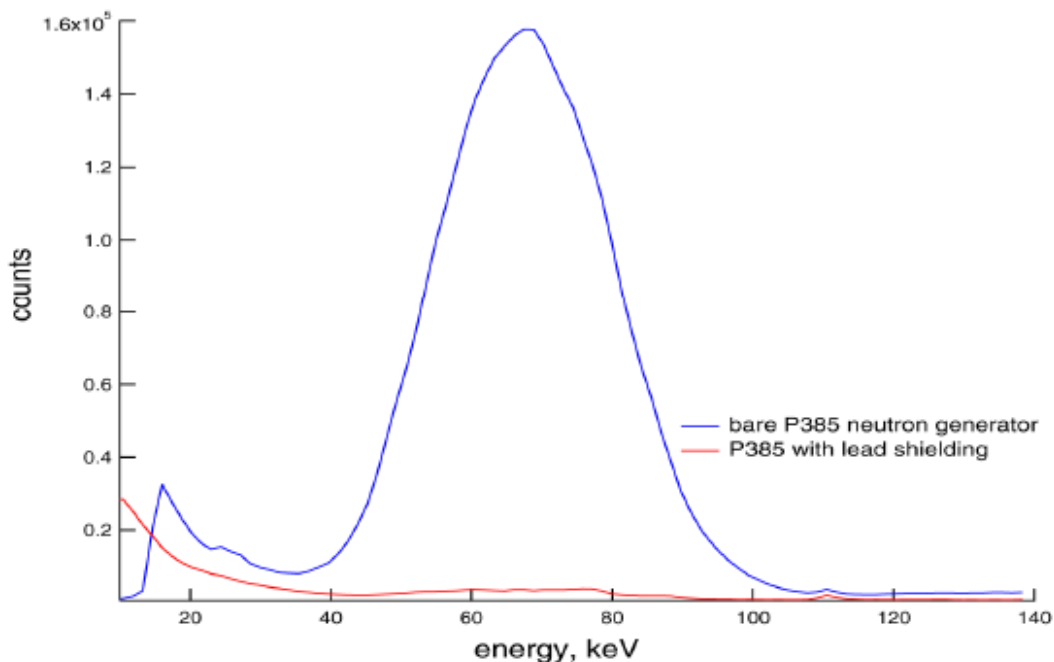


Figure 2.5 DD generator x-ray spectra (using HPGe), with and without lead shielding [207]. Reproduced with permission of AIP.

2.3.2.2 MCNP Dose and Iron Gamma-Ray Count Approximation

The dose received by a human patient is a factor which governs the manner in which an individual may be exposed in a given APNEI system as well as for how long such an exposure may continue. In this feasibility study, the focus was ultimately to estimate the effective dose to the liver and to the whole body in order to provide a basis for approximating a reasonable exposure time to a given neutron flux – one that would yield a maximal iron gamma-ray signal as well as allow for the generation of a meaningful 2D image of the iron-containing voxel in the liver. Using the average cell flux tally in MCNPX and neutron flux-to-dose conversion factors from the literature, the equivalent dose to the whole liver was simulated. Upon simulation of $2\text{E}9$ neutron histories from the isotropic source, the equivalent dose to the whole liver was 140 μSv . In order to estimate the effective dose to the liver, the equivalent dose to the liver was multiplied by the

tissue weighting factor of the liver (0.05), yielding an effective dose of 7 μSv [83]. Similarly, the equivalent doses to all organs inside the human body were simulated. The effective dose to the whole body was calculated by multiplying each organ's equivalent dose with the corresponding tissue weighting factor and then adding the results. The effective whole body dose was found to be 23 μSv . Because some organs in the model were composed of multiple cells (e.g. 5 total compartments made up the 2 lungs), the dose to each of the cells was weighted according to the proportional volume of the respective organ such that the average dose to the organ could be calculated and related appropriately to the whole body effective dose. In some cases, the volumes of different cells were calculated using rough geometries; so, the effective whole body dose presented above is an approximation. Additionally, it is worthwhile to note that whole bone volumes of the femurs, scapulae, spine, ribs, pelvis, and clavicles were used to conservatively estimate the whole body dose burden to the red bone marrow. In general, however, the simulated dosimetry values are within the range of those which would be expected given the cumulative experience with *in vivo* neutron activation analysis of those in the authors' lab.

The annual limit on whole body effective dose to a radiation worker is 50 mSv. In general, a whole body effective dose equivalent of less 5 mSv or an organ dose equivalent of less than 50 mSv (whichever is reached first) is considered acceptable in a medical capacity, given a reasonable justification of benefit versus risk. For an extra measure of conservatism, the limit on dose equivalent to the liver for the following calculations will be set at 5 mSv (10% of the 50 mSv organ dose equivalent mentioned previously). The simulations and calculations outlined thus far indicate that $2\text{E}9$ neutrons emitted isotropically in this APNEI model deliver 140 μSv equivalent dose to the liver and 23 μSv effective dose to the whole body. Therefore, to reach an acceptable equivalent dose to the liver of 5 mSv, a maximum of $7.14\text{E}10$ neutrons can be isotropically emitted from the defined point source. Hence, the iron gamma-ray counts normalized to 5 mSv dose equivalent to the liver were calculated and are shown in Table 2.2.

Table 2.2 – Number of iron gamma-ray counts normalized to 5 mSv equivalent dose to the liver

Fe (ppm)	100	500	1000	2500	5000	10,000
Counts	17.9 ± 3.9	71.4 ± 7.9	142.8 ± 11.4	357.1 ± 17.5	714.2 ± 25.0	1392.7 ± 35.4

Note that there is no time component specified for the 7.14×10^{10} neutrons. With an isotropic flux on the order of 1×10^9 neutrons/second, 7.14×10^{10} neutrons can be achieved in just over a minute. However, the neutron flux may be restricted in an APNEI application by the limitation of beam spot diameter for maintaining image resolution as well as gamma detection saturation considerations. The research summarized in the following chapters will follow up on the feasibility study to determine whether the iron gamma-ray counts will be detectable at low iron concentrations and to more directly evaluate what the detection limit would be in an experimental setup.

2.3.2.3 Tritium Buildup and 14 MeV Neutrons

For the purposes of dosimetry as well as neutron activation analysis energy thresholds, it may become important to consider that a competing reaction at the titanium target in the neutron generator produces tritium (i.e. $H^2(d,p)H^3$). If one assumes that the target becomes impregnated with tritium just as it became embedded with deuterium, then the DT fusion reaction becomes possible, which yields much higher energy 14 MeV neutrons as well as correspondingly higher nuclear reaction thresholds and the accompanying high energy gamma-rays. However, a simple bounding calculation demonstrates that DT neutron contributions would remain nominal even in a DD neutron generator operated for hundreds of hours.

For example, imagine a DD generator has been operating for 350 hours at an isotropic flux of 1×10^9 per second. For each DD neutron generated, it is assumed that a single competing $H^2(d,p)H^3$ reaction takes place, in which case 1.26×10^{15} tritium nuclei would have been produced. In the case of deuterium atoms becoming embedded in the titanium lattice (with a lattice constant of 295 pm and approximate area density of 1.7×10^{15} atoms/cm²), it is expected that the total number of deuterium atoms in the target would be about 3.5×10^{18} , assuming a DD fusion target area of 6.28 cm² and that there is a single deuterium atom for every titanium atom. This means that there are 3.6×10^{-4} titanium atoms for each deuterium atom. Because the DT reaction yield is two orders of magnitude greater than that of the DD reaction, the ratio might increase to approximately 3.6% - meaning that 3.6×10^7 DT neutrons would theoretically be produced per second in a DD generator with an isotropic flux of 1×10^9 /s. However, this is an optimal bounding calculation; the DT neutron output from a DD generator in an experimental setting would be expected to be significantly lower. In fact, a previous study in the authors' lab which utilized aluminum powder as the irradiation

target, proved that 14 MeV neutron production was negligible. DT neutrons are capable of inciting the $^{27}\text{Al} (n,\alpha) ^{24}\text{Na}$ reaction, which interestingly, is an important nuclide for quickly screening workers or members of the public after a criticality event. Na-24 has a half-life of 14.96 hours and decays by β^- decay with accompanying gamma-rays which may be used as a diagnostic criterion at a triage center, for example, to identify individuals that have been subjected to high neutron doses. However, in the case of the aluminum powder, after a 5-minute DD neutron irradiation and counting by HPGe for 30 minutes, the Na-24 gamma-ray peaks were not discernible [71]. This indicated that the contribution of the DT reaction to the overall neutron output was insignificant regarding dose, particularly considering DD neutrons are more biologically damaging than DT neutrons at a given fluence rate.

From a health physics perspective, the potential buildup of tritium in the target of the neutron generator presents radiological concerns for which there are few precedents. For example, considering the $1.26\text{E}15$ tritium nuclei calculated previously for 350 hours of runtime of a $1\text{E}9/\text{s}$ DD neutron generator, the tritium activity produced would be approximately $2.25\text{E}6$ Bq or 60.85 μCi . According to 10CFR20 Appendix C, the quantity of licensed tritium requiring labeling is $1,000$ μCi , an amount which is likely unreachable over the lifetime of a DD neutron generator. However, the behavior of the tritium atoms within the generator is unknown. Perhaps they become entrained within the titanium target lattice as assumed, but if an activity of 60 μCi of tritium were to become airborne and to combine with moisture upon tube maintenance, for example, an individual could receive a dose of 3.75 mrem in the worst case [208]. A dose of this magnitude is likely to be of very little concern and can be argued to be within ALARA requirements given its unlikelihood, but the fact remains that even portable neutron generators are capable of producing this so-called accelerator-produced radionuclide. And while activities of tritium on the order of 100 μCi are not likely to trip any regulatory thresholds with regard to hazardous materials transportation or waste disposal, the burden is on the operator and facility administration to justify that the amount of tritium produced is of no consequence. Because tritium is used in boosted fission weapons and thermonuclear weapons and because objects even as mundane as tritium exit signs require special regulatory considerations regarding possession, transfer, and disposal and have been the subject of public concern in an age of terrorism and enhanced nuclear anti-proliferation efforts, it is as important as ever for all users of devices capable of producing tritium to be accountable for its potential biological impacts, security, and ultimate transfer as waste or to

another user. Thorough recordkeeping and concise, transparent communication are necessary in order to foster trust not only in the nuclear fuel cycle industry but in medical and academic facilities where radiological controls may not be as well defined and where novel pursuits preclude the use of established protocols.

2.3.3 Image Simulation

2.3.3.1 Idealistic APNE Image

Using the iron inelastic scatter gamma-ray counts at the gamma-ray detectors for particular iron concentrations in the liver voxel as well as some preliminary time constraints on exposure as determined by the simulated equivalent dose to the liver, an image representing the iron concentration within the voxel was generated. As discussed previously, an equivalent dose of 5 mSv to a human subject's liver would allow for the isotropic emission of $7.14E10$ source neutrons in the defined setting. Though the range of nonheme iron content in the liver of a healthy adult varies greatly [209], 1,000 ppm provides a good baseline for liver iron concentration in this APNEI simulation as both a high-end healthy liver estimate and a low-end estimate for a region of liver tissue in which elemental homeostasis has been affected by some state of disease. Therefore, assigning an iron concentration of 1,000 ppm to the target voxel in the liver, $7.14E10$ source neutrons would yield the detection of approximately one hundred forty-three 846.8 keV inelastic scatter gamma-rays according to the MCNPX simulation. Assuming ideal timing and spatial resolution, each detected gamma-ray could be perfectly associated with the x-y-z position of an iron nucleus. If each gamma-ray arose from the inelastic scatter of a DD neutron with a different iron nucleus in the target voxel, then there would be 143 data points with which to construct a 3D image. By tracing the randomly assigned coordinates of interaction within the target voxel through the position of the perfect source spot (i.e. the neutron point source) to a plane located 5 cm beyond the source spot (i.e. the supposed pixelated imaging plate), a theoretical 2D image was contrived. Figure 2.6 shows such an image – for a $7.14E10$ isotropic point neutron source as situated in the MCNPX simulation, a liver voxel iron concentration of 1,000 ppm, and the corresponding number of Fe-56 inelastic scatter gamma-ray counts of 143. The principles behind APNEI – at least in the projective dimension – are illustrated ideally in Figure 2.6, where each of the supposed Fe-56 nuclei are perfectly resolved. The output information provided by MCNPX was used as the input

for an independent algorithm which allowed post-processing of the data to produce images following the APNEI event sequence.

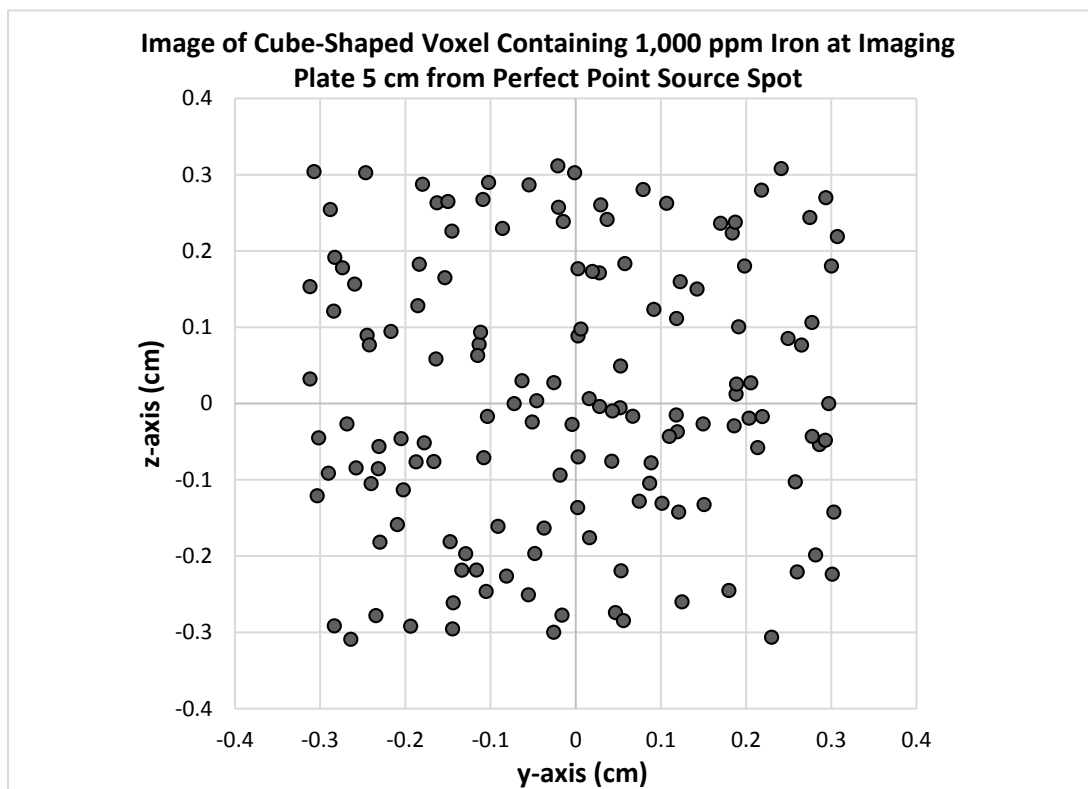


Figure 2.6 Cube-shaped voxel simulation with perfect reflection about point source spot

Note that the voxel is in the shape of a cube for the purposes of image simulation. Not only did a cube provide a good illustration of phenomena such as blur as the result of poor spatial resolution, but a cube allowed for the straightforward implementation of a random number generator to assign the coordinates of inelastic scatter interactions within the voxel (i.e. the parameters for the range of each randomly selected coordinate were the same for x , y , and z dimensions rather than being depth dependent as they would be in a sphere, for example).

2.3.3.2 Realistic APNE Image

Figure 2.6 represents an image that might be obtained if the neutron source spot were indeed acting as an ideal pinhole camera – the source itself being an infinitesimally small point about which the positional information of the iron nuclei in the target voxel may be reflected. Other sources of uncertainty aside, one can begin to approximate what would be the spatial resolution of

the 1 cm³ voxel by introducing important variables such as neutron beam spot diameter and detector timing error. Again employing the parameters used to generate the image in Figure 2.6, a second image was generated (Figure 2.7) which illustrated the image blur inherent of the use of a non-dimensionless neutron beam spot as well as He-3 ion and gamma-ray detector timing resolutions yielding a total timing error of 138 ps. This timing error was previously derived by Koltick and Nie [9], and although their calculation assumed the use of NaI gamma-ray detectors, their total timing error was employed here for the preliminary illustration of spatial uncertainty in 2D. It is expected that the total timing error for an APNEI system utilizing germanium detectors would be comparable – if marginally increased in a state-of-the-art HPGe system – because the gamma-ray detection electronics and gamma-ray spatial accuracy upon detection dominate the total timing resolution and are generally similar for NaI and germanium-based systems [9]. In Figure 2.7, a random number generator was used to assign points of origin to each tagged neutron across a beam spot with a width of 2 mm, thereby rendering a more realistic spatial resolution at the supposedly ideal pixelated imaging plate.

Additionally, the presumed location of interaction of each neutron with an iron nucleus in the target voxel was shifted randomly according to a Gaussian distribution along the neutron path of travel to simulate more realistic timing resolutions of the ion and gamma-ray detectors. The Gaussian distribution had a 95% confidence interval of (-0.3 cm, 0.3 cm), as derived from the 138 ps total timing error described above. The 0.3 cm reflects the distance a 2.5 MeV DD neutron may travel in 138 ps. This is an advantage of DD neutrons over DT neutrons; for a given timing uncertainty, DD neutrons have the potential for better depth resolution due to their lower energy and velocity. The remainder of the variables were defined to be identical to those used to generate Figure 2.6. The square drawn on Figure 2.7 illustrates approximately where the image borders of the cube-shaped voxel would have been without the blur introduced by increasing the neutron beam spot size and simulating detector timing error. However, the image resolution was still idealized in this case because considerations were not made for neutron beam spot depth or pixel size in the pixelated detector, though neutron beam spot size is by far the most important variable in the determination of resolution in the x,y dimensions. This is because pixelated ion detectors with effective pixel dimensions of < 1 mm are readily available [9], whereas decreasing the neutron beam spot size is a more pressing technical issue in sealed tube neutron generators with regard to balancing neutron flux capability and target cooling. In the post-processing of the MCNPX

simulations and generation of the image in Figure 2.7, a 2 mm source spot diameter was selected as it has been achieved in some imaging-based neutron generators and was confirmed by Koltick and Nie [9]. The feasibility study contributing to the content of this dissertation may be thought of as an extension of the pioneering work of Koltick and Nie in the field of APNEI for use in medical diagnostics.

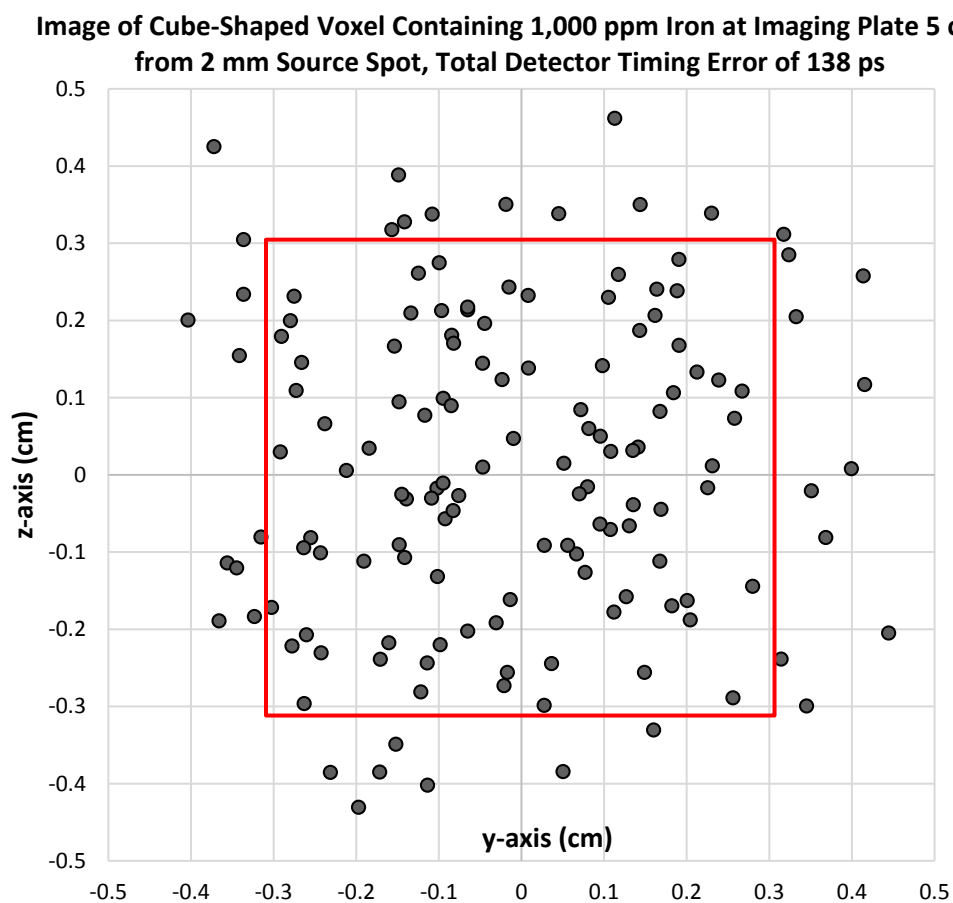


Figure 2.7 Cube-shaped voxel simulation with reflection about 2 mm source spot and simulated detector resolution

Imagine a cube as the target object of a pinhole camera. Theoretically, a two-dimensional image of the cube would be represented on a flat surface on the opposite side of the pinhole, the image having undergone inversion as a result of the optical projection. As the pinhole grows larger, the resolution fades as in the so-called camera obscura presented in Figure 2.8. This principle explains the majority of the blur beyond the red outline in Figure 2.7. One can also visualize how the pixel size would impact resolution by observing the x,y grid, where it is apparent

that there may not be enough data to support very small pixel sizes, while very large pixel sizes would completely wash out the image. Again, the pixel size of the associated particle detector was not specifically taken into account in this feasibility study; it will be examined in the next chapter. In this case, the apparent (x,y,z) positions of iron nuclei were mapped directly – without grayscale shading per pixel as would likely be applicable in a clinical setting – in order to convey full transparency of the method by which the APNE imaging took place. Finally, though the image is further degraded in the projective dimension due to limited timing resolution, the majority of the blur due to timing uncertainty is introduced in the depth dimension, as expected. This will also be examined in greater detail in chapter 3.

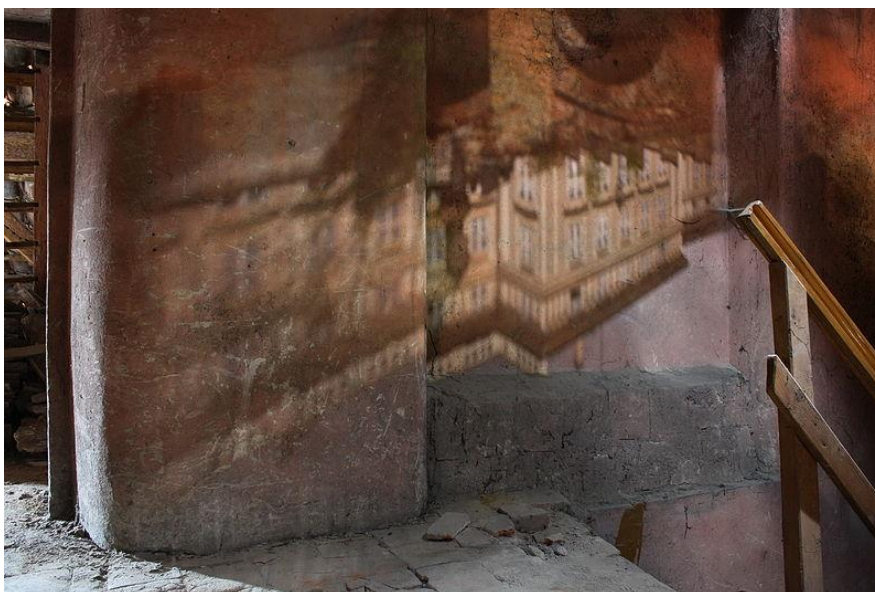


Figure 2.8 Example of a pinhole image - palace in Prague projected onto a wall through a hole in the ceiling.

2.4 Discussion

In the study composing this chapter, a rudimentary model was defined in MCNPX to simulate the basic application of APNEI techniques for *in vivo* elemental analysis in disease diagnostics. The case explored in this chapter utilized DD neutrons and was for a 1 cm^3 iron-containing voxel within a human liver. The feasibility of applying APNEI *in vivo* depends upon a number of factors, including timing resolution of the He-4 or He-3 ions and inelastic scatter gamma-rays, neutron beam spot size, pixel size in the pixelated detector, detector efficiencies, and

target voxel depth, all of which contribute to the determination of voxel resolution and elemental sensitivity. The relatively simple model in this study idealized a majority of these factors to focus predominantly on the response of the system to iron, the idea being that if the simulation results indicated that APNEI *in vivo* was not feasible in this most basic sense, it would not be practical in more realistic scenarios.

One detail to consider in future APNEI simulations – particularly those involving iron and the liver – is the inelastic scatter gamma-ray signal that may be the result of the interaction of neutrons with iron in the blood. Given that the vascular capacitance (i.e. blood volume) of the liver is 600 mL (~12% of all blood in the human body), it is anticipated that the amount of iron present in the liver as part of the components in blood would be significant [210]. The ability to differentiate between the iron in liver tissue and that entrained in the blood should therefore be investigated. For instance, because about 65% of the iron in the body is bound to hemoglobin in red blood cells, the concentration of iron in blood in adults can be expected to be around 500 ppm [211]. By comparison, the upper limit of the normal range of liver iron concentration is around 1,800 ppm [72, 212], though iron distribution in the liver is often not homogeneous and can be an order of magnitude higher in certain disorders [213]. Indeed, the liver is the most important source of reserve iron in the body [214]. It is interesting to note that upon achieving adequate spatial resolution of iron in an APNEI system, the visualization of large blood vessels or of regions of angiogenesis or hemorrhage may be possible.

In general, the response to iron of the modeled APNEI system was higher and more easily discernible than would be expected in a real-world setup, particularly given 1) the oversized germanium gamma-ray detectors, 2) the assumption of perfect temporal resolution of the associated particles at the pixelated and germanium detectors, and 3) the lack of competing interactions which would contribute to the background signal. Additionally, the attenuation of the 846.8 keV gamma-ray in soft tissue is not insignificant ($\mu = 0.08 \text{ cm}^{-1}$), so fewer relevant counts would be expected in a real-world setup even considering the shallow depth of the target voxel in the body and the optimally-oriented HPGe detectors [215]. Furthermore, although the detector volumes were rather large, they were meant to increase the probability of detection of the relevant inelastic scatter gamma-rays. The large, singular detectors can be considered a simple approximation of an array of smaller detectors, which would be more feasible. Also, as detector size increases, temporal resolution (and thus depth resolution) may decrease when considering the

time gating required in APNEI [216]. But as this study was largely preliminary and the model simplified timing uncertainties, inelastic scatter gamma-ray detection and identification was paramount. Regardless, in true APNEI with successful time gating of He-3 or He-4 ions and gamma-rays, it is the objective that only gamma-rays incited to emission by tagged neutrons would contribute to the signal acquired in the energy bin(s) of interest. And by significantly decreasing background counts, the minimum detectable limit of the target nucleus would correspondingly decrease. Because the neutron source is present while the sample signal is being gathered, such background reduction through coincidence counting is of interest to increase the signal-to-noise ratio [217]. It is this keystone of APNEI that the model presented in this paper illustrates in an ideal sense.

In short, the model presented in this study demonstrated how varying concentrations of iron in the distal region of a human liver may be quantified and visualized. The model may be further improved by 1) including a pixelated detector with realistic, sub-millimeter pixels [9], 2) by examining target voxels as a function of depth in the human body, 3) by including multiple, adjacent voxels to visualize a grayscale image of a heterogeneous elemental distribution 4) by including realistic timing protocols to approximate representative background signals, 5) by including iron distributed in other areas of the body to simulate the iron naturally present outside – or within – the local region of interest (e.g. in the blood), 6) by examining other elements such as phosphorus and cadmium with inelastic scatter cross sections to DD neutrons conducive to APNEI [218], and 7) by more accurately modeling the neutron beam spot dimensions and emission characteristics and including the components of a relevant DD neutron accelerator. A majority of these improvements were implemented in the simulation model and will be expounded upon in the next chapter.

2.5 Conclusion

A basic model has been defined in MCNPX to simulate the use of APNEI to visualize an iron-containing liver voxel *in vivo* using DD source neutrons. Though extensively optimized, the model allows for the simulation of an image which represents iron concentration in the target voxel at a biologically relevant level. According to the simulation, data for such an image may be collected while imparting an equivalent dose of 5.0 mSv to the liver and an effective dose of 0.82 mSv to the whole body. The model provides a foundation upon which more complex APNEI

scenarios may be built in MCNPX and lays the groundwork for beginning experimental study with a DD-based APNEI system or a surrogate fast neutron prompt gamma-ray analysis apparatus. The contents of this chapter therefore serve as the basis for the simulation-based as well as experimental research presented in chapters 3 and 4 of this dissertation.

CHAPTER 3. MONTE CARLO SIMULATIONS OF SPATIAL RESOLUTION

3.1 Overview

As a potentially viable technology for *in vivo* trace elemental imaging in disease diagnostics (as indicated in chapter 2), the pathway to more in-depth analysis of the technique and more clearly defining achievable spatial resolution using realistically defined variables for the neutron source spot diameter, the pixelated associated particle detector, and the overall timing resolution became clear and was the next logical step. After all, if APNEI is ever to be useful in the clinic, then the spatial resolution must not be relegated to ideal circumstances but evaluated using real world limitations. For example, in the previous chapter, the individual iron nuclei themselves were visualized to approximate blur, predominantly in the projective dimension – irrespective of approximate pixel size because the ion detector resolution was not finite. Correspondingly, initial proof-of-concept simulations utilized a perfect point neutron source or a 2 mm diameter neutron source with uniform as opposed to Gaussian-distributed neutron emission characteristics. Finally, the detector timing resolution was optimal and needed to be considered not only with regard to the pulse production and processing capability of HPGe detectors but in the depth dimension itself, rather than only as a slight component of the blur in the projective dimensions. This necessitated a more complicated iron-containing target – one that could easily be manipulated to demonstrate true three-dimensional resolving power as the contribution of the system timing regime to depth resolution is far more significant than that to resolution in the projective plane. Indeed, resolution in the z -dimension – as it is governed by different system attributes – should be quantified separately from the resolution in the x,y -dimensions. And that is the prevailing purpose of the research contributing to this chapter – to realistically evaluate the spatial resolution achievable in each dimension using simulations of neutron elemental imaging using the associated particle technique with a model that has been significantly improved over that used in the feasibility study in chapter 2.

In other words, the purpose of the study presented in this chapter was to develop and employ a Monte Carlo simulation model of associated particle neutron elemental imaging in order to determine the three-dimensional imaging resolution of such a system by examining relevant physical and technological parameters and to thereby begin to explore the range of clinical

applicability of APNEI to fields such as medical diagnostics, intervention, and etiological research. Again, the model was built upon that introduced in the previous chapter – with a focus on more precisely defining resolution-related parameters within the APNEI system in order to realistically approximate spatial resolution to a high degree of certainty, such as may be attained using technologies available currently.

The presented APNEI model was defined in MCNP by a Gaussian-distributed and isotropic surface source emitting deuterium + deuterium neutrons, iron as the target element, nine iron-containing voxels (1 cm^3 volume each) arranged in a 3-by-3 array as the interrogated volume of interest, and finally, by high-purity germanium (HPGe) gamma-ray detectors anterior and posterior to the 9-voxel array. The MCNP f8 pulse height tally was employed in conjunction with the PTRAC particle tracking function to not only determine the signal acquired from iron inelastic scatter gamma-rays but to quantitate each of the 9 target voxels' contribution to the overall iron signal – each detected iron inelastic scatter gamma-ray being traced to the source neutron which incited its emission.

With the spatial, vector, and timing information of the series of events for each relevant neutron history as collected by PTRAC, realistic grayscale images of the distribution of iron concentration in the 9-voxel array were simulated in both the projective and depth dimensions. With an overall 225 ps timing resolution, 6.25 mm^2 imaging plate pixels assumed to have well localized scintillation, and a DD neutron, Gaussian-distributed source spot with a diameter of 2 mm, projective and depth resolutions of $< 1 \text{ cm}$ and $< 3 \text{ cm}$ were found to be achievable, respectively, for iron-containing voxels on the order of 1,000 ppm Fe.

The imaging resolution offered by APNEI of target elements such as iron lends itself to potential applications in disease diagnosis and treatment planning (high resolution) as well as to ordnance and contraband detection (low resolution). However, it was apparent upon completion of the research contributing to this chapter that experimental study beyond simulation is required to optimize the layout and electronic configuration of APNEI system components – including realistic shielding and phantom materials – for background signal reduction in order to accurately determine the detection limits and spatial resolution of iron and other elements of interest on a case-by-case basis.

A more comprehensive explanation of the associated particle technique as well as a schematic of APNEI are provided in the previous chapter and in the authors' previous work, which

explores the application of APNEI to *in vivo* medical diagnostics for diseases with elemental signatures [9, 10]. Building upon those preliminary studies regarding elemental response and the technological variables associated with maximizing *in vivo* imaging resolution, this chapter will focus predominantly on small-scale image simulations using MCNP – with target voxel volumes and a general APNEI system layout which would be relevant in clinical applications. As expounded upon previously, diseases that are often associated with changes in elemental homeostasis in affected tissues include Alzheimer’s, Parkinson’s, and certain cancers. It is interesting to note that such physiological changes in trace metal concentrations frequently occur prior to the development of apparent or distinguishing symptoms in an individual affected by some state of disease [219], in which cases an elemental imaging system with a clinically valuable *in vivo* resolution could offer pathways to early disease detection, management, and lesion differentiation.

Contributions in the field of APNEI are thus expected to foster the development of a new tool in the field of medical imaging – one that is capable of detecting some asymptomatic diseases earlier than ever before, as well as to offer insight into the etiology and differentiation of certain cancers and to allow the direction of therapeutic interventions according to the observable elemental profile distributions. In the pursuit of clinically relevant APNEI, it is critical to explore achievable spatial resolution *in vivo* and its accompanying variables. The concept of optimizing image resolution has only been briefly introduced, in papers which included overviews of important system characteristics such as neutron beam spot diameter, ion detector pixel size, and ion and gamma-ray detector timing resolutions [9, 10].

This chapter is composed primarily of material included in a publication in the journal of *Medical Physics* entitled “Monte Carlo Simulations of Elemental Imaging Using the Neutron Associated Particle Technique” [11], which was co-authored by Dr. Linda Nie. Some material from the publication has been included previously for the purpose of introducing the topics of APNEI and NAA in general, particularly with regard to the imaging process and the determination of resolution in three dimensions. As for the publication primarily contributing to the previous chapter, the right to re-use of the publication (other than in journal articles) – in whole or in part – was retained by the author in the Wiley Copyright Transfer Agreement. The chapter, therefore, continues to build upon the pioneering work of Nie and Koltick, proceeding from theoretical calculations, to an APNEI feasibility study based in MCNP simulations as illustrated in the

previous chapter, and now to refined simulations developed to more thoroughly quantitate the spatial resolution of a neutron elemental imaging system.

Similar to the illustration in Figure 1.25(B), the model presented in this study defines an array of voxels as the target region, as opposed to a single 1 cm^3 voxel as in the study presented in the previous chapter. The array of 1 cm^3 voxels were situated in a 3-by-3 cluster with no inter-voxel space. Iron was selected as the element of interest because it is known to frequently be present at elevated concentrations in cancerous tissue and diseased brain tissue as opposed to healthy tissue [2, 179, 220]. Additionally, as in the APNEI feasibility study presented in chapter 2 [10], the simulated system employed HPGe gamma-ray detectors and DD source neutrons. The overarching objectives of the study were to examine how beam spot diameter, ion detector pixel size, and detector timing capabilities limit achievable spatial resolution in an associated particle imaging simulation and to ultimately quantify a 3D imaging resolution for the simulated APNEI system. In the future, the simulated images and APNEI parameters will serve as a stepping stone toward experimental study using element-doped phantoms at a scale relevant to *in vivo* applications in medical imaging.

3.2 Materials and Methods

3.2.1 Monte Carlo Simulations

The Monte Carlo Neutral Particle (MCNP) radiation transport code developed by Los Alamos National Laboratory is a valuable tool for modeling the interactions of radiation with matter. The code permits the simulation of DD source neutrons and detector geometries as well as accounts for the release of secondary photons from nuclear interactions using experimentally-derived cross section libraries. MCNP thus provides a framework upon which neutron and secondary photon transport may be simulated and tracked, thereby offering a means to tabulate the spatial and temporal information as would be collected for image construction in APNEI. The authors chose to utilize MCNP as opposed to other transport codes due to recent successes in the validation of experimental neutron activation analysis applications using MCNP-driven simulations in their lab [139, 140]. For reference, the authors used version MCNPX, in which the X stands for eXtended – essentially expanding the capabilities of MCNP5 to more particle types and potential secondary interactions.

3.2.2 Simulation Model and Technical Basis

To simulate the application of APNEI in a small-scale laboratory or clinical setting, a simple, hypothetical phantom was modeled as a 9-voxel array (3 per side) of perfectly adjacent 1 cm^3 voxels. The 1 cm dimensions of each voxel were chosen as an estimate of spatial resolution which would be valuable for *in vivo* applications [11, 205]. The 9-voxel target array was suspended in air such that the leading edge of the center voxel was exactly 8 cm from the neutron source spot. The source spot – that from which the 2.45 MeV DD neutrons were emitted – was defined as a circular surface source with negligible depth, 2 mm diameter, and a Gaussian-distributed and isotropic emission profile. Note that the Gaussian emission profile refers to spatial emission across the source spot and not to the energy spectrum of the neutrons. Previous studies have indicated that a $< 2 \text{ mm}$ diameter beam focusing limit is achievable with proper focusing voltage and target cooling [9, 194, 221]. To achieve the Gaussian-distributed and approximately isotropic pattern of neutron emission as would be expected from a DD fusion source [221], the -41 Gaussian distribution function provided in MCNP was employed, with inputs of the full width at half maximum (FWHM) and the mean for each of the projective dimensions. In this way, a two-dimensional Gaussian sampling distribution was defined for the points of emission of source neutrons from the DD fusion spot. And because no vector biasing was included in the source definition, neutrons were emitted from the Gaussian-distributed source uniformly in 4π steradian.

The other components of the model relevant to APNEI were the HPGe gamma-ray detectors, imaging plate, and neutron shields. Each of the two HPGe detectors was represented as a cylinder with a radius of 11.5 cm and thickness of 10 cm – one anterior and one posterior to the array of target voxels. In building upon the feasibility study presented in chapter 2, the detectors were oriented such that the trunk of a reference man might be imagined to fill the space between the voxel array and the detectors, in which case the detectors would be flush with the body to maximize signal acquisition, and the voxels would be present in an organ such as the liver, which has a naturally heterogeneous iron distribution that when perturbed may be indicative of metastatic lesions or other disease [10]. However, while the present focus is *in vivo* application of APNEI, the model presented in this chapter is broadly defined to explore neutron elemental imaging theory and technological parameters as a means to transition to small scale laboratory experimentation; so, a soft tissue model was excluded in favor of a simple hypothetical phantom (i.e. 9-voxel array). Although some reverse electrode coaxial HPGe detector crystals do approach 10 cm thicknesses

[222], the large 11.5 cm radius for each of the detectors was chosen both to increase statistical significance of the MCNP inelastic scatter gamma-ray response and as a simple approximation of an arrangement of smaller detectors (each with approximately 100% relative efficiency) used in tandem. With strong computational statistics, the HPGe gamma-ray detector response may be assumed to scale down linearly with a decrease in detector volume, as will likely be applicable in future studies.

The imaging plate, which would classically be composed of a gallium-doped zinc oxide scintillator applied as a position-sensitive transducer [192, 196], was illustrated by a placeholder in the presented model. Because the simulated images were constructed using post processing techniques and because the source spot was treated as a 2.45 MeV neutron source rather than as a true DD associated particle source, the action of the imaging plate in the simulation was immaterial. In other words, because both the position of emission and the path of travel of each neutron was tracked in MCNP, the position at which the associated He-3 ion would impact the imaging plate could be geometrically inferred. This is because the He-3 ion is the so-called associated particle of the DD neutron, another result of the fusion of two deuterium atoms. Because the DD reaction takes place essentially at rest, the neutron and He-3 ion are produced traveling in opposite directions at fixed velocities (i.e. 180° coincidence). Therefore, the plate was included as a separate geometry for the purpose of demonstration, but the cell contained the same material as the surrounding media (i.e. air) so as not to unnecessarily complicate the neutron and neutron-induced photon transport calculations. The center of the imaging plate – in both the model placeholder and post processing calculations – was positioned 2 cm from the source spot on the side opposite the 9-voxel target array. The imaging plate was assigned 6.25 mm² pixels arranged in a 5-by-5 configuration with no inter-pixel space. The square pixels with 2.5 mm sides were conservatively low resolution as sub-millimeter pixels are readily available [223]. Because quasi-monoenergetic DD neutrons travel at approximately 3 times the speed of their He-3 associated particles, the imaging plate needed to be at least a factor of 3 times closer to the neutron source than the target or object to be interrogated. In this case, a 2 cm plate-to-source distance satisfied this criterion while at the same time providing a convenient geometry where the borders of the 9 interior imaging plate pixels exactly corresponded to the borders of each of the voxels in the target array, assuming a perfect pinhole projection image. In other words, the imaging plate was a quarter of the distance to the neutron source spot as the distance from the source spot to the 9-voxel target

array. With this geometry, the 2.5 mm-per-side pixel dimensions correspond directly with the 10 mm-per-side voxel dimensions – by a factor of 4.

Finally, to simplify MCNP outputs and to limit the amount of data sorting necessary in post-simulation image construction, two idealized neutron shields were included in the model to perfectly “kill” neutron histories which were not going to impact the target region (since neutrons are emitted in 4π), thereby bolstering computational statistics and improving simulation runtime. Rather than including imperfect fast neutron shields such as polyethylene which would have introduced orders of magnitude more neutron inelastic scatter reactions as those extraneous neutrons were moderated, the shields were defined in MCNP explicitly as void space with a neutron importance of zero. In this way, neutrons incapable of undergoing a first collision in the target region – as evidenced by entry into the neutron void – were quickly ignored rather than being traced to their ultimate terminations. On average, this improved simulation runtime by a factor of 10 and correspondingly decreased particle tracking data file sizes. The two shields were defined as rectangular sheets which intersected the innermost plane of the imaging plate and were oriented between the neutron source spot and HPGe detectors. Each shield was 9 cm wide, 20 cm long, and 0.1 cm thick. Figure 3.1 shows a transverse cross section (top-down view) of the imaging model at the height of the center of the neutron source, which is the same as the height of the center voxel in the target array. Note that the HPGe detectors are slightly truncated in the figure. The image for Figure 3.1 was obtained from the MCNPX Visual Editor – Version X_22S, which is a supplement to the MCNP radiation transport code that allows for the viewing of the geometries defined in the simulation.

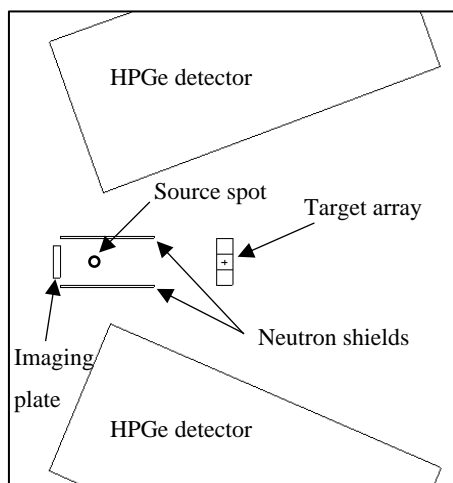


Figure 3.1 A transverse cross section of the imaging model at the height of the center of the neutron source spot and central target voxel

It is evident in Figure 3.1 that no neutron generator components, laboratory neutron / gamma-ray shielding materials, or supporting apparatus are included in the imaging model. This was to optimize the simulation runtime for particle histories on the order of $1E9$ as well as to allow straightforward isolation of the variables directly responsible for limiting spatial imaging resolution in APNEI. Additionally, while it is expected that the inclusion of such materials would decrease elemental sensitivity, the time-of-flight collimation technique would allow for the significant exclusion of competing signals, thereby providing for differentiation of target elemental signals from the region of interest [9, 10].

It follows then that because the element targeted for imaging in this study was iron, the only iron-bearing cells in the imaging model were those in the 9-voxel target array. Not only is iron (Fe-56) known to be a distinguishing marker in several disease signatures, but it is a logical target element in AP fast neutron analysis studies because of its relatively high inelastic scatter cross section to DD neutrons (approximately 1 barn) [10]. For the purpose of using the neutron AP technique to image iron, the desired nuclear collision and subsequent de-excitation is $\text{Fe-56} + n \longrightarrow \text{Fe-56}^* + n' \longrightarrow \gamma$. The non-iron component of each voxel was defined as water, a material which would be relevant to *in vivo* application (soft tissue approximation) as well as potentially to eventual phantom construction. With regard to the differences between DD and DT neutron generators, the strengths and weaknesses of each system are well defined in the literature and have been introduced previously, suffice it to say that a DD source was employed in this study because the lower energy neutrons (2.45 MeV versus 14.1 MeV for DT) would limit the background signals from organic and environmental media and simplify the overall gamma-ray spectrum, as well as allow for enhanced depth resolution and more modest shielding requirements [9, 189]. Additionally, in the case of DD neutrons inelastically scattering with Fe-56, nearly all of the Fe-56* decay occurs through the emission of an 846.8 keV gamma-ray, an advantageous situation in terms of the simplified gamma-ray profile; in other words, there were no higher order excited states with which to be concerned [9, 190].

3.2.3 Projective Resolution

By assigning different iron concentrations to each voxel in the 9-voxel target array, the interplay between APNEI system parameters and their effects on overall spatial resolution could be simulated, as evidenced by increases or decreases in blur in the final images. Figure 3.2

illustrates the iron concentration (in ppm) and voxel ID number assigned to each of the 9 water-containing voxels in the target array, as viewed in the projective dimension from the position of the neutron source spot.

#1 1,000	#2 5,000	#3 1,000
#4 500	#5 10,000	#6 1,000
#7 0	#8 1,000	#9 2,500

Figure 3.2 A cross section of the target array in the projective dimension showing the iron concentration in ppm assigned to each of the 9 voxels. The non-iron component of each voxel was water.

The iron concentrations in the target array were chosen for consistency with the previous APNEI feasibility study, which examined non-heme liver iron *in vivo* through MCNP simulations [10]. The concentration of iron in liver tissue is often heterogeneous and can increase by a factor of 10 in some disorders [72]. For reference, normal non-heme iron concentration in a healthy liver can approach 1,800 ppm [209, 212, 213].

The number of data points (i.e. neutron-induced inelastic scatter photons) from each of the 9 target voxels which would contribute to the elemental imaging of iron were collected using the f8 tally in MCNP. The f8 pulse height tally acted as a multi-channel analyzer (MCA) and generated a histogram of the number of detected gamma-rays across the selected energy range. In this study, the relevant energy was defined over a range from 0 to 0.85 MeV with energy bins with a width of 0.001 MeV (i.e. simulating very high energy resolution as attainable using some HPGe gamma-ray detectors) [224]. The energy bin of interest included the 846.8 keV gamma-rays from the de-excitation of Fe-56*. In this way, the f8 tally provided the iron signal from each of the voxels of interest in the simulation model; however, for the purpose of generating realistic neutron associated particle images, spatial and temporal information from the system needed to be collected. For this reason, the pulse height tally was coupled with the MCNP particle tracking (PTRAC) function, which generated a separate output file of user-filtered events. By including

the f8 tally as part of the event filter in the PTRAC definition, only those neutrons which incited the emission of a gamma-ray which contributed to the pulse height tally in the supposed HPGe MCA would be tagged and their histories logged. Additional filters for particle history selection included neutrons as the particles of interest, source and collision events as the occurrences to log, and the identifying number of the voxel within the 9-voxel target array that was currently being observed. Because the contribution of each individual voxel to the overall Fe-56 gamma-ray signal was required, the simulation process was iterative – revising successive runs of the simulation to examine each voxel in turn. The PTRAC output file then provided not only the number of iron inelastic scatter gamma-rays from a particular voxel (as would be given by the f8 pulse height tally alone), but related each iron inelastic scatter gamma-ray to the neutron which caused its emission and then tabulated the spatial coordinates of the tagged neutron's origin, the spatial coordinates of its point of collision in the target array, its energy, and the time which elapsed between its emission (i.e. source event) and its collision. A simple program written in Visual Basic further selected applicable events from the PTRAC output file and imported them in tabular form into Microsoft Excel. These data provided the basis by which APNEI images of the distribution of iron within the target array would be simulated.

It is important to consider that much of the information available from the PTRAC output of the APNEI simulation would not be available in a real-world AP fast neutron imaging system. Indeed, the process by which the spatial information of elemental nuclei would be obtained in the laboratory would involve only the stimulated pixel on the imaging plate and timing calculations between associated particle and gamma-ray detection, assuming a favorable (i.e. coincidence-tagged) inelastic scatter nuclear collision in the interrogated volume. Therefore, in the construction of the simulated neutron elemental images, such idealizations of the simulated APNEI system were taken into account to the extent possible to render the images more realistic. For example, in the case of modeling projective imaging resolution, the vector of neutron travel was traced to the imaging plate to find the point of intersection. This represented the point at which the He-3 associated particle would be detected by the position-sensitive transducer (given 180° coincidence with the DD neutron). While the geometry of the imaging plate was a placeholder in the simulation model, it was expected that the He-3 ion would interact with very high relative efficiency with a ZnO:Ga plate at that location, just like an alpha particle in the case of a DT neutron generator [225].

In this way, each of the 846.8 keV iron inelastic scatter gamma-rays logged by the f8 pulse height tally and PTRAC was related to a supposed associated particle detection at the imaging plate. With the point of intersection of each of the vectors with the imaging plate, a count of the number of hits within each pixel was tabulated, which was indicative of realistic imaging plate resolution. These counts per pixel – once normalized to 1,000 counts for the central voxel of the array – then served as a means to assign a grayscale shade to each of the pixels, which was done using a simple algorithm applied to the RGB color model [where the values of R, G, and B were equal to $255 - (255/1000) * \# \text{ counts}$]. Intuitively, a darker grayscale shade indicated more concentrated elemental iron. As apparent in Figure 1.25, the projective imaging resolution was governed by the imaging plate pixel size and the neutron source spot dimensions.

3.2.4 Depth Resolution

In modeling depth resolution, the timing information from PTRAC became the primary differentiator, and although the relevant spatial and temporal event information was collected from MCNP through implementation of the f8 pulse height tally and PTRAC as described previously, the 9-voxel array was rotated 90° about the central voxel such that blur in the depth dimension could be more effectively illustrated. The array as oriented in the system for demonstrating depth resolution is shown in Figure 3.3, as well as the direction of rotation from the orientation initially shown in Figure 3.1. The iron concentration in each voxel was left unchanged (as shown in Figure 3.2).

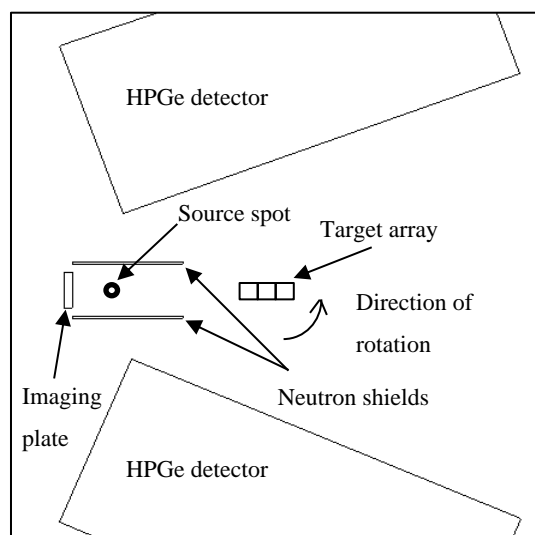


Figure 3.3 A transverse cross section of the imaging model at the height of the center of the neutron source spot and central target voxel, with a change in orientation of the target array for modeling depth resolution.

As described for the projective image, the vector along which the tagged DD neutrons and their associated He-3 ions traveled was known. Correspondingly, the timescale of each of the tagged sequences of events was known. However, in MCNP, neither the timing resolution of the ion detector nor the timing resolution of the HPGe gamma-ray detectors was taken into account. Therefore, in order to model depth resolution realistically, the overall timing resolution (including the error attributed to both the position-sensitive ion detector and HPGe detectors) was introduced mathematically. While timing resolutions for NaI-based systems and HPGe-based systems traditionally range from 100 - 1000 picoseconds (ps), respectively, the timing resolution of HPGe detectors has been observed to approach that achievable using NaI detectors by employing constant fraction discrimination to allow much more rapid pulse processing [9, 205, 226]. Therefore, because the total timing error is expected to be dominated by the gamma-ray detector timing uncertainty, 225 ps was chosen as the total timing error (σ) in this study – representative of a readily achievable NaI timing resolution and optimized HPGe timing resolution. Then, by applying Gaussian-distributed uncertainty with $\sigma = 225$ ps along each tagged neutron's travel vector to its simulated point of first collision with a Fe-56 nucleus in the target array, an image of iron concentration which was indicative of realistic depth resolution was obtained. In other words, the (x, y, z) coordinates where tagged neutrons interacted in the array (as obtained from PTRAC) were shifted according to a Gaussian distribution ($\sigma = 225$ ps) to replicate detector uncertainty in a laboratory setting. Thus, the AP time of flight measuring error was introduced into the data obtained from MCNP as the basis for simulating APNEI depth resolution.

3.2.5 Three-Dimensional Resolution

Finally, both the projective and depth resolutions taken together allowed the construction of a 3D tomographic elemental image from the MCNP simulation. For simplicity, the 9-voxel array was again oriented parallel to the imaging plate, as in the projective imaging approach. While the projective and depth resolutions modeled separately were analogous to 2D spatial slices, the final tomographic images represented the blur in all dimensions – as the result of an imperfect neutron source spot, finite imaging plate pixels, and limited detector timing resolutions. The 3D images may be considered to be projective tomography because the iron inelastic scatter gamma-ray signal was spatially attributed to 6 slices – each corresponding to 0.5 cm in the depth dimension – as well as to one of 25 pixels (arranged 5-by-5 as resolved by the imaging plate) in the projective

dimension, and all the information necessary for generating the images was obtained from one angle (as opposed to the multi-angle analysis and image construction algorithms necessary in computed tomography). Finally, in all MCNP simulation runs of the APNEI model, $2E9$ neutron histories were employed to yield relative errors at least as low as 0.10 without extending computation time unnecessarily. For reference, each run of the APNEI model in MCNP took approximately 6 hours using one node of two 10-core Intel Xeon-E5 processors in a supercomputer cluster.

3.3 Results

3.3.1 Projective Resolution

Using the MCNP particle tracking function filtered by the f8 pulse height tally for 846.8 keV inelastic scatter gamma-rays, the iron signal attributable to each of the voxels in the target array was simulated. Furthermore, each detected inelastic scatter gamma-ray was related to the neutron which incited its emission by colliding with a Fe-56 nucleus. The history of each of these tagged neutrons was tracked and logged, thereby providing a means to obtain the spatial information relevant to simulating projective resolution in a simple APNEI system. Although the associated particle of each DD neutron was not a part of the MCNP simulation, each known neutron path of travel allowed for the geometric inference of where the imaging plate would be impacted by each He-3 ion, and thus which pixel would accumulate a coincident count (assuming well localized position sensitivity, as expected from a ZnO:Ga detector) [192, 225]. In the projective dimension, the target array was treated as a 9-voxel slice with a depth of 1 cm. The iron concentration in each target voxel dictated the number of coincident iron inelastic scatter gamma-ray counts which were registered to the corresponding pixel(s) of the imaging plate.

Analogous to Figure 3.2, Figure 3.4 illustrates the iron concentration within each voxel in the interrogated array by assigning a grayscale color with an intensity inversely proportional to iron concentration (i.e. darker shade corresponds to higher iron concentration). The 0 – 10,000 ppm iron concentration range was scaled across the entire grayscale spectrum, from white to black, respectively. A quasi-perfect image of the array on the 5-by-5-pixel imaging plate is shown in Figure 3.5, and the corresponding numbers of coincident counts per pixel optimally predicted by MCNP (normalized to 1,000 counts for the central voxel of the array, with the highest iron

concentration of 10,000 ppm) are listed in Table 3.1. Note that to an outside observer, the image in Figure 3.5 is inverted in both the x and y dimensions as would be the case in a pinhole camera. Due to the selected dimensions of the pixelated imaging plate (2.5 mm per side per pixel) and because the imaging plate is one-quarter the distance from the neutron source spot compared to the source-to-target distance, the nine interior imaging pixels exactly correspond to the 1 cm^3 voxels in the array. The only differences between Figures 3.4 and 3.5 are the reflection and projective scale; the 2D image is faithful and without blur. Both the object as shown in Figure 3.4 and the image as shown in Figure 3.5 are viewed from the position of the neutron source spot (between the object and pixelated detector), which is why the image appears to only be reflected in the y -dimension. The uncertainties tabulated in Table 3.1 are derived from the relative error from each f8 pulse height tally for the 9 target voxels. The f8 tally operates on the basis of aggregate contributions across all neutron histories (i.e. $2\text{E}9$) rather than on a per event basis like PTRAC.

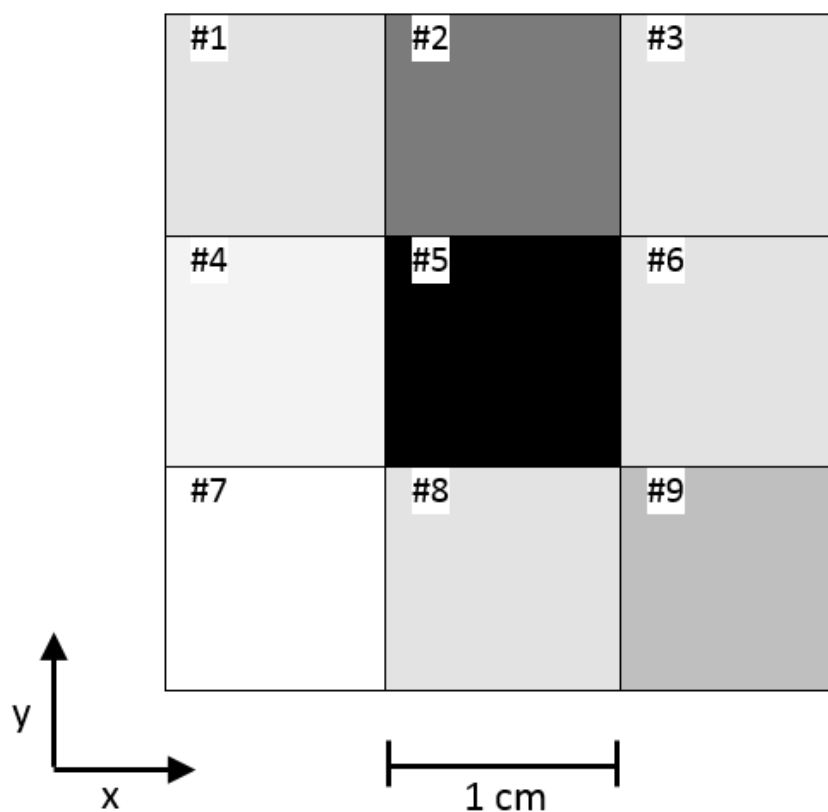


Figure 3.4 Nine-voxel interrogated object, shaded according to iron concentration. Each voxel is 1 cm per side. Viewed from the position of the source spot.

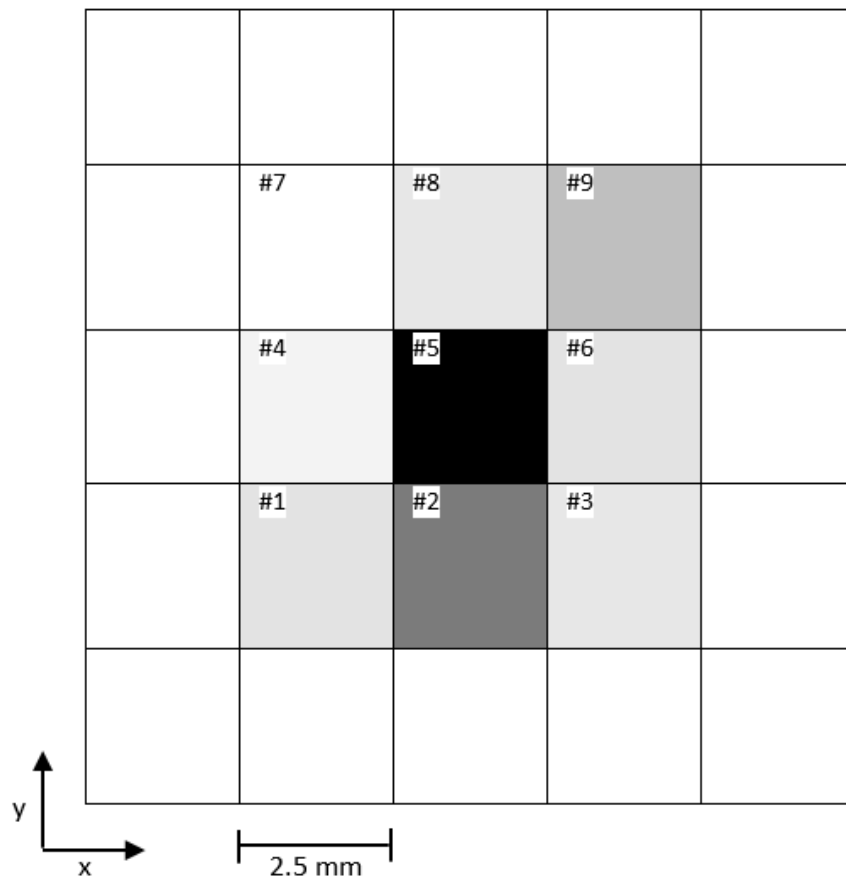


Figure 3.5 Quasi-perfect 2D image of the target object on the pixelated imaging plate, with grayscale shades assigned according to the number of coincident counts per pixel. Each pixel is 2.5 mm per side. Viewed from the position of the neutron source spot.

Table 3.1 – Ideal coincident count contributions from target voxels to corresponding pixels on the imaging plate, normalized to 1,000 counts for the center voxel iron concentration of 10,000 ppm

Pixel ID	#1	#2	#3	#4	#5	#6	#7	#8	#9
Voxel Fe Concentration (ppm)	1,000	5,000	1,000	500	10,000	1,000	0	1,000	2,500
Counts at corresponding pixel	109.4 ± 6.0	515.6 ± 29	93.8 ± 5.7	46.9 ± 2.5	1,000 ± 56	109.4 ± 5.8	0.0 ± 0	93.8 ± 5.3	250.0 ± 14

However, because the neutron source spot in the simulation had a diameter of 2 mm with a Gaussian-distributed emission profile, the realistic projective imaging resolution was not as ideal as shown in Figure 3.5. In other words, the neutron source spot did not function as an infinitesimally small pinhole, as in optical theory, but instead allowed for spatial uncertainty. With

$2E9$ neutrons emitted isotropically from the 2 mm diameter surface source located 8 cm from the leading edge of the center voxel of the target array, the simulated number of neutrons per unit area inside the center voxel was approximately $2.2E6$ n/cm², with very slightly decreased relative flux at the periphery of the array. Additionally, a truly perfect image must assume ideal counting statistics (i.e. a voxel containing 1,000 ppm iron will always yield the same number of coincident counts as any other voxel containing 1,000 ppm iron), but even in the small scale and simplistic simulation presented in this study, this was not the case (hence why the image presented in Figure 3.5 is only quasi-perfect). Multiple voxels containing 1,000 ppm in the target array differed in their contributions to the relevant energy bin in the HPGe pulse height tally by nearly 20%, owing to differing spatial orientation and stochastic radiation transport processes (see Table 3.1). With these considerations in mind, the realistic projective image of the target array at the imaging plate is shown in Figure 3.6.

The number of coincident counts on a per pixel basis was used to assign a shade in grayscale to each pixel of the imaging plate; the realistic numbers of coincident counts from MCNP were again normalized to 1,000 counts for the quasi-perfect central voxel at 10,000 ppm iron and are indicated in Figure 3.6 for comparison to those in Table 3.1. Note that the numbers of coincident counts per pixel which led to the simulated image in Figure 3.6 could not be conveniently presented in tabular form as some counts contributed to pixels outside of those ideally geometrically related to the target array (i.e. greater than 9 pixels were impacted as a result of the non-dimensionless source spot). The grayscale algorithm applied to the RGB color model was meant to allow for the visual comparison of perceived iron distribution in the interrogated volume in a relative rather than absolute sense. Regardless, Figures 3.5 and 3.6 are good illustrations as to the difference between ideal and realistic projective resolution in APNEI, respectively. Note that the total number of counts contributing to Figure 3.5 across all pixels is the same as that in Figure 3.6 because the number of neutron interactions with iron in the target array did not change; instead, the neutron source spot dimensions and the statistics of radiation detection altered where the inelastic neutron collisions would be resolved in the projective dimension – introducing blur. Because a finite number of neutron histories allowed for the detection of an exact number of supposed He-3 ions and associated iron inelastic scatter gamma-rays in the APNEI MCNP simulation, the tracked events in the PTRAC file were used to generate the realistic image in Figure 3.6. These events were all-or-nothing; either a neutron passed the PTRAC filter parameters and was tagged and

logged in the output file, or it did not and was not tracked. The associated uncertainties are therefore not displayed in Figure 3.6. Correspondingly, it is important to note that the normalization process coupled with the all-or-nothing nature of the PTRAC function caused quantized count values, which are apparent in Figure 3.6.

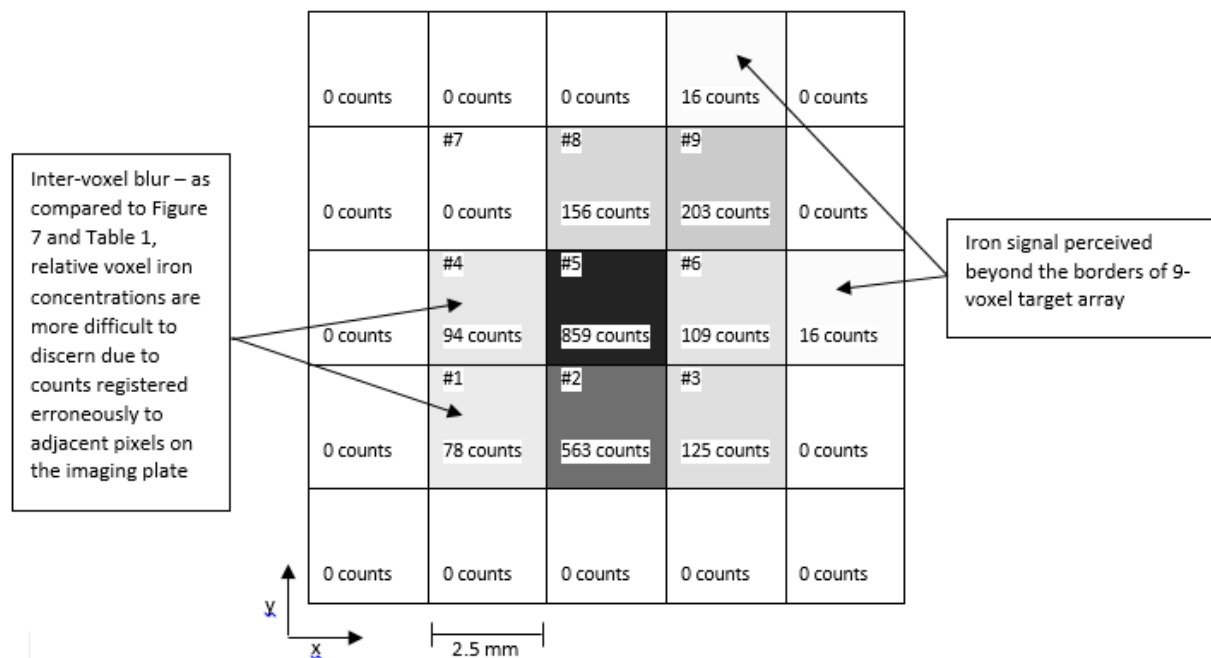


Figure 3.6 Realistic 2D image of the target object on the pixelated imaging plate, with grayscale shades assigned according to the number of coincident counts per pixel, as normalized to 1,000 counts for 10,000 ppm Fe in the central voxel of the quasi-perfect image in Figure 3.5. Note that as compared to Figure 3.5, the relative Fe concentrations are more difficult to discern as a result of inter-voxel blur. Additionally, some signal was collected within pixels outside of the 9 interior (ideal) pixels, indicative of blur resulting from the imperfect neutron source spot. Each pixel is 2.5 mm per side. Viewed from the position of the neutron source spot.

Figure 3.6 indicates a projective resolution for the simulated APNEI system of < 1 cm. However, there are two imaging phenomena worth describing. The first relates to the blur that extends beyond the ideal borders of the 9-voxel target array. It has been heretofore described that the 9 interior pixels of the imaging plate geometrically correspond to the 9 voxels of the target array, assuming pinhole reflection. However, because the neutron source was a Gaussian-distributed surface source with a diameter of 2 mm, some He-3 associated particles were detected within pixels on the imaging plate which were not perfectly representative of where the corresponding neutrons inelastically scattered with Fe-56 in the target object. In the APNEI simulation, this projective uncertainty translated to the perception of iron in space where iron was not actually present.

Nevertheless, in the simple 9-voxel model presented in this study, the borders of the target array remain relatively clearly defined. The second noteworthy difference between Figure 3.5 and Figure 3.6 pertains to the inter-voxel blur where instead of iron signal being attributed to a volume in space where no iron was present, the signal is attributed to an adjacent iron-containing voxel – thereby making the relative iron concentration of each voxel appear different from what is true. This may be described as a whitewashing effect; in other words, voxels containing high concentrations of iron appear to contain less iron upon imaging, and voxels containing low concentrations of iron appear to contain more iron upon imaging. For example, the pixel geometrically corresponding to the center voxel of the target array (i.e. #5) containing 10,000 ppm iron accrued only 859 coincident counts in Figure 3.6, as compared to the 1,000 counts to which the center pixel was normalized in Figure 3.5. The center pixel was therefore assigned a lighter grayscale shade in Figure 3.6. Correspondingly, the iron signal arising from the center voxel was registered among all surrounding pixels on the imaging plate in Figure 3.6 due to blur resulting from the 2 mm source spot diameter, thereby increasing the perceived iron concentrations in those voxels. For example, voxel #3 which contained 1,000 ppm iron yielded 94 coincident counts at the corresponding pixel on the imaging plate in Figure 3.5. Conversely, the same pixel registered 125 counts in Figure 3.6, thereby increasing the apparent iron concentration in voxel #3 by 33%. Indeed, in the idealized setup shown in Figure 3.5, the iron signal attributable to voxel #3 was 9.38% (10% expected) that of the signal attributable to voxel #5. In Figure 3.6, the voxel #3 iron signal was 14.6% that of the voxel #5 iron signal. This whitewashing or middling effect could complicate the relation of different elemental concentrations in adjacent volumes in a target object using APNEI. As in all imaging modalities, it will remain important to experimentally define a minimum detectable concentration for each target element and to maintain a calibrated APNEI system specific to the application at hand.

It is apparent from Figure 3.6 that source spot size, counting statistics, and imaging pixel size govern resolution in the projective dimension. For example, even slightly increasing the neutron source spot diameter and imaging plate pixel size in some combination would likely blur the image of the target array to such an extent that it would be unusable in medical diagnostics, an application requiring high resolution. However, an application such as bulk material characterization in mining or security would not be constrained by such stringent technological requirements; low resolution images in the projective dimension could yet provide actionable

information. Such broad potential applicability in the realm of APNEI is why system parameters and overall layout must be examined and if possible, tested, on a case-by-case basis. The relative abundance of the element(s) of interest in the task at hand would also govern the necessary flux of the neutron source as well as corresponding detector shielding and timing regimes for the exclusion of clutter with regard to maximizing SNR [5]. In the case of trace elemental iron on an *in vivo* scale as presented in this chapter, it was necessary that the source spot and pixelated detector dimensions remain state-of-the-art by today's technology in order to yield a clinically valuable projective resolution of the target array [5, 183, 197].

3.3.2 Depth Resolution

In simulating APNEI depth resolution, the 9-voxel array was transformed 90° (Figure 3.3) in order to better illustrate blur in the depth dimension. Because the central voxel of the array remained in the same space upon 90° rotation in the simulation, the neutron fluence (approximately 2.2E6 n/cm²) remained applicable for the central voxel for 2E9 neutron histories. However, because the target array spanned 3 cm in the depth dimension after rotation, the fluence ranged from approximately 2.8E6 n/cm² at the voxel nearest the neutron source to approximately 1.7E6 n/cm² at the voxel furthest from the neutron source – the inverse square law becoming a significant consideration. This was important to keep in mind with regard to the interpretation of the target elemental signal from each voxel in the array as it related to iron concentration as counting statistics decline with increasing depth and decreasing neutron fluence.

While the neutron points of interaction in the target array were derived from PTRAC and the f8 pulse height tally as heretofore described for the demonstration of projective resolution, the temporal resolution was the principal determinant of depth resolution. Therefore, the timing uncertainty of the APNEI coincident detector system (pixelated imaging plate together with HPGe detectors) was mathematically incorporated and assumed to be 225 ps. A time slice of 225 ps translates to a depth of approximately 0.5 cm for DD neutrons which travel at a velocity of 2.2 cm/ns. So, while each 1 cm³ voxel in the target array would ideally correspond to 2 time slices, the timing resolution was such that the coincident contributions to each slice varied according to Gaussian-distributed uncertainty, thereby yielding realistic APNEI spatial depth resolution (i.e. blur into adjacent time slices). To introduce credible total timing uncertainty to the MCNP dataset, the location of interaction of each neutron with an iron nucleus in the target array was shifted

according to a Gaussian distribution along the neutron flight vector. In each case of a neutron collision with Fe-56, this process yielded a revised (x, y, z) spatial data point and thus a time slice contribution in line with what would be expected in an experimental APNEI setup. The Gaussian distribution of the timing error had a 95% confidence interval of $(-1.0 \text{ cm}, 1.0 \text{ cm})$, as derived from the 225 ps total timing uncertainty and the velocity of a DD neutron.

The coincident counts from iron inelastic scatter gamma-rays were thus no longer associated with the true locations of neutron collisions with Fe-56 nuclei in the target array but with the perceived locations of neutron collisions, as would be the case in a true APNEI system with limited timing resolution. Then, as performed for the projective image, the number of coincident counts on a per-time-slice basis was used to assign a shade in grayscale (applying an RGB color model algorithm similar to that mentioned previously) to each slice in the depth dimension (analogous to a time-dependent pixel). Similar to Figure 3.5, a quasi-perfect image of the target array in the depth dimension is shown in Figure 3.7. As before, the numbers of coincident counts from MCNP were normalized to 1,000 counts for the idealized central voxel containing 10,000 ppm iron for ease of comparison; the number of coincident counts per pixel optimally predicted by MCNP are listed in Table 3.2. However, in Figure 3.7, it is important to note that because the 225 ps time slices corresponded to 0.5 cm in depth, the sum of the coincident counts from the two slices which intersected each voxel would be equivalent to the corresponding value tabulated in Table 3.2 (due to 1 cm voxel dimensions). Due to changes in radiation transport and statistics with depth in the target array, the adjacent spatially-oriented time slices did not register equal counts per slice even though each half of an individual voxel contained the same iron concentration.

Indeed, the image is not quite ideal for the same reason as that of Figure 3.5; that is, finite counting statistics and changes in flux across the 9-voxel target array – especially in the depth dimension – yielded different gamma-ray signals from voxels containing the same iron concentration. Regardless, there is no blur in Figure 3.7 as the result of radiation detector timing error. Figure 3.7 thus represents the depth resolution prior to introduction of the Gaussian-distributed 225 ps total σ . Conversely, following the introduction of Gaussian error along the neutron flight vector according to the process described above, Figure 3.8 shows the image as defined by timing resolution currently available in pulse processing and detector technologies (i.e. 225 ps as chosen for the convenience of time slices which correspond to 0.5 cm in depth or one-half of the depth of each voxel). As in Figure 3.6, the values in Figure 3.8 are quantized and

presented without precise uncertainties as a result of the limitations of the PTRAC function in MCNP.

Table 3.2 – Ideal coincident count contributions from target voxels to corresponding time-defined pixels in the depth dimension, normalized to 1,000 counts for the center voxel iron concentration of 10,000 ppm

Pixel ID	#1	#2	#3	#4	#5	#6	#7	#8	#9
Voxel Fe Concentration (ppm)	1,000	5,000	1,000	500	10,000	1,000	0	1,000	2,500
Counts at corresponding pixel	160.7 ± 7.6	535.7 ± 31	71.4 ± 5.1	71.4 ± 3.4	1,000 ± 60	53.6 ± 4.2	0.0 ± 0	89.3 ± 5.5	178.6 ± 13

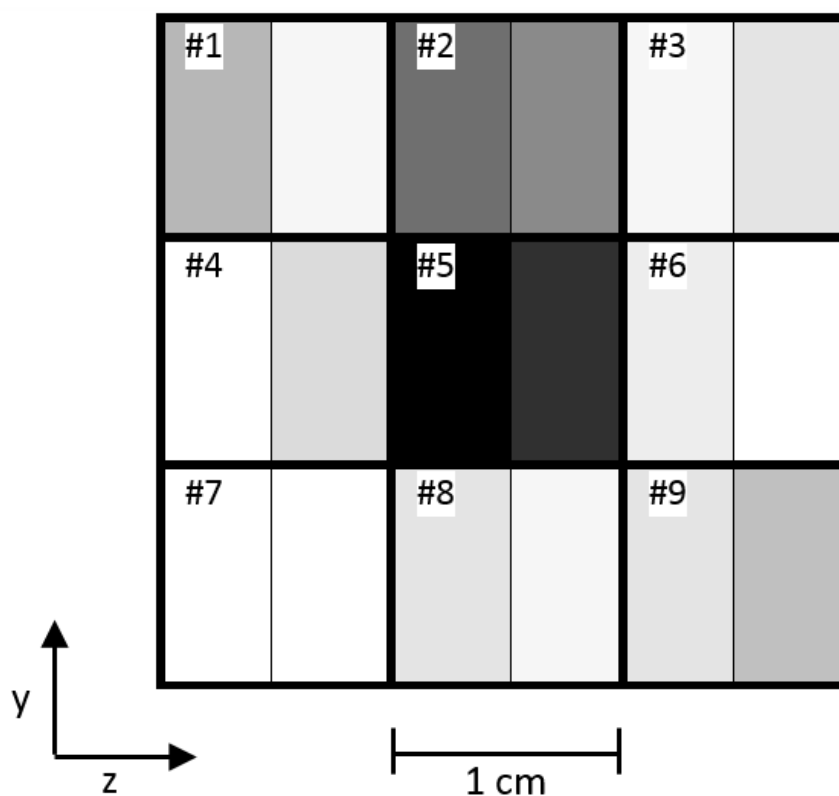


Figure 3.7 Quasi-perfect 2D image of the target object in the depth dimension (z), with grayscale shades assigned according to the number of coincident counts (normalized to 10,000 ppm Fe in voxel #5) per spatially-oriented time slice. Each time slice corresponds to 0.5 cm, thereby cutting each voxel in the target array in half. Changes in flux across the array yield different iron signals from volumes containing the same iron concentration. The geometry of the system and finite Monte Carlo counting statistics also contribute to the imperfect appearance of the image. Detector timing error, however, has not yet been accounted for.

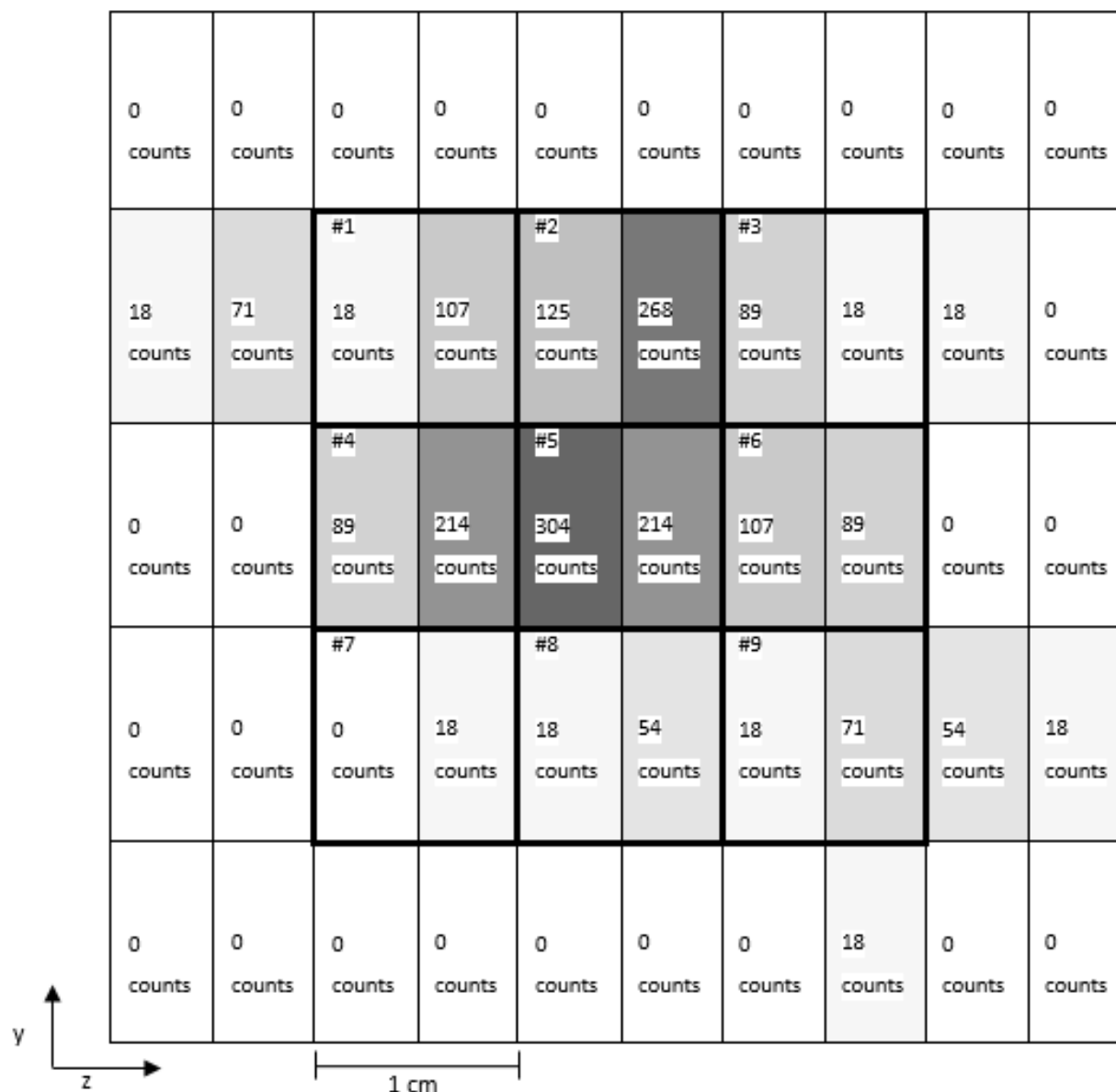


Figure 3.8 Realistic image of the target object in the depth dimension (z) in space, with grayscale shades assigned according to the number of coincident counts per spatially-oriented time slice, as normalized to 1,000 counts for 10,000 ppm Fe in the central voxel of the quasi-perfect image in Figure 3.7. Note that as compared to Figure 3.7, the relative Fe concentrations are more difficult to discern and to localize as a result of the apparent concentration gradients introduced by the Gaussian-distributed total detector timing error.

Figures 3.7 and 3.8 illustrate the difference between ideal and realistic total detector timing error (i.e. temporal resolution) in APNEI, respectively. Note that there is no inversion or alteration in scale as in the simulation of projective resolution. The temporal error calculations for

determining the coincident count contributions to each time slice were applied directly to the target array at full scale (rather than at an imaging plate on the opposite side of the neutron source spot), and so the pinhole camera-like reflection did not apply.

Comparing the normalized coincident counts in Table 3.2 to those in Table 3.1, it is apparent that those central voxels which did not change orientation in space (i.e. #2, #5, and #8) yielded very similar results – within $\pm 5\%$. However, the iron-containing voxels which moved closer to the neutron source (i.e. #1 and #4) and were thus exposed to a higher neutron flux produced a greater number of iron inelastic scatter gamma-rays, while the opposite occurred for target voxels in the array which rotated away from the neutron source (i.e. #3, #6, and #9). In these cases, the normalized coincident counts per voxel differed by as much as $\pm 50\%$, an expected result arising from changes in flux across the target array and slight changes in gamma-ray detector solid angle coverage and gamma-ray attenuation. A feature of the quasi-perfect image presented in Figure 3.7 is that the leading halves of several of the voxels appear to have higher concentrations than the trailing halves (as oriented to the neutron source), which is because more neutron inelastic scatter events with iron nuclei take place in regions of higher neutron flux, thereby yielding higher numbers of detected 846.8 keV inelastic scatter gamma-rays.

Then, in Figure 3.8, the depth resolution is more realistically illustrated than in Figure 3.7 because the Gaussian-distributed total detector timing error causes the iron signal to blur into a concentration gradient where – analogously to the whitewashing effect described for Figure 3.6 – regions of high iron concentration appear lower upon imaging while regions of low iron concentration appear higher upon imaging. However, as the spatial resolution in the depth dimension as the result of detector timing uncertainty is worse than the spatial resolution in the projective dimension, the gradient effect is more pronounced. For example, the pair of time-oriented pixels geometrically corresponding to the center voxel of the target array (i.e. #5) containing 10,000 ppm iron accrued only 518 total coincident counts in Figure 3.8, as compared to the 1,000 counts to which the center pixel was normalized in Figure 3.7. The center pixels were therefore assigned lighter grayscale shades in Figure 3.8. Correspondingly, the iron signal arising from the center voxel was registered in a Gaussian distribution predominantly among adjacent pixels in the z -dimension in Figure 3.8 due to blur resulting from detector timing uncertainty, thereby increasing the perceived iron concentrations in those voxels.

For example, voxel #3 which contained 1,000 ppm iron yielded 71 total coincident counts in the corresponding time-pixels in Figure 3.7. Conversely, the same pixels registered 107 total counts in Figure 3.8, thereby increasing the total apparent iron concentration in voxel #3 by 51%. This perceived increase in iron concentration resulted primarily from blur from voxel #2, as evidenced by an increase in perceived iron concentration heavily biased toward the leading half of voxel #3 (i.e. the half closer to voxel #2). In the idealized setup shown in Figure 3.7, the total iron signal attributable to voxel #3 was 7.14% that of the total signal attributable to voxel #5. In Figure 3.8, the total voxel #3 iron signal was 20.7% that of the total voxel #5 iron signal. While this depth differential could pose problems for the meaningful application of APNEI in 3D, it is expected that a system calibrated for a specific application could internally compensate for decreasing neutron flux with depth as well as the gradient effect, at least so long as counting statistics remained reliable and the neutron yield and emission profile at the source spot remained steady.

Unlike Table 3.1 and Figure 3.6, the total number of counts in Table 3.2 is not equivalent to that in Figure 3.8. While the number of neutron interactions with iron in the target array was the same in the simulations contributing to Figures 3.7 and 3.8, some of the true neutron collisions with iron were perceived to take place outside of the target array upon introduction of the timing error. Those collisions which were perceived to shift predominantly in the depth dimension (z) or in the y -dimension were accounted for and contributed to the blur evident in Figure 3.8. However, some collisions – approximately 5% – shifted appreciably in the x -dimension and thus would contribute to the number of coincident counts in an adjacent pixel on the imaging plate (i.e. oriented into or out of the page) coupled with the associated time slice. This occurred because each neutron path of travel was mapped in three dimensions, and some Gaussian-distributed shifts as the result of timing error – particularly at the periphery of the target array – yielded significant error in the projective x -dimension as well as the depth z -dimension. In these cases, the corresponding coincident count was no longer associated with any of the time-dependent pixels (i.e. slices) of interest for illustration of depth resolution. In other words, the illustration of projective resolution was a truly two-dimensional endeavor, but depth resolution (while illustrated for convenience in 2D) took place by varying the 3D (x , y , z) spatial coordinates of nuclear collisions according to a Gaussian distribution of error. Therefore, while shifts in the projective y -dimension are illustrated in Figure 3.8 (i.e. only one affected time-pixel accruing 18 coincident counts at the bottom of the Figure), shifts in the projective x -dimension yielded iron signal

attributable to locations outside of the 1 cm thick volume, and thus did not contribute to the image of depth resolution.

It is evident that projective information from PTRAC was retained in simulating the images shown in Figures 3.7 and 3.8 because 9 voxels may be optimally discerned in the target array, rather than only 6 time slices along the depth of the array. Therefore, while depth resolution has been modeled in two dimensions for the sake of conceptual simplicity, Figures 3.7 and 3.8 may be thought of as 1 cm 3D slices in the projective dimension. The logical follow-up was to apply the parameters explored in simulating projective and depth resolution in order to simulate realistic 3D APNE images, where all data in all dimensions contributed to the final images.

3.3.3 Three-Dimensional Resolution

As it is likely that APNEI will first be applied in clinical studies as a single-angle imaging technique, projective tomography was chosen as the best approach to model 3D resolution of the system as defined in MCNP. With the 9-voxel array oriented parallel to the imaging plate, the tomographic set of images was obtained by simulating 6 slices in the depth dimension, each of which corresponded to a thickness of 0.5 cm. Furthermore, in the projective dimension of each slice, the perceived points of origin of the coincident iron inelastic scatter gamma-ray counts were assigned to spatial voxels as defined by the simulated associated particle detector pixel response and as limited by the 2 mm DD source spot diameter and Gaussian-distributed neutron emission profile.

With regard to the 6 time slices in the depth dimension, it is important to note that the central slices (i.e. #3 and #4) were assumed to correspond perfectly with the actual spatial location of the target array. In other words, only slices #3 and #4 would ideally have registered signal from coincident iron inelastic scatter gamma-rays given perfect timing resolution and would have looked very similar to the image in Figure 3.6. The only differences would be that the number of coincident counts per pixel would have been approximately halved in slices #3 and #4 because they are 0.5 cm slices rather than 1 cm (after accounting for the change in neutron flux over the depth of the 1 cm array). Additionally, the tomographic images in slices #3 and #4 would be portrayed at the scale of the target array in space rather than reflected onto the imaging plate as in Figure 3.6. However, because timing resolution was Gaussian-distributed with $\sigma = 225$ ps and was the dominant source of spatial uncertainty in the simulation (as evidenced previously), 2 slices

on each side of the target array were necessary to accommodate blur in the depth dimension, thereby rendering a more realistic 3D view of the target array as might be obtained using detector and digital processing technologies currently available in radiation instrumentation laboratories. Over 98% of the total iron signal resolved by the simulated APNEI system was contained within the 6 half-cm slices oriented in this fashion. The slice orientation used to generate the tomographic images of the target array is illustrated in Figure 3.9, as viewed in the depth (z) dimension.

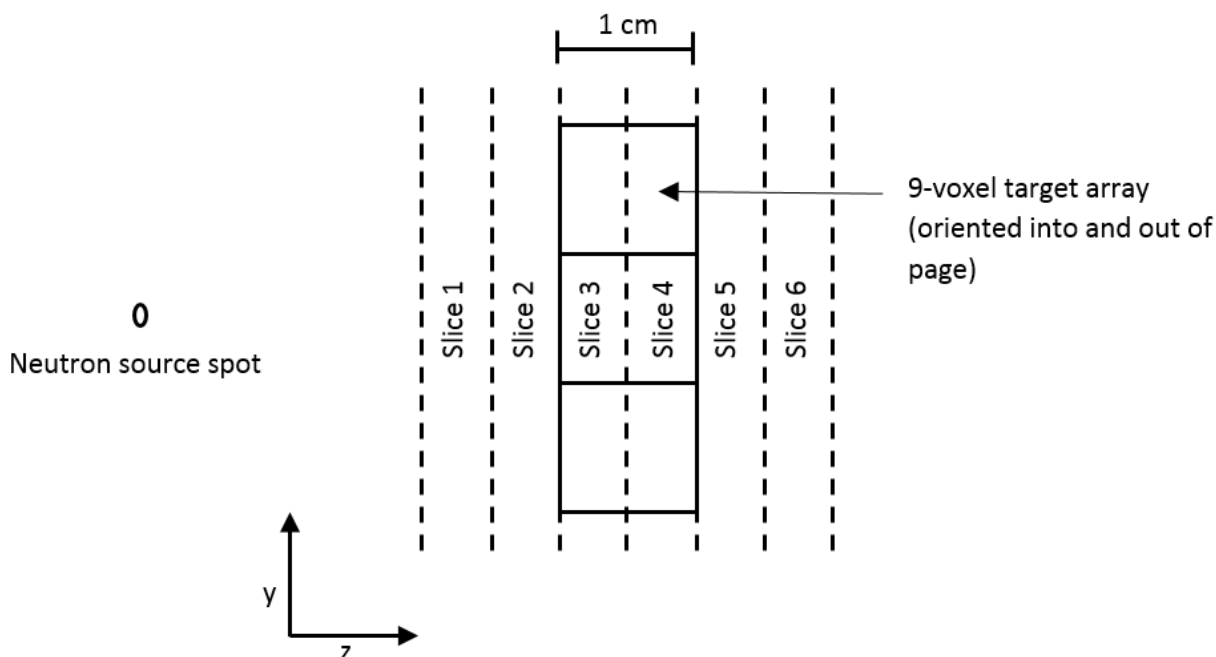


Figure 3.9 Time slice layout in the depth dimension (z), for generating tomographic images of the target array. Note that slices #3 and #4 correspond to the actual target array, whereas slices #1, #2, #5, and #6 only register blur as a result of APNEI total detector timing uncertainty. The HPGc detectors and imaging plate are not shown. The distance between the neutron source spot and target array is not to scale.

It was valuable to first consider the 6 slices registered as one (i.e. all coincident iron inelastic scatter gamma-ray signals superimposed into a single slice in the depth dimension). Though the iron signals could have been assigned to a time slice at this juncture, the dimensions and iron concentrations present in the 9-voxel target array were known, so it was useful to compare the aggregate image to the 6 separate tomographic images to qualitatively determine the resolvability of the target array. Again, each tomographic slice as well as the aggregate slice were considered on the basis of a 5-by-5 pixelated grid, as defined by the pixels of the imaging plate and their corresponding geometry with the target array. Table 3.3 lists the number of coincident counts per

pixel in the aggregate image, again normalized to 1,000 counts for the central voxel containing 10,000 ppm iron. The uncertainties presented in Table 3.3 were derived from the f8 pulse height tally in MCNP, and it is apparent that the Table 3.3 values are very similar to those presented for the simplified projective image in Table 3.1; however, the values are not identical because approximately 1.4% of coincident iron counts did not fall within the 6-slice range and were thus not tabulated by the APNEI system. Additionally, the aggregate (i.e. 6 stacked 0.5 cm slices) image is not quasi-perfect as in Figure 3.5 (Table 3.1), so there is blur in the projective dimension (i.e. counts outside of the ideal borders of the target array). The 6-slice aggregate image is shown in Figure 3.10. Finally, for comparison to the image in Figure 3.10 (which is a good overall representation of the known target array), Figure 3.11 presents the 6 slices separately, as delineated to each 0.5 cm of spatial depth as perceived by the simulated APNEI system. The number of iron inelastic scatter gamma-ray coincident counts per pixel are delineated in each slice presented in Figure 3.11. The grayscale shades were assigned as before using an algorithm normalized to the greatest number of coincident counts (i.e. highest perceived iron concentration) in the aggregate image, with the separate tomographic images scaled relative to the aggregate image maximum. Additionally, due to all-or-nothing event filtering by PTRAC, uncertainties based on the relative errors calculated by MCNP are not specified in Figures 3.10 and 3.11.

Table 3.3 – Coincident count contributions (Fe-56 inelastic scatter gamma-rays) from target voxels to corresponding pixels in space (6-slice aggregate), normalized to 1,000 counts for the center voxel iron concentration of 10,000 ppm

Pixel ID	#1	#2	#3	#4	#5	#6	#7	#8	#9
Voxel Fe Concentration (ppm)	1,000	5,000	1,000	500	10,000	1,000	0	1,000	2,500
Counts at corresponding pixel	112.9 ± 6.2	548.4 ± 31	96.8 ± 5.9	48.4 ± 2.6	1,000 ± 56	129.0 ± 6.8	0.0 ± 0	96.8 ± 5.5	193.6 ± 11

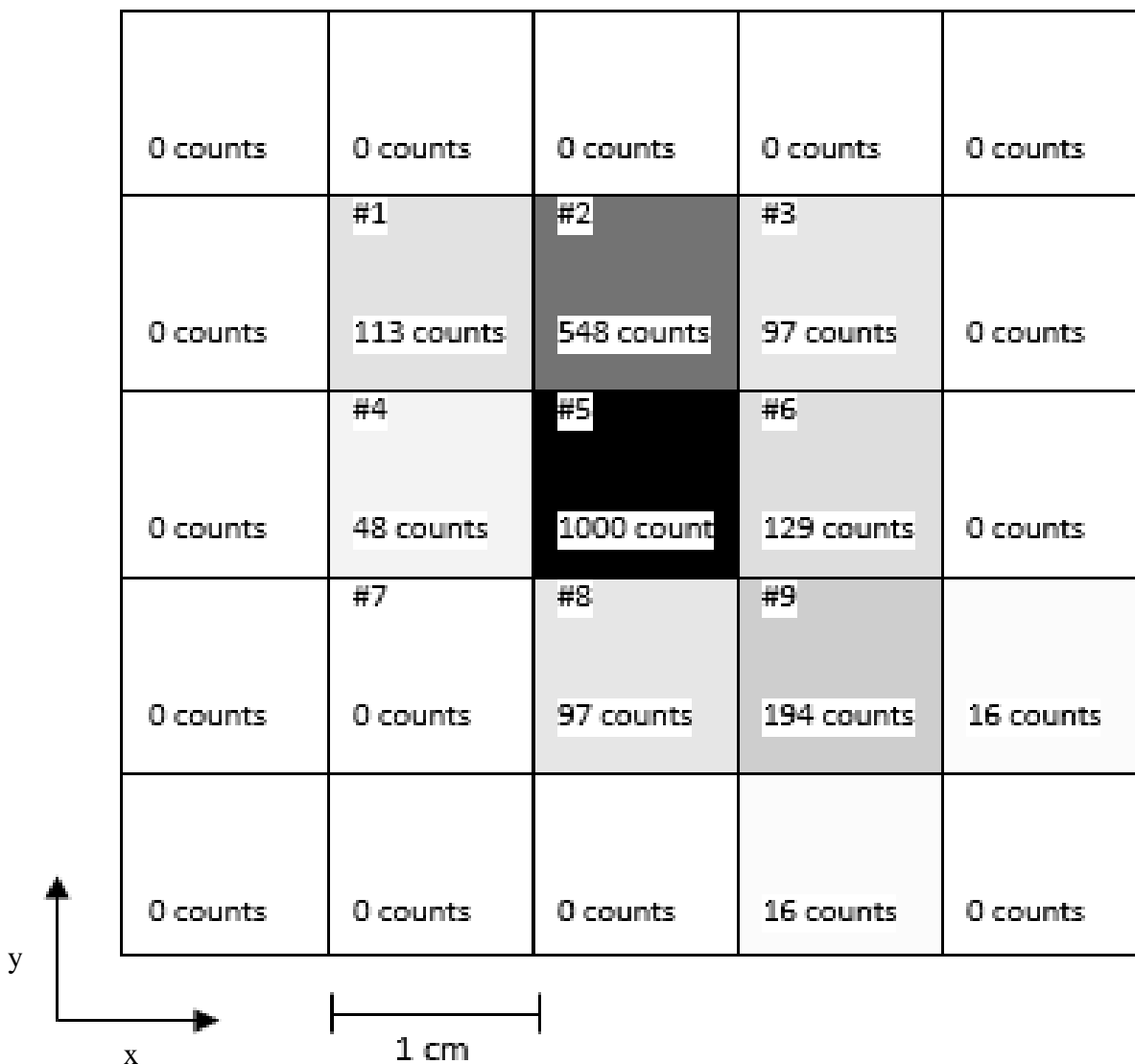
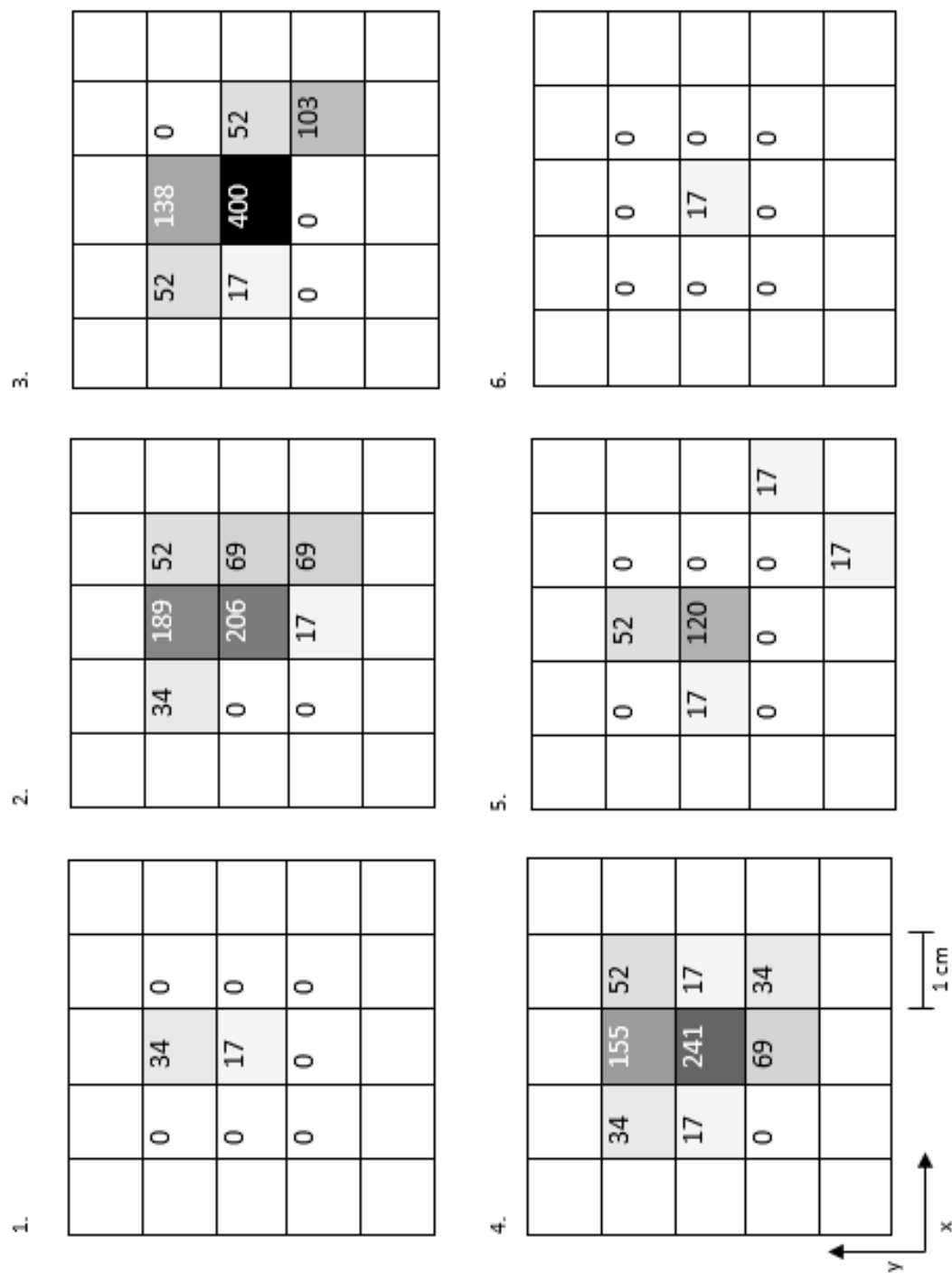


Figure 3.10 Realistic 6-slice aggregate image of the 9-voxel target array, with grayscale shades assigned according to the number of coincident counts per pixel, as normalized to 1,000 counts for 10,000 ppm Fe in the central voxel. Note that the image is very similar to that presented in Figure 3.6 because the depth resolution is essentially neglected in favor of a multi-slice, superimposed projective image of the known target array. However, consideration of the depth dimension explains why the number of coincident counts per pixel are not identical to those presented in Table 3.1; some of the spatial coordinates resolved by the simulated APNEI detector system were outside of the 6-slice boundary, as governed by total detector timing resolution. Also, these data were assigned to voxels in space rather than to a 2D pixel on the associated particle imaging plate.



In observing the final 3D results in both Figures 3.10 and 3.11, it is apparent that depth resolution is the limiting variable in determining overall APNEI resolution. With a Gaussian-distributed neutron source spot of 2 mm diameter and 6.25 mm² imaging plate pixels, the projective resolution of the simulated APNEI system was less than 1 cm. Indeed, blur in the projective dimension outside of the known borders of the 9-voxel array was nominal as evidenced by only 2 pixels acquiring 16 coincident counts each in Figure 3.10 (or 17 coincident counts each in slice #5 of Figure 3.11). Additionally, the inter-voxel blur did not appreciably affect the perceived iron concentration in each voxel relative to the central voxel, with an average relative error of only 1.93%. The projective resolution predominantly relied upon the geometry of the system and thus was determined by the errors inherent of imaging plate and neutron source spatial uncertainty, which have been realistically minimized in the presented simulation.

However, the depth resolution approaches 3 cm as a result of the total APNEI detector timing error with $\sigma = 225$ ps. Because the total detector timing error – that dominated almost entirely by the HPGe detector timing uncertainty even when added in quadrature to the uncertainty expected of a ZnO:Ga imaging plate – was assumed to be Gaussian in nature, the 99% confidence interval for $\sigma = 225$ ps came to (-1.3, 1.3), an overall interval of 2.6 cm for DD neutrons traveling at 2.2 cm/ns. This relatively wide range in depth yielded slices in Figure 3.11 which did not consistently reflect the depth-independent image in Figure 3.10. For example, voxel #5 had twice the iron concentration of voxel #2 in the target array, which was well represented by the inelastic scatter gamma-ray coincident count tallies in Figure 3.10 where 54.8% of the number of counts attributed to voxel #5 were attributed to voxel #2. In slice #3 of Figure 3.11 however, the pixel associated with voxel #2 yielded only 34.5% of the number of counts from the pixel associated with voxel #5. Additionally, in slice #4 of Figure 3.11, the pixel associated with voxel #2 was assigned 64.3% of the number of coincident counts assigned to the pixel associated with voxel #5. And as expected, the iron-containing voxel concentrations became more skewed further from the “true” slices which spatially related to the target array – slices #3 and #4.

Another feature of the tomographic images is that higher neutron flux at the leading edge of the target array seems to have introduced a bias which manifested as a greater number of coincident counts being shifted in the direction of the neutron source spot, in which case the simulated APNEI system registered greater numbers of counts in the forward rather than trailing direction. Slices #2 and #5 demonstrated this well. Note the skewed relationship between pixels #2 and #5 in each of

the slices; while the proportion of counts in pixel #2 to pixel #5 was 91.7% in slice #2, the proportion of counts in pixel #2 to pixel #5 was 43.3% in slice #5. More fundamentally, there were 636 total normalized counts attributed to slice #2 (i.e. leading slice), whereas there were only 223 total normalized counts attributed to slice #5 (i.e. trailing slice). Such results point toward potential artifacts upon APNEI application in projective tomography that may cause areas of interest to appear closer to the neutron source spot than they are.

3.4 Discussion

In this study, a model was defined in MCNP to simulate an APNEI system and to examine image resolution at a scale that would be clinically relevant in disease diagnostics. The generalized case investigated in this project used DD neutrons to interrogate a target array composed of nine distinct 1 cm^3 voxels, each of which contained a known concentration of iron. By selecting a neutron source spot diameter, detector timing error, and imaging plate pixel area relevant to technologies available today, the spatial data collected from MCNP allowed the construction of 3D tomographic images with realistic projective and depth resolutions. And while APNEI has been explored through simulation for decades [227], only recently have detector and sealed tube neutron generator technologies allowed for the optimization of parameters which would render *in vivo* application a possibility [9, 10]. However, because a specific *in vivo* application was not the focus of this study, dose constraints were not taken into account. For reference, the authors' APNEI feasibility study presented in the previous chapter performed using MCNP for a single iron-containing voxel in the liver found the equivalent dose to the liver and effective dose to the whole body for $2\text{E}9$ DD neutrons emitted isotropically to be approximately $140 \text{ }\mu\text{Sv}$ and $23 \text{ }\mu\text{Sv}$, respectively [10]. By normalizing the APNEI irradiation time to a dose limitation deemed acceptable (and thereby increasing the number of neutron histories in the simulation), counting statistics and thus imaging resolution would be expected to improve.

Dose considerations aside, it is apparent upon reviewing the results of the APNEI system simulated in this project that the limitation of depth resolution is the primary area of concern with respect to high resolution *in vivo* applications. Specifically, the projective imaging resolution of the target array was approximately 3 times finer than the depth resolution. This is because the depth resolution was predominantly governed by the temporal uncertainty inherent to the HPGe detectors in logging each coincident neutron inelastic scatter event. Additionally, changes in

neutron flux across the depth of the array introduced statistical error which accompanied changes in geometry and attenuation, thereby causing voxels containing identical iron concentrations to register significantly different numbers of coincident counts. It is expected though that the calibration of an APNEI system to a particular application and set of target elements would allow the depth resolution to be significantly improved by accounting for changes in neutron flux, geometry, attenuation, and thus signal through the target medium. Such directed calibration would alleviate the gradient and whitewashing effects which hindered qualitative target voxel discernibility and quantitative iron concentration determination in the depth dimension in the proposed model.

Future improvements to the APNEI simulation will include 1) a detailed accounting of concepts such as field-of-view, projective matrix size, and Gaussian beam dynamics in order to more effectively quantitate three-dimensional resolution, 2) background iron and potentially other elements of interest to accurately simulate the noise-canceling properties of the associated particle technique, 3) the geometry of the human body and internal organs specific to a potential *in vivo* imaging application, 4) a large array of voxels – potentially at the scale of an entire organ – to mimic the elemental distribution within the tissue as well as the spatial dependence of the neutron fluence across the larger target volume in order to evaluate the case-specific sensitivity and specificity of APNEI, and 5) the components of a DD neutron accelerator and gamma-ray detector array optimized for projective imaging. Furthermore, it is evident in the current model that thick slices (i.e. > 1 cm) in the depth dimension could yield significant preferential signal phenomena which would need to be algorithmically corrected for the task at hand. An alternative would be to explore the application of APNEI in true computed tomography (CT), a basis for which exists in the literature [8]. While it is expected that projective tomography (i.e. interrogating the target from a single angle) would be convenient in relatively superficial *in vivo* applications (particularly those requiring a transportable APNEI system), CT in conjunction with an image construction algorithm such as filtered back projection could yield higher resolution images with depth. Dose, though, would become limiting.

While there is a strong, developing foundation in simulation [8, 10, 227, 228], there are knowledge gaps in APNEI theory that require the development of a prototype APNEI system. For example, beam spot diameter and high count rate HPGe limitations must be explored in the laboratory. While high DD neutron fluxes are sought after in APNEI applications for short count

times and statistical strength, the limitation of beam spot diameter to maximize projective resolution would restrict neutron flux as well as present target cooling challenges. These complications are in addition to competing reactions at the deuterium-loaded target, which yield protons and tritium ions, thus further confounding the trigger processes by which the pixelated associated particle detector may be stimulated [228, 229]. Additionally, large volume HPGe detectors have traditionally been known to encounter pulse pile-up issues at count rates on the order of 10 kcps [222]. Novel designs such as electrode segmentation and pulse processing techniques such as constant fraction discrimination will likely need to be employed in tandem to successfully utilize HPGe detectors in a laboratory or clinical APNEI system to obtain useful energy and time-of-flight information from the relevant inelastic scatter gamma-rays [222, 226, 230]. Indeed, the overall timing error of an APNEI system as presented in the current model is governed by the limitations of the HPGe gamma-ray detector, as the timescale of the scintillation processes in a pixelated imaging transducer composed of YAP:Ce or ZnO:Ga would be an order of magnitude faster than would be expected of the electron-hole drift in a semiconducting crystal, inclusive of the conventionally long pulses which lead to pile-up issues [231].

Furthermore, because all gamma-ray detection in an APNEI system would need to be performed online (i.e. during neutron irradiation), much consideration must be given to the explicit purpose of the system, the apparatus layout, the placement of shielding materials, and gamma-ray signal discrimination. It is for these reasons that the authors plan to build upon the background in simulation presented in this and the previous paper [10] presented in chapter 2 by constructing a rudimentary fast neutron inelastic scatter analysis (FNISA) system. Needless to say, such real-world detector, material, and signal processing nuances lie outside the scope of the imaging simulations set forth in this chapter. The purpose of the forthcoming FNISA system will thus be to optimize the HPGe setup and online data collection process, while devising an efficient offline method for sorting and refining the gamma spectroscopic data, as will be necessary in true APNE image construction. Correspondingly, the time-of-flight data would need to be logged and analyzed in APNE imaging; however, a FNISA device would employ physical collimation as a surrogate for temporally-actuated electronic collimation in order to increase the signal-to-noise ratio. While the timing component of APNEI would not be initially included in the FNISA system, FNISA will nevertheless offer insight into the minimum detectable concentration of iron or other

elements of interest by allowing representative calibration curves to be obtained from the analysis of a series of soft tissue phantoms doped with varying concentrations of the target elements.

3.5 Conclusion

A model has been defined in MCNP to simulate the generalized application of a DD-based APNEI system to visualize an array of iron-containing voxels at a scale and range of iron concentrations that would be useful in medical diagnostics *in vivo*. Though not entirely representative of a real world APNEI imaging system, the model incorporates realistic APNEI parameters such as neutron beam spot size and emission profile, associated particle detector pixel area, and HPGe-relegated temporal resolution to detect and spatially assign the coincident counts from 846.8 keV iron inelastic scatter gamma-rays in 3D. While the depth resolution appeared limiting (i.e. < 3 cm) in the proposed model as compared to projective resolution (i.e. < 1 cm), stark changes in elemental iron concentration in the target array were readily observable in all dimensions. Furthermore, it is expected that phantom-based calibration of such a system would improve depth resolution as well as elemental detection limits by decreasing the gradient effects induced by Gaussian-distributed timing error. The APNEI model presented in this chapter thus provides a foundation upon which *in vivo* APNEI applications may be explored on a case-by-case basis in MCNP; moreover, the remaining questions concerning detector, shielding, and electronics optimization provide a targeted baseline from which to begin study using a FNISA system as an initial surrogate to true APNEI.

CHAPTER 4. FAST NEUTRON SCATTER ANALYSIS AS A SURROGATE

4.1 Overview

With data indicating the feasibility of APNEI as well as actionable three-dimensional resolution at the clinical scale as shown in chapters 2 and 3, experimentation using a DD generator iron-containing target, and photon detector was necessary to begin to explore the challenges of online gamma spectroscopy and background discrimination. Furthermore, with the established success demonstrated in the previous chapters utilizing MCNP, MC modelling could be used in tandem to bridge the gap between fast neutron inelastic scatter analysis (FNISA) and true APNEI. In this way, an experimentally derived LLD and SNR for the iron inelastic scatter gamma-ray peak may be compared to simulated results, in order to validate the accuracy and consistency of the model. And with a solid computational basis derived from laboratory data, the MCNP model could be altered to approximate the expected improvement in LLD and SNR upon incorporation of the associated particle (AP) methodology, thereby providing evidence of its efficacy and further motivation to investigate its potential applicability in neutron-based medical diagnostic imaging.

The purpose of the study presented in this chapter is therefore twofold; first, a prompt gamma-ray neutron activation analysis (PGNAA) system was constructed and employed in order to find the approximate sensitivity to elemental iron upon spectroscopic analysis. Concurrently, a Monte Carlo (MC) simulation model of the same PGNAA system was defined such that the neutron source and resulting gamma-ray emissions were temporally collimated using the neutron associated particle (AP) technique. The experimental and simulated gamma-ray spectra were then compared – taking into account the technological parameters and physical limitations of the PGNAA system – to determine how the sensitivity of the system may be improved due to photon signal discrimination inherent to the application of AP timing.

The presented PGNAA system utilized a deuterium-deuterium (DD) neutron generator with an isotropic flux on the order of $1E9/s$ and a 2" x 2" thallium-doped sodium iodide (NaI(Tl)) detector integrated with a Canberra Digital Spectrum Analyzer (DSA-1000). The accompanying MC model was defined in MCNP by an isotropic 2.5 MeV DD neutron source, iron as the target element, the components of the neutron generator, the supporting apparatus and shielding materials, and finally, by a volume of sodium iodide analogous to the experimental detector to serve as the

spectroscopic focal point. The MCNP f8 pulse height tally – in combination with Gaussian energy broadening – was used to generate the simulated gamma-ray spectra, while collimation settings within MCNP enabled the simulation of time-filtered spectra with significant background reduction as would be possible upon employing the AP technique.

The experimental PGNA system provided only macroscopic sensitivity to elemental iron, as confirmed by the unfiltered MCNP simulations. However, upon incorporation of AP collimation, the apparent iron sensitivity increased by a factor of nearly 8, with an accompanying increase in signal-to-noise ratio (SNR) of over 700% in the spectral region of interest. Even with modest detection capabilities in a rudimentary PGNA system, AP coincident time gating allowed for a simulated lower limit of detection (LLD) for iron < 0.5 kg, a sensitivity which may be further improved by including multiple, larger gamma-ray detectors as a means to approach *in vivo* elemental concentrations which are important in medical diagnostics as distinctive markers of the development and progression of a variety of diseases.

The sensitivity to elements such as iron offered by AP-gated PGNA lends itself to potential applications in material characterization in homeland security and most intriguingly, to noninvasive tissue analysis where elemental disease signatures may be defined and explored as a means to novel diagnostic and interventional pathways. Incorporation of associated particle imaging transducers and electronics in forthcoming sealed tube neutron generator designs will not only allow for the experimental determination of elemental detection limits on a case-by-case basis but the capability to spatially orient quantified elemental distributions in three dimensions. Though preliminary, the results of the research contributing to this chapter indicate the efficacy of AP collimation with regard to increasing SNR and provide an important basis for refining future PGNA systems.

As introduced previously, prompt-gamma neutron activation analysis (PGNA) is an analytical technique in which an object or target volume is interrogated with neutrons which incite nuclear excitations; subsequently, the excited nuclei de-excite by emitting quantized gamma-rays which may be used to characterize the elemental composition of the assayed material. The timescale of gamma-ray emission following nuclear excitation ranges from a fraction of a second (i.e. essentially instantaneous) to perhaps minutes in the case of some short-lived activation products [232, 233], which is why the gamma-rays are defined as prompt. This differs from traditional (i.e. delayed-gamma) neutron activation analysis (NAA) in that gamma-ray

spectroscopy is performed in the presence of the neutron source (i.e. online counting), and there is no period of decay between irradiation and sample counting with which to preferentially select elements of interest based on half-life. Correspondingly, PGNAA presents unique challenges with regard to experimental setup and the placement of moderation and shielding materials – striking a balance between the desired neutron energy spectrum, the neutron fluence rate at the target material, the gamma-ray count rate at the detector(s), the attenuation of sought after de-excitation gamma-rays, and in the case of *in vivo* studies, dose rates at the target and neighboring tissues as well as to the surroundings [234].

A particular type of PGNAA is known as fast neutron inelastic scatter analysis (FNISA), which specifies the use of fast (1-20 MeV) neutrons and that the gamma-rays of interest are the products of the de-excitation of nuclei which have undergone inelastic scattering with a source neutron [235]. FNISA has been employed for decades in applications ranging from naval reconnaissance to gauging human body composition and quantifying heavy metal toxicity [4, 13, 16, 142]. However, elemental sensitivities achievable using PGNAA have lagged behind those of DGNAA due to the necessity of online gamma spectroscopy and the associated technological restrictions pertaining to the energy resolution of gamma-ray counting systems in a high count rate and high background environment – not only with many competing gamma-ray signatures but with fast neutrons as additional spectroscopic confounders [164]. This operational gap has inspired research into methodologies by which source neutrons may be selectively tracked, thereby reducing the impacts of non-tagged neutrons and their incited emissions on the photon spectrum. This type of electronic collimation may be achieved for a point source of neutrons, eliminating the prolonged scan times and intensive data processing required for raster scanning or neutron stimulated emission computed tomography [9, 176, 236].

One method by which elemental sensitivity may be increased in a PGNAA system is integration of the associated particle (AP) technique, which may be employed in systems utilizing sealed tube neutron generators given the fundamental properties of the fusion reaction of interest. For example, in a DD generator, the target fusion reaction is ${}^2\text{H}(d,n){}^3\text{He}$, where the 2.5 MeV neutron and accompanying helium-3 ion are the products. Because the reaction may be taken to occur at rest, the neutrons and helium-3 ions can be considered to be associated particles because they are emitted at approximately 180° from one another at static speeds – to conserve momentum. Therefore, if the direction of the helium-3 ion is known, then the path of travel of the neutron can

be inferred. This is the crux of associated particle collimation – that by spatially resolving associated ions (i.e. tagging particular DD neutrons) and initiating a time gate after each detected event (similar to that in coincident gamma-ray counting in positron emission tomographic (PET) imaging), the tagged neutron-induced gamma-rays from target nuclei in the interrogated sample may be discerned, while discriminating against gamma-rays which originate outside the target volume or which are of no spectroscopic interest. Furthermore, by collecting time-of-flight information from within the predetermined temporal interval, the depth at which the neutron incites the emission of a prompt gamma-ray from inside the interrogated volume may be calculated given that the neutron's path of travel is known – a vector between the point of associated particle detection and the neutron source spot. The AP technique is therefore three-dimensional and may be used for volumetric imaging of trace elemental concentrations. A more comprehensive description as well as a schematic of the AP technique are included in chapters 1 and 2 – particularly pertaining to the feasibility of *in vivo* associated particle neutron elemental imaging (APNEI) with regard to quantifying and appropriating elemental signatures in diseases such as cancer [10]. The investigators expounded upon the achievable 3D spatial resolution of a DD-based APNEI system in chapter 3, which examined variables such as neutron beam spot diameter, ion detector pixel size, and detector timing capabilities [11].

Building upon these previous studies, this chapter progresses to experimental PGNAAs application supplemented by MC simulations as a basis for spectral validation as well as for subsequently modelling the AP collimation technique and approximating the increase in diagnostic yield for iron. As in the authors' previous studies, iron was chosen as the target element because its homeostasis is known to be affected in a number of neurological diseases, liver disorders, and solid cancers [213, 219, 237], and its inelastic scatter cross section to 2.5 MeV DD neutrons is relatively high and dominated by a single spectral line for ease of simulation and data analysis [10, 190]. FNISA is the brand of PGNAAs employed because it is particularly relevant when considering the associated particle technique as applied to a DD-based analytical system. Not only is fast neutron inelastic scattering with Fe-56 the target nuclear interaction, but the fast neutron should ideally be a source neutron having undergone no previous interactions; otherwise, as in DGNAAs, spatial information is lost and electronic collimation is impossible. This necessitates the use of online spectroscopy and coincident detector timing protocols, hallmarks of the AP collimation methodology.

This chapter is composed primarily of material included in a proposed (i.e. not accepted as of this writing) publication in the journal of *Nuclear Instruments & Methods in Physics Research Section A: Accelerators, Spectrometers, Detectors and Associated Equipment* entitled “Improving the Sensitivity of Fast Neutron Inelastic Scatter Analysis to Iron Using Associated Particle Collimation” [238], which was co-authored by Dr. Linda Nie. As for content composing the previous chapters, the right to re-use of the publication (other than in journal articles) – in whole or in part – was retained by the author in the Elsevier Copyright Transfer Agreement.

In short, in the study presented in this chapter, an FNISA system was used to approximate the sensitivity to elemental iron of a PGNAA setup which utilized a 2” x 2” sodium iodide detector and Canberra multi-channel analyzer (MCA) – a system which produced photon spectra that were not enhanced by using the associated particle technique. The resulting experimental spectrum was then compared to MCNP spectral outputs for a geometrically matching FNISA apparatus as a basis for validating findings and for extrapolating to AP-collimated signal enhancement and background discrimination. Therefore, the overarching objective of this study was to compare experimental and simulated prompt photon spectra and to ultimately quantify the expected increase in SNR and iron sensitivity as a result of associated particle temporal collimation.

4.2 Materials and Methods

4.2.1 Fast Neutron Inelastic Scatter Analysis

The FNISA system employed in this chapter was similar to many PGNAA systems employed in the literature in order to form a broadly applicable baseline with which to examine iron sensitivity using only geometrical biasing and physical shielding. The components of the system were a DD-based neutron generator (i.e. Model DD-110M by Adelphi Technology, Inc.), a Bicon 2MW2/2 sodium iodide detector with an optically-coupled Model 2007 Canberra photomultiplier tube (including tube base pre-amplifier), and finally, BNC connection of the NaI detector assembly to a Canberra DSA-1000 with subsequent connection to a laptop – for relatively mobile and convenient digital spectrum analysis. The experimental apparatus also included large volumes of high-density polyethylene (HDPE) to mitigate neutron dose to the NaI detector as well as the surroundings in addition to some 0.125” lead sheeting and 2”x4”x8” lead bricks to attenuate x-rays emitted during operation of the neutron generator and to directionally orient the NaI detector

to gamma-rays emitted from the target volume of iron, thereby reducing background counts to the extent practicable.

4.2.1.1 Adelphi DD Neutron Generator

The Adelphi DD-110M neutron generator produces mono-energetic 2.45 MeV neutrons with approximately isotropic emission. The generator produces neutrons through the DD fusion reaction, which is instigated by accelerating a beam of deuterium ions onto a deuterium-loaded titanium target. The deuterium source is a cylinder of deuterium gas, the contents of which are first ionized by the device's magnetron. Over the course of the FNISA trials, the neutron generator was operated with the following parameters: 4.5 kV magnetron voltage, 75 mA magnetron current limit, 110 kV target voltage, and 40 mA target current limit. It should be noted that though magnetron voltage was set to 4.5 kV, the actual running voltage was generally around 3.8 kV. Correspondingly, although the target current limit was set to 40 mA to prevent damage to the generator in the event of an abnormal arcing event or other transient condition, the running current was usually between 33 and 35 mA. The deuterium flow rate from the cylinder to the active volume of the neutron generator was maintained at 1.80 standard cubic centimeters per minute. A secondary reaction which occurs at the target as a product of the deuterium bombardment results in the emission of electrons; these electrons are subsequently accelerated within the generator head and impinge upon aluminum at the ion source aperture producing bremsstrahlung x-rays with a maximum energy of 110 keV. For this reason, a 0.125" thick lead shroud was placed over the neutron generator to diminish photon dose rates adjacent to the system as well as to prevent x-ray contributions to the prompt gamma spectrum. It has been shown previously that such a shroud nearly completely attenuates bremsstrahlung x-rays which arise as a result of high voltage neutron generator operation [207].

4.2.1.2 Sodium Iodide Detector and Photomultiplier Tube

The gamma-ray detection component of the FNISA system was a Bicon 2MW2/2 NaI detector, the model number for which indicates a 2" height and 2" crystal diameter. As a relatively inexpensive and modestly-sized detector, the Bicon 2MW2/2 provided a realistic benchmark for application in PGNA – one that is readily achievable in most radiological instrumentation laboratories. Such a detector would normally be characterized as unsuitable for use in high count

rate applications requiring high energy resolution and effective background discrimination. Indeed, nearly all PGNAA studies in the literature predominantly utilize high-purity germanium (HPGe) detectors [9, 16, 142, 164, 205, 234], and HPGe-based systems have been the focus of the authors' previous APNEI Monte Carlo simulation studies [10, 11]. However, the 2" diameter NaI detector was selected for this study as a stepping stone toward HPGe detector application, as well as with the consideration that NaI detector(s) may yet need to be incorporated in future AP-collimated systems due to their superior timing (i.e. faster pulse processing) characteristics over HPGe detectors [9, 205, 226]. Additionally, the small NaI detector helped to emphasize SNR improvement as the result of simulated AP technique application as well as provided low-risk neutron fluence rate, activation, and dosimetry data at the spectroscopic focal point such that a HPGe detector may be confidently employed in a follow-up study considering its much higher cost, complexity, and potential for neutron damage [143].

The Canberra Model 2007 photomultiplier tube (PMT) coupled to the NaI detector was operated at a high voltage of 850 volts, providing consistent charge multiplication and a calibrated energy range of approximately 3 MeV across 2,500 channels upon spectral analysis using the DSA-1000. The detector, pre-amplifier, and PMT assembly was calibrated using a liquid multi-nuclide standard source (i.e. Eckert and Ziegler Isotope Products, Inc. Catalog No. 7500) containing Cs-137 and Co-60. In general, the highest energy gamma-ray of interest was 2.2 MeV, the prompt photon emission resulting from thermal neutron capture by a hydrogen nucleus, which is synonymous with PGNAA as well as neutron dosimetry. It turned out that the calibrated 3 MeV upper energy boundary corresponded with the stated capability of the Bicron 2MW2/2 detector, which has a listed effective energy range of 15 keV – 3 MeV [239]. The other operating parameters of the NaI detector, PMT, and DSA-1000 – including coarse gain, fine gain, rise time, flat top, and fast discriminator – were left unchanged from the default values provided by the Canberra DSA system for a NaI scintillation detector. The default settings provided good sensitivity and energy resolution upon calibration using the multi-nuclide standard source as well as fundamental applicability to nonspecific NaI counting applications for comparative evaluation. However, a digital oscilloscope included in the DSA-1000 software package was used to adjust the pole/zero setting to achieve actionable performance of the spectroscopy system at high count rates.

4.2.1.3 Supporting Apparatus and Operating Protocol

Oriented around the detector assembly and neutron generator were HDPE and lead in order to physically collimate – to a limited extent – the neutrons and gamma-rays which would contribute to noise in the photon spectrum. A cutaway schematic of the basic layout is shown in Figure 4.1 with corresponding photos in Figures 4.2 and 4.3. Not only was it important to manage the photon contributions to the spectrum by using lead bricks, but it was necessary to moderate the neutron fluence rate at the detector to prevent the activation of sodium and iodine nuclei in the crystal. Early iterations of the FNISA system yielded spectra which were not useable due to the ingrowth of short-lived activation products which obscured all other spectral features; without sufficient HDPE between the neutron source and detector, the NaI crystal produced contact dose rates on the order of hundreds of micro-rem after only a few minutes of neutron exposure as a result of activation product decay. The predominant isotopes of concern were I-128 and Na-24 with half-lives of 25 minutes and 15 hours, respectively, where I-128 decay can quickly dominate the low end of the energy spectrum while Na-24 decay can obscure the higher energy ranges in NaI detectors used in PGNAA applications [240]. In the final experimental setup, 8” of HDPE was placed in between the NaI detector and iron-bearing sample materials – with more HDPE placed along the hypotenuse between the detector and neutron generator head. Additionally, a combination of 2”x4”x8” lead bricks and 0.125” lead sheeting was used to surround the NaI detector to attenuate gamma-rays not originating from the direction of the target iron.

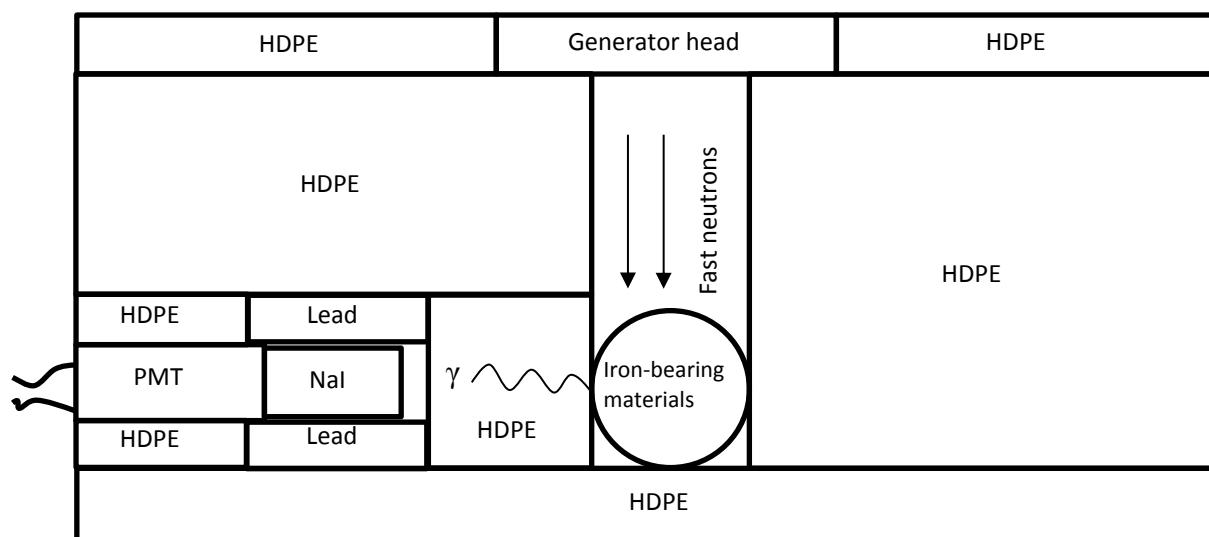


Figure 4.1 Schematic of FNISA System – not to scale

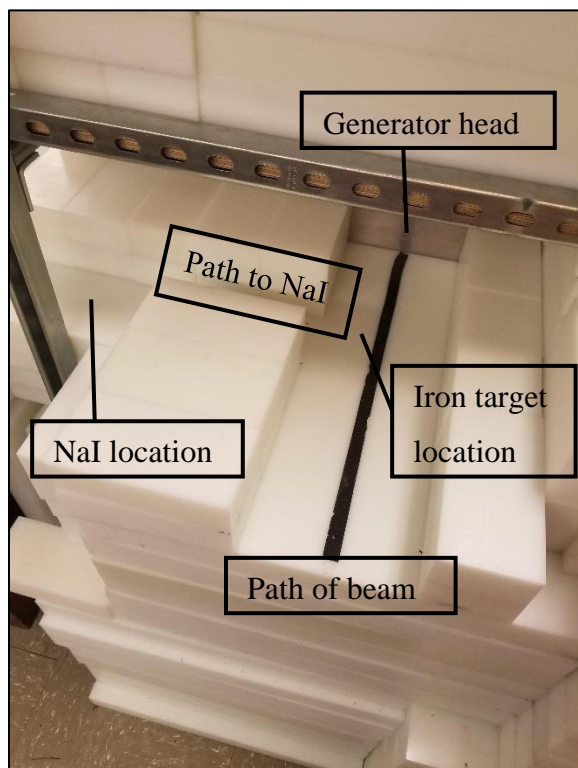


Figure 4.2 Incomplete shielding arrangement of FNISA system to visualize both the neutron beam channel and the path that iron inelastic scatter gamma-rays travel to the NaI detector. Although the intervening HDPE has been removed for this purpose of this photo, each HDPE brick is 8” in length – the dimension which was chosen to provide neutron protection of the NaI detector (i.e. the distance between the interrogated iron materials and NaI crystal). Note that the DD neutrons are emitted essentially isotropically, though with a slight bias in the forward direction (i.e. the beam path). The black piece of tape marks the centerline of the neutron source spot within the generator head.

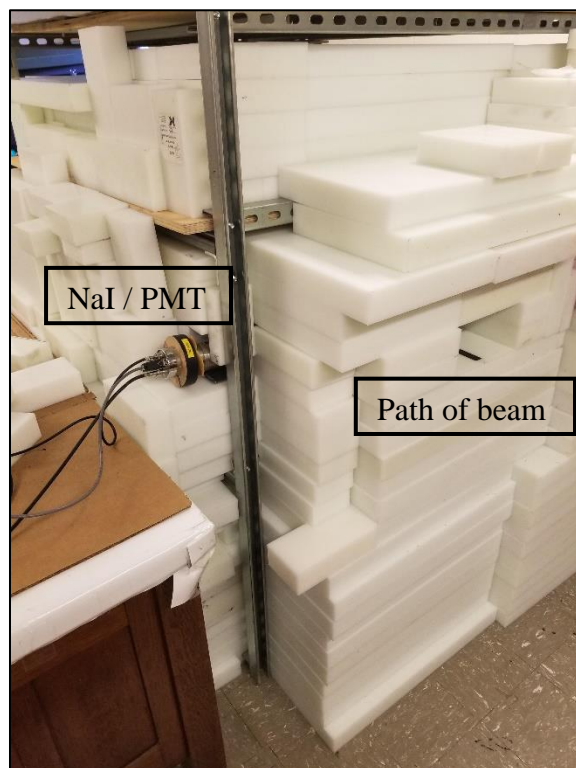


Figure 4.3 Complete shielding arrangement of the FNISA system with only the HDPE at the end of the beam path removed for spatial reference. The black tape is again visible in the photo – indicative of the centerline of the generator head. Not pictured are the lead bricks and sheeting which surround the NaI crystal within the HDPE arrangement. The detector assembly is necessarily free of lead at the front end to allow for detection of the target iron inelastic scatter gamma-rays and at the rear for running the high voltage and signal connections.

With the HDPE and lead shielding in place, the inelastic scatter interaction of interest was $\text{Fe-56} + n \rightarrow \text{Fe-56}^* + n' \rightarrow \gamma$, where the promptly emitted gamma-ray has a characteristic energy of 846.8 keV. Because a uniform iron block of sufficient size was not available, an assortment of asymmetrical iron objects were combined into a single rigid volume such that successive irradiations were geometry independent, at least as far as the interrogated object. The iron-containing volume was iteratively increased in mass and then held constant over the course of the project in order to find the optimized FNISA setup and operational LLD for iron; the final object consisted of cast iron and 18/0 stainless steel, with a total iron mass of 3.45 kg. The mass

of iron interrogated needed to be relatively high to offset the small size of the NaI detector, the system's dead time at very high count rates, and the attenuation of the 846.8 keV gamma-rays through the 8" of HDPE, which is estimated to have diminished the intensity of the iron inelastic scatter gamma-ray signal by a factor of 5.

A benefit of FNISA is that the irradiation time and counting time does not need to be prolonged in order to allow for the buildup and subsequent counting of activation products; decay time is also irrelevant. Because the Fe-56 nuclei emit prompt inelastic scatter gamma-rays and because the counting process is performed during irradiation, counting time may be relegated to a matter of minutes provided the associated counting statistics are strong and the sensitivity of the system to the elements of interest is adequate. This is particularly important for *in vivo* applications where neutron and gamma-ray doses are of concern [165]. Therefore, a 5-minute irradiation protocol was utilized in the study contributing to this chapter as it provided adequate SNR for resolving the expected characteristic spectral peaks. Correspondingly, the NaI detector was set to automatically collect data only during the period of neutron irradiation. The automation and gamma spectroscopy were performed using the Canberra Genie 2000 Gamma Analysis Software. The aforementioned Eckert & Ziegler Cs-137/Co-60 source was intermittently placed within the lead shielding around the NaI crystal in order to provide reference peaks on the photon spectrum. A gamma/neutron electronic pocket dosimeter (i.e. NRF31, Fuji Electric Co.) was also intermittently placed at the position of the NaI crystal or in the irradiation cave to quantitate the consistency of the neutron and photon emissions of the FNISA system during operation. It is important to note that although several FNISA system layouts were iteratively tested, only the final, optimized apparatus is discussed in this chapter.

4.2.2 Monte Carlo Simulations

Scientists at Los Alamos National Laboratory developed and continue to contribute to the improvement and validation of the Monte Carlo Neutral Particle (MCNP) radiation transport code. The code is well suited to PGNAAs studies as it may be used to simulate DD neutron emission and nuclear interactions which result in the production of secondary radiations. Congruently, a realistic detector volume (i.e. NaI detector) may be included in the simulated model to approximate spectroscopic capabilities achievable in the laboratory. The authors chose to utilize MCNP (i.e. version MCNPX) in this study given the breadth of experience with MCNP validation of NAA

applications in their lab group as well as to directly build on their previous APNEI simulation studies [10, 11, 165, 241]. The ENDF 7 continuous energy nuclear cross section library formed the probabilistic basis for the neutron interactions which took place over the course of each simulation [242].

4.2.2.1 FNISA Monte Carlo Model

Parallel with experimental FNISA application regarding the detection of iron, a model of the PGNAA apparatus was defined in MCNP in order that the real and simulated gamma-ray spectra could be compared. It was important to establish some basis of similarity between the uncollimated spectra to validate that the ultimate inclusion of associated particle collimation within the simulation would yield results analogous to a true NaI-based FNISA system. Regardless, some aspects of the MCNP model were simplified, such as the exclusion of the PMT and associated electronics, the simplified geometry of the NaI crystal (i.e. without encapsulation and perfectly cylindrical), the definition of the neutron source as symmetrically isotropic and dimensionless, and the designation of the interrogated object as a 3.45 kg rectangular prism of pure iron as opposed to a heterogeneous collection of cast iron and stainless steel objects. Previous studies have found that such streamlined assumptions negligibly affect the overall simulation results, particularly regarding the determination of general elemental response. The neutron source spot dimensions and emission characteristics would play a greater role in relegating projective resolution in true associated particle imaging of elemental distributions [9, 11].

Longitudinal and transverse cross sections of the MCNP model are shown in Figures 4.4 and 4.5, respectively. The 2" x 2" NaI detector – a cylindrical volume of 103 cm³ – was positioned about 10" from the 3.45 kg iron block (i.e. 8" of HDPE and a small air gap as in the experimental setup), and the interrogated iron target was placed 8" from the neutron generator head. For reference, the iron block had a volume of 438 cm³ with dimensions of approximately 3.15" x 3.15" x 2.7" and was positioned flush with the intervening HDPE within the irradiation cave. The neutron generator – including the majority of its internal components, the volumes of HDPE and lead, and the supporting apparatus were modeled similarly to the final iteration of the FNISA experiment.

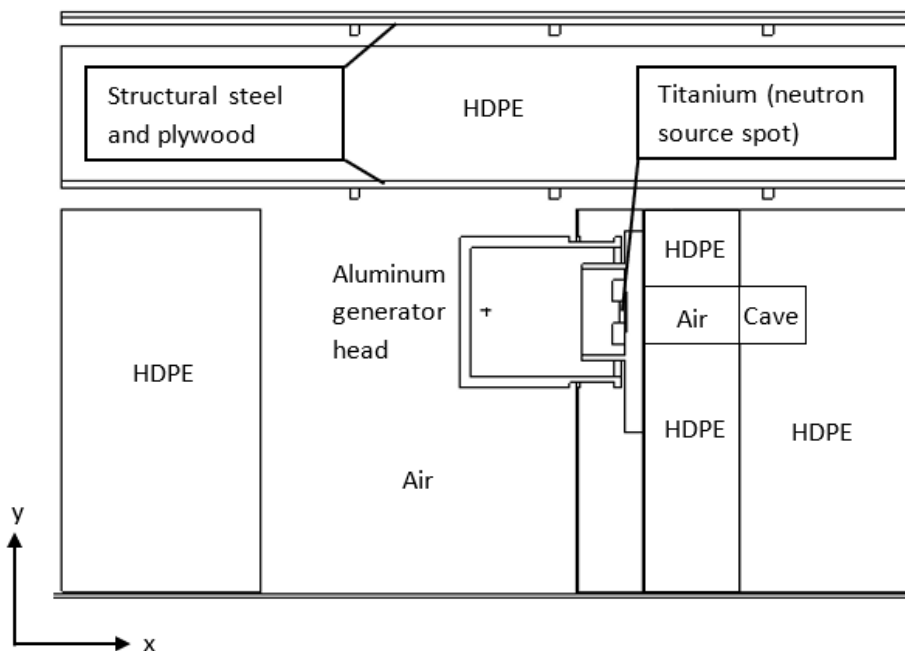


Figure 4.4 Longitudinal cross section (side view) of the FNISA system as defined in MCNP. For the purposes of the simulation, the neutron generator head and its internal structure were defined, while the supporting aluminum and electronics were not as they were not likely to significantly impact the MCNP output. The majority of the internal apparatus of the FNISA system is open space and was therefore treated as air.

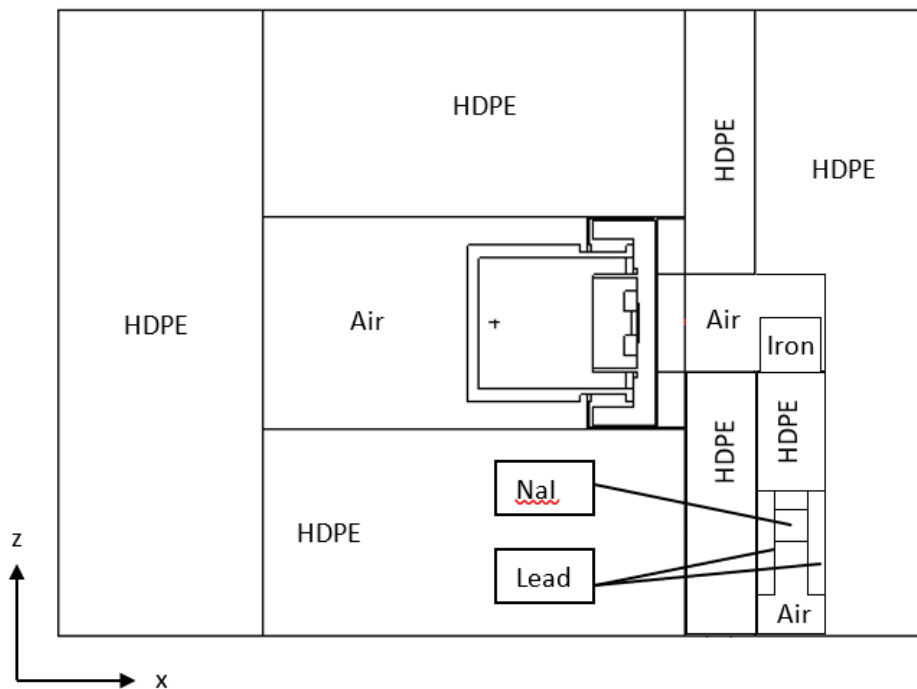


Figure 4.5 Transverse cross section (top-down view) of the FNISA system as defined in MCNP. Note the small relative size of the NaI detector and the absence of the PMT and electrical components.

4.2.2.2 Gaussian Energy Broadening of Gamma Spectra

Though fundamental, the model illustrated in Figures 4.4 and 4.5 very closely approximated the geometries and arrangement of the FNISA setup. This was evident upon examining the f8 pulse height tally for the NaI detector cell in MCNP, which very nearly matched the experimental spectrum after multiplying each number of counts per channel by a constant in order to reconcile the total number of neutron histories run in the simulation (i.e. 2E8) with the 5 minute FNISA runtime, 1E9 isotropic flux of the actual DD generator, and the NaI detector dead time recorded by the DSA-1000 as a result of online high count rate operation. The MCNP f8 pulse height tally served as a hypothetical multi-channel analyzer, providing counts per channel and thereby generating an energy dependent histogram of photon counts both across the defined energy range and within the selected energy intervals. Although 1 keV energy intervals were defined for the f8 tally – which would be more typical of state-of-the-art HPGe detector resolution than NaI detector resolution – the Gaussian Energy Broadening (GEB) function was used to modify the f8 tally in order to replicate the inherent limitations of the 2” NaI detector employed in the FNISA experiments. Background on the use and efficacy of the GEB function in MCNP is broad [243-245], suffice it to say that individual detector coefficients may be determined to satisfy the following nonlinear function (Eq. 4.1) for the full width at half maximum (FWHM) of the physical detector being modeled:

$$FWHM = a + b\sqrt{E + cE^2} \quad \text{Eq. 4.1}$$

where E is the energy of the radiation, c is a constant, and a and b are in terms of MeV and MeV^{1/2}, respectively. By including the GEB modifier as part of the f8 tally definition, the energy actually scored for a particular gamma-ray registered within the NaI volume in MCNP was sampled from a Gaussian distribution with a realistic, energy-dependent FWHM for the true NaI detector in the given FNISA system. In this way, more accurately shaped spectra were obtained for validation purposes.

The GEB function in MCNP requires input of approximate values for *a*, *b*, and *c* to complete the aforementioned FWHM function (Eq. 4.1). Examples exist in the literature of determination of the values for as many as 15 spectral peaks across an energy range of greater than 4 MeV [244];

however, for the purposes of this study, consideration of only the peaks from Cs-137 and Co-60 (from the multi-nuclide source) was considered sufficient to approximate the three coefficients for defining the GEB modifier such that the MCNP f8 pulse height tally would more directly reflect the energy resolution of the 2" NaI detector used in the FNISA experiments. The FWHM for each of the peaks of interest is included in Table 4.1, where the NaI detector was used to take a 5-minute measurement of the multi-nuclide source in the absence of neutron irradiation. Then, by using the method of least squares, the contribution of each coefficient to Eq. 4.1 was calculated. Correspondingly, the *a*, *b*, and *c* values entered into the MCNP GEB function were -0.01, 0.076, and -0.105, respectively. These values correspond closely with those obtained by another lab group for a 3" diameter NaI detector and the use of Cs-137 and Co-60 sources [245]. Also indicated in Table 4.1 are the calculated FWHM for the reference peaks using the GEB coefficients and their corresponding relative errors (RE). Good agreement was achieved, which meant that a strong fit between the experimental and simulated spectra – particularly with regard to energy resolution – was expected.

Table 4.1 – Experimental vs simulation full-width at half maxima

Nuclide	Energy (MeV)	NaI FWHM (MeV)	MCNP FWHM (MeV)	RE (%)
Cs-137	0.662	0.049	0.0496	1.22
Co-60	1.17	0.068	0.0670	1.47
Co-60	1.33	0.073	0.0713	2.33

4.2.2.3 Associated Particle Collimation

Finally, with both the overall FNISA system geometry and NaI detector capabilities defined in MCNP, realistic gamma-ray spectra could be produced. Note that the contribution of the Eckert & Ziegler multi-nuclide source to the photon spectrum was also modeled in MCNP and iteratively superimposed onto the FNISA simulation f8 tally, which served to provide a direct comparison to the experimental spectra as well as to verify that the prominent Cs-137 and Co-60 photoelectric peaks were consistent in terms of amplitude and resolution. These peaks provided valuable reference points. Then, once the final FNISA Monte Carlo spectrum was validated against the experimental spectrum, all that remained was to institute associated particle collimation within

MCNP in order to quantitate the projected increase in SNR for the interrogated volume of iron. This is the aspect of APNEI which allows for signal discrimination by employing coincident counting within a predefined timing window. Because the employed FNISA system did not contain the components necessary for APNEI (i.e. a specialized sealed tube neutron generator with an integrated fiber optic, pixelated imaging plate and associated ultra-fast digital processing circuitry) and because imaging was not a primary objective of this study, a simplified spatial-temporal filtering protocol was employed in MCNP to simulate the spectroscopic improvement that would occur as the result of associated particle collimation.

The process for simulating the AP-collimated spectra was relatively straightforward. Building upon the results of the authors' previous work [11], neutron kill zones were incorporated into the simulation in order to mimic the associated particle collimation process which ideally tags only neutron histories which are relevant to the analytical procedure at hand. In other words, regions were defined in MCNP to have zero neutron importance (i.e. kill zones) such that neutron histories entering those regions would be terminated and thus have no further opportunity to contribute to the f8 pulse height tally. By selectively surrounding the DD neutron point source with these kill zones, a spatial aperture was created which corresponded to the dimensions of a hypothetical imaging plate (i.e. He-3 ion detector). In this way, the projective dimension of the neutron source was collimated as in AP imaging, where only those neutrons which have an associated particle that is detected at the pixelated imaging transducer are tracked. As introduced in the authors' previous paper (summarized in Chapter 3), the supposed pixelated imaging plate was assumed to be 2 cm from the neutron source spot with dimensions of 1.25 cm per side [11]. The projective spatial aperture (i.e. opening through the neutron kill zones) was then located opposite the imaging plate – 8 cm from the neutron source spot. It follows from similar triangles that because the aperture was located 4 times further from the neutron source than the theoretical imaging plate, its opening was 4 times as large – 5 cm per side. The projective aperture collimated the DD neutron source emissions in 2 dimensions, approximating neutrons tagged as the result of He-3 ions impacting the imaging plate. The third dimension of collimation was accounted for by including a final neutron kill zone beyond the iron target, such that neutrons which generated gamma-rays after passing through the region of interest would be ignored. This was analogous to an AP timing filter, where gamma-rays which are detected by the system outside of the predetermined temporal interval are perceived to have originated outside of the region of interest

and therefore do not contribute to the photon spectrum. Because the velocity of the DD neutrons is known and because the depth resolution of a NaI detector-based APNEI system is expected to be better than 3 cm [11], it was straightforward to consider timing resolution as a function of spatial certainty. The neutron kill zones therefore realistically simulated the associated particle collimation process in 3D. A diagram of the collimation process in MCNP is provided in Figure 4.6, illustrating the advantageous noise reduction possible in AP-based neutron tagging.

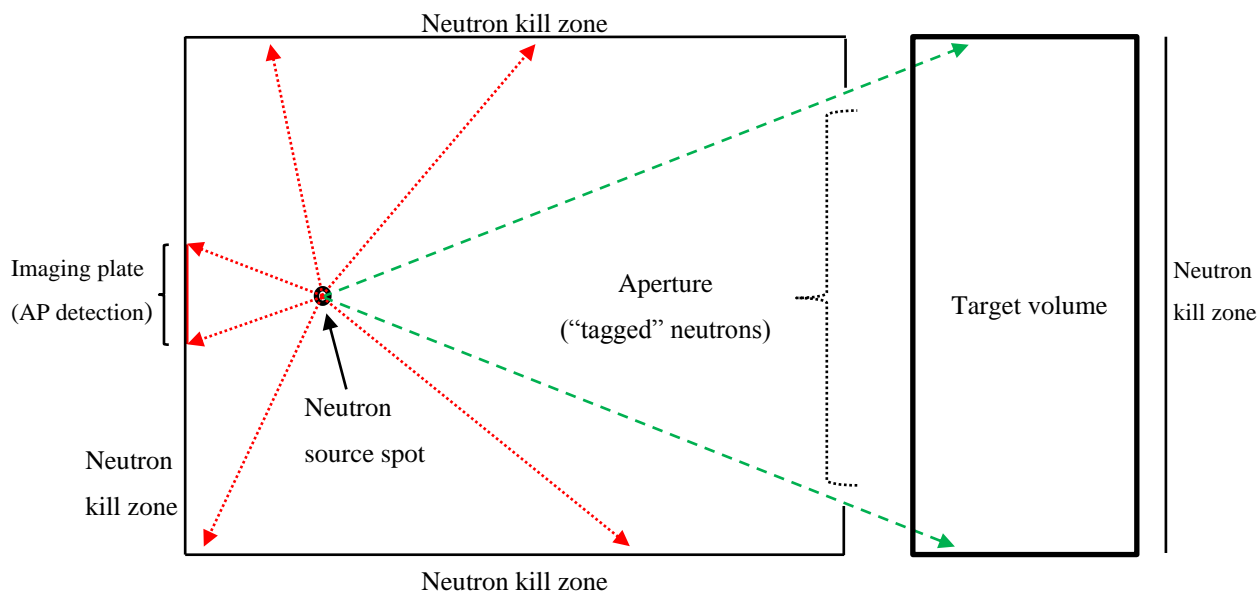


Figure 4.6 Diagram of the spatial collimation employed in MCNP using neutron kill zones. The aperture provides collimation in the projective dimensions while the rightmost neutron kill zone is analogous to the timing component of an AP-based FNISA system – limiting contributions to the photon spectrum from nuclei beyond the region of interest. Note that these physical parameters in the MC model are surrogates for the true AP collimation process, which utilizes electronic discrimination through spatiotemporal filtering. The dashed lines represent tagged (i.e. accepted) neutron histories which have the potential to interact within the target volume. The dotted lines represent neutron histories which have been terminated (i.e. killed) and thus have no further opportunity to contribute to the photon spectrum.

As before, the f8 pulse height tally in tandem with the GEB modifier was used in MCNP to view the photon energy spectrum resolved by the NaI detector, now preferentially enhanced in 846.8 keV iron inelastic scatter gamma-rays due to the noise reduction provided by the neutron tagging process illustrated in Figure 4.6. Because the multi-nuclide Cs-137 and Co-60 peaks were previously added iteratively to the MC spectrum and therefore lay outside of the modeled collimation process, they were not included in the final spectrum. The exclusion of the reference peaks also facilitated comparison of the iron inelastic scatter gamma-ray peak between the experimental and simulated spectra, the true region of interest.

Another benefit of the spatial filtering in MCNP was its streamlining effect on the simulation, which boosted computational statistics and improved expected runtime by a factor of 2.85. For instance, while 2E8 neutron histories were employed in the non-collimated simulations discussed previously due to computational burden, it was possible to employ 2E9 histories in the AP surrogate model. Final f8 tally contributions therefore had relative errors $< 10\%$ for the 846.8 keV energy bin of interest. This relative error was determined for the target energy bin prior to applying the GEB function as the Gaussian broadening process subsequently reduced statistical strength as the number of counts was assigned across a range of channels. However, it is expected that the simulated Gaussian peaks remained consistent with those that would be expected in the experimental spectra, particularly given the close agreement between the reference multi-nuclide peaks' range and amplitude and their consistency with expected NaI resolution from the literature [245]. For reference, each run of the non-collimated MCNP model at 2E8 neutron histories took approximately 24 hours, while each run of the AP-collimated MCNP model at 2E9 neutron histories took approximately 84 hours. The simulations were performed using two 10-core Intel Xeon-E5 processors in Purdue University's Rice supercomputer cluster.

4.3 Results

4.3.1 FNISA Surrogate Experiment

The FNISA system – with 3.45 kg of iron as the target – was operated for 5 minutes to provide an experimental photon energy spectrum. Neutron irradiation occurred for 5 minutes with concurrent, online gamma spectroscopy in the presence of the Eckert & Ziegler reference source. The spectrum is shown in Figure 4.7.

Features of the plot presented in Figure 4.7 worth noting are 1) the high noise at low energies, 2) the apparent absence of the expected 2.2 MeV prompt gamma-ray peak from the capture of thermal neutrons by hydrogen nuclei, and 3) the very slightly discernible 846.8 keV peak indicative of the presence of the iron target volume. Though the substantial amount of relatively low energy noise was perhaps the most prominent characteristic of the photon spectrum, it was an expected result given the small volume of the detector employed and the inherent limitations of the NaI crystal and PMT. The so-called noise peak is nearly universal in the literature concerning scintillation-based gamma spectroscopy and was likely the result of a combination of electrical

and physical phenomena – including low-energy rise, PMT fatigue, glass scintillation, pulse pileup, true background counts, and Compton contributions [164, 246-248]. Note that the noise peak is truncated in Figure 4.7 in order to focus on the peaks of greater spectroscopic interest.

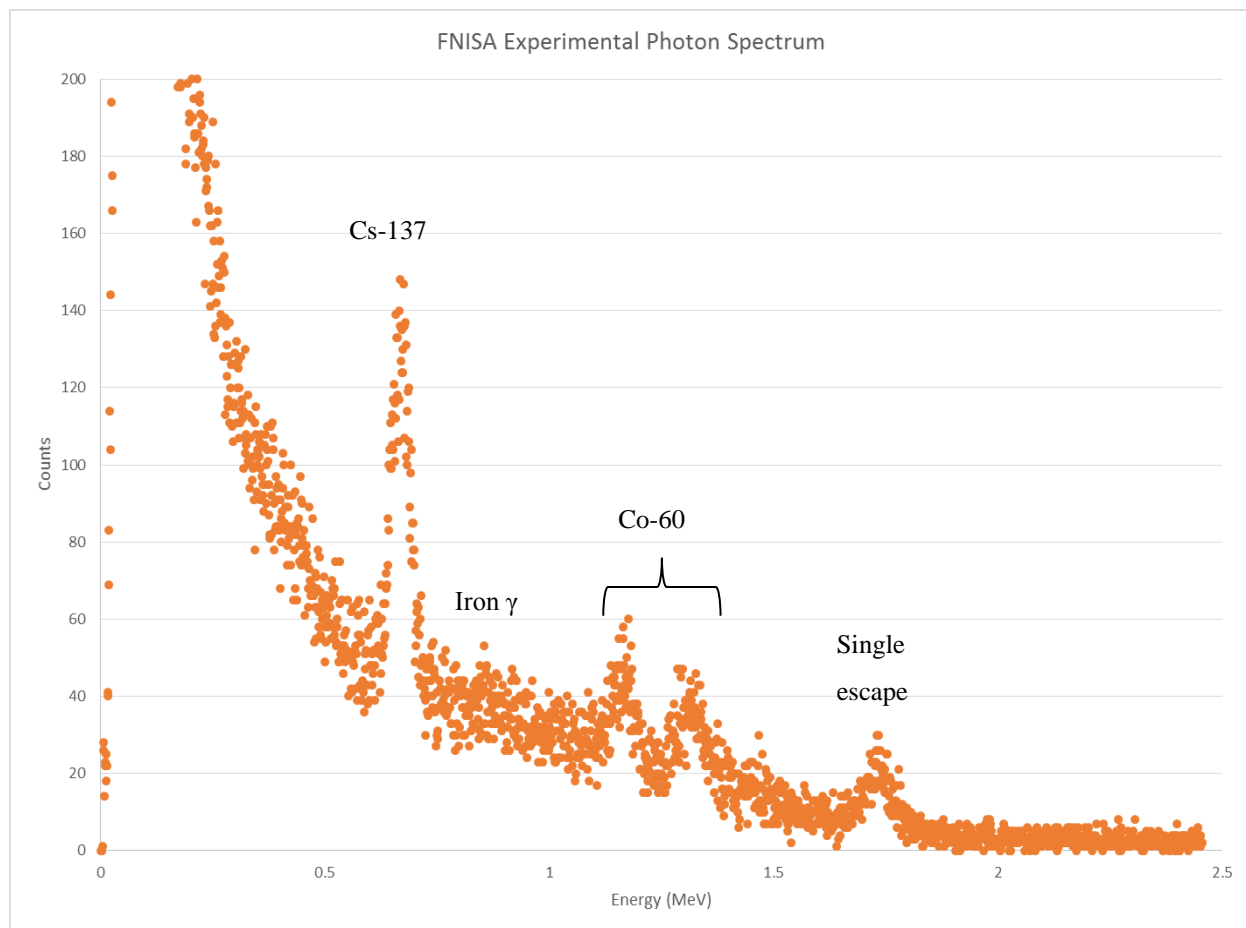


Figure 4.7 Photon spectrum from NaI-based FNISA system. Note the Cs-137 and Co-60 reference peaks from the multi-nuclide source, as well as the single escape peak from 2.2 MeV prompt gamma-rays.

An apparent anomaly within the spectrum was the absence of the 2.2 MeV prompt gamma-ray peak from the de-excitation of hydrogen nuclei, a feature which should theoretically be quite prominent given the large volumes of hydrogen-rich, high-density polyethylene positioned around the neutron generator. It is possible that the NaI detector lost some of its high energy functionality in the presence of the high flux neutron/gamma field. Indeed, the detector was tested separately using a high activity Co-60 source to verify the presence of the sum peak at approximately 2.5 MeV, and the detector was confirmed to have the capability to resolve such high energy events near the limit of its functional range. Nevertheless, the incidence of the 2.2 MeV gamma-rays

upon the detector was confirmed by the 1.7 MeV single escape peak, which was caused by a 2.2 MeV gamma-ray interacting in the detector volume via pair production, in which case one of the 0.511 MeV annihilation photons subsequently escaped the detector volume without interacting. Because photoelectric interaction probability decreases with increasing photon energy and Compton scattering produces a continuum of spectroscopic contributions, it is likely that the single escape peak became the most prominent feature of the 2.2 MeV gamma-rays – with particular emphasis given the significant dead time at high count rates and small volume of the detector system.

The peak from 846.8 keV Fe-56 prompt inelastic scatter gamma-rays was evident, though not outwardly impressive given the relatively large amount of iron present in the irradiation cave. This was as expected. In fact, that the inelastic scatter gamma-rays contributed noticeably to the photon spectrum in a NaI-based FNISA system is noteworthy, particularly considering that HPGe detectors are nearly exclusively used in PGNAAs for their superior energy resolution and background discrimination [164]. The slight peak at approximately 847 keV therefore offered compelling evidence that the employed FNISA system was well optimized with regard to physical collimation and geometry. As a step toward HPGe application and eventually AP-regulated electronic collimation, the system provided an important baseline. It is important to note that although there was some iron present in the experimental apparatus and in the surrounding environment, no prompt gamma-ray peak was present at 846.8 keV upon removal of the 3.45 kg target volume from the irradiation cave. Furthermore, the background signal over the range from 0.7 MeV to 1 MeV was approximately linear, which was beneficial when performing a simple peak fitting of the 847 keV inelastic scatter gamma-ray peak. The peak fitting process was performed using a MATLAB program developed at Purdue University which has been employed successfully in several quantitative studies utilizing radiation-producing equipment and photon spectroscopy [165, 241, 249]. Importantly, the Fe-56 inelastic scatter gamma-ray peak was quantifiable and can thus be utilized in minimum detectable concentration (MDC) calculations in future studies with more specific applications in medical diagnostic imaging or perhaps, civil defense.

As the FNISA spectrum qualitatively indicated, the 3.45 kg target volume approached the LLD of the system for iron. Nevertheless, the spectroscopic contributions from Fe-56 inelastic

scatter gamma-rays were discernibly above background and fitted successfully according to a least-squares algorithm and the following function (Eq. 4.2):

$$f(x) = A_0 e^{\frac{-(x-B_0)^2}{2\sigma^2}} + A_1 x \quad \text{Eq. 4.2}$$

where A_0 is the amplitude of the peak, B_0 is the position of the peak, σ represents the width of the peak, and A_1 is the constant which completes the linear background term. Figure 4.8 shows the FNISA spectrum in the Fe-56 prompt gamma-ray region of interest with the corresponding fitted curve. The reduced χ^2 of the iron measurement was 1.07.

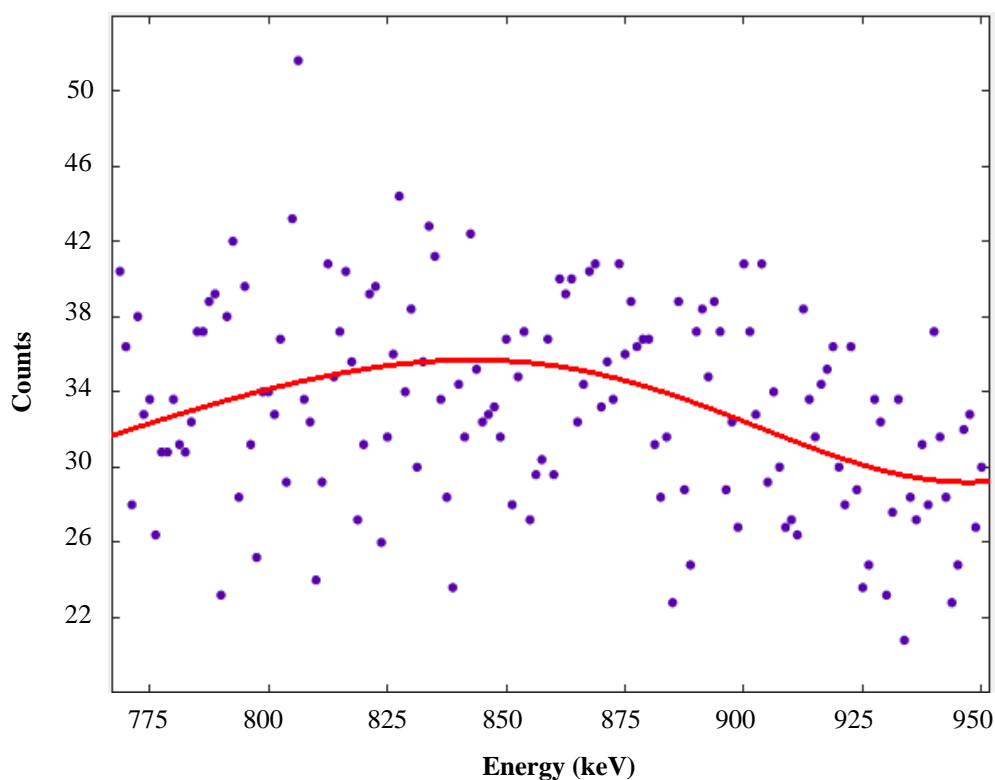


Figure 4.8 Photon spectrum from the iron inelastic scatter gamma-ray region of interest with fitted curve.

Though relatively low amplitude and broad, the fitted curve in Figure 4.8 demonstrates that the distribution of the Fe-56 prompt gamma-ray counts remained approximately Gaussian, as expected. The reason for the slightly non-zero skewness of the distribution was not immediately apparent and remains an opportunity for improvement in future PGNAA studies.

4.3.2 Spectral Validation Using Monte Carlo Simulations

With a quantifiable iron signal using the optimized FNISA system, the next step was to model the iron sensitivity and NaI detector energy resolution using MCNP in order to validate the spectral results before introducing spatiotemporal collimation to the MC input definition. Figure 4.9 illustrates the photon spectrum as derived from the MCNP f8 pulse height tally with corresponding GEB function as compared to the experimental spectrum introduced in Figure 4.7. As previously described, the MCNP spectrum was iteratively composed in order to include the Cs-137 and Co-60 reference peaks. Additionally, the entire spectrum was shifted by multiplying by a constant in order to resolve the difference between the achievable number of neutron histories in MCNP and the integrated isotropic flux of the FNISA system.

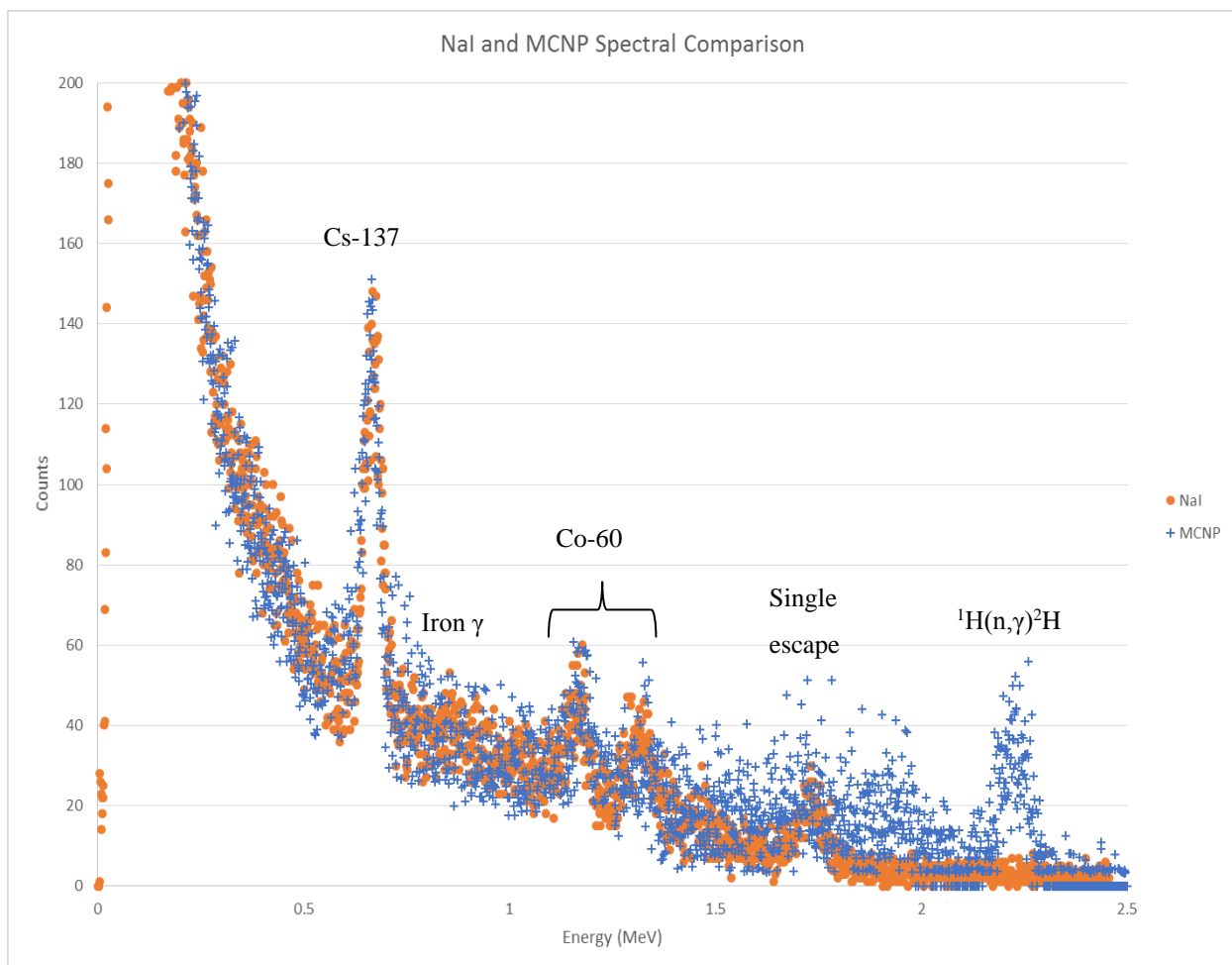


Figure 4.9 Photon spectrum from the MCNP f8 pulse height tally overlaying the experimental spectrum from the NaI-based FNISA system. Note the excellent agreement in the region < 1.5 MeV, including the reference peaks and 750-950 keV region of interest.

In general, good agreement was achieved between the experimental and simulated spectra. The prevailing discrepancy was the presence of a clearly defined 2.2 MeV photopeak in the MCNP spectrum, which was not nearly as prominent in the experimental spectrum. This was likely the result of certain MCNP idealizations such as the neutron thermalizing process and photon transport mechanisms, particularly given the large amount of polyethylene in the simulation and correspondingly higher statistical weight given to neutron interactions with hydrogen nuclei due to the relative abundance of hydrogen in the simulated apparatus. Nevertheless, the statistical analysis of aggregate bins across a majority of the simulated and experimental spectra yielded an overall relative difference of $< 5\%$, indicative of acceptable overall agreement between the data sets. The MCNP and experimental data were not significantly different at the $p = 0.05$ level below 1.5 MeV. Taken separately, the data were much more significantly dissimilar (i.e. $p \ll 0.001$) in the upper energy ranges (i.e. > 1.5 MeV) due to biasing in MCNP toward tabulating the results of hydrogen interactions. Nevertheless, the simulated spectrum was consistent with the experimental result in the regions of the reference peaks and iron prompt gamma-ray response. The similarity of the simulated reference peaks to those obtained with the NaI detector validated the accuracy of the GEB function with regard to introducing realistic energy resolution. Furthermore, the 846.8 keV gamma-ray peak from fast neutrons inelastically scattering with Fe-56 nuclei was confirmed to be almost negligible (i.e. near the LLD). It was established upon viewing the MCNP output without Gaussian energy broadening that appreciable signal attributable to Fe-56 prompt gamma-rays was reaching the detector; however, the signal was lost in the background noise upon accounting for the NaI detector's physical energy resolution.

4.3.3 Collimated vs Un-collimated Gamma Spectra

Finally, with a solid basis of comparison between the experimental and simulation results, it was possible to confidently implement a collimation methodology in MCNP comparable to that which could be achieved using associated particle coincident event filtration. As observed in the previous simulation, the Fe-56 prompt gamma-ray signal became indistinguishable from the background noise upon incorporation of the GEB function. Similarly, the 846.8 keV peak from the NaI detector was not well defined; it would certainly have been a challenge to attempt to quantify the signal from a smaller mass of iron than the aforementioned target volume. In this sense, it was practical to consider 3.45 kg of iron to be the working LLD of the FNISA system.

However, by employing the noise-canceling effect of the associated particle technique in MCNP, it was possible to predict how the LLD might be improved due to increased SNR – even for the simple PGNAA apparatus utilized in the study contributing to this chapter.

AP collimation was modeled using spatially-defined neutron kill zones in both the projective and depth dimensions to replicate imaging plate event acceptance and timing regime discrimination, respectively. While this allowed for an increased number of neutron histories to be utilized in the simulation, there were no other changes to the MCNP input definition. The discrepancy in the number of neutron histories between non-collimated and AP-collimated MCNP photon spectra was resolved by normalizing to 2E8 histories to maintain a consistent frame of reference. Figure 4.10 shows the AP-collimated spectrum as compared to the non-collimated spectrum – both of which were simulated in MCNP using the f8 pulse height tally and identical GEB definitions. Recall that the Cs-137 and Co-60 reference peaks were not included in these models because the iterative process interfered with the AP collimation methodology. Note that as expected, the overall 846.8 keV iron inelastic scatter gamma-ray signal from each of the simulations differed by < 10%. After all, the collimation process cannot increase the absolute signal, it can only increase the relative signal by decreasing the surrounding noise (i.e. increasing SNR). This explains the similar iron prompt gamma-ray peak amplitude between the two spectra, but the AP-collimated peak is much more clearly defined due to noise reduction in adjacent energy channels.

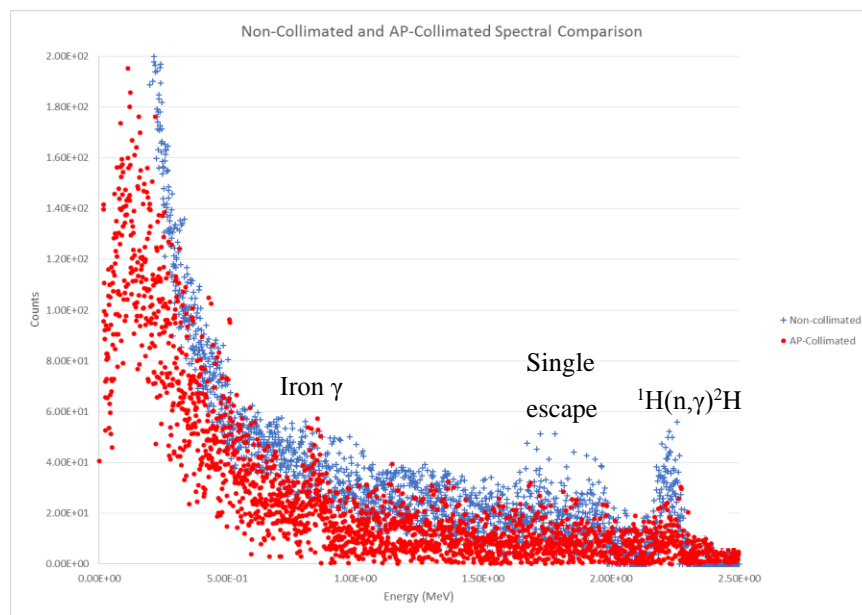


Figure 4.10 Comparison of photon spectra from MCNP. The AP-collimated spectrum is overlaying the non-collimated spectrum.

It is apparent in Figure 4.10 that noise across the entire spectrum was reduced as a result of the collimation process employed in MCNP. Notably, the low energy background peak as well as the $^1\text{H}(n,\gamma)^2\text{H}$ peak and its corresponding single escape peak were significantly reduced in amplitude relative to the non-collimated spectrum. Furthermore, the region of the 846.8 keV inelastic scatter gamma-ray from Fe-56 was made more diagnostically evident – with a well-defined peak unobscured by the nevertheless substantial, lingering background. In a quantitative sense, the SNR of the 846.8 keV iron prompt gamma-ray peak increased by $700\pm 80\%$ considering the relative errors associated with each MCNP f8 energy bin in quadrature. Figure 4.11 shows the region of interest from 0.7 MeV to 1.0 MeV for the non-collimated and AP-collimated MCNP photon spectra. It was impressive that such an increase in SNR could be achieved for the iron prompt gamma-ray peak considering the small volume of the NaI detector, its relatively poor energy resolution, its intrinsically deficient background discrimination as compared to more traditionally used HPGe detectors, and the inherent attenuation of the 846.8 keV gamma-rays through the polyethylene neutron shielding between the iron target and NaI detector. Included in Figure 4.11 is a least-squares MATLAB fitting similar to that performed in the spectrum in Figure 4.8. The fitting was applied only to the AP-collimated MCNP data as the peak was unremarkable for the non-collimated data. The reduced χ^2 of the FNISA simulation was 1.38. This was acceptable given the variability of the data and the likelihood that the error variance was underestimated.

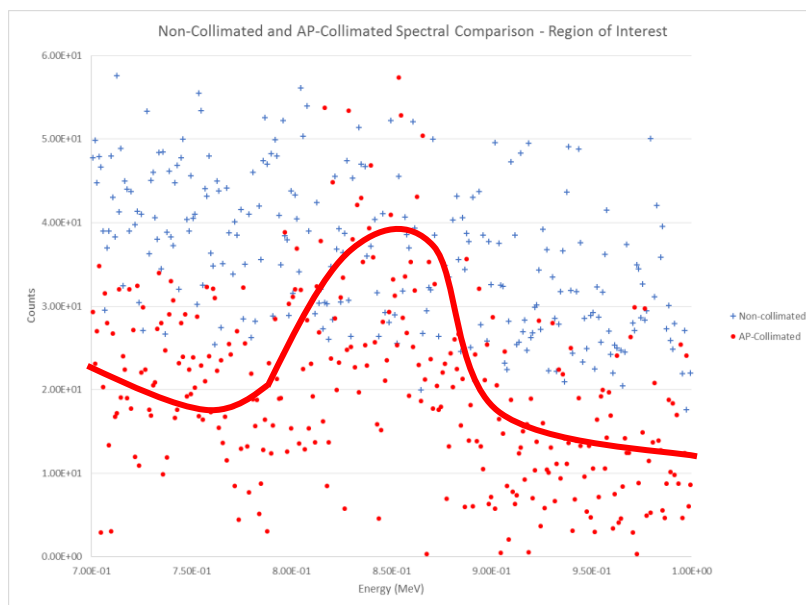


Figure 4.11 Comparison of photon spectra from MCNP in the Fe-56 inelastic scatter gamma-ray region of interest.

4.3.4 Improved Iron LLD due to Associated Particle Collimation

Next, with such a promising increase in SNR for the Fe-56 prompt gamma-ray peak upon inclusion of the AP collimation methodology in the MCNP model, it was of interest to approximate an improved LLD for the FNISA system. This was done by running the same simulation, only with half and then two-thirds of the iron target removed. In this way, a second and third set of AP-collimated data were gathered and fitted such that a theoretical calibration curve could be constructed. Due to the straightforward f8 tallied response to iron in the MCNP model, only three points were used to perform the linear regression – those obtained from 3.45 kg, 1.73 kg, and 1.15 kg masses of iron in the irradiation cave. It was assumed that subsequent simulations with varying masses of iron would produce a nearly perfectly linear (i.e. $R^2 > 0.999$) response, as was observed in one of the authors' previous studies – with the only differences owing to statistical variability and self-attenuation [10]. As before, the peak fitting was performed using the method of least squares and the basic formula given in Eq. 4.2. Indeed, the fitted curves appeared very similar to that in Figure 4.11 but with a proportionately decreased amplitude and area. The reduced χ^2 of the second and third fitted curves for the AP-collimated FNISA simulation with half and one-third of the initial target mass of iron were 1.44 and 1.51, respectively. These were consistent with the reduced chi-squared statistic of the originally simulated AP-collimated iron inelastic scatter gamma-ray signal curve. Opportunely, the majority of the MATLAB least-squares parameters were applicable for the second and third fitting procedures.

Figure 4.12 shows the MCNP-derived calibration curve from which the theoretical LLD was calculated using Equation 4.3:

$$\text{LLD} = 2 * \sigma_{0\text{kg}} \quad \text{Eq. 4.3}$$

where $\sigma_{0\text{kg}}$ is equal to the quotient of 1) the square root of the number of background (i.e. when iron was entirely absent from the irradiation cave) counts under the 846.8 keV iron inelastic scatter gamma-ray peak – the width of which was determined in each least squares fitting for a supposed irradiation of 5 minutes – and 2) the slope of the simulated calibration line in Figure 4.12. The linear regression yielded an R^2 value of 0.9998 and a corresponding LLD of 0.44 kg iron for the modeled FNISA system. As expected, the LLD was relatively high given the large amount of background noise across the region of interest. Nevertheless, relative to the presumed LLD of

both the FNISA experiment and non-collimated MCNP simulation, the LLD improved by a factor of approximately 7.8 upon incorporation of AP collimation.

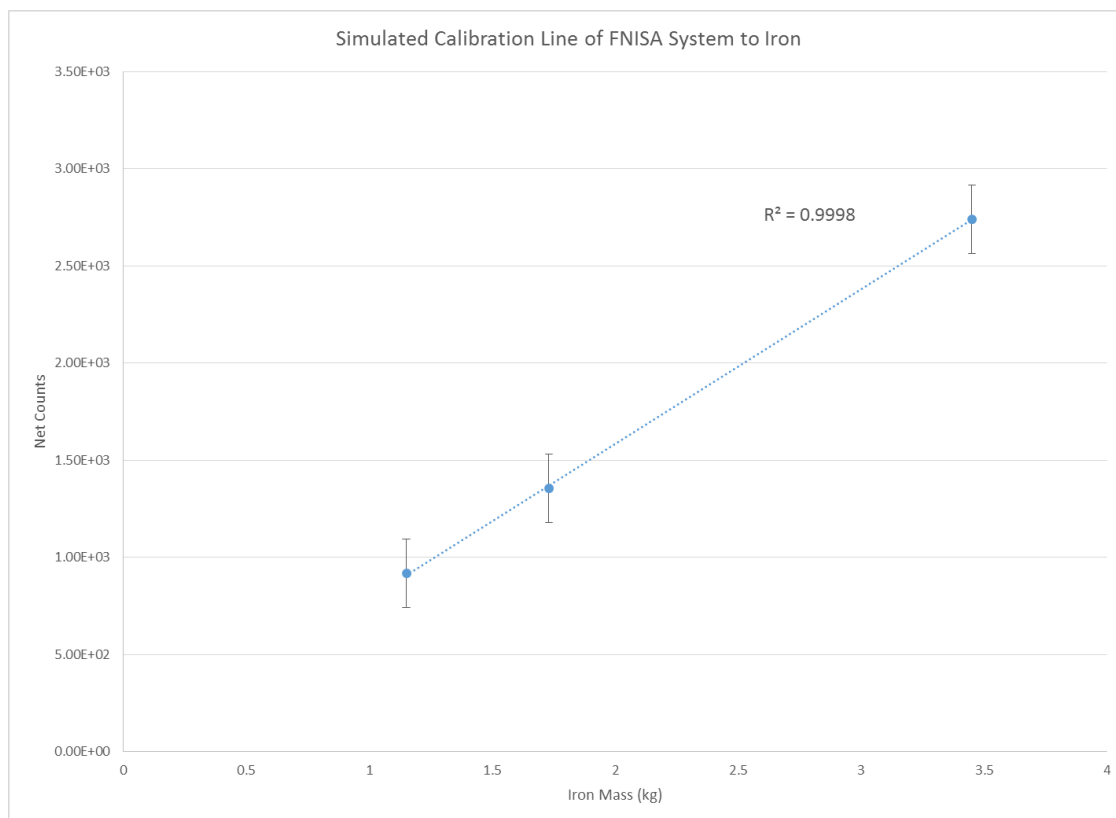


Figure 4.12 Calibration line for iron in the simulated FNISA system

4.4 Discussion

In the study contributing to this chapter, a PGNA system – specifically meant to utilize DD fast neutrons and to characterize inelastic scatter reactions from iron – was developed and optimized with the ultimate objective of comparing the experimental photon energy spectrum with that obtained from a corresponding model defined in MCNP. With real time data supporting the validity of the pulse height output from the MC simulations, the model system was then redefined to include a close approximation of the associated particle collimation process, in which the SNR of the iron inelastic scatter gamma-ray signal could be significantly improved – with parallel enhancement of the simulated LLD for Fe-56. The improvement in SNR and LLD provided by spatiotemporal collimation were certainly impressive (i.e. nearly an order of magnitude) and are reflective of realistic diagnostic gains expected from the application of the AP technique in a sealed

tube neutron generator-based FNISA system. And while the FNISA apparatus employed in this study was relatively rudimentary and utilized a small and unremarkable NaI(Tl) detector, it is an important stepping stone toward more specific elemental analysis and imaging applications which justify the use of state-of-the-art scintillators, HPGe gamma spectroscopy, and refined pulse processing and temporal filtering methods. Furthermore, the spectroscopic agreement between the system and its simulated counterpart was encouraging, laying the groundwork for confidently developing more sensitive systems, such as may be employed in medical diagnostics of diseases with elemental signatures. Although the sensitivity of the system presented in this chapter is not capable of trace elemental quantification even when AP enhanced, the goal was to establish a basic system which could be modeled precisely in MCNP as the basis for justifying further study regarding the associated particle collimation process. Furthermore, the collection of the spatial data from the imaging plate (i.e. pixelated detector) and timing regime would yield coordinates for establishing elemental density distributions in 3D, a nuance which has been explored in the authors' previous work using simulations [10, 11] and which may now be approached in the laboratory – with the promising preliminary data presented in this chapter as a starting point.

The apparatus and accompanying MC model developed in this study were for a relatively broad application or benchmark – one which can be extrapolated to currently available detector and neutron generator technologies which feasibility studies indicate would allow for *in vivo* trace elemental imaging [9-11]. However, the gamma and neutron dose rates acquired by the Fuji NRF31 electronic dosimeter (which constituted operational data not otherwise included in this chapter) were used to monitor overall consistency of the radiation fields in the irradiation cave of the FNISA system. This was to confirm system stability – given the potential for transient high voltage divergences – rather than to provide reference dose data for a perceived *in vivo* application. Such dose constraints would nevertheless certainly be a critical consideration when performing an *in vivo* study. Though not included here, the authors previously performed a simulation-based study regarding the quantification of iron concentrations in the liver using APNEI, where the equivalent dose to the liver and effective dose to the whole body for a similarly defined DD neutron generator were approximated [10]. Suffice it to say, the dose rates indicated acceptable irradiation times on the order of minutes, providing adequate information for imaging iron distributions in the liver with < 1 cm resolution.

Apart from dose considerations, it is evident from the performance of the FNISA system developed in this study that the spectral noise produced in the NaI detector in the presence of the operating DD neutron generator posed the most significant difficulty with regard to assaying the target volume of iron. Even with HDPE and lead shielding in an arrangement optimized for the preferential acquisition of signal from the relatively large Fe-56 target, the 846.8 keV iron inelastic scatter gamma-ray peak was broad and poorly defined. Indeed, the MCNP simulation of the same measurement verified that even in the somewhat idealized mechanics of the computer model, the peak-of-interest was nearly indiscernible and the SNR essentially unity. However, it was confirmed that by modifying the simulation such that the neutron generator acted as if equipped with an AP temporal collimator, the SNR and LLD for the Fe-56 scatter gamma-ray peak improved significantly. It is the authors' interest to continue to refine the experimental and simulation models by incorporating HPGe gamma spectroscopy to enhance energy resolution and background discrimination. In this effort, a large volume n-type detector would be ideal as it would be far more resistant to neutron damage than a traditional p-type detector due to the typical nature of neutron-induced defects and the inverse relationship of electron-hole majority charge carriers between the two semiconductor detector types [143]. Furthermore, it is expected that a larger detector or array of smaller detectors would provide greater SNR. According to the following definition of SNR (Eq. 4.4), the SNR would increase by a factor of 1.4 each time the detector volume in a fixed geometry is doubled:

$$SNR = \frac{2 S}{\sqrt{2} \sigma} \quad \text{Eq. 4.4}$$

where S is the average signal and σ is the standard deviation of the noise. There is certainly much opportunity for improvement in this aspect of the presented FNISA system. A greater overall detector volume would also allow for better counting statistics and peak fitting – both in the experimental apparatus and in MCNP simulations. It is possible that the recurring slight asymmetry of the target peak was the result of poor solid angle coverage, a detail which may be rectified in future studies. Furthermore, the inclusion of at least one n-type HPGe detector along with an arrangement of NaI detectors would offer a great deal of flexibility in system design, where each detector could serve a more precisely defined purpose, such as overall event timing, gamma spectroscopy, or background monitoring. This would permit a variety of setups where the inherent

weaknesses of PGNAAs like detector activation, pulse pileup, and target gamma-ray attenuation could be mitigated – as suited to the task at hand. Indeed, the NaI crystal activation that occurred in early iterations of the FNISA system in this study may be used to quantitate the neutron fluence rate at the detector, thereby providing a means to calculate – at that location – the time that an n-type HPGe detector may be subjected to the neutron field before exhibiting degradation in energy resolution as the result of induced damage.

Future improvements to the FNISA system will therefore include 1) incorporation of the AP time gating process and subsequent background discrimination using a specialized sealed tube neutron generator and ultra-fast pulse processing electronics, 2) more sophisticated iron-doped targets in order to quantify the LLD of the system in the laboratory, 3) larger NaI(Tl) detectors, an array of multiple ultra-fast scintillation detectors, and likely an n-type HPGe detector used in parallel to further increase the SNR while providing excellent timing information and energy resolution, 4) connection of the system to a computer bank where the large data volume may be processed and filtered according to the selected collimation parameters, 5) overall component arrangement and phantom construction geared toward a specific *in vivo* diagnostic application as system sensitivity increases, 6) comprehensive dose assessment for the assay at hand, and 7) using the AP technique to not only reduce noise but to explore true 3D elemental imaging. Furthermore, the MCNP model will continue to be revised to reflect the upgrades made to the FNISA system, serving as a means to take the next step past what is accomplished in the laboratory – a form of feasibility assurance and validation as the material assay and imaging processes become more complex. For example, upon experimentally employing the AP technique as investigated in this paper using MCNP, further simulations can bridge the gap to other clinical applications (e.g. by defining a heterogeneous elemental distribution within the entire volume of an organ such as the liver within a reference man), thereby allowing for AP-driven projective tomography which may be tested in the laboratory in a follow-up study. As supported by the excellent agreement between the true and model FNISA systems in this paper, MCNP simulations will continue to provide an avenue for extrapolating to case-specific trace elemental sensitivity and specificity as the diagnostic roles APNEI could play in characterizing soft tissue disease become better defined.

4.5 Conclusion

A fundamental PGNA system utilizing DD fast neutrons has been constructed in order to determine the sensitivity to Fe-56 inelastic scatter gamma-rays originating from a target volume of iron in the irradiation cave. The system was correspondingly modeled in MCNP in order to validate the experimental photon spectra as well as to predict how the diagnostic yield of the system would improve upon simulated integration of the associated particle collimation process. The purpose of the FNISA apparatus and accompanying simulations was to build a basis of comparison between the two as well as to justify the pursuit of AP collimation in prompt gamma-ray neutron activation elemental assays by computing the expected increase and decrease in SNR and LLD, respectively. As expected, because the 2" NaI(Tl) detector used in the FNISA system was only physically collimated to the extent practicable during the 5-minute irradiation procedure, the 846.8 keV iron inelastic scatter gamma-ray peak was relatively unremarkable – with a SNR near unity and practical LLD of nearly 3.5 kg. However, upon employing an analog to associated particle spatiotemporal collimation in MCNP, the SNR and LLD of the system each improved by nearly a factor of 8. This study therefore provides a macroscopic frame of reference regarding how the AP technique may be used to improve the sensitivity of most PGNA systems, some of which already have documented roles in *in vivo* trace elemental analyses. The next step therefore is to translate the surrogate FNISA system to a true APNEI device tailored to a specific clinical application where soft tissue phantoms doped with biologically relevant concentrations of target elements will provide further opportunities for trace elemental quantification, sensitivity determination, and ultimately, 3D imaging of elemental distributions as diagnostic markers of disease etiology and progression.

CHAPTER 5. SUMMARY AND FUTURE DIRECTIONS

In general, the final sections of chapters 2, 3, and 4 outline the ongoing points of discussion pertaining to the topic of associated particle neutron elemental imaging (APNEI) and highlight opportunities for the improvement of study methods, predominantly relating to the development of optimized Monte Carlo models and the use of specialized imaging equipment and pulse processing hardware and protocols to achieve 3D images of elemental distributions at concentrations relevant to medical diagnostics. The body of work contributing to this document is relatively linear – each chapter building upon the preceding chapter. Conversely, the literature concerning the topic of applied indirect neutron imaging is fledgling and relatively disjointed; it is therefore the authors' wish that this document be a comprehensive collection of the academic and operational progress performed to date, as well as to take a meaningful step toward *in vivo* imaging which can one day make a difference for those afflicted with diseases characterized by changes in trace elemental homeostasis and insidious onset.

Because the subject of neutron imaging – particularly indirect elemental imaging with a focus on identifying disease signatures – is rather broad and multifaceted, the background included on the topic is correspondingly extensive. In this regard, chapter 1 functions to define the current state of neutron analytical methods as well as how an existing gap in the field of clinical diagnostic imaging may be filled by APNEI – a means for identifying elemental signatures of diseases such as cancer, Alzheimer's, and Parkinson's *in vivo*. By visualizing known compositional changes in a particular organ system, it is possible to more clearly specify a precise disease type or state of progression, offering opportunities for early diagnosis as well as revealing potential interventional pathways. And while delayed and prompt gamma-ray neutron activation analysis have been employed previously to quantitate elemental concentrations in humans and animals, section 1.5 introduces and describes the critical process by which neutron imaging of *trace* elemental concentrations is possible – the associated particle (AP) technique. Associated particles are a natural phenomenon which accompany the fusion reaction which takes place in sealed tube neutron generators, where if the path of travel of the associated ion is known, the path of travel of the source neutron may be inferred due to the conservation of momentum. This spatiotemporal method of neutron tagging is essentially a coincident event tracking method which allows background signals to be reduced and to therefore yield theoretically useful sensitivities to

elements such as iron which are important markers in disease etiology. And due to the physics of the associated particle tabulation process – with ultrafast timing and a pixelated imaging plate built into the sealed tube neutron generator – spatial information is collected for imaging in three dimensions. Such spatially-allocated elemental information would serve as a useful complement to existing diagnostic imaging modalities such as CT, PET, or MRI.

To begin to pursue the feasibility of the novel concept of APNEI, chapter 2 describes a Monte Carlo-based study which explores the sensitivity of a basic neutron elemental imaging system to an iron-containing voxel in the liver of a reference man, with an accompanying preliminary look at achievable projective resolution of the 1 cm³ liver voxel given realistic neutron source spot dimensions and timing system uncertainty. The MCNP model is based on a conceptual APNEI system design with an isotropic 2.45 MeV DD neutron source spot and HPGe detectors oriented anterior and posterior to the trunk of the body in order to maximize solid angle coverage at the height of the liver. Under the assumption of significant background reduction as a result of the associated particle collimation process, iron concentrations as low as 100 ppm were resolved in the simulated *in vivo* model. Given that healthy liver iron concentrations can be an order of magnitude higher and that diseased liver conditions can yield concentrations an order of magnitude higher still, the sensitivity of an APNEI system to small volumes of soft tissue was confirmed to be promising.

A benefit of the MCNP model was that a precise number of iron nuclei were detected for a given number of neutron histories. Therefore, it was a straightforward matter to resolve the location of each target nucleus in 3 dimensions and to thereby generate an image of the liver voxel with a cross sectional thickness of 1 cm. For example, at 1,000 ppm iron within the target voxel and 2E9 neutron histories, 4.0 ± 0.32 counts were registered from 847 keV iron inelastic scatter gamma-rays. The neutron flux tracking in MCNP also allowed for organ and whole body dose determination, where a 5 mSv equivalent dose to the liver was employed as a realistic clinical limitation. Normalizing to 5 mSv equivalent dose to the liver, the number of allowable neutron histories increased to 7.14E10 – with a corresponding increase in the number of iron gamma-ray counts to 142.8 ± 11.4 (i.e. 143 data points with which to construct an image of the iron distribution in the liver voxel). The image was then generated using projective geometrical calculations, a 2 mm neutron source spot diameter, and a 138 ps total timing error derived for a theoretical APNEI system previously described in the literature. The image illustrated excellent projective resolution

of < 1 cm, as expected, for an analytical procedure which would take only about one minute to perform and would yield a whole body effective dose of < 1 mSv. The study described in chapter 2 thereby laid the groundwork for the increasingly complex Monte Carlo models utilized in chapters 3 and 4 as well as for beginning preliminary prompt gamma-ray neutron analytical experimentation.

As a progression of the study performed in chapter 2, chapter 3 outlines many of the ways in which the initial feasibility study was improved to look at achievable APNEI projective and depth resolution in greater detail. The most significant additions to the Monte Carlo model were the incorporation of multiple, adjacent iron-containing voxels, a Gaussian-distributed neutron source spot with a FWHM of 2 mm, and a simulated timing protocol which approximated real world application of a sodium iodide or HPGe-based neutron elemental imaging system. A more readily available 225 ps timing resolution was selected and was used in tandem with a similarly conservative theoretical imaging plate with pixels each of 6.25 mm^2 . These changes allowed for simulations of projective tomography, where multi-slice images could be obtained for a given target array at a single interrogation angle. Due to the velocity of the DD neutrons and the total detector timing resolution, each slice corresponded to 0.5 cm in the depth dimension. As indicated in chapter 2, the study presented in chapter 3 reinforced the finding that projective resolution in an APNEI system with adequately fine neutron source spot and imaging plate pixel dimensions was < 1 cm and likely precise enough to offer actionable clinical information about trace elemental distributions. However, the study also revealed that depth resolution would become limiting – only offering spatial certainty around 3 cm. Furthermore, the decrease in neutron flux with depth in the target introduced image artifacts which would need to be algorithmically corrected in future imaging studies, perhaps limiting the technology to relatively superficial clinical applications as counting statistics decrease rapidly with depth. Nevertheless, in a qualitative sense, differences in iron concentration across the multi-voxel array were discernible in all dimensions – a characteristic which is only expected to improve as systems are developed with appropriate calibration curves and physical as well as electronic optimization. The remaining weakness of the studies described in chapters 2 and 3 was a lack of experimental trials as a means to explore many of the variables associated with elemental sensitivity and resolution of APNEI. The foray into fast neutron inelastic scattering analysis in chapter 4 was therefore a critical complement to the ongoing Monte Carlo simulation studies, offering opportunities for exploring the challenges associated with online

gamma spectroscopy, equipment selection, background discrimination, pulse processing, and layout of a fast neutron analytical system.

The final study contributing to this dissertation provided valuable insight into the practicality of performing elemental assays using fast neutrons and prompt gamma-ray detection technologies. As a step toward APNEI, fast neutron inelastic scatter analysis (FNISA) was employed using a NaI detector, digital spectrum analyzer, and physical collimation materials (i.e. lead and high-density polyethylene) in order to find the sensitivity of a fundamental DD-based neutron system to iron. At the same time, a model of the system was defined in MCNP to validate the experimental results as well as establish confidence in MCNP as a basis for predicting improvement in signal-to-noise ratio and detection limit as a result of associated particle collimation. As expected, given the limited detection capabilities of the FNISA system and poor NaI background discrimination characteristics, the operational lower limit of detection for iron was found to be 3.45 kg. This result was confirmed in the MCNP simulation, where the iron inelastic scatter gamma-ray peak at 847 keV was also relatively unremarkable – even for the macroscopic mass of iron placed in the irradiation cavity. Nevertheless, the physical and simulated photon spectra were quantitatively similar – particularly in the energy range of interest.

Therefore, the spatiotemporal background filtering method was included in the MCNP model in order to predict its effects on the system's operational performance. In short, the signal-to-noise ratio and sensitivity of the system were found to improve by nearly an order of magnitude upon implementation of an analog to the associated particle technique. Curve fittings of the MCNP iron inelastic scatter gamma-ray peaks using the least-squares method allowed for the calculation of the detection limit of the experimental system if the spatial and temporal collimation process inherent to AP gating were available in the laboratory – indicating a decrease in LLD from 3.45 kg to 0.44 kg. Though still a relatively large amount of iron when compared to *in vivo* concentrations, the improvement in sensitivity of the system was impressive, particularly given the limitation of the apparatus to a single 2" diameter NaI detector. The study presented in chapter 4 – though limited in technological complexity – therefore provides a valuable benchmark regarding the improvement of prompt gamma neutron analytical systems by employing the AP collimation technique.

Building upon the current, established uses of such neutron-based systems in biological assays, future studies will include more robust gamma-ray detection and spectroscopic equipment,

as well as utilize soft tissue phantoms for determining trace elemental sensitivities relevant to *in vivo* diagnostics. And upon successfully prototyping an APNEI device, the spatial information may be employed to not only reduce confounding gamma-ray signals and achieve clinically-valuable elemental detection limits, but to approximate to a high degree of certainty the coordinates of interaction of each tagged source neutron within the target volume – providing a means to map elemental distributions as a precursor to disease signature detection and differentiation.

LIST OF REFERENCES

1. Lovell, M.A., J.D. Robertson, W.J. Teesdale, J.L. Campbell, and W.R. Markesbery, *Copper, iron and zinc in Alzheimer's disease senile plaques*. J Neurol Sci, 1998. 158(1): p. 47-52.
2. Semenza, G.L., *Tumor metabolism: cancer cells give and take lactate*. J Clin Invest, 2008. 118(12): p. 3835-7.
3. Chwiej, J., *The use of cluster and discriminant analysis in the investigations of the role of trace metals in the pathogenesis of Parkinson's Disease*. J. of Trace Elements in Med and Biol, 2010. 24(2): p. 78-88.
4. Mitra, S., *Body composition to climate change studies – the many facets of neutron induced prompt gamma-ray analysis*. Environmental Sciences Department, Brookhaven National Lab, 2009: p. 1-10.
5. Garrett, R. and S. Mitra, *A feasibility study of in vivo 14-MeV neutron activation analysis using the associated particle technique*. Med Phys, 1991. 18(5): p. 916-20.
6. Cohn, S.H., K.J. Ellis, D. Vartsky, I. Zanzi, and J.F. Aloia, *Medical application of in vivo neutron activation analysis*. Medical Research Center, Brookhaven National Lab, 1978. Symposium on Nuclear Activation Techniques in the Life Sciences: p. 1-19.
7. Shypailo, R.J., B. Workeneh, and K.J. Ellis, *Assessment of the associated particle prompt gamma neutron activation technique for total body nitrogen measurement in vivo*. Journal of Radioanalytical Nuclear Chemistry, 2012. 296: p. 143-48.
8. Evans, C.J. and Q.B. Mutamba, *The use of associated particle timing based on the D + D reaction for imaging a solid object*. Appl Radiat Isot, 2002. 56(5): p. 711-6.
9. Koltick, D.S. and L.H. Nie, *Associated particle neutron imaging for elemental analysis in medical diagnostics*. IEEE Transactions on Nuclear Science, 2013. 60(2): p. 824-829.
10. Abel, M.R., D.S. Koltick, and L.H. Nie, *Associated particle neutron elemental imaging in vivo: a feasibility study*. Medical Physics, 2016. 43(11): p. 5964-5972.
11. Abel, M.R. and L.H. Nie, *Monte Carlo simulations of elemental imaging using the neutron associated particle technique*. Medical Physics, 2018. 45(4): p. 1631-1644.

12. Lankosz, M.W., M. Grzelak, B. Ostachowicz, A. Wandzilak, M. Szczerbowska-Boruchowska, P. Wrobel, E. Radwanska, and D. Adamek, *Application of the total reflection x-ray fluorescence method to the elemental analysis of brain tumors of different types and grades of malignancy*. Spectrochimica Acta, 2014. Part B(101): p. 98-105.
13. Valkovic, V., D. Sudac, and D. Matika, *Fast neutron sensor for detection of explosives and chemical warfare agents*. Appl. Radiat. Isot., 2010. 68: p. 888-892.
14. Verri, G., F. Mezzetti, A. Da Re, A. Bortolotti, L. Rapezzi, and V.A. Gribkov, *Fast neutron activation analysis of gold by inelastic scattering $^{197}\text{Au}(n,n'\gamma)^{197}\text{Au}^m$, by means of a plasma focus device*. Nukleonika, 2000. 45(3): p. 189-191.
15. Nonie, S.E. and K. Randle, *Cylindrical annular geometry in analysis by fast neutron inelastic scattering using an isotopic neutron source*. Chemical Geology, 1990. 80: p. 101-107.
16. Cohn, S.H. and R.M. Parr, *Nuclear-based techniques for the in vivo study of human body composition*. Clin. Phys. Physiol. Meas., 1985. 6(4): p. 275-301.
17. Tahir, S.N.A., D.R. Chettle, S.H. Byun, and W.V. Prestwich, *Feasibility of measuring selenium in humans using in vivo neutron activation analysis*. Phys. Meas., 2015. 36: p. 2217-2230.
18. Bhatia, C., S.H. Byun, D.R. Chettle, M.J. Inskip, and W.V. Prestwich, *A neutron activation technique for manganese measurements in humans*. Trace Elements in Medicine and Biology, 2015. 31: p. 204-208.
19. Chamberlain, M., J.L. Grafe, Aslam, S.H. Byun, D.R. Chettle, L.M. Egden, G.M. Orchard, C.E. Webber, and F.E. McNeill, *The feasibility of in vivo quantification of bone-fluorine in humans by delayed neutron activation analysis: a pilot study*. Physiol. Meas., 2012. 33: p. 243-257.
20. Mitra, S. and I. Dioszegi, *Development of an instrument for non-destructive identification of unexploded ordnance using tagged neutrons – a proof of concept study*. Environmental Sciences Department, Brookhaven National Lab, 2011: p. 1-3.
21. Ellis, K.J. and R.J. Shypailo, *COHN analysis: body composition measurements based on the associated particle imaging and prompt-gamma neutron activation analysis techniques*. Radioanalytical Nuclear Chemistry, 2008. 276(1): p. 79-83.

22. Gurusamy, K., M. Farquharson, C. Craig, and B. Davidson, *An evaluation study of trace element content in colorectal liver metastases and surrounding normal livers by X-ray fluorescence*. *BioMetals*, 2008. 21(3): p. 373-378.
23. Gholap, D.S., A. Izmer, B.D. Samber, J.T. van Elteren, V.S. Selih, R. Evens, K. De Schamphelaere, C. Janssen, L. Balcaen, I. Lindemann, L. Vincze, and F. Vanhaecke, *Comparison of laser ablation-inductively coupled plasma-mass spectrometry and micro-X-ray fluorescence spectrometry for elemental imaging in Daphnia magna*. *Analytica Chimica Acta*, 2010. 664: p. 19-26.
24. Pisonero, J., N. Bordel, and V.S. Smentkowski, *Elemental imaging*. *J. Anal. At. Spectrom.*, 2013. 28: p. 970-972.
25. Waldron, B., R.M. Moran, and B.J. Hurson, *Biopsy problems in patients with musculoskeletal tumors*. *I.J.M.S.*, 1990. 159(8): p. 246-248.
26. Scott, R.B. and L.A. Ballard, *Problems of cervical biopsy*. *Annals NY Acad. of Sci*, 1962. 16: p. 767-781.
27. Chagpar, A.B., R.C.G. Martin II, L.J. Hagendoorn, C. Chao, and K.M. McMasters, *Lumpectomy margins are affected by tumor size and histologic subtype but not by biopsy technique*. *The American Journal of Surgery*, 2004. 188: p. 399-402.
28. Xie, Y., Y. Fu, R. Ouwerkerk, S.M. Shea, T. Ehtiati, D. Kedziorek, G. Huang, W.D. Gilson, M. Solaiyappan, R. Krieg, and D.L. Kraitchman, *Dual CT and MRI in vivo tracking of stem cell therapy in peripheral artery disease*. *Journal of the American College of Cardiology*, 2010. 55(10): p. A176.
29. Jiang, R., X. Dong, W. Zhu, Q. Duan, Y. Xue, Y. Shen, and G. Zhang, *Combining PET/CT with serum tumor markers to improve the evaluation of histological type of suspicious lung cancers*. *PLoS ONE*, 2017. 12(9): p. 1-14.
30. Page, K.E., K.N. White, C.R. McCrohan, D.W. Killilea, and G.J. Lithgow, *Aluminum exposure disrupts elemental homeostasis in Caenorhabditis elegans*. *Metallomics*, 2012. 4: p. 512-522.
31. Sarita, P. G.J. Naga Raju, and S. Bhuloka Reddy, *Studies on changes in trace elemental content of serum of uterine cervix cancer patients using PIXE*. *J Radioanal Nucl Chem*, 2014. 302: p. 1501-1506.

32. Sun, W.H., R.A. Kreisle, A.W. Phillips, and W.B. Ershler, *In vivo and in vitro characteristics of interleukin 6-transfected B16 melanoma cells*. *Cancer Research*, 1992. 52: p. 5412-5415.
33. Motevich, I.G., N.D. Strekal, N.M. Papko, M.I. Glebovich, A.V. Shulha, and S.A. Maskevich, *Application of x-ray fluorescence analysis to determine the elemental composition of tissues from different ovarian neoplasms*. *Journal of Applied Spectroscopy*, 2015. 82(1): p. 98-103.
34. Amaral, A.F.S., M. Porta, D.T. Silverman, R.L. Milne, M. Kogevinas, N. Rothman, K.P. Cantor, B.P. Jackson, J.A. Pumarega, T. Lopez, A. Carrato, L. Guarner, F.X. Real, and N. Malats, *Pancreatic cancer risk and levels of trace elements*. *Gut*, 2012. 61: p. 1583-1588.
35. Farzin, L., M.E. Moassesi, F. Sajadi, and M.A.A. Faghieh, *Evaluation of trace elements in pancreatic cancer patients in Iran*. *ME Journal of Cancer*, 2013. 4(2): p. 79-86.
36. Theodorakou, C. and M. J. Farquharson, *Human soft tissue analysis using x-ray or gamma-ray techniques*. *Phys. Med. Biol.* 2008. 53: p. R111-R119.
37. Strumylaite, L., *Cancer risk in relation to exposure to trace elements*. *Environmental Medicine*, 2011. 14(1): p. 7-12.
38. Ouwerkerk, R., M.A. Jacobs, K.J. Macura, A.C. Wolff, V. Stearns, S.D. Mezban, N.F. Khouri, D.A. Bluemke, and P.A. Bottomley, *Elevated tissue sodium concentration in malignant lesions detected with non-invasive ²³Na MRI*. *Breast Cancer Res Treat*, 2007. 106: p. 151-160.
39. Wenstrup, D., W.D. Ehman, and W.R. Markesbery, *Trace element imbalances in isolated subcellular fractions of Alzheimer's disease brains*. *Brain Research*, 1990. 533(1): p. 125-131.
40. Wenk, G.L., *Neuropathologic changes in Alzheimer's Disease*. *J. Clin. Psychiatry*, 2003. 64(9): p. 7-10.
41. Tiraboschi, P., L.A. Hansen, L.J. Thal, and J. Corey-Bloom, *The importance of neuritic plaques and tangles to the development and evolution of AD*. *Neurology*, 2004. 62(11): p. 1984-1989.
42. Bouras, C., P.R. Hof, P. Giannakopoulos, J.P. Michel, and J.H. Morrison, *Regional distribution of neurofibrillary tangles and senile plaques in the cerebral cortex of elderly patients*. *Cereb. Cortex*, 1994. 4(2): p. 138-150.
43. Matsuda, H. and E. Imabayashi (Eds.), *Structural neuroimaging in Alzheimer's disease*. *Neuroimaging Diagnosis for AD and Other Dementias*. Tokyo, 2007: p. 21-38.

44. Ronson, C.E. (Ed.), *Alzheimer's diagnosis*. New York, 2011: p. 137-174.
45. Xudong, H., *Redox-active metals oxidative stress and Alzheimer's disease pathology*. Annals NY Acad. Sci., 2004. 1012: p. 153-163.
46. Jacobs, R.W., T. Duong, R.E. Jones, and A.B. Sebeibel, *A re-examination of aluminum in Alzheimer's disease*. Soc. Neurosci. Abstr., 1988. 14: p. 1083.
47. Panayi, A.E., N.M. Spyrou, and P. Part, *Differences in trace element concentrations between Alzheimer and "normal" human brain tissue using instrumental neutron activation analysis (INAA)*. Journal of Radioanalytical and Nuclear Chemistry, 2001. 249(2): p. 437-441.
48. Alcantar, N.A., J. Jimenez, and D. Morgan, *Direct observation of the kinetic mechanisms for AB peptide aggregation: towards elucidating Alzheimer plaque dissolution*. Alzheimer's & Dementia, 2010. 6(4): p. 247.
49. Dhanjal, J.K., S. Goyal, S. Sharma, R. Hamid, and A. Grover, *Mechanistic insights into mode of action of potent natural antagonists of BACE-1 for checking Alzheimer's plaque pathology*. Biochemical and Biophysical Research Communications, 2014. 443: p. 1054-1059.
50. Kalia, L.V. and A.E. Long, *Parkinson's disease*. Lancet, 2015. 386(9996): p. 896-912.
51. Sveinbjonsdottir, S., *The clinical symptoms of Parkinson's disease*. J. Neurochem., 2016. 139(1): p. 318-324.
52. Corboy, M.J., P.J. Thomas, and W.C. Wigley, *Aggresome formation*. Methods Mol. Biol., 2005. 301: p. 305-327.
53. Tredici, K.D. and J.E. Duda, *Peripheral Lewy body pathology in Parkinson's disease and incidental Lewy body disease: four cases*. Journal of Neurological Sciences, 2011. 310: p. 100-106.
54. Gtz, E.M., *The relevance of iron in the pathogenesis of Parkinson's disease*. Annals NY Acad. Sci., 2004. 1012: p. 193-208.
55. Dexter, D.T., A. Carayon, F. Javoy-Agid, Y. Agid, F.R. Wells, S.E. Daniel, A.J. Lees, P. Jenner, and C.D. Marsden, *Alterations in the levels of iron, ferritin and other trace metals in Parkinson's disease and other neurodegenerative diseases affecting the basal ganglia*. Brain, 1991. 114: p. 1953-1975.
56. Verma, A.K. A.K. Keshari, J. Raj, R. Kumari, T. Kumar, V. Sharma, T.B. Singh, S. Srivastava, and R. Srivastava, *Prolidase-associated trace elements (Mn, Zn, Co, and Ni) in patients with Parkinson's disease*. Biol. Trace Elem. Res., 2016. 171: p. 48-53.

57. Szczerbowska-Boruchowska, M., M. Lankosz, D. Adamek, J. Ostachowicz, A. Krygowska-Wajs, A. Szczudlik, S. Bohic, A. Simionovici, and J. Chwiej, *Determination of trace elements in Parkinson's diseased brain tissue using microbeam of synchrotron radiation*. Journal of Neurochemistry, 2003. 85: p. 23.
58. Sikorska, K., A. Bernat, and A. Wroblewska, *Molecular pathogenesis and clinical consequences of iron overload in liver cirrhosis*. Hepatobiliary Pancreat. Dis. Int., 2016. 15(5): p. 461-479.
59. Acharya, G.K., H. Liao, S. Frunza-Stefan, R. Patel, and M. Khaing, *Autoimmune hepatitis: diagnostic dilemma when it is disguised as iron overload syndrome*. Journal of Clinical and Experimental Hepatology, 2017. 7(3): p. 269-273.
60. Causey, M.W., S.R. Steele, Z. Farris, D.S. Lyle, and A.L. Beitler, *An assessment of different scoring systems in cirrhotic patients undergoing nontransplant surgery*. The American Journal of Surgery, 2012. 203: p. 589-593.
61. *Handout on Health: Osteoporosis*. National Institute of Arthritis and Musculoskeletal and Skin Diseases. Bethesda, MD 20892. HHS.gov. Retrieved 16 May 2015 (Archived).
62. *Prevention and Management of Osteoporosis*. WHO Technical Report Series 921. World Health Organization, Geneva, 2003.
63. *Screening for osteoporosis: U.S. preventive services task force recommendation statement*. Annals of Internal Medicine, 2011. 154(5).
64. Aaseth, J., G. Boivin, and O. Andersen, *Osteoporosis and trace elements – an overview*. Journal of Trace Elements in Medicine and Biology, 2012. 26: p. 149-152.
65. Specht, A.J., Y. Lin, J. Xu, M. Weisskopf, and L.H. Nie, *Bone lead levels in an environmentally exposed elderly population in Shanghai, China*. Science of the Total Environment, 2018. 626: 96-98.
66. Fleming, D.E.B., M.R. Gherase, and K.M. Alexander, *A miniature x-ray tube approach to measuring lead in bone using L-XRF*. X-Ray Spectrom., 2011. 40: p. 343-347.
67. Hoppin, J.A., A.C.A. Aro, P.L. Williams, H. Hu, and P.B. Ryan, *Validation of K-XRF bone lead measurement in young adults*. Environmental Health Perspectives, 1995. 103(1): p. 78-83.

68. Specht, A.J., Y. Lin, M. Weisskopf, C. Yan, H. Hu, J. Xu, and L.H. Nie, *XRF-measured bone lead (Pb) as a biomarker for Pb exposure and toxicity among children diagnosed with Pb poisoning*. *Biomarkers*, 2016. 21(4): p. 347-352.
69. Liu, Y., D. Rolle-McFarland, F. Mostafaei, Y. Zhou, Y. Li, W. Zheing, E. Wells, and L.H. Nie, *In vivo neutron activation analysis of bone manganese in workers*. *Physiol. Meas.*, 2018. 39: p. 1-9.
70. McNeill, F.E. F. Mostafaei, A. Pidruczny, and D.R. Chettle, *Correlation between fluorine content in tea and bone assessed neutron activation analysis in a Canadian urban population*. *J. Radioanal. Nucl. Chem.*, 2016. 309: p. 389-395.
71. Byrne, P., F. Mostafaei, Y. Liu, S.P. Blake, D. Koltick, and L.H. Nie, *The study of in vivo quantification of aluminum in human hand bone with a compact DD generator-based neutron activation analysis (NAA) system*. *Physiol. Meas.*, 2016. 37: p. 649-660.
72. St Pierre, T.G., P.R. Clark, W. Chua-Anusorn, A.J. Fleming, G.P. Jeffrey, J.K. Olynyk, P. Pootrakul, E. Robins, and R. Lindeman, *Noninvasive measurement and imaging of liver iron concentrations using proton magnetic resonance*. *Blood*, 2005. 105(2): p. 855-61.
73. *Iron*. Micronutrient Information Center, Linus Pauling Institute. Oregon State University, Corvallis, Oregon. April 2016. Retrieved 6 March 2018.
74. Greenwood, N.N. and A. Earnshaw, *Chemistry of the Elements. Iron, ruthenium, and osmium*. Pergamon Press, 1984. Burlington, MA; p. 1098-1104.
75. Kikuchi, G., T. Yoshida, and M. Noguchi, *Heme oxygenase and heme degradation*. *Biochemical and Biophysical Research Communications*, 2005. 338(1): p. 558-567.
76. Nanami, M., T. Ookawara, Y. Otaki, K. Ito, R. Moriguchi, K. Miyagawa, Y. Hasuike, M. Izumi, H. Eguchi, K. Suzuki, and T. Nakanishi, *Tumor necrosis factor- α -induced iron sequestration and oxidative stress in human endothelial cells*. *Arteriosclerosis, Thrombosis, and Vascular Biology*, 2005. 25(12): p. 2495-2501.
77. Roualt, T.A., *How mammals acquire and distribute iron needed for oxygen-based metabolism*. *PLoS Biology*, 2003. 1(3): p. E9.
78. Beguin, Y., M. Aapro, H. Ludwig, L. Mizzen, and A. Osterborg, *Epidemiological and nonclinical studies investigating effects of iron in carcinogenesis – a critical review*. *Critical Reviews in Oncology/Hematology*, 2014. 89(1): p. 1-15.

79. Fleming, R.E. and P. Ponka, *Iron overload in human disease*. N. Engl. J. Med., 2012. 366: p. 348-359.
80. Khalil, M., C. Langkammer, S. Ropele, K. Petrovic, M. Wallner-Blazek, M. Loitfelder, M. Jehna, G. Bachmaier, R. Schmidt, C. Enzinger, S. Fuchs, and F. Fazekas, *Determinants of brain iron in multiple sclerosis*. Neurology, 2011. 77: p. 1691-1697.
81. De Sanctis, V., A.T. Soliman, G. Candini, C. Kattamis, G. Raiola, and H. Elsedfy, *Liver iron concentration and liver impairment in relation to serum IGF-1 levels in thalassaemia major patients: a retrospective study*. Mediterr. J. Hematol. Infec. Dis., 2015. 7(1): 1-3.
82. Gerlach, M., D. Ben-Shachar, P. Riederer, and M.B.H. Youdim, *Altered brain metabolism of iron as a cause of neurodegenerative diseases?* J. of Neurochem., 1994. 63(3): p.793-807.
83. ICRP 1991 Recommendations of the International Commission on Radiological Protection. Publication No. 60, (Annals of the ICRP).
84. Novelize, R., *Squire's Fundamentals of Radiology*. Harvard University Press, 5th ed., 1997.
85. Krane, K., *Introductory Nuclear Physics*. Wiley, NJ, 1st ed., 1988.
86. Behling, R., *Modern diagnostic x-ray sources, technology, manufacturing, and reliability*. Boca Raton, FL: Taylor and Francis, CRC Press, 2015.
87. Gotzsche, P.C. and K.J. Jorgensen, *Screening for breast cancer with mammography*. Cochrane Database System, 2013. 6(6): CD001877.
88. Reed, S.J.B., *Electron microprobe analysis and scanning electron microscopy in geology*. Cambridge University Press, 2nd ed., 2005.
89. Reena, S., S.D. Sharma, S. Pawar, A. Chaubey, S. Kantharia, and D.A.R. Babu, *Radiation dose to patients from x-ray radiographic examinations using computed radiography imaging system*. Journal of Medical Physics, 2015. 40(1): p. 29-37.
90. Shrimpton, R.C., B.F. Wall, D.G. Jones, E.S. Fisher, M.C. Hiller, and G.M. Kendall, *A national survey of doses to patients undergoing a selection of routine x-ray examinations in English hospitals*. London: NRPB-R200; 1986.
91. Faulkner, K. and R.H. Corbett, *Reference doses and image quality in medical imaging*. Br. J. Radiol., 1998. 71: p. 1001-1002.
92. Laguitton, D. and W. Parrish, *Experimental spectral distribution versus Kramers' Law for quantitative x-ray fluorescence by the fundamental parameters method*. X-Ray Spectrometry, 1977. 6(4): p. 201.

93. Bushberg, J.T., *The Essential Physics of Medical Imaging*. Philadelphia: Lippincott Williams & Wilkins, 2nd ed., 2002.
94. Herman, G.T., *Fundamentals of computed tomography: Image reconstruction from projection*. Springer, 2nd ed., 2009.
95. Radon, J., *On the determination of functions from their integral values along certain manifolds*. IEEE Transactions on Medical Imaging, 1986. 5(4): p. 170-176.
96. Naidich, D.P., *Imaging of the airways: functional and radiologic correlations*. Philadelphia: Lippincott Williams & Wilkins, 1st ed., 2005.
97. Wichmann, J.L., *Cardiac CT – Radiology Reference Article*. Radiopaedia.org. Retrieved 22 November 2017.
98. Buckwalter, K.A., *Musculoskeletal imaging with multislice CT*. AJRonline.org. Retrieved 22 May 2010.
99. Hall, E.J. and D.J. Brenner, *Cancer risks from diagnostic radiology*. The British Journal of Radiology, 2008. 81(965): p. 362-378.
100. Furlow, B., *Radiation dose in computed tomography*. Radiologic technology, 2010. 81(5): p. 437-450.
101. *Do CT scans cause cancer?* Harvard Medical School, March 2013. Harvard.edu. Retrieved 9 December 2017.
102. NCRP 2009 Ionizing Radiation Exposure of the Population of the United States. Publication No. 160.
103. Brenner, D.J. and E.J. Hall, *Computed tomography – an increasing source of radiation exposure*. N. Engl. J. Med., 2007. 357(22): p. 2277-2284.
104. Redberg, R.F. and R. Smith-Bindman, *We are giving ourselves cancer*. New York Times, 30 January 2014.
105. Ritt, P., J. Sanders, and T. Kuwert, *SPECT/CT technology*. Clin. Transl. Imaging, 2014. 2: p. 445-457.
106. Khalil, M.M., *Elements of gamma camera and SPECT systems*. Heidelberg: Springer, 1st ed., 2010.
107. Saha, G.B., *Physics and radiobiology of nuclear medicine*. New York: Springer, 3rd ed., 2006.

108. Abdollahi, H., I. Shiri, Y. Salimi, M. Sarebani, R. Mehdinia, M.R. Deevband, S.R. Mahdavi, A. Sohrabi, and A. Bitarafan-Rajabi, *Radiation dose in cardiac SPECT/CT: an estimation of SSDE and effective dose*. *European Journal of Radiology*, 2016. 85: p. 2257-2261.
109. Miele, E., G.P. Spinelli, F. Tomao, A. Zullo, F. De Marinis, G. Pasciuti, L. Rossi, F. Zoratto, and S. Tomao, *Positron emission tomography (PET) radiotracers in oncology – utility of 18F-fluoro-deoxy-flucose (FDG)-PET in the management of patients with non-small-cell-lung cancer (NSCLC)*. *Journal of Experimental Clinical Cancer Research*, 2008. 27: p. 52.
110. Bailey, D.L., D.W. Townsend, P.E. Valle, and M.N. Maisey, *Positron emission tomography: basic sciences*. Secaucus, NJ: Springer-Verlag, 1st ed., 2005.
111. Carlson, N., *Physiology of behavior. Methods and Strategies of Research*. Pearson, 11th ed., 2012.
112. Mettler Jr., F.A., W. Huda, T.T. Yoshizumi, and M. Mahesh, *Effective doses in radiology and diagnostic nuclear medicine: a catalog*. *Radiology*, 2008. 248(1): p. 254-263.
113. Phelps, M.E., *PET: physics, instrumentation, and scanners*. Springer, 1st ed., 2006.
114. Minamimoto, R., A. Iagaru, M. Jamali, D. Holley, A. Barkhodari, S. Vasanawala, and G. Zaharchuk, *Conspicuity of malignant lesions on PET/CT and simultaneous time-of-flight PET/MRI*. *PLoS ONE*, 2017. 12(1): e0167262.
115. Shibuya, K., F. Nishikido, T. Tsuda, T. Kobayashi, C. Lam, T. Yamaya, E. Yoshida, N. Inadama, and H. Murayama, *Timing resolution improvement using DOI information in a four-layer scintillation detector for TOF-PET*. *Nuclear Instruments and Methods in Physics*, 2008. 593: p. 572-577.
116. Rogers, J.G., C. Moisan, E.M. Hoskinson, M.S. Andreaco, C.W. Williams, and R. Nutt, *A practical block detector for depth-encoding PET camera*. *IEEE Transactions on Nuclear Science*, 1996. 43(6): p. 3240-3248.
117. Seidel, J., J.J. Vaquero, S. Siegel, W.R. Gandler, and M.V. Green, *Depth identification accuracy of a three layer phoswich PET detector module*. *IEEE Transactions on Nuclear Science*, 1999. 46(3): p. 485-490.
118. Vandenbroucke, A., A.M.K. Foudray, P.D. Olcott, and C.S. Levin, *Performance characterization of a new high resolution PET scintillation detector*. *Phys. Med. Biol.*, 2010. 55: p. 5895-5911.

119. Kaul, M., S. Surti, P.R. Menge, and J.S. Karp, *Characterizing the spatial resolution performance of continuous and thick LYSO crystals*. IEEE Nuclear Science Symposium and Medical Imaging Conference, 2011.
120. Kaul, M., S. Surti, and J.S. Karp, *Combining surface treatments with shallow slots to improve the spatial resolution performance of continuous, thick LYSO detectors for PET*. IEEE Trans. Nucl. Sci., 2013. 60(1): p. 44-52.
121. Karp, J.S. and G. Muehllehner, *Performance of a position-sensitive scintillation detector*. Phys. Med. Biol., 1985. 30(7): p. 643-655.
122. *Magnetic Resonance Imaging*. University of Wisconsin. wisc.edu. Retrieved 14 March 2016.
123. Johnson, K.A., *Basic proton MR imaging: tissue signal characteristics*. Harvard Medical School. harvard.edu. Retrieved 14 March 2016.
124. *ACR-ASNR practice guideline for the performance and interpretation of magnetic resonance imaging (MRI) of the brain*. American Society of Neuroradiology. asnr.org. Retrieved 1 June 2018.
125. Husband, J., *Recommendations for cross-sectional imaging in cancer management: computed tomography, magnetic resonance imaging, and positron emission tomography*. Royal College of Radiologists, 2008.
126. Lee, S.C., K. Kim, J. Kim, S. Lee, J.H. Yi, S.W. Kim, K.S. Ha, and C. Cheong, *One micrometer resolution NMR microscopy*. Journal of Magnetic Resonance, 2001. 150: p. 207-213.
127. Jansen, J.F., W.H. Backes, K. Nicolay, and M.E. Kooi, *1H MR spectroscopy of the brain: absolute quantification of metabolites*. Radiology, 2006. 240(2): p. 318-332.
128. Huettel, S.A., A.W. Song, and G. McCarthy, *Functional magnetic resonance imaging*. Massachusetts: Sinauer, 2nd ed., 2009.
129. Schneider, M., *Characteristics of SonoVue*. Echocardiography, 1999. 16(7): p. 743-746.
130. Grinvald, A., E. Lieke, R. Frostig, C. Gilbert, and T. Wiesel, *Functional architecture of cortex revealed by optical imaging of intrinsic signals*. Nature, 1986. 324: p. 361-364.
131. Xu, M. and L.H. Wang, *Photoacoustic imaging in biomedicine*. Review of Scientific Instruments, 2006. 77(4): p. 041101.
132. Xia, J., J. Yao, and L.V. Wang, *Photoacoustic tomography: principles and advances*. Electromagnetic Waves, 2014. 147: p. 1-22.

133. Kim, C., T.N. Erpelding, L. Jankovic, M.D. Pashley, and L.V. Wang, *Deeply penetrating in vivo photoacoustic imaging using clinical ultrasound array system*. Biomed Opt Express, 2010. 1(1): p. 278-284.
134. Ku, G., B.D. Fornage, X. Jin, M. Xu, K.K. Hunt, and L.V. Wang, *Thermoacoustic and photoacoustic tomography of thick biological tissues toward breast imaging*. Technology in Cancer Research and Treatment, 2005. 4(5): p. 559-565.
135. Anderson, I.S., H.Z. Bilheux, and R. McGreevy, *Neutron imaging and applications: a reference for the imaging community*. Springer, 1st ed., 2009.
136. Anderson, J., S.B. Osborn, R.W. Tomlinson, D. Newton, J. Rundo, L. Salmon, and J.W. Smith, *Neutron activation analysis in man in vivo: a new technique in medical investigation*. Lancet, 1964. 2(7371): p. 1201-1205.
137. Brown, M. and P.B. Parks, *Neutron radiography in biologic media: techniques, observations, and implications*. Am. J. Roentgenol. Radium Ther. Nucl. Med., 1969. 106: p. 472-485.
138. Chettle, D.R. and J.H. Fremlin, *Techniques of in vivo neutron activation analysis*. Med. Biol., 1984. 29(9): p. 1011-1043.
139. Liu, Y., D. Koltick, P. Byrne, H. Wang, W. Zheng, and L.H. Nie, *Development of a transportable neutron activation analysis system to quantify manganese in bone in vivo: feasibility and methodology*. Phys. Meas., 2013. 34(12): p. 1593-1609.
140. Liu, Y., P. Byrne, H. Wang, D. Koltick, W. Zheng, and L.H. Nie, *A compact DD generator-based NAA system to quantify manganese (Mn) in bone in vivo*. Phys. Meas., 2014. 35(9): p. 1899-1911.
141. Boyd, G.E., *Method of activation analysis*. Nucleonics and Analytical Chemistry Symposium, 1949. 21(3): p. 335-347.
142. Kacperek, A., W.D. Morgan, A. Sivyer, J. Dutton, and C.J. Evans, *The application of a pulsed fast neutron beam to partial body in vivo activation analysis of minerals and trace elements*. Radioanalytical Nuclear Chemistry, 1990. 140(1): p. 141-151.
143. Seabury, E.H., C.D. Van Sicle, J.B. McCabe, C.J. Wharton, and A.J. Caffrey, *Neutron damage in mechanically-cooled high purity germanium detectors for field-portable prompt gamma neutron activation analysis (PGNAA) systems*. IEEE Nuclear Science Symposium and Medical Imaging Conference, 2013: p. 1-5.

144. Descovich, M., I.Y. Lee, P.N. Luke, R.M. Clark, M. Cromaz, M.A. Deleplanque, R.M. Diamond, P. Fallon, A.O. Macchiavelli, E. Rodriguez-Vieitez, F.S. Stephens, and D. Ward, *Effects of neutron damage on the performance of large volume segmented germanium detectors*. Nuclear Instruments and Methods in Physics, 2005. 545(1-2): p. 199-209.
145. Greenberg, R.R., P. Bode, and E.A.D.N. Fernandes, *Atomic Spectroscopy*. Spectrochimica Acta, 2011. 66: p. 193.
146. Sjostrand, N.G. and J.S. Story, *Cross sections and neutron yields for U^{233} , U^{235} , and Pu^{239} at 2200 m/sec*. Aktiebolaget Atomenergi, 1960: p. 1-34.
147. Axton, E.J., *The thermal neutron capture cross-section of ^{55}Mn* . Annals of Nuclear Energy, 1985. 12(6): p. 315-317.
148. *For chemical analysis: neutron activation analysis*. info@nmi3.edu. Retrieved 29 June 2018.
149. *Reduced decay schemes: $^{25}Mn^{56}$* . nucleonica.com. Retrieved 29 June 2018.
150. Holbert, K.E., *EEE460-Handout: Neutron reactions*. holbert.faculty.asu.edu. Retrieved 29 June 2018.
151. Mostafaei, F., S.P. Blake, Y. Liu, D.A. Sowers, and L.H. Nie, *Compact DD generator-based neutron activation analysis (NAA) system to determine fluorine in human bone in vivo: a feasibility study*. Phys. Meas., 2015. 36(10): p. 2057-2067.
152. *Postgraduate educational course in radiation protection and the safety of radiation sources (PGEC)*. International Atomic Energy Agency, Vienna, 2002. slideplayer.com. Retrieved 2 July 2018.
153. Yates, S.W., A.J. Filo, C.Y. Cheng, and D.F. Coope, *Elemental analysis by gamma-ray detection following inelastic neutron scattering*. Journal of Radioanalytical Chemistry, 1978. 46: p. 343-355.
154. Wylie, A.W. and P.L. Eisler, *Prospecting with neutrons*. Philips Technical Review, 1969. 30(4): p. 97-105.
155. Peisach, M., *Nondestructive activation analysis: prompt techniques*. New York: Elsevier, 1981.
156. Herzenberg, C.L., N.M. O'Fallon, B.S. Yarlagadda, R.W. Doering, C.E. Cohn, K.G. Porges, and D. Duffery, *Neutron-induced gamma spectrometry for on-line compositional analysis in coal conversion and fluidized-bed combustion plants*. Int. Conf. on Nucl. Meth. in Env. and Energy Res., 1977: p. 1-11.

157. Gehrke, R.J. and W.A. Propp, *Performance test results of noninvasive characterization of RCRA surrogate waste by prompt gamma neutron activation analysis*. Idaho National Engineering and Environmental Laboratory, 1997: p. 1-10.
158. Hall, J.M., S. Asztalos, P. Bilotto, J. Church, M.A. Descalle, T. Luu, D. Manatt, G. Mauger, E. Norman, D. Petersen, J. Pruet, S. Prussin, and D. Slaughter, *The nuclear car wash: neutron interrogation of cargo containers to detect hidden SNM*. Nuclear Inst. and Methods in Physics Research, B, 2007. 261(1-2): p. 337-340.
159. Martin, R.C., J.B. Knauer, and P.A. Balo, *Production, distribution, and applications of californium-252 neutron sources*. Applied Radiation and Isotopes, 1999. 53(4-5): p. 785-792.
160. Arai, M. and K. Crawford, *Neutron imaging and applications*. Springer, 2nd ed., 2009.
161. Watanabe, N., *Neutronics of pulsed spallation neutron sources*. Reports on Progress in Physics, 2003. 66(3): p. 339-381.
162. Csikai, J., *Utilization of intense neutron generators in science and technology*. Nuclear Inst. and Methods in Physics Research, A, 1989. 280(2): p. 233-250.
163. Drosig, M., *Complete Monte Carlo simulation of neutron scattering experiments*. AIP Conference Proceedings, 2011. 1412(1): p. 86-92.
164. Lindstrom, R.M. and Z. Revay, *Prompt gamma neutron activation analysis (PGAA): recent developments and applications*. J. Radioanal. Nucl. Chem., 2017. 314: p. 843-858.
165. Liu, Y., F. Mostafaei, D. Sowers, M. Hsieh, W. Zheng, and L.H. Nie, *Customized compact neutron activation analysis system to quantify manganese (Mn) in bone in vivo*. Physiol. Meas., 2017. 38: p. 452-465.
166. Mitra, S., *Identification of UXO using the associated particle neutron time-of-flight technique, final report*. Brookhaven National Laboratory, 2011. 2: p. 1-34.
167. Mitra, S., *Applications of the associated particle neutron time-of-flight interrogation technique – from sheep to unexploded ordnance*. AIP Conference Proceedings, 2013. 1525: p. 422-427.
168. DiPrete, D.P. and R.A. Sigg, *Neutron activation analysis detection limits using ²⁵²Cf sources*. Transactions of the American Nuclear Society, 2000. 82: p. 97-98.
169. Zamboni, C.B., L.C. Oliveira, and L. Dalaqua Jr., *Diagnostic application of absolute neutron activation analysis in hematology*. IPEN/CNEN-SP, 2004: p. 1-12.

170. Frejaville, J.P. and P. Kamoun (eds.), *Guide des examens de laboratoire*. Paris: Flammarion, 1981.
171. Kapadia, A., *Accuracy and patient dose in neutron stimulated emission computed tomography for diagnosis of iron overload: simulations in GEANT4*. Duke University, 2007.
172. Kapadia, A.J., A.C. Sharma, G.D. Tourassi, J.E. Bender, C.R. Howell, A.S. Crowell, M.R. Kiser, B.P. Harrawood, R.S. Pedroni, and C.E. Floyd, Jr., *Neutron stimulated emission computed tomography for diagnosis of breast cancer*. IEEE Transactions on Nuclear Science, 2008. 55(1): p. 501-509.
173. Agasthya, G.A., B.C. Harrawood, J.P. Shah, and A.J. Kapadia, *Sensitivity analysis for liver iron measurement through neutron stimulated emission computed tomography: a Monte Carlo study in GEANT4*. Phys. Med. Biol., 2012. 57: p. 113-126.
174. Viana, R.S., G.A. Agasthya, H. Yoriyaz, and A.J. Kapadia, *3D element imaging using NSECT for the detection of renal cancer: a simulation study in MCNP*. Phys. Med. Biol., 2013. 58: p. 5867-5883.
175. Sharma, A.C., G.D. Tourassi, A.J. Kapadia, B.P. Harrawood, J.E. Bender, A.S. Crowell, M.R. Kiser, C.R. Howell, and C.E. Floyd Jr., *Design and development of a high-energy gamma camera for use with NSECT imaging: feasibility for breast imaging*. IEEE Transactions on Nuclear Science, 2007. 54(5): p. 1498-1505.
176. Price, A., W. Harris, and A. Kapadia, *Using associated particle imaging and time-of-flight spectroscopy for eliminating tomographic imaging for NSECT: a simulation study*. Med. Phys., 2015. 42(6): p. 3715.
177. Robison, G., T. Zakharova, S. Fu, W. Jiang, R. Fulper, R. Barrea, M.A. Marcus, W. Zheng, and Y. Pushkar, *X-ray fluorescence imaging: a new tool for studying manganese neurotoxicity*. PLoS ONE, 2012. 7(11): p. 1-9.
178. Robison, G., T. Zakharova, S. Fu, W. Jiang, R. Fulper, R. Barrea, W. Zheng, and Y. Pushkar, *X-ray fluorescence imaging of the hippocampal formation after manganese exposure*. Metallomics, 2013. 5: p. 1554-1565.
179. Zheng, W., H. Nichol, S. Liu, Y.N. Cheng, and E.M. Haacke, *Measuring iron in the brain using quantitative susceptibility mapping and x-ray fluorescence imaging*. NeuroImage, 2013. 78(1): p. 68-74.

180. Du, G., T. Liu, M.M. Lewis, L. Kong, Y. Wang, J. Connor, R.B. Mailman, and X. Huang, *Quantitative susceptibility mapping of the midbrain in Parkinson's disease*. *Movement Disorders*, 2015. 31(3): p. 317-324.
181. Acosta-Cabronero, J., M.J. Betts, A. Cardenas-Blanco, S. Yang, and P.J. Nestor, *In vivo MRI mapping of brain iron deposition across the adult lifespan*. *Journ. of Neurosci.*, 2016. 36(2): p. 364-374.
182. Langkammer, C., F. Schweser, N. Krebs, A. Deistung, W. Goessler, E. Scheurer, K. Sommer, G. Reishofer, K. Yen, F. Fazekas, S. Ropele, and J.R. Reichenbach, *Quantitative susceptibility mapping (QSM) as a means to measure brain iron? A post mortem validation study*. *NeuroImage*, 2012. 62(3): p. 1593-1599.
183. Wu, Y., J.P. Hurley, Q. Ji, J. Kwan, and K.N. Leung, *Development of a RF-driven neutron generator for associated particle imaging*. *IEEE Transactions of Nuclear Science*, 2009. 56(3): p. 1306-1311.
184. Reijonen, J., *Compact neutron generators for medical, homeland security, and planetary exploration*. *Proceedings of the IEEE*, 2005: p. 49-53.
185. *Neutron generator models DD-109M & DD-110M operation manual*. Adelphi Technology, Inc., 2016.
186. Fedorin, M.A. and B.G. Titov, *Method of radial sounding and elemental analysis of formations during well logging using inelastic scattering gamma time-of-flight spectrometry*. *Russian Geology and Geophysics*, 2010. 51(12): p. 1295-1303.
187. Mitra, S., J.E. Wolff, and R. Garrett, *Calibration of a prototype in vivo total body composition analyser using 14 MeV neutron activation and the associated particle technique*. *Appl. Radiat. Isot.*, 1998. 49(5-6): p. 537-539.
188. ICRP 2007 Recommendations of the International Commission on Radiological Protection. Publication No. 103, (Annals of the ICRP).
189. Peto, G.C., *Prospects of imaging by associated particle timing with D+D and D+T neutrons*. *Appl. Radiat. Isot.*, 1998. 49(5-6): p. 553-4.
190. Montague, J.H. and E.B. Paul, *Cross Sections for the production of gamma rays by the inelastic scattering of neutrons from iron*. *Nuclear Physics*, 1961. 30: p. 93-109.

191. Neal, J.S., L.A. Boatner, N.C. Giles, L.E. Halliburton, and S.E. Derenzo, *Comparative investigation of the performance of ZnO-based scintillators for use as α -particle detectors*. Nuclear Instruments and Methods in Physics Research, A, 2006. 568: p. 803.
192. Cooper, J.C., D.S. Koltick, J.T. Mihalcz, and J.S. Neal, *Evaluation of ZnO(Ga) coatings as alpha particle transducers within a neutron generator*. Nuclear Instruments and Methods in Physics Research, A, 2003. 505(1): p. 498-501.
193. Gorin, A., K. Kuroda, I. Manuilov, A. Riazantsev, T. Ishikawa, H. Kamitsubo, M. Suzuki, and H. Toyokawa, *Fundamental properties of YAP imager*. Nuclear Instruments and Methods in Research, A, 2003. 510: p. 76.
194. Koltick, D.S., S.Z. Zane, M. Lvovsky, E.K. Mace, S.M. McConchie, and J.T. Mihalcz, *Characterization of an associated particle neutron generator with ZnO:Ga alpha-detector and active focusing*. IEEE Transactions on Nuclear Science, 2009. 56(3): p. 1301-1305.
195. Lehmann, W., *Edge emission of n-type conducting ZnO and CdS*. Solid State Electronics, 1966. 9: p. 1107-1110.
196. Bourret-Courchesne, E.D., S.E. Derenzo, and M.J. Weber, *Development of ZnO:Ga as an ultra-fast scintillator*. Nucl. Inst. and Methods, 2009. 601: p. 358-363.
197. Ji, Q., B. Ludewigt, J. Wallig, W. Waldron, and J. Tinsley, *Development of a time-tagged neutron source for SNM detection*. Physics Procedia, 2015. 66: p. 105-110.
198. ICRU 1989 Tissue Substitutes in Radiation Dosimetry and Measurement. Report No. 44, (Bethesda: International Commission on Radiation Units and Measurements).
199. ICRP 1975 Report of the Task Group on Reference Man. Publication No. 23, (New York: International Commission on Radiological Protection).
200. NCRP 1971 Protection Against Neutron Radiation. Report No. 38 (Bethesda: National Council on Radiation Protection and Measurements).
201. ICRP 1973 Data for Protection Against Ionizing Radiation from External Sources. Publication No. 21, (New York: International Commission on Radiological Protection).
202. Kwon, S.G., K.E. Kim, C.W. Ha, P.S. Moon, and C.C. Yook, *Calculation of neutron and gamma-ray flux-to-dose rate conversion factors*. Journal of the Korean Nuclear Society, 1980. 12(3): p. 171-79.
203. *ANSI 1977 Neutron and Gamma-Ray Flux-to-Dose Rate Factors*. American Nuclear Society. ANSI/ANS-6.1.1-1977.

204. Jurgensen, R.C., A.J. Donnelly, and M.P. Dolciani, *Modern geometry: structure and method*. Boston, MA: Houghton-Mifflin, 1963. 22.
205. Evans, C.J., G.C. Peto, S. Al-Lehyani, and J.B. Darko, *The elemental analysis of the human body using associated particle timing based on the D+D reaction*. Appl. Radiat. Isot., 1998. 49(5-6): p. 549-51.
206. Allen, F.J., A.T. Futterer, and W.P. Wright, *Neutron transmission versus thickness for some common materials*. Ballistic Research Laboratories, Report No. 1174, 1962, pp. 21-22.
207. Wharton, C.J., E.H. Seabury, D.L. Chichester, A.J. Caffrey, J. Simpson, and M. Lemchak, *X-ray measurements of a Thermo Scientific P385 DD neutron generator*. AIP Conference Proceedings, 2011. 1336: p. 538-540.
208. Standards for protection against radiation, Title 10, Part 20, Code of Federal Regulations.
209. Sturgeon, P. and A. Shoden, *Total liver storage iron in normal populations of the USA*. Am. J. Clin. Nutr., 1971. 24(4): p. 469-74.
210. Lutt, W.W., *Hepatic circulation: physiology and pathophysiology*. San Rafael (CA): Morgan & Claypool Life Sciences, 2009. Chapter 4.
211. Porth, C.M., *Essentials of pathophysiology: concepts of altered health states*. Philadelphia: Wolters Kluwer Health, 2011: p. 281.
212. Bassett, M.L., J.W. Halliday, and L.W. Powell, *Value of hepatic iron measurements in early hemochromatosis and determination of the critical iron level associated with fibrosis*. Hepatology, 1986. 6(1): p. 24-29.
213. St Pierre, T.G., P.R. Clark, and W. Chua-Anusorn, *Measurement and mapping of liver iron concentrations using magnetic resonance imaging*. Ann. NY Acad. Sci., 2005. 1054: p. 379-385.
214. Conrad, M.E. and J.N. Umbreit, *Disorders of iron metabolism*. N. Engl. J. Med., 2000. 342(17): p. 1293-1294.
215. Vartsky, D., L. Wielopolski, K.J. Ellis, and S.H. Cohn, *Use of nuclear resonant scattering of gamma rays for in vivo measurement of iron*. Conference on X- and gamma-ray sources and applications, 1981: p. 1-18.
216. Rhodes, E., C.E. Dickerman, and C.W. Peters, *Associated particle sealed-tube neutron probe for characterization of materials*. Argonne National Lab, 1993(Active Probe Technologies Conference of International Symposium on Substance Identification Technologies): p. 1-13.

217. Gardner, R.P., C.W. Mayo, W.A. Metwally, W. Zhang, W. Guo, and A. Shehata, *Coincidence prompt gamma-ray neutron activation analysis*. Nuclear Engineering Department, North Carolina State University, 2002: p. 1-22.
218. Cohn, S.H., *In vivo neutron activation analysis: a new technique in nutritional research*. Journal of Nutritional Biochemistry, 1992. 3(8): p. 378-86.
219. Leonard, S.S., J.J. Bower, and X. Shi, *Metal-induced toxicity, carcinogenesis, mechanisms, and cellular responses*. Mol and Cell Biochem, 2004. 255: p. 3-10.
220. Lamy, P., A. Durigova, and W. Jacot, *Iron homeostasis and anemia markers in early breast cancer*. Clinica Chimica Acta, 2014. 434(1): p. 34-40.
221. Bergaoui, K., N. Reguigui, C.K. Gary, C. Brown, J.T. Cremer, J.H. Vainionpaa, and M.A. Piestrup, *Development of a new deuterium-deuterium (D-D) neutron generator for prompt gamma-ray neutron activation analysis*. Appl. Radiat. Isot., 2014. 94: p. 319-327.
222. Cooper, R.J., M. Amman, P.N. Luke, and K. Vetter, *A prototype high purity germanium detector for high resolution gamma-ray spectroscopy at high count rates*. Nuclear Instruments and Methods in Physics, 2015. 795: p. 167-173.
223. Hamamatsu Photonics, *Multianode Photomultiplier Tube Assembly H7546A, H7546B*. U.S. Patent 5,410,211, Sep. 2007.
224. Friedrich, S., S.F. Terracol, T. Miyazaki, O.B. Drury, Z.A. Ali, M.F. Cunningham, T.R. Niedermayr, T.W. Barbee, Jr., J.D. Batteux, and S.E. Labov, *Design of a multi-channel ultra-high resolution superconducting gamma-ray spectrometer*. Lawrence Livermore National Lab, 2004. (SPIE Conf. Proc UCRL-CONF-208296): p. 1-11.
225. Hausladen, P.A., J.S. Neal, J.T. Mihalcz, *An alpha particle detector for a portable neutron generator for the nuclear materials identification system (NMIS)*. Nucl. Inst. and Methods, 2005. 241(1-4): p. 835-838.
226. Fallu-Labruyere, A., H. Tan, W. Hennig, and W.K. Warburton, *Time resolution studies using digital constant fraction discrimination*. Nucl. Inst. and Methods, 2007. 579(1): p. 247-251.
227. Tunnell, L.N., *Data simulation for the associated particle imaging system*. Special Technologies Laboratory, 1994. (Conf. Proc CONF-940216--2): p. 1-6.
228. Zhang, X., J.P. Hayward, J.W. Cates, P.A. Hausladen, M.A. Laubach, J.E. Sparger, and S.B. Donnal, *Benchmarking the Geant4 full system simulation of an associated alpha-particle detector for use in a D-T neutron generator*. Appl. Radiat. Isot., 2012. 70: p. 1485-1493.

229. Yan, Y., L. Xiaolong, W. Zheng, Y. Siqi, L. Changlin, W. Junrun, W. Jie, and Y. Zeen, *Study on the method with associated particle for measuring the neutron yield of D-D neutron generator*. Nucl. Inst. and Methods, 2015. 773: p. 52-55.
230. Jenkins, D.G., R. Glover, R.D. Herzberg, A.J. Boston, C. Gray-Jones, and A. Nordlund, *Proof-of-principle for fast neutron detection with advanced tracking arrays of highly segmented germanium detectors*. Nucl. Inst. and Methods, 2009. 602: p. 457-460.
231. Cates, J.W., J.P. Hayward, X. Zhang, P.A. Hausladen, and B. Dabbs, *Timing resolution study of an associated particle detector for fast neutron imaging*. IEEE Transactions of Nuclear Science, 2012. 59(4): p. 1750-1756.
232. Abu-Talib, M., Z. Alamoudi, and A.M. Hassan, *Delayed and prompt gamma-ray neutron activation analysis of Saudi aluminium and iron alloys using isotopic neutron sources*. Rad. Phys. and Prot. Conf., 2004. EG0500266: p. 139-147.
233. Dahing, L.N., R. Yahya, R. Yahya, and H. Hassan, *Non destructive multi elemental analysis using prompt gamma neutron activation analysis techniques: preliminary results for concrete sample*. AIP Conf. Proc., 2014. 1614: p. 20-25.
234. Stamatelatos, I.E., K. Kasviki, S. Green, M. Gainey, J. Kalef-Ezra, and A. Beddoe, *Prompt-gamma neutron activation analysis facility for in vivo body composition studies in small animals*. Analytical and Bioanalytical Chemistry, 2004. 379(2): p. 192-197.
235. Carron, N.J., *An introduction to the passage of energetic particles through matter*. CRC Press, 1st ed., 2006: p. 308.
236. Kapadia, A.J., B.P. Harrawood, and G.D. Tourassi, *GEANT4 simulation of NSECT for detection of iron overload in the liver*. SPIE Conf. Proc., 2008. 6913: p. 691309-691309-7.
237. Gouget, B., C. Sergeant, Y. Llabador, G. Deves, M.H. Vesvres, M. Simonoff, and J. Benard, *Trace metals and cancer: the case of neuroblastoma*. Nucl Inst and Methods in Physics, 2001. 181(1-4): p. 465-469.
238. Abel, M.R. and L.H. Nie, *Improving the sensitivity of fast neutron inelastic scatter analysis to iron using associated particle collimation*. Nucl Inst and Methods in Physics Section A: Accelerators, Spectrometers, Detectors and Associated Equipment, 2019. Submitted.
239. *Integrated Scintillation Detectors*. Saint-Gobain Ceramics & Plastics, Inc., 2017.

240. Gardner, R.P., E. Sayyed, Y. Zheng, S. Hayden, and C.W. Mayo, *NaI detector neutron activation spectra for PGNAA applications*. Applied Radiation and Isotopes, 2000. 53: p. 483-497.
241. Coyne, M.D., C. Neumann, X. Zhang, P. Byrne, Y. Liu, C.M. Weaver, and L.H. Nie, *Compact DD generator-based in vivo neutron activation analysis (IVNAA) system to determine sodium concentrations in human bone*. Physiol. Meas., 2018. 39(5): 055004.
242. Chadwick, M.B., et al., *ENDF / B-VII.1 Nuclear data for science and technology: cross sections, covariances, fission product yields and decay data*. Nuclear Data Sheets, 2011. 112: p. 2887-2996.
243. Metwally, W.A., R.P. Gardner, and A. Sood, *Gaussian broadening of MCNP pulse height spectra*. Transactions of the American Nuclear Society, 2004. p. 1-3.
244. Hakimabad, H.M., H. Panjeh, and A. Vejdani-Noghreiyani, *Response function of a 3x3 in. NaI scintillation detector in the range of 0.081 to 4.438 MeV*. Asian J. Exp. Sci., 2007. 21(2): p. 233-237.
245. Mouhti, I., A. Elanique, and M.Y. Messous, *Monte Carlo modelling of a NaI(Tl) scintillator detector using MCNP simulation code*. J. Mater. Environ. Sci., 2017. 8(12): p. 4560-4565.
246. Staples, P., T. Prettyman, and J. Lestone, *Imaging of heterogeneous materials by prompt gamma-ray neutron activation analysis*. Nucl. Inst. and Methods in Phys., 1999. 422(1): p. 906-908.
247. Congedo, T.V., A.R. Dulloo, F.H. Ruddy, D.H. Weigie, R.P. Williams, and J.G. Seidel, *Treatability study using prompt gamma neutron activation analysis (PGNAA) technology phase I*. U.S. Department of Energy, 1995. DOE/MC/20177-5047.
248. Smith, Jr., H.A. and M. Lucas, *Gamma-ray detectors*. Los Alamos National Laboratory, 1991.
249. Zhang, X., A.J. Specht, M.G. Weisskopf, J. Weuve, and L.H. Nie, *Quantification of manganese and mercury in toenail in vivo using portable x-ray fluorescence (XRF)*. Biomarkers, 2018. 23(2): p. 154-160.